GPS and Seismicity Constraints on the Current Tectonics of the Northern Canadian Cordillera

by

Lucinda J. Leonard
B.A., Trinity College Dublin, 2001

A Dissertation Submitted in Partial Fulfillment of the
Requirements for the Degree of

DOCTOR OF PHILOSOPHY

in the School of Earth and Ocean Sciences

University of Victoria

GPS and Seismicity Constraints on the Current Tectonics of the Northern Canadian Cordillera

by

Lucinda J. Leonard
B.A., Trinity College Dublin, 2001

Supervisory Committee

Dr. Roy D. Hyndman (Pacific Geoscience Centre, Geological Survey of Canada and School of Earth and Ocean Sciences)
Supervisor

Dr. George D. Spence (School of Earth and Ocean Sciences)
Co-Supervisor

Dr. Kelin Wang (Pacific Geoscience Centre, Geological Survey of Canada and School of Earth and Ocean Sciences)
Departmental Member

Dr. Herb Dragert (Pacific Geoscience Centre, Geological Survey of Canada and School of Earth and Ocean Sciences)
Departmental Member

Dr. Eileen Van der Flier-Keller (Department of Geography)
Outside Member

Dr. Thomas James (Pacific Geoscience Centre, Geological Survey of Canada and School of Earth and Ocean Sciences)
Additional Member

Supervisory Committee

Dr. Roy D. Hyndman
Supervisor

Dr. George D. Spence
Co-Supervisor

Dr. Kelin Wang
Departmental Member

Dr. Herb Dragert
Departmental Member

Dr. Eileen Van der Flier-Keller
Outside Member

Dr. Thomas James
Additional Member

ABSTRACT

This thesis presents new precision Global Positioning System (GPS) data, new analyses of earthquake deformation rates, and geological analyses, which constrain current deformation in Yukon and adjacent areas of the northern Cordillera. The integration of these data with additional thermal constraints facilitates the large-scale characterization of intense deformation associated with the collision of the composite oceanic-continental Yakutat block with North America in the corner of the Gulf of Alaska. Two main approaches are used to constrain the first-order current tectonic deformation pattern: (1) high-precision continuous and campaign GPS measurements; (2) seismic deformation rates calculated using earthquake statistics from the seismicity catalogue. The oblique Yakutat-North America collision is mainly accommodated by thrust and strike-slip faulting in the Saint Elias region, but associated deformation extends a great distance (> 800 km) into the North America crust of eastern Alaska, Yukon and western Northwest Territories. The data indicate westward motion and counter-clockwise rotation of the southeastern Alaska forearc along the arc of the right-lateral Denali fault. Right-lateral transpression north of the Denali fault in Alaska is accommodated by clockwise rotation of a number of NE-trending crustal blocks bounded by sinistral strike-slip faults. To the northeast of the Yakutat collision, GPS data indicate a northeastward crustal motion across the Cordillera towards the eastern foldbelt.

Earthquake mechanisms indicate strain accommodation mainly by thrusting in the Mackenzie Mountains and N-S dextral strike-slip faulting in the Richardson Mountains. It is likely that a small northward component of motion is transferred further north to the offshore Mackenzie Delta region, where infrequent large earthquakes may result, despite little historical seismicity.

An additional study is presented on the use of quantitative estimates of coastal coseismic subsidence in great earthquakes at the Cascadia subduction zone. Seismic hazard assessments for Cascadia megathrust earthquakes are largely based on the rupture area predictions of dislocation models constrained by geodetic and thermal data. The models for the 1700 great Cascadia earthquake are tested against compiled coastal coseismic subsidence for past great earthquakes, as estimated from paleoelevation studies. Models for strain accumulation of 550-800 years (in the range of event frequency from marsh dating and offshore turbidites), predict coastal subsidence in good agreement with marsh paleoseismic data, except that discrepancies occur at the ends of the subduction zone. Estimated slip from comparisons of dislocation models with marsh coseismic data for the 1700 event is consistent with the magnitude 9 earthquake indicated by Japanese tsunami records.

TABLE OF CONTENTS

APPENDICES (Included on Compact Disc):

LIST OF TABLES

LIST OF FIGURES

ACKNOWLEDGEMENTS

"The most incomprehensible thing about the world is that it is at all comprehensible."
Albert Einstein

Many people are owed my gratitude for the essential parts they played, large or small, in helping me complete this thesis, and in doing so, try to understand the world a little better. I would like to thank my supervisor, Roy Hyndman, firstly for enabling me to work on such an interesting project in the wild and beautiful Yukon, and also for his direction, support, open door, and inspiring ideas. I thank the rest of my supervisory committee - George Spence, Herb Dragert, Tom James, Kelin Wang, and Eileen Van der Flier-Keller – for their encouragement and helpful comments. Thanks also to my external examiner, Kristine Larson, for her time and suggestions. Huge thanks are due to Stéphane Mazzotti, for generously sharing his knowledge of GPS and deformation, and for not closing the door to the many questions.

GPS fieldwork played a large role in this thesis, and would not have been possible without the technical expertise, time and support of Mike Schmidt. Also, a big thank-you to Lisa Nykolaishen, for preparing equipment, and for sharing the delights, hardships, and adventures of northern fieldwork! The Yukon Geological Survey provided northern help - thanks to Charlie Roots for the use of the crew house in Dawson City, and to Craig Hart, John Mair, and Lara Lewis, for following us around the Yukon, and for the bug shelter, beer and fun on Canada Day at MacMillan Pass. And for keeping away the bears with the helicopter! Thank-you also to the anonymous construction workers for lending us a spare tyre (and changing it) after our 2nd puncture on the remote Dempster Highway, and Greg and Murray of Ross River for protecting us at the "bear site". There was no fieldwork involved in the Cascadia part of the thesis, but thanks to John Clague and Jenn Sabine for showing me the buried soils in Washington and how the marsh data is collected.

Thanks to Ali Kharagani and Vern Vogt of the BC Ministry of Sustainable Resources, Base Mapping and Geomatic Services, for making available the many tapes of GPS data. To Sigrún Hreinsdóttir and Andy Freed for providing Denali co- and postseismic predictions. Also to Brian Schofield for downloading Alaskan data, John Ristau for moment tensor solutions, and Yuan Lu for writing data conversion scripts.

I have benefited from technical and administrative support at both the Pacific Geoscience Centre and the School of Earth and Ocean Sciences – especially from Sussi Arason, Steve Taylor, Bruce Johnson, Robert Kung, Elena Jenner, Darlene Upton, and Terry Russell. Also at this point I will acknowledge the GMT software (Wessel and Smith, 1995), used for many of the figures in this thesis.

Many friends have shared in the joys and trials of student life in Victoria and at conferences far and wide. Thanks to my officemates Amanda Bustin, John Ristau, and Yan Hu for a great office atmosphere. Thanks John for all the treats, and Amanda for sharing every step of the thesis journey and introducing me to chai latte. Special thanks also to Lisa Nykolaishen, Sheri Molnar, and Maiclaire Bolton. Thanks to Joe for leading the way. And the many others, near and far, who have contributed to the fun and great memories.

A big thank-you to my family, especially my parents Michael and Sue, without whose constant encouragement and support I would never have got where I am (and I am sorry that is so far away). Finally, thanks to David for making sure my life is about a lot more than work, for amazing cooking, and for dissolving my stress like magic.

CHAPTER 1

Introduction

This thesis primarily deals with the current tectonics of the northern Cordillera, related to the interaction of the Pacific and North America plates along the Gulf of Alaska coast (Figure 1.1). Tectonic plate boundaries occur along the entire length of western North America, mostly involving the Pacific oceanic plate and the North America continental plate (Figure 1.1). All three major categories of plate margin occur: divergent, transform, and convergent. Each type of boundary produces different tectonic consequences in the adjacent North American continent.

The Pacific/North America plate boundary changes from a divergent (rifting) margin in Mexico to the San Andreas transform boundary of California. A triple junction occurs in northern California, and from there northward to southern British Columbia, Canada, the Juan de Fuca oceanic plate system, consisting of the Gorda, Juan de Fuca, and Explorer plates, subducts eastward beneath the North America plate along the Cascadia subduction zone. North of the Explorer-Pacific-North America triple junction, the Pacific plate moves north relative to North America along the Queen Charlotte-Fairweather transform boundary. Further north in the Gulf of Alaska, the Pacific-North America boundary becomes convergent, resulting in northward subduction of the Pacific plate along the Aleutian subduction zone. However, in the corner of the Gulf of Alaska between the transform and subduction boundaries, collision occurs between North America and the small composite oceanic-continental Yakutat block. This block appears to have moved northward along the coast with the Pacific plate until limited by the margin corner in the Gulf of Alaska (e.g., Bruns, 1983).

The definition of a tectonic plate as having little internal deformation implies narrow zones of deformation and associated seismicity along plate boundaries. However, seismicity within the North America crust extends a great distance (> 800 km) north and northeast of the Yakutat collision zone. Such widely-distributed plate boundary deformation occurs at other collision zones including the India-Eurasia continental collision in the Himalayas, and the European Alps.

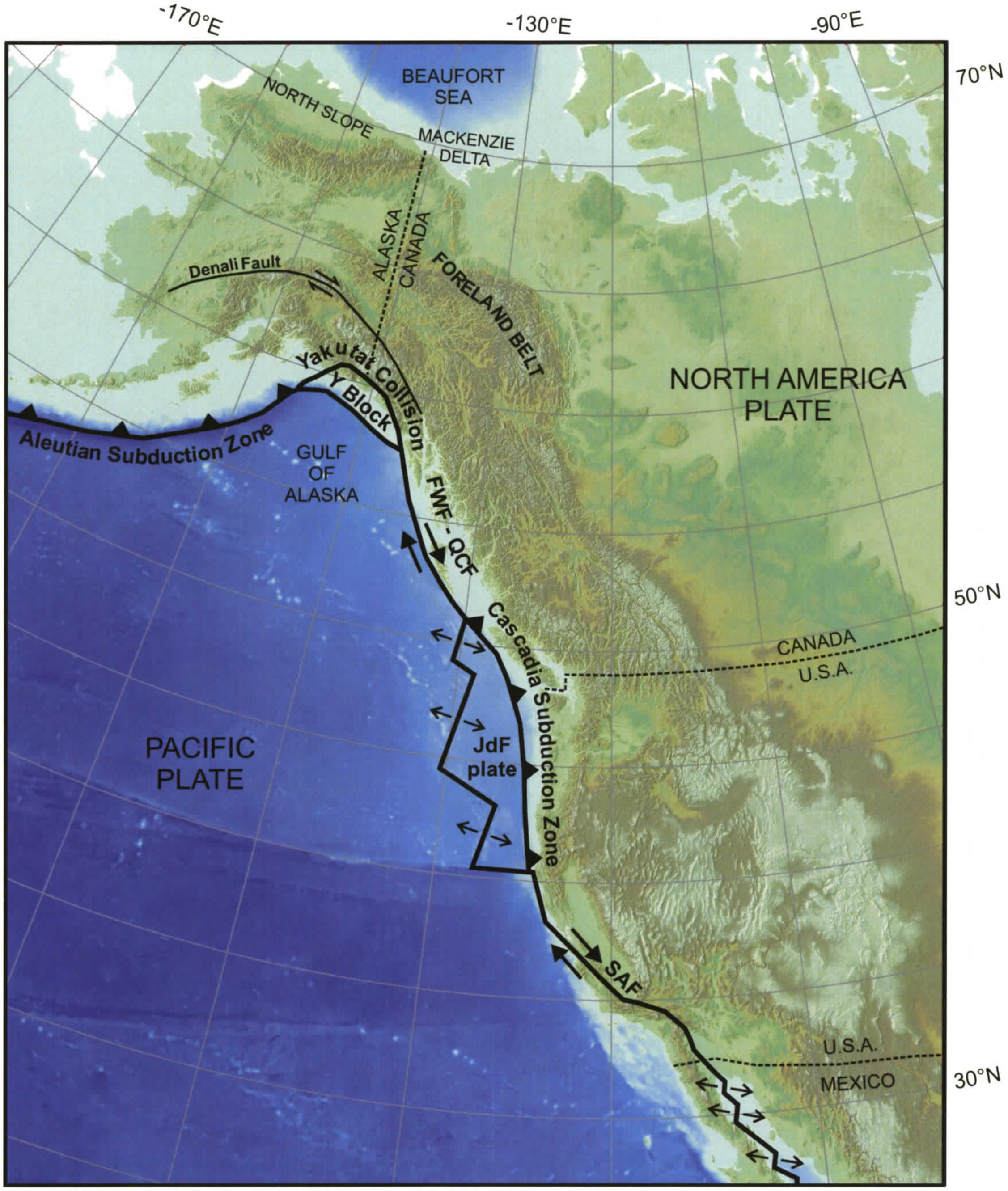

Figure 1.1. Plate tectonic boundaries along the western coast of North America. JdF: Juan de Fuca; Y Block: Yakutat block; FWF: Fairweather fault; QCF: Queen Charlotte fault; SAF: San Andreas fault.

The large-scale characterization of deformation associated with the Yakutat collision, representing the interaction between the oceanic Pacific plate and continental North America, is the main focus of this thesis. A separate final chapter deals with another of the western North America convergent margins: the Cascadia subduction zone (Figure 1.1), in which the oceanic Juan de Fuca plate subducts beneath the North American continental margin. The main objective of that study, previously published in Leonard et al. (2004), is to provide constraints on coastal subsidence and fault rupture associated with great earthquakes on the megathrust boundary.

CURRENT TECTONICS OF THE NORTHERN CANADIAN CORDILLERA

Detailed study of contemporary regional deformation in northwestern Canada and eastern Alaska is in its infancy, perhaps due to difficult access and the relatively low seismic risk to the small human population and limited infrastructure. Regional tectonic investigation has generally been associated with the energy and mining industries, particularly in recent planning for oil and gas pipeline routing and construction. Seismic hazard assessment of the Denali fault in the 1970's prior to construction of the north-south Trans-Alaska oil pipeline from Prudhoe Bay resulted in the implementation of precautionary measures that were justified when the pipeline survived the 2002 M 7.9 earthquake rupture that caused up to 8 m of offset. Similarly, much current research is fuelled by the plans for new natural gas pipelines from the Mackenzie Delta and from the North Slope of Alaska (Figure 1.1), the detailed routes of which are yet to be decided.

Although the seismic risk in the region is low because of the small population, the seismic potential is high. A better understanding of the tectonics and seismicity can be widely applied to other parts of the world where similar tectonics pose a far greater threat to human populations. Conversely, existing detailed studies of other regions aid our understanding of the Yakutat region, a continental collision zone in its early stages. Although the collision zone is small in a North American perspective, it is comparable in area to the Alps of Western Europe and has tectonic consequences over a large area.

The dextral-oblique collision of the Yakutat block with North America is accommodated mainly by a mixture of thrust and strike-slip faulting in the Saint Elias region. Some dextral slip also occurs on the Denali fault, a major inland continental-scale fault that runs northwest through SW Yukon and Alaska (Figure 1.1). However, the seismicity pattern and preliminary geodetic measurements indicate that a significant portion of the strain is accommodated further inland (Mazzotti and Hyndman, 2002; Flück, 2003; Hyndman et al., 2005a). Earthquake mechanisms from a concentration of seismicity at the eastern front of the foreland belt in Canada (Figure 1.1) indicate that thrusting and strike-slip faulting occur in response to NE-SW to NNE-SSW compression 600-800 km northeast of the Yakutat collision zone.

Mazzotti and Hyndman (2002) proposed a first-order model to explain this northeastward strain transfer. In their model, the high heat flow measured in the northern Cordillera allows decoupling of the upper crust from the weak lower crust, causing "orogenic float" (Oldow et al., 1990) to occur, whereby the upper crust moves to the northeast essentially intact over a lower crustal detachment. Deformation is taken up in the weak foreland sedimentary thrust belt, with the stable craton acting as a backstop. This model is a simple two-dimensional approximation in an area that clearly has complex three-dimensional deformation. In order to test and refine such models, further constraints on the regional deformation are needed.

This study uses two main approaches to constrain the first-order current tectonic deformation pattern of the northern Canadian Cordillera: (1) high-precision (few millimetre accuracy) Global Position System (GPS) measurements and (2) calculation of seismic deformation rates using the earthquake catalogue. Other constraints on deformation include: (1) the tectonic history of mapped faults; (2) the seismicity pattern; (3) earthquake focal mechanisms that provide faulting and regional stress directions; (4) thermal data that provide information on the variable susceptibility of the lithosphere to deformation; (5) thermochronological data that provide information on the timing and rates of uplift.

CASCADIA MEGATHRUST COSEISMIC SUBSIDENCE

In contrast to the limited seismic risk to populations in northwestern Canada and eastern Alaska, the Cascadia subduction zone presents a major threat to coastal populations between northern California and Vancouver Island, Canada. Since the realization in the 1980's that great earthquakes accompanied by large tsunamis have occurred on the Cascadia megathrust boundary, regional tectonic studies have greatly intensified, with the deployment of dense seismic and GPS networks. Public interest was also recently renewed with the 2004 occurrence of a devastating similar event on the Sumatra subduction zone.

Evidence for past great earthquakes at Cascadia, most recently in the year 1700, is provided by: (1) buried coastal marsh soils that document coseismic subsidence (e.g., Atwater, 1987; Jennings and Nelson, 1992; Hemphill-Haley, 1995a; Peterson et al., 1997; Hughes et al., 2002); (2) present (interseismic) uplift of the coast from geodetic measurements (e.g., Savage and Lisowski, 1991; Dragert et al., 1994; Hyndman and Wang, 1995; Miller et al., 2001), inferring a cycle of coastal interseismic uplift and coseismic subsidence; (3) correlation of the most recent event (dating of plants submerged in 1700, e.g., Yamaguchi et al., 1997) with a tsunami recorded in Japan inferred by the wave heights to be magnitude ~ 9.0 (Satake et al., 1996).

Seismic hazard assessments at Cascadia are currently based on the results of geodetically-constrained simple elastic dislocation models, but these models had not been checked against evidence for the rupture displacement and area for the 1700 and earlier events. The predicted coastal subsidence may be compared with the geological evidence available from coastal marshes for past events. Chapter 6 presents a detailed compilation of coastal coseismic subsidence data (from the literature) for the 1700 and previous great earthquakes. A comparison of these results with the subsidence predictions of an elastic dislocation model (modified from Flück et al., 1997) provides constraints on the rupture area and on along-margin variations in fault slip in the 1700 and previous events. The marsh data are also used to estimate the net interseismic uplift since 1700.

This work on the 1700 megathrust earthquake was published in the Geological Society of America Bulletin (Leonard et al., 2004), and the additional analysis of pre-

1700 events was included in an unpublished report to the U.S. Geological Survey (Hyndman et al., 2004).

THESIS OUTLINE

Chapter 2 provides a brief outline of the current tectonic setting of the northern Canadian Cordillera and eastern Alaska. This is followed by a description of the tectonic history of the region. Information on the distribution of mapped faults and their inferred Cenozoic motion provides a critical constraint on current deformation. Many older structures are favourably aligned for reactivation under the current stress field.

Chapter 3 provides constraints on current deformation from GPS measurements. Up to seven years' worth of data (1999-2005) were analyzed from a sparse network of 28 continuous stations in eastern Alaska, Yukon Territory, western Northwest Territories and British Columbia, and a more closely-spaced network of 24 campaign sites located in Yukon Territory and adjacent British Columbia and Northwest Territories. New campaign GPS data were collected for this analysis in 2004 and 2005, to add to earlier data collected by others since 1999. Only a small amount of data had previously been processed from the continuous stations in this study. Thus, the present analysis represents a significant improvement in numbers of stations and data quality on the earlier analysis of Flück (2003). There have also been some improvements in processing methods. Data processing provides GPS site vectors showing the direction and rate of movement (with calculated error) of sites with respect to stable North America.

Chapter 4 comprises two main sections. The first describes the historical seismicity of the northern Canadian Cordillera and eastern Alaska. For each geographic area, the pattern and nature of seismicity are described. Information available from earthquake focal mechanisms, principal stress directions from stress inversion, and analyses of large events is also included. The second part of Chapter 4 deals with the estimation of seismic deformation rates from catalogue seismicity for many of the areas described in the first section. This method assumes that most deformation is taken up seismically, and uses the seismicity statistics of each area to calculate the rate of seismicity within a crustal volume characterized by a particular style of faulting. Seismic slip rates are then estimated for each seismic zone, assuming that the seismicity accommodates relative motion between adjacent blocks.

Chapter 5 involves the integration of constraints on the current deformation of the northern Canadian Cordillera and eastern Alaska, as determined from Chapters 2-4. The resultant large-scale pattern of deformation is discussed and conclusions about its origin are drawn. The chapter ends with suggestions for future work.

Finally, Chapter 6 presents the study of constraints on coseismic rupture in megathrust earthquakes on the Cascadia subduction zone. This work is not located in the same specific region as the primary study, but it examines another aspect of the interaction of an oceanic plate with the continental North America plate, and the associated seismic hazard. Although previously published, the study is included in the thesis for complete documentation of the research of this PhD project.

CHAPTER 2

Tectonic Setting and History of the Northern Canadian Cordillera

CURRENT TECTONIC SETTING

As the current tectonics of the northern Canadian Cordillera and eastern Alaska are the focus of Chapters 3-5, only a brief overview is given here. The tectonic setting is shown in Figure 2.1. The Yakutat terrane, a composite oceanic-continental terrane, is colliding obliquely with earlier accreted terranes of the North America plate in the corner of the Gulf of Alaska (e.g., Plafker et al., 1994). To the west, the Pacific plate subducts beneath North America along the Aleutian trench. The Yakutat block is bounded to the southwest by the Transition fault, which originated as a dextral transform, but is currently undergoing reactivation as a thrust fault along its southeastern part (e.g., Bruns, 1985). The Yakutat block is currently moving with the Pacific plate, but at a slightly lower velocity, and appears to be rotating counterclockwise around the corner of the Gulf of Alaska (e.g., Fletcher and Freymueller, 1999).

To the east, dextral strike-slip motion along the Fairweather fault (the northern extension of the Queen Charlotte transform plate boundary) accommodates most of the differential motion between the Pacific and North America plates. Inland to the north, the convergent component of the oblique collision is taken up mainly by thrusting in the Chugach-Saint Elias Mountains, and a smaller amount of dextral motion occurs on a series of strike-slip faults further inland, most notably the Denali fault.

The seismicity pattern (Chapter 4) suggests that deformation related to the Yakutat collision occurs far to the northwest and northeast. A series of sinistral strike-slip faults (see Figure 4.5, Chapter 4) appear to be accommodating right-lateral transpression between the Denali and Tintina-Kaltag fault systems in Alaska. Northeast of the Denali fault in Canada, a low level of seismicity is indicated across the Cordillera, with a slight epicentral concentration along the right-lateral strike-slip Tintina fault. However, significant seismicity occurs at the eastern foreland belt mountain front, where dextral

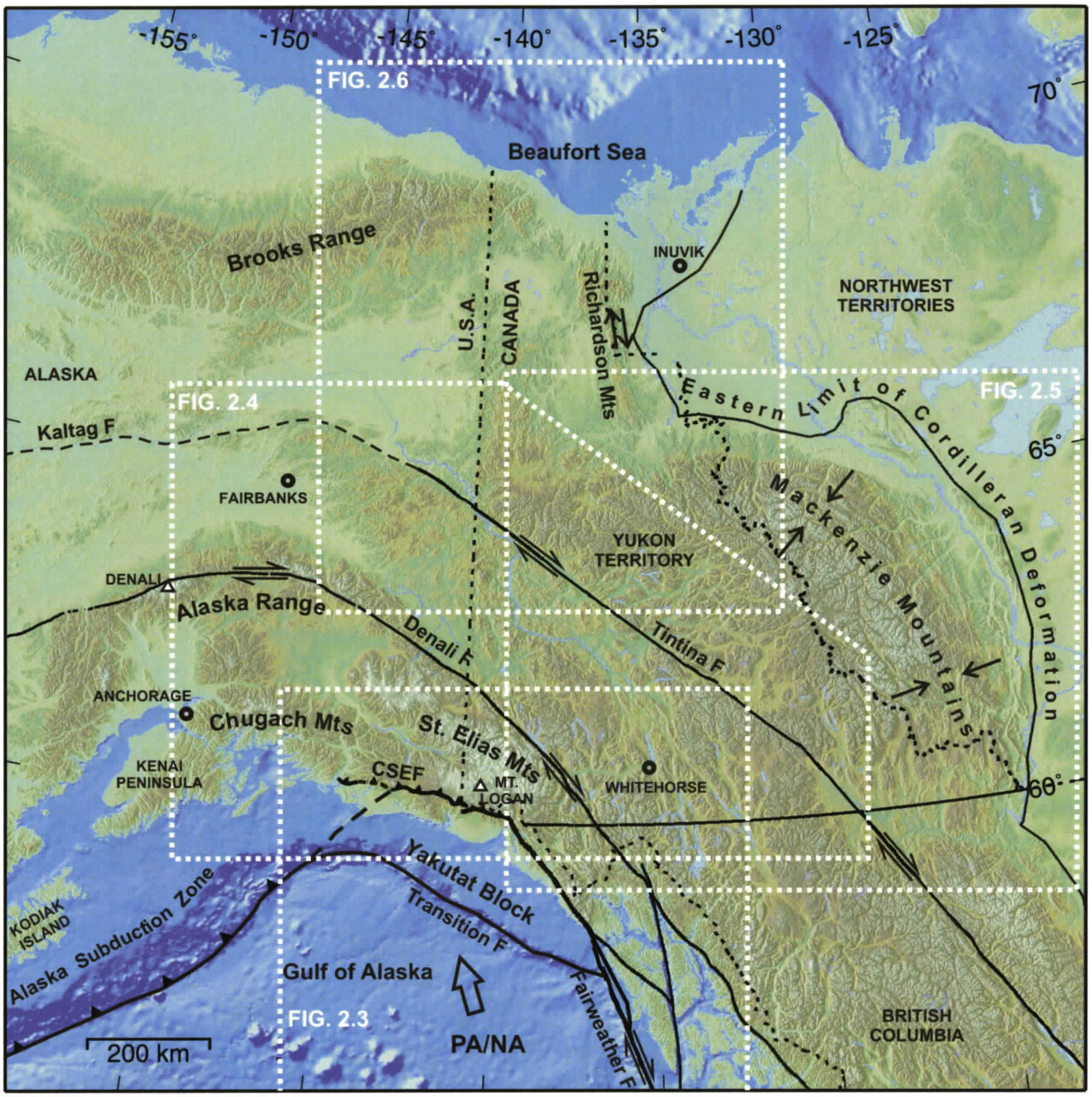

Figure 2.1. Current tectonic setting of the northern Canadian Cordillera and eastern Alaska. Boxes show extent of later figures. Large arrow shows the direction of motion of the Pacific plate relative to North America. CSEF: Chugach-St. Elias fault.

strike-slip motion in the Richardson Mountains and thrusting in the Mackenzie Mountains are consistent with NE-SW compression. Lower rates of seismicity in the northeastern Brooks Range and the Beaufort Sea (see Chapter 4) are likely also the result of the Yakutat collision far to the south.

MORPHOLOGY OF THE CANADIAN CORDILLERA

The northern Canadian Cordillera consists of a number of lithological terranes of different origins and ages (e.g., Coney et al., 1980; Gabrielse et al., 1991). Most of these terranes were successively accreted to western North America from the middle Jurassic onwards (Monger et al., 1982) and subsequently transported northwards along continental-scale strike-slip faults, including the Tintina/Northern Rocky Mountain Trench and Denali faults (e.g., Gabrielse, 1985). The Canadian Cordillera can be divided into five morphogeological belts, as shown and described in Figure 2.2, from east to west: the Foreland, Omineca, Intermontane, Coastal, and Insular belts (e.g., Gabrielse et al., 1991; Price, 1994; Abraham et al., 2001). All five belts were affected by Cordilleran orogenesis, which involved transpressional deformation ~ 185-60 Ma, followed by extension ~ 59-40 Ma mainly in southern British Columbia (Monger and Price, 2002).

A summary of North American Cordilleran evolution is provided by Dickinson (2004). Neoproterozoic (~ 750 Ma) rifting of the supercontinent Rodinia was followed by passive margin sedimentation until the Devonian to produce rocks that are found in the Foreland belt. Oceanic terranes were thrust over the continental margin from the Late Devonian to the Early Triassic prior to the Triassic initiation of an arc-trench system that has essentially persisted to the present-day (e.g., Engebretson et al., 1985). Mesozoic-Cenozoic subduction complexes, batholiths, and accreted island arcs make up the majority of the Omineca, Intermontane, Coastal and Insular belts. Transform faulting along the continental margin began in the early- to mid-Cenozoic due to impinging seafloor-spreading systems and led to the development of strike-slip faulting within the adjacent continent.

The northern Cordillera continues into Alaska, which is thought to mostly comprise allochthonous terranes that also originated to the south and most began their northward displacement post mid-Cretaceous (Johnston, 2001). The Yakutat terrane (part of the Insular belt), discussed in more detail below, is the latest to accrete to North America, having completed its northward translation along the Queen Charlotte/Fairweather fault system.

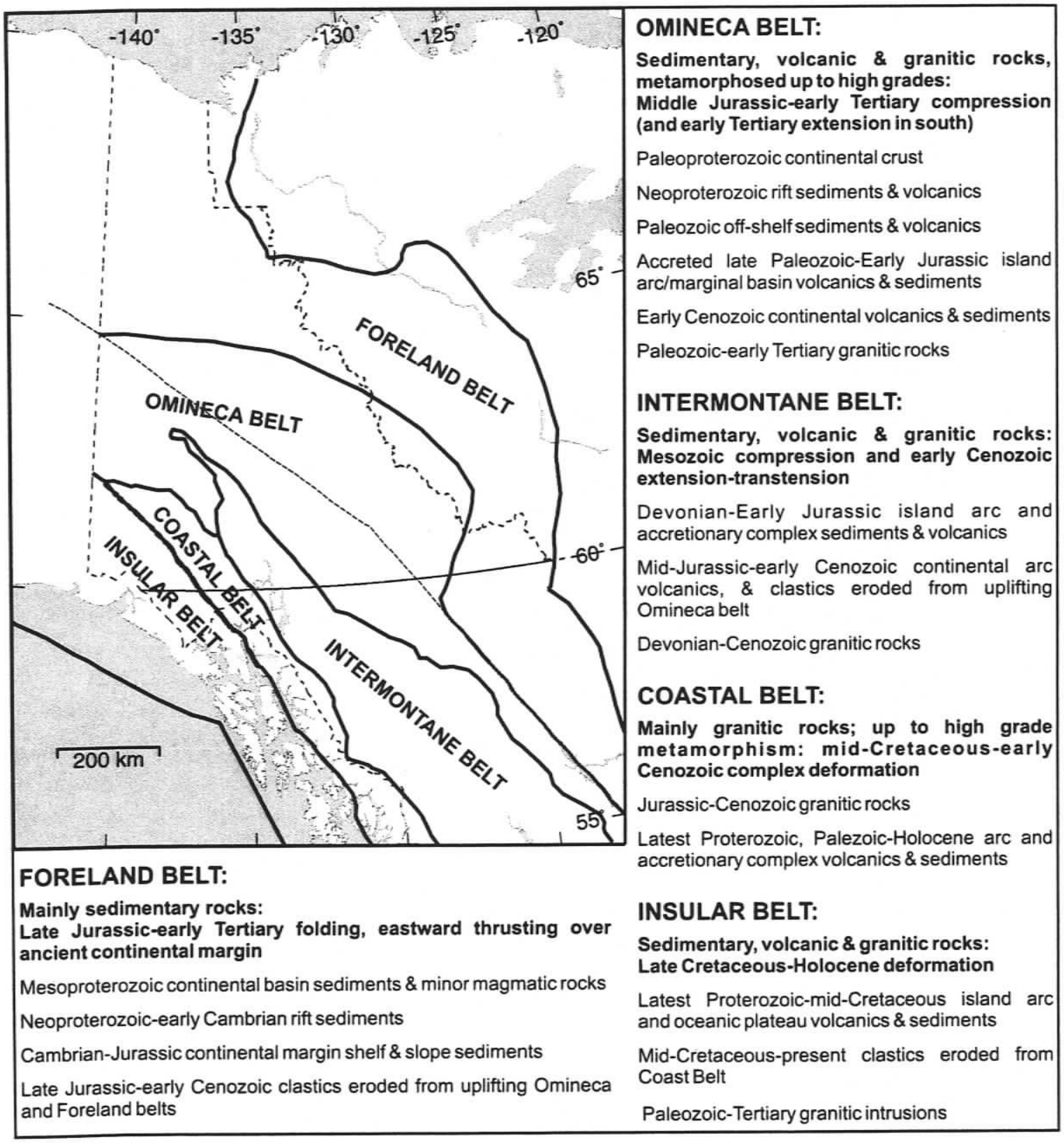

Figure 2.2. Extent and summary descriptions of the five morphogeological belts of the Canadian Cordillera. Map after Price (1994); descriptions after Monger and Price (2002).

TECTONIC HISTORY

Yakutat-Saint Elias Region

In Paleogene time, the southern Alaskan continental margin was characterized by rapid subduction of the Kula plate (Plafker et al., 1989). The Chugach terrane, an accretionary complex, formed at this convergent margin from latest Triassic to earliest Tertiary time (e.g., Plafker et al., 1994). It was juxtaposed against and up to 40 km beneath arc assemblages to the north (Wrangellia composite terrane) along the Border Ranges fault system (Figure 2.3; MacKevett and Plafker, 1974; Page et al., 1986; Plafker et al., 1989; Kusky et al., 1997). Reactivation of the Border Ranges fault system between latest Cretaceous and Early Eocene (~ 50 Ma) accommodated up to several hundred kilometres of dextral strike-slip motion, consistent with oblique convergence (Smart et al., 1996). Kula plate subduction ceased with subduction of the Kula-Farallon spreading centre ~ 50 Ma (e.g., Plafker et al., 1989). Formation and deformation of the Chugach accretionary prism was completed prior to emplacement of post-tectonic plutons of middle to late Paleocene age on Kodiak Island (Figure 2.1), and of early to middle Eocene age on the mainland to the east (Plafker et al., 1994). Early Tertiary magmatism may be attributable to a Kula-Farallon slab-window (Plafker et al., 1989).

The slightly younger part of the accretionary wedge, the Cenozoic Prince William terrane, is juxtaposed against and beneath the older Chugach terrane along the Paleogene subduction thrust boundary: the Contact fault system (Figure 2.3; e.g., Bruhn et al., 2004). Current dextral reactivation of the Contact fault is suggested by geodetic measurements and post-Eocene faulting (Savage and Lisowski, 1986; Bruhn et al., 2004).

A tectonic map of the Yakutat region is shown in Figure 2.3. From the middle Eocene to the present, 4-6 cm/yr northwestward motion of the Pacific plate has occurred relative to the continental margin (e.g., Plafker et al., 1989). The Queen Charlotte-Fairweather dextral transform fault, which forms part of the current Pacific-North America plate boundary, was initiated inboard of the Yakutat block in the late Oligocene/early Miocene (e.g., Plafker et al., 1994).

The basement of the eastern third of the Yakutat block (east of the Dangerous River zone; Figure 2.3) consists of a probable Mesozoic to Paleocene subduction

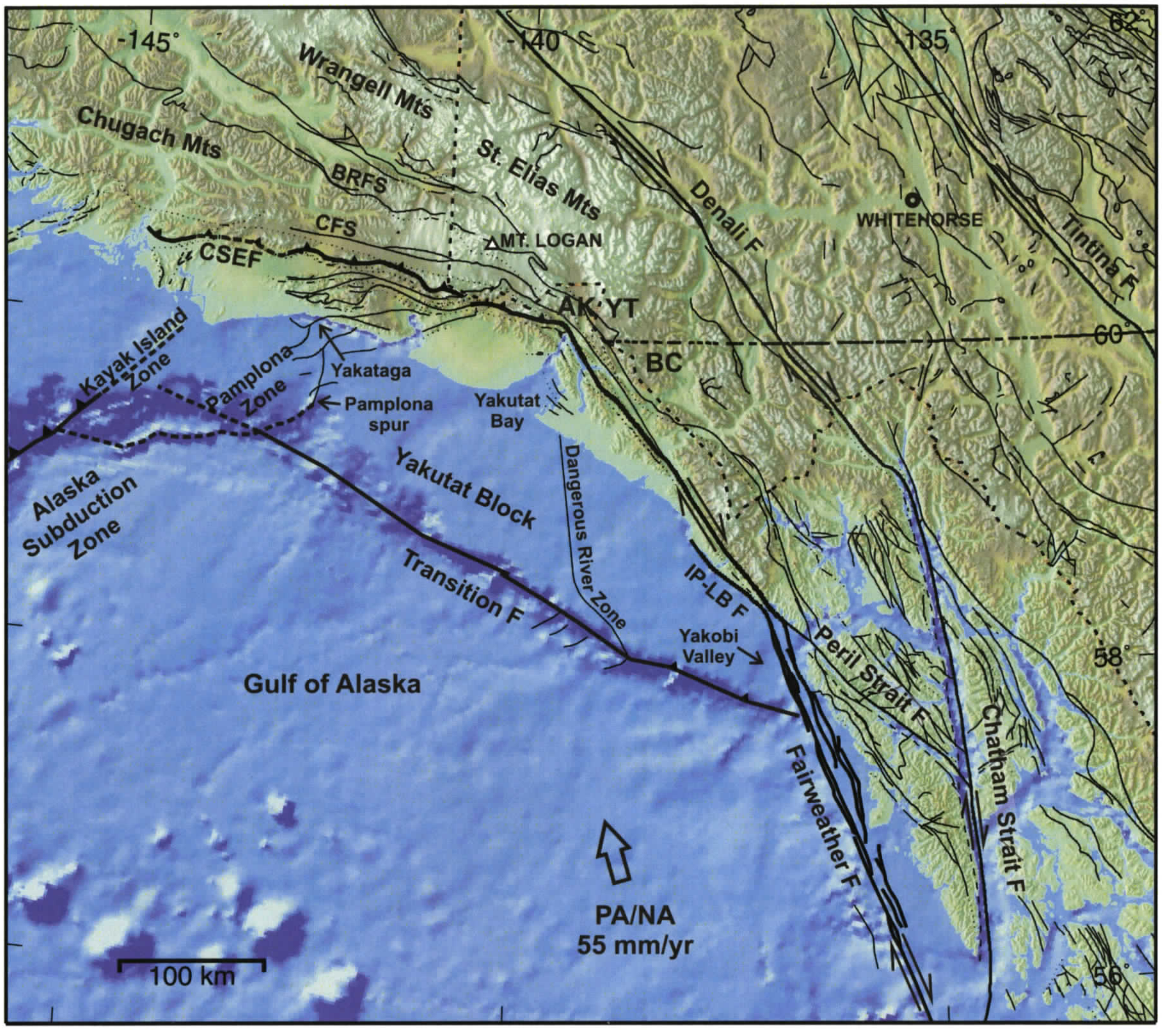

Figure 2.3. Tectonic fault and topographic/bathymetric map of the Yakutat region. Large arrow shows the direction of motion of the Pacific plate relative to North America. Triangles on thrust faults indicate down-dip direction. CSEF: Chugach-St. Elias fault; CFS: Contact fault system; BRFS: Border Ranges fault system; IP-LB F: Icy Point – Lituya Bay fault.

complex, whereas the western basement comprises Paleocene to early Eocene oceanic basalt (Bruns, 1985). The Yakutat basement is overlain by a thick sequence of Paleogene clastic sedimentary rocks, of which only the upper Cenozoic (post-late Miocene) sequence (Yakataga Formation) is derived from the adjacent Chugach-Saint Elias Mountains (e.g., Bruns, 1985; Plafker et al., 1989).

The Yakutat block is bounded to the southwest by the Transition fault zone, which juxtaposes the Mesozoic to Eocene rocks of the Yakutat block against younger Oligocene basalts of the Pacific plate. Such juxtaposition is consistent with a dextral transform origin for the Transition fault. Bruns (1983; 1985) infers that it was active from the Paleogene until the end of the Oligocene, when the initiation of the Queen Charlotte-Fairweather transform sliced the Yakutat block from the continental margin such that it subsequently moved with the Pacific plate. Seismicity along the southeastern part of the Transition fault suggests that it is currently being reactivated to facilitate some underthrusting of the Pacific plate (see Chapter 4).

Geologic and paleomagnetic data suggest that the Yakutat block was displaced to its present position during late Cenozoic time by dextral strike-slip along the Fairweather-Queen Charlotte transform fault system from a site along the continental margin ~ 600 km to the southeast (Bruns, 1983; 1985; Plafker, 1987). The block has since rotated ~ 20° counterclockwise. Convergence and underthrusting of the Yakutat terrane beneath the Chugach terrane to the north resulted in the formation of a fold and thrust belt along the Chugach-Saint Elias fault system and the onset of andesitic volcanism in the Wrangell Mountains at ~ 20 Ma (e.g., Plafker et al., 1989). The eastern two-thirds of the Yakutat block are relatively undeformed and show little current seismicity (see Chapter 4), whereas the Pamplona zone to the west (Figure 2.3) is a young, seismically-active fold and thrust belt developed within strata of the Yakutat block. The belt propagated to the southeast from the Kayak Island zone (Plafker, 1987). Multichannel seismic lines have been interpreted to indicate minor shortening (4-10 km) across the Pamplona zone, most of which has occurred in the Quaternary (Bruns, 1983; Plafker, 1987).

To the northwest, oceanic crust of the western Yakutat terrane was subducted beneath North America during the Neogene (Fruehn et al., 1999); a prominent magnetic anomaly marking the Transition fault continues beneath the continental margin as far west as the Kenai Peninsula (e.g., Schwab et al., 1979; Bruns, 1985; Griscom and Sauer, 1990). Shallow portions of the subducted Yakutat terrane were imaged with wide-angle refraction by Brocher et al. (1994). A receiver function analysis beneath the central Alaska Range by Ferris et al. (2003) imaged a low velocity zone (interpreted as thickened oceanic crust) of approximately 15 km thickness above the subducting plate between 60 and 150 km depth. This anomalously thick subducting oceanic crust may be the down-dip continuation of the Yakutat block, which would therefore have a down-dip extent of ~ 500 km and have started to subduct no later than ~ 9 Ma (Ferris et al., 2003). Plafker et al. (1994) also suggest that the Wrangell volcanic arc was related to subduction of the oceanic western part of the Yakutat terrane. The Wrangell volcanoes have not been highly eruptive for ~ 3 m.y. The thickened oceanic crust of the subducted Yakutat block may represent an oceanic plateau, whose buoyancy may drive slab flattening and contribute to mountain building (Ferris et al., 2003).

The ongoing transpression has resulted in intense seismicity (see Chapter 4) and rapid uplift of the Chugach and Saint Elias mountains, with concurrent deposition of voluminous clastic sediments onto the adjacent continental margin, beginning in the Miocene (e.g., Plafker et al., 1978; Campbell and Dodds, 1991; Sheaf et al., 2003). An apatite fission track analysis of Mount Logan in the Saint Elias Mountains reveals an apparent acceleration in uplift in the Pliocene, which may reflect a change in relative motion between the North American and Pacific plates at ~ 5.6 Ma, and/or collision of the Yakutat block (O'Sullivan and Currie, 1996, and references therein).

Fairweather fault

The Fairweather fault, which bounds the Yakutat block to the east and northeast (Figure 2.3), has ruptured throughout its length in a number of earthquakes since 1927 (see Chapter 4). It is currently moving at close to the full displacement rate between the North American and Pacific plates, but it may have been doing so only since the late Pleistocene. Only 5-6 km of post-Miocene dextral displacement is observed on the onshore portion of the Fairweather fault, and ~ 4 or 5 km on the Denali fault (Plafker et al., 1978). Landward of the Fairweather fault, the Chatham Strait and Peril Strait faults show respectively about 100 and 11 km of dextral strike-slip motion since the Oligocene (e.g., Hudson et al., 1982; Carlson et al., 1988). Thus, the bulk of the hundreds of kilometres of relative motion between the two plates during the last 10 Ma must have been taken up on one or more offshore faults, for example the Transition fault zone (Plafker et al., 1978; Fletcher and Freymueller, 1999).

Where the Fairweather fault runs offshore to the southeast, it consists of two sets of en-echelon faults 6-12 km apart that extend to the SSE for ~ 225 km before merging and continuing to the SSE to eventually become the Queen Charlotte fault (Figure 2.3). Carlson et al. (1988) cite Holocene seafloor scarps and seismic reflector discontinuities to conclude that the western fault zone is relatively more active than the eastern zone, although it is the eastern zone that trends into the active onshore Fairweather fault. Further, they estimate ~ 20 km dextral offset in the past ~ 330 k.y. of the offshore glacially-carved Yakobi Valley where it crosses the Fairweather fault, and suggest that some of the relative plate motion may have been taken up on the western trace of the Fairweather fault and its northern extension, the Icy Point-Lituya Bay fault (Figure 2.3).

Apatite U-Th/He thermochronometric analysis of rocks in the region of the Fairweather fault in SE Alaska (McAleer and Spotila, 2005) reveals cooling ages of less than 5 Ma (as young as 1.6 Ma; mostly 2-3 Ma). These cooling ages represent the time that the rocks cooled below ~ 70°C (e.g., Wolf et al., 1996), i.e., when they were exhumed through the uppermost crust. This suggests rapid denudation during the mid-Pliocene. As almost pure strike-slip motion is thought to occur on the Fairweather fault at present, McAleer and Spotila (2005) suggest either a recent change in plate motions or a transpressional component across the Fairweather fault to account for the uplift. GPS and tide gauge measurements (e.g., Larsen et al., 2004; 2005; this study, Chapter 3) show that most of southeastern Alaska is currently undergoing uplift. The model of Larsen et al. (2004; 2005) predicts postglacial rebound of this region in response to rapid ice loss in the Glacier Bay region over the past ~ 250 years.

The Denali and Tintina Fault Systems

The Denali and Tintina faults (Figure 2.4) are continental-scale dextral strike-slip faults that strike NW-SE through Yukon and easternmost Alaska. The trend of the Denali fault then changes to E-W and then SW-NE around the hinge of the Alaskan orocline (e.g., Stone, 1980). In Alaska, the NW-SE-trending Tintina fault splays into a number of SW-NE-trending faults, including the right-lateral Kaltag fault.

Denali fault

In the eastern Alaska Range, geophysical studies show the Denali fault to be a near-vertical feature extending to at least 10 km, and probably 30 km depth (Kikuchi and Yamanaka, 2002; Wright et al., 2003; Fisher et al., 2004). The Denali fault in this region represents the Paleocene-Eocene suture zone between two composite terranes:

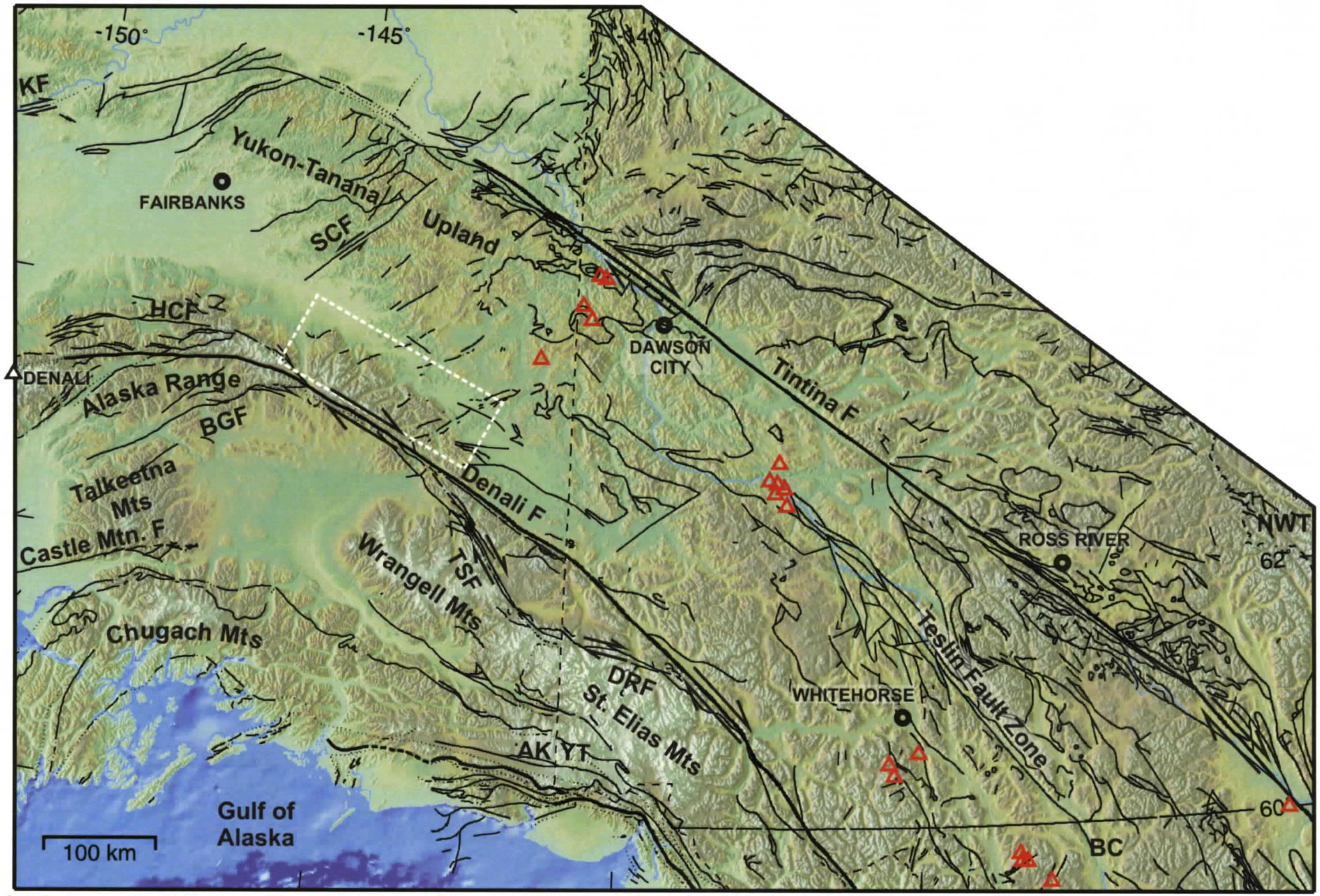

Figure 2.4. Tectonic fault and topographic map of the Denali-Tintina region. Red triangles: location of Neogene-Recent Northern Cordilleran Volcanic Province centres from Edwards and Russell (2000). TSF: Totschunda fault; DRF: Duke River fault; KF: Kaltag fault; HCF: Hines Creek fault; BGF: Broxson Gulch fault; SCF: Shaw Creek fault. White dashed box: occurrence of sinistral offsets of the frontal Alaska Range.

Wrangellia of the Insular belt to the south, and the Yukon-Tanana terrane of the Omineca belt to the north. Cenozoic transpression across the Denali fault in the Alaska Range is believed to have produced a positive flower structure, evidenced by earthquake hypocentres that dip towards the Denali fault, and oblique-slip faults to the north and south that were active in the Cenozoic (Fisher et al., 2004), e.g., the Hines Creek and Broxson Gulch faults (Figure 2.4; Wahrhaftig et al., 1975; Nokleberg et al., 1985).

The highest mountain in North America, Denali (Mount McKinley) is located at the apex of the arcuate Denali fault in the central Alaska Range (Figure 2.4). An apatite fission track study of samples from Denali implies that rapid uplift began ~ 6 Ma (Fitzgerald et al., 1993; 1995). This timing is similar to the start of the latest phase of uplift in the Saint Elias Mountains (O'Sullivan and Currie, 1996), and likely reflects collision of the Yakutat block.

The Denali fault system has accommodated dextral displacement of ~ 400 km, of which ~ 350 km occurred between 55 and 38 Ma, and up to 40 km since then (Lanphere, 1978). Observed post-Miocene dextral displacement totals only ~ 4 or 5 km (Plafker et al., 1978). The Denali fault system in south-central Alaska shows good evidence for Holocene motion, with dextral offsets of up to 350 m and vertical displacements up to 10 m (Richter and Matson, 1971; Stout et al., 1973; Plafker et al., 1977; Matmon et al., 2006). Holocene dextral offsets of up to ~ 150 m are also documented on the Totschunda fault, which splays off the Denali fault to the southeast (Figure 2.4; Plafker et al., 1977; Matmon et al., 2006). Late Quaternary strike-slip offsets across the Denali fault decrease east of the intersection with the Totschunda fault to near-zero in Yukon Territory, although limited dip-slip motion has occurred (Richter and Matson, 1971; Clague, 1979). Observed late Quaternary offsets also decrease to zero along the westernmost Denali fault in Alaska (Plafker et al., 1977).

Right-lateral motion on the Denali fault has continued to the present as indicated by the seismicity (see Chapter 4). In 2002, an M_w 7.9 earthquake occurred on part of the Denali fault in the eastern Alaska Range; rupture also propagated along the Totschunda fault (e.g., Eberhart-Phillips et al., 2003a). Details of this earthquake are discussed in Chapters 3 and 4.

Tintina fault

For much of its length, the Tintina fault system (Figure 2.4) is marked at the surface by a long topographic depression that can be seen from space: the Tintina Trench. The Tintina fault is sampled by two Lithoprobe seismic lines in southeastern Yukon. SNORCLE (Slave-Northern Cordillera Lithospheric Evolution) reflection line 2a and refraction line 21 cross the fault near Watson Lake (~ 60°N); reflection line 3 and refraction line 31 provide a transect near Ross River (~ 62°N). Data analyses suggest that the Tintina fault is a steeply-dipping, but non-vertical feature that penetrates at least the entire crust (Welford et al., 2001; Creaser and Spence, 2005; Snyder et al., 2005). The fault system in S. Yukon comprises several steeply-dipping fault strands over a 30-km wide zone at the surface, narrowing in the mid-crust and widening to more than 60 km in the lower crust (Snyder et al., 2005). Contrasting isotopic signatures in Recent basalts on either side of the Tintina fault (near Watson Lake) imply that different lithospheric mantle sources are juxtaposed by the high-angle fault, which must therefore penetrate the upper mantle as well as the crust (Abraham et al., 2001).

Dextral displacement of at least ~ 425 km has occurred on the Tintina fault system, mostly from the mid-Cretaceous to the Eocene (Roddick, 1967; Gabrielse, 1985; Murphy and Mortensen, 2003). A low level of current motion along the fault is suggested by the seismicity (see Chapter 4). Mortensen and Von Gaza (1992) find evidence for relatively recent activity along the Tintina fault near Dawson City, Yukon, in the form of fresh fault scarps and sag ponds (pull-apart basins) in glacial sediments. Their analysis of Landsat imagery reveals (1) large-scale NW-SE-trending lineaments that likely represent strike-slip strands of the Tintina fault zone, some of which have undergone late normal offset, and (2) smaller-scale NE-SW trending lineaments that cut obliquely across the Tintina Trench and probably represent younger faults that postdate major strike-slip displacement along the Tintina fault. These NE-SW trending lineaments may relate to NE-trending faults between the Denali and Tintina faults in Alaska (discussed below).

Between the Denali and Tintina faults

Cenozoic NE-trending faults are evident in the Yukon-Tanana upland between the Denali and Tintina faults in eastern Alaska (Figure 2.4). The best observed of these, the

Shaw Creek fault, shows both left-lateral strike-slip and SE-side-up high-angle reverse displacement (Foster et al., 1994). Development of these faults occurred after the intrusion of mid-Cretaceous (~ 90 Ma) granitoid plutons; NW-SE-directed compressional folding is apparent in Upper Cretaceous and probable early/middle Miocene sedimentary rocks in the eastern Yukon-Tanana upland (Foster and Cushing, 1985). Apatite fission track analyses suggest widespread exhumation of the Yukon-Tanana upland prior to post-40 Ma vertical offsets along some of the NE-trending faults (Dusel-Bacon and Murphy, 2001). Geomorphic studies of these faults suggest displacement as young as Holocene (Page et al., 1995).

NE-SW sub-parallel faults have also been inferred from aligned seismicity in the Fairbanks region; earthquake focal mechanisms indicate sinistral strike-slip faulting (Biswas and Tytgat, 1988; Page et al., 1991; see Chapter 4). Page et al. (1995) propose that these faults separate narrow blocks that are rotating clockwise to accommodate dextral transpression between the Denali and Tintina faults. Possible supporting evidence comes from apparent sinistral offsets of the northern front of the Alaska Range between ~ -143 and -146°E (Figure 2.4); if the range front was originally continuous and parallel to the Denali fault, approximately 15° clockwise rotation of each block is indicated (Page et al., 1995). However, paleomagnetic data from basalts in the Fairbanks area indicate ~ 1° counter-clockwise rotation since the early Eocene (Roe and Stone, 1993), suggesting that wholesale anticlockwise rotation in the hinge of the Alaskan orocline has had a greater total effect since the early Eocene than the clockwise rotation of individual blocks.

The NW-trending Teslin fault zone of south-central Yukon is over 200 km long and 10-20 km wide and consists of two main faults (Figure 2.4). Seismic data indicate that the fault zone dips shallowly to the east, soling into a mid-crustal detachment (Snyder et al., 2005; Creaser and Spence, 2005). Right-lateral, west-over-east transpressive movement on the fault occurred prior to the emplacement of Early Jurassic (~ 212-185 Ma) undeformed cross-cutting plutons (Hansen, 1996; Gordey et al., 1998). Most deformation has been attributed to the docking of outboard terranes (e.g., Snyder et al., 2005). Surface metamorphic fabrics trend NNW; steep westward dips occur in the western part of the zone, flattening to the east (Hansen, 1986). The Teslin fault zone merges southward in northern BC with the Thibert fault, on which up to 200 km of Mid-

Jurassic to Early Cretaceous dextral displacement is inferred (Gabrielse et al., 1991). Minor seismicity appears to align with the Teslin fault zone, suggesting possible dextral transpressive reactivation (see Chapter 4).

The Northern Cordilleran Volcanic Province (NCVP; Edwards and Russell, 1999) is a belt of Neogene to Quaternary (20 Ma – 200 yr) alkaline volcanic centres that extend for ~ 1200 km through northern British Columbia and Yukon. In Yukon (and easternmost Alaska), volcanic centres are confined to the area between the Denali and Tintina faults (Figure 2.4). The alkaline nature of the NCVP volcanism is consistent with decompression melting caused either by the presence of a mantle plume or slab window or by crustal extension (e.g., Edwards and Russell, 1999). Edwards and Russell (1999; 2000) suggest that incipient rifting of the continental margin is causing extension similar to the Basin and Range province in the western United States, in response to changes in relative plate motions. However, the volume of magmatism is relatively low, and evidence for widespread pervasive extensional faulting is lacking.

Most of the northern volcanic centres are aligned over a NW-trending, 500-km-thick low-velocity zone imaged in the seismic tomography study of Frederiksen et al. (1998), indicating a region of unusually hot asthenosphere in the upper mantle. This thermal anomaly is most likely the result of upwelling driven by the presence of a slab window following the subduction of the Pacific-Farallon spreading ridge ~ 43 Ma (Thorkelson and Taylor, 1989; Frederiksen et al., 1998).

Hart and Villeneuve (1999) observe a correlation between Tertiary ENE- to NE-trending faults and ENE-trending dykes and outcrops of the Miles Canyon basalts south of Whitehorse. They favour the slab window hypothesis for magmatism and suggest that volcanism has exploited extensional transfer zones between the Denali and Tintina faults. The northernmost cluster of volcanic centres (northwest of Dawson City; Figure 2.4) also appear to be spatially related to local NE-trending faults; recent extension on nearby NW-SE trending lineaments was documented by Mortensen and Von Gaza (1992), as mentioned above.

Extensional transfer between the Denali and Tintina faults has also been suggested by Lowe and Cassidy (1995). Their receiver function analysis shows thinner crust beneath Dawson City (~ 35 km) than beneath Whitehorse (~ 39 km). The thinner crust is characterized by a Bouguer gravity high north of ~ 63°N that extends into east-central Alaska and may represent a large region that has undergone early Tertiary and younger crustal extension (Lowe and Cassidy, 1995).

Mackenzie, Selwyn and Franklin Mountains

The Mackenzie fold and thrust belt (part of the Cordilleran Foreland belt described briefly above) formed as a result of Late Cretaceous to early Tertiary east-west compression (Eisbacher, 1981; Cook, 1991). The belt is convex to the east, lies between the Selwyn foldbelt (of the Omineca belt) and the western margin of the northern interior platform, and has an arcuate length of 950 km (Figure 2.5; Norris, 1985). Significant seismicity occurs throughout most of the Mackenzie and Selwyn Mountains, but has not been linked to any particular structures (see Chapter 4).

The Mackenzie Mountains are the site of a regional isostatic gravity high that indicates significant undercompensation (Lowe et al., 1994; Lynn et al., 2005). High Bouguer gravity values in the St. Elias Mountains can be explained by high uplift rates due to mountain building (e.g., O'Sullivan and Currie, 1996; Symons et al., 2005); orogenic uplift may also partly explain the Mackenzie Mountains isostatic anomaly. However, another likely explanation is mechanical support by strong underlying lithosphere; calculations of effective elastic lithospheric thickness for the region suggest that the relatively strong edge of the cratonic lithosphere extends beneath the Mackenzie Mountains (Flück et al., 2003; Hyndman et al., 2005a).

The southern Mackenzie Mountains mark a change at ~ 59°N from northwest-trending structures in the northern Rocky Mountains to the south, to north- and northeast-trending structures to the north. The southern Mackenzie Mountains are characterized by relatively broad synclines and narrow, locally en-echelon anticlines that are cut by east- and west-directed steep reverse faults and late-stage north-northeast-striking dextral strike-slip faults, e.g., the Spirit fault (Figure 2.5; Cook, 1991). Movement on many of these right-lateral strike-slip faults likely resulted from reactivation of favourably-aligned Precambrian faults (Cook, 1983).

The dominant structure of the west-central Mackenzie Mountains is the ~ 270-km-long, gently west- to southwest-dipping Plateau thrust fault (Gabrielse et al., 1973).

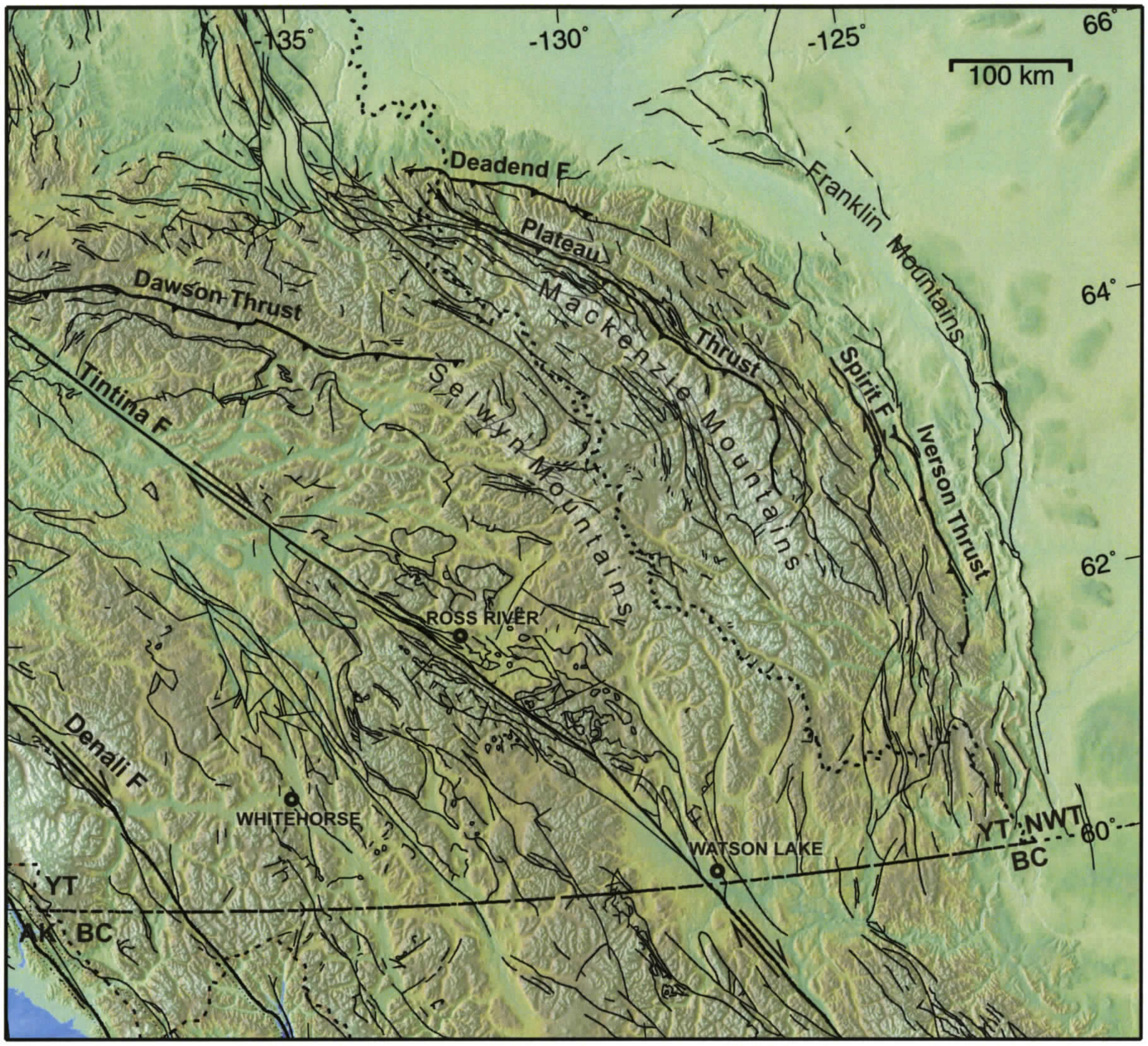

Figure 2.5. Tectonic fault and topographic map of the Mackenzie Mountains region. Triangles on thrust faults indicate down-dip direction.

The fault is shallowly detached above a Middle Proterozoic gypsum unit. The hanging wall of the fault has moved as much as 35 km to the northeast over Paleozoic carbonates and shales (Cecile et al., 1982); lateral displacement of at least 35 km may also have occurred on the fault (Cecile and Cook, 1981). Contrasting with folded rocks to the west and east, undeformed flat to gently-dipping hanging wall strata form an elevated plateau (Redstone Plateau) up to 30 km in width (Cook, 1991). More pervasive deformation to the west reflects a facies change from competent carbonate units to the incompetent argillaceous rocks that form the Selwyn Mountains (Figure 2.5; Cook, 1991).

Structures of the northern Mackenzie Mountains comprise broad, regionally continuous anticlines and relatively narrow synclines. The northern fold and thrust belt is ~ 125 km wide from the Plateau fault (Figure 2.5) in the west to the eastern mountain front. The fold belt is dominated by three broad anticlines, which are cut by steeply-dipping thrust faults showing minor displacements. The 170-km-long Deadend fault is the longest of these thrusts and forms part of the mountain front, which is otherwise shaped by the eastern limb of an anticline. Proterozoic and Paleozoic strata in the anticline cores are offset by minor north-trending Precambrian faults that underwent dextral strike-slip reactivation under Late Cretaceous and early Tertiary compression (Cook, 1991) and may show similar movement under the current compressional regime (see Chapter 4).

At least two levels of detachment are believed to occur beneath the Mackenzie Mountains; deep detachments are inferred by concentric folds, their greater scale in the north implying much deeper detachment there than to the south, while the Plateau fault and thrusts of the Franklin Mountains represent shallow detachments (Cecile et al., 1982; Cook, 1991).

Deformation of the Cordilleran foreland migrated, and decreased in magnitude, from west to east. The Selwyn Mountains were deformed prior to the emplacement of mid-Cretaceous plutons and underwent over 150 km of shortening, whereas Paleocene strata are deformed in the Franklin Mountains, and shortening across the Mackenzie and Franklin Mountains is estimated at only 45-55 km (Gordey, 1981; Cecile et al., 1982; Cook, 1991). Structures of the Mackenzie Mountains appear to be undergoing thrust and strike-slip reactivation under the current NE-SW-oriented stress regime (Chapter 4).

Dawson Thrust Fault

The south-dipping Dawson thrust fault (Figure 2.6) trends approximately E-W for over 300 km on the northeastern side of the Tintina fault in Yukon Territory, and represents the boundary between Selwyn Basin sediments of the Omineca belt to the south and the Wernecke and Ogilvie Mountains of the Foreland belt to the north. The Dawson thrust originated as an extensional structure that acted as a boundary between

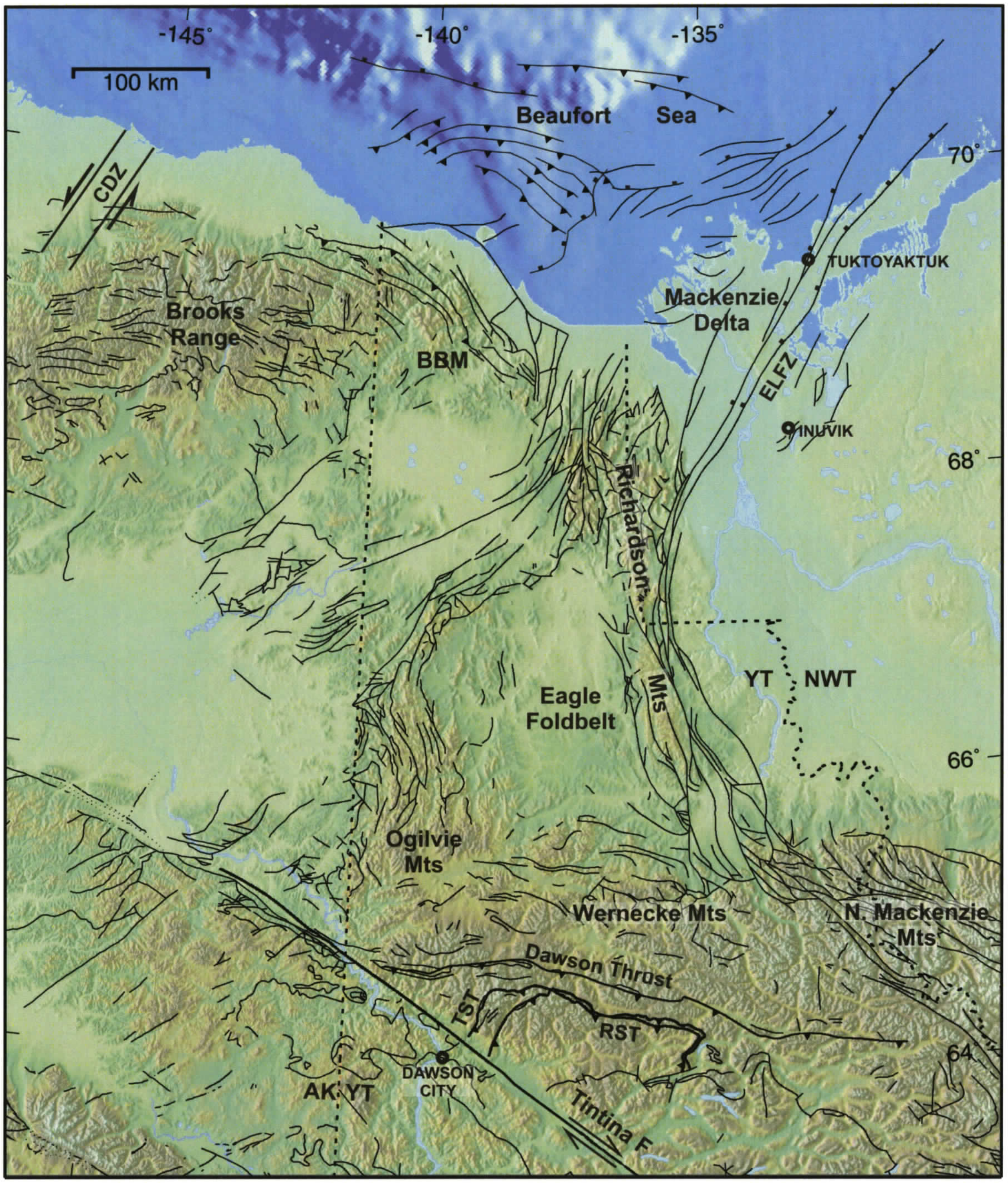

Figure 2.6. Tectonic fault and topographic map of the northernmost Cordillera. Triangles on thrust faults indicate down-dip direction and blocks on normal faults indicate downthrown side. TST: Tombstone thrust; RST: Robert Service thrust; ELFZ: Eskimo Lakes fault zone; BBM: British-Barn Mountains; CDZ: Canning displacement zone, from Grantz et al. (1983).

basinal and platformal deposition in the Neoproterozoic and early Paleozoic (e.g., Abbott, 1997; Mair et al., 2006).

The fault was reactivated as a low-angle thrust in the Late Jurassic-Early Cretaceous, when the Tombstone and Robert Service thrusts to the south also became active (e.g., Poulton and Tempelman-Kluit, 1982; Murphy, 1997). These thrusts are inferred to sole into the same basal detachment (e.g., Abbott, 1997). Structural overlap and intra-thrust-sheet deformation suggest that the Tombstone and Robert Service thrusts may have accommodated as much as 100 km or more of shortening, whereas relatively minor displacement on the Dawson thrust implies that it acted as a northern backstop to compressive deformation (Mair et al., 2006). Metamorphic fabrics within the thrust sheets also indicate a high degree of shear strain (Mair et al., 2006).

Initial shortening is interpreted as NNE-SSW-oriented, with a later change to NW-directed movement (Mair et al., 2006). Original thrusting predates the mid-Cretaceous emplacement of Tombstone suite plutons (e.g., Marsh et al., 2003), but paleomagnetic data from the 91-Ma Deadman pluton within the Dawson thrust sheet suggest post-91-Ma tilting and northward displacement of several tens of kilometres, perhaps along the sole detachment (Symons et al., 2006). Seismicity in the region of the Dawson, Tombstone and Robert Service thrust sheets suggests reactivation of these structures to accommodate transpression (see Chapter 4).

Wernecke and Ogilvie Mountains

North of the Dawson thrust fault in the southern Ogilvie and Wernecke Mountains (Figure 2.6), E-W-trending thrust faults are thought to root in a single gently south-dipping detachment; most thrust displacements are estimated at ~ 0.5-2 km, inferring total shortening of ~ 25% (Abbott, 1997). The intensity of deformation, metamorphic grade, and amount of shortening all decrease northwards, while the age of deformation appears to decrease; rocks as young as Paleocene-Eocene are deformed in the northern Ogilvie and Wernecke Mountains (Abbott, 1997; Symons et al., 2006).

The Wernecke Mountains are characterized by Mesozoic-Tertiary NW-trending steeply NE- or shallowly south-dipping thrust faults and broad folds similar to structures in the Mackenzie Mountains and indicative of northward translation (Thompson, 1991). In the southern Ogilvie Mountains, folds and thrusts are cut by late-stage N- and W-trending sub-vertical faults, many of which are strike-slip faults with both sinistral and dextral offsets greater than 2 km; many of these are likely reactivated Precambrian structures (Thompson, 1991). A change in structural style occurs from the E-W-trending folds of the southern Ogilvie Mountains to the N-S folds of the northern Ogilvies.

Richardson Mountains

The southern Richardson Mountains (Figure 2.6) consist of a 360-km-long, 90-km-wide, northwest-trending anticlinorium (Gabrielse, 1957) that lies between the northern interior platform to the east and the Eagle foldbelt to the west (Norris, 1985; Gabrielse and Yorath, 1991). The anticlinorium and the northern Richardson Mountains are both cut by steeply-dipping, north-trending faults of the Richardson fault array, strands of which show dextral displacements of up to 40 km (e.g., Norris, 1985). The Richardson fault array extends for ~ 600 km from the Mackenzie Mountains to offshore Tuktoyaktuk Peninsula; it controlled the development of both the early to mid-Paleozoic Richardson trough and later contractional deformation (e.g., Lane, 1996). Fault motion was probably mainly dextral strike-slip from mid-Proterozoic to Devonian time, but Carboniferous and younger formations apparently lack horizontal displacements across faults of the array (Norris, 1985). Inversion of the Richardson trough to form the anticlinorium was caused by Late Cretaceous to early Tertiary, mainly dip-slip, reactivation (Norris, 1985; Lane, 1996).

A positive gravity anomaly in the southern Richardson Mountains suggests the involvement of basement in a local thick-skinned deformation zone, whereas the gravity low of the northern Richardsons implies thin-skinned deformation (Lane, 1996). The north-south trend of structures in the Richardson Mountains reflects regional Late Cretaceous to early Tertiary east-west convergence (e.g., Lane, 1995), and 30% tectonic shortening across the southern Richardson Mountains has been inferred (Lane, 1996). The Richardson Mountains are characterized by significant seismicity that is greater in the south than the north (Chapter 4). The current mainly strike-slip earthquake mechanisms indicate that the most recent phase of deformation is again mainly strike-slip (see Chapter 4), although this motion has not been clearly identified in the geological data.

Brooks Range, British-Barn Mountains and Beaufort-Mackenzie Region

Structures in the northernmost Cordillera are the result of a varied Mesozoic-Tertiary tectonic history. Formation of the Brooks Range began in the Late Jurassic with southward subduction of a continental margin beneath an island-arc terrane (e.g., Fuis et al., 1995). From the late Jurassic to mid-Cretaceous, northwestward rifting to create the western Arctic Ocean basin led to listric extensional faulting (e.g., Eskimo Lakes fault zone, Figure 2.6) and sedimentation in the Beaufort-Mackenzie region (Stephenson et al., 1994; Lane, 1997).

Late Paleocene-middle Eocene deformation resulted in a broad arcuate onshore-offshore fold and thrust belt encompassing north-trending structures in northeastern Yukon, northwest trends in the British-Barn Mountains and offshore Beaufort shelf, and east-trending structures in the eastern Brooks Range of Alaska (Figure 2.6; Gabrielse and Yorath, 1991; Lane, 2002). The orocline likely resulted from simultaneous N-S Cordilleran compression and E-W shortening related to the opening of the North Atlantic (Lane, 1998; 2002). Latest Cretaceous to Cenozoic shortening of at least 45 km is estimated across the northeastern Brooks Range (Fuis et al., 1995). Rapid Early Eocene uplift and denudation is documented by apatite fission track data from the onshore Beaufort-Mackenzie region (O'Sullivan and Lane, 1997).

The latest phase of Cordilleran deformation occurred in the Late Miocene, although local Holocene deformation is apparent (Lane, 2002). North-directed compression produced long E-W-trending folds concentrated in the distal Beaufort-Mackenzie basin (Lane, 2002). Basement-involved thrusting of the northeastern Brooks Range beneath the Beaufort coastal plain is inferred (Potter and Moore, 2004), along with reactivation of Jurassic-Cretaceous normal faults and early Tertiary structures (Lane, 2002). Local strike-slip features are also apparent, particularly in the southeastern part of the basin, where a broad transition occurs from thick strong basement south of the basin to thin basement overlain by sediments up to 16 km thick (e.g., Lane, 2002). Lane and Dietrich (1995) suggest that right-lateral oblique extension occurred across this transition to accommodate Tertiary deformation to the west while the rigid crust to the east remained undeformed.

A NE-trending belt of seismicity in the northeastern Brooks Range approximately aligns with the Canning displacement zone (Figure 2.6), a young sinistral strike-slip shear zone identified by Grantz et al. (1983; see Chapter 4). Focal mechanisms suggest transtension. Current seismicity in the offshore Beaufort Sea region is poorly constrained and poorly understood. It may represent extension in the lower crust/upper mantle (~ 40 km depth) due to flexural loading under the thick sequence of Mackenzie Delta sediments (Hasegawa et al., 1979; Hyndman et al., 2005c; Chapter 4).

CHAPTER 3

Current Deformation in the Northern Canadian Cordillera Inferred from Global Positioning System Measurements

INTRODUCTION

This chapter deals with Global Positioning System (GPS) measurements used to constrain the current deformation of the northern Canadian Cordillera with respect to the stable North America plate. First, the Global Positioning System is described, with an explanation on how the position of a site can be determined to the level of precision of a few millimetres required for studies of tectonic motion. Next, the GPS network used in this study is introduced; it includes both continuous and short-term campaign sites. The fieldwork methods for collection of campaign data are then outlined, followed by a description of how the data are processed. Finally, the results of the processing and data corrections are presented and discussed.

This study provides GPS vectors showing the direction and rate of movement (with calculated error) of sites with respect to stable North America. The GPS solutions, in conjunction with geological and seismicity data (Chapters 2; 4), provide constraints on the current tectonics of the area, as summarized in Chapter 5.

GLOBAL POSITIONING SYSTEM

The NAVSTAR (NAVigation Satellite Timing And Ranging) Global Positioning System (GPS) is a satellite-based navigation system funded and controlled by the United States Department of Defense and fully operational since 1995 (see Hofmann-Wellenhof et al., 2001 for a comprehensive description of GPS). Apart from the original military use, GPS now has many civilian applications, especially since the elimination of

Selective Availability (SA) in 2000. SA involved a degradation of the satellite signals that only the U.S. military could decode, and was thus intended to provide them with a military advantage. With SA, real-time position estimation for civilian users was limited to about a hundred metres; without it, precision of less than ten metres is possible. However, the advent of differential GPS, where site position is determined relative to a fixed site or number of sites, overcame most of SA to achieve far greater precision (within millimetres). Precision was also much improved with the availability of precise satellite orbits generated by the IGS (International Global Satellite Service), as described below. Precision GPS has become the geodetic method of choice for studying large-and small-scale tectonic deformation (Segall and Davis, 1997).

Principle of Single-Point Positioning with GPS

The GPS constellation currently consists of 29 satellites at an altitude of 20,200 km that orbit the earth in six orbital planes approximately every 12 hours. This constellation provides the user with at least 6 satellites above the horizon at any point on the earth at any time. The user needs an antenna and a receiver to receive and process microwave signals sent out by the satellites. Once it receives these signals, the GPS receiver estimates the range to the satellites. The satellites' estimated positions are included in the signals they send out, and the distance to the satellite is estimated; thus with four satellites the receiver can calculate its own position (latitude, longitude, elevation).

Satellite signal

The signal from each GPS satellite contains several components, all derived from the fundamental frequency of the satellite oscillator f_0 (Table 3.1). Carriers L_1 and L_2 are both modulated by the Precise (P) code; L_1 is also modulated by the Coarse Acquisition (C/A) code and the Navigation Message. The Navigation Message includes information about the satellite orbit, its clock, and its "health" status. The P-code and the C/A-code consist of pseudo-random noise (PRN) sequences. The C/A-code has a length of 1023 bits and repeats itself every millisecond; each satellite is assigned a unique C/A-code. The P-code is approximately 2.3547 x 10^{14} bits long (~ 267 days), but is partitioned into thirty-seven one-week segments. One segment is assigned to each satellite, and each satellite's P-code repeats itself every week. The time interval between bits is ten times smaller than for the C/A-code, corresponding to approximately 30 m rather than 300 m; the potential accuracy of the P-code is therefore ten times higher than the C/A-code.

Table 3.1. Components of the satellite signal (after Hugentobler et al., 2001)

Component	Frequency (MHz)	Wavelength
Fundamental frequency	10.23 (f_0)	
Carrier L_1	1575.42 ($f_1 = 154 f_0$)	$\Lambda_1 \sim 19.0$ cm
Carrier L_2	1227.60 ($f_2 = 120 f_0$)	$\Lambda_2 \sim 24.4$ cm
P (Precise)-code $P(t)$	10.23 (f_0)	
C/A (Coarse Acquisition)-code $C(t)$	1.023 ($f_0 / 10$)	
Navigation message $D(t)$	50×10^{-6} ($f_0 / 204600$)	

The receiver has an internal clock that is synchronized with those of the satellites. It also contains the code information necessary to co-generate the code structure, such that cross-correlation of the received signal with its internal code will allow determination of a time delay (the signal transit time). The distance, or range, from the satellite to the receiver is given by the transit time multiplied by the speed of light. However, the range estimate contains errors in satellite position and in satellite and receiver clock timing, as well as the effects of path delays, and is therefore called the pseudorange.

For geodetic purposes, higher precision than is possible with basic processing is generally necessary (e.g., this project requires detection of tectonic motion of only a few to tens of millimetres per year). Higher precision is achieved using the L_1 and L_2 carrier phase information. When the receiver has started to track a satellite, it measures the fractional part of the arriving signal phase and thereafter tracks the phase continuously. Due to the short wavelength, the resulting fractional phase length measurement is much more precise (1 mm accuracy) than a simple code measurement. However, the number of wavelengths between source and receiver is initially unknown, and must be determined by a process of ambiguity resolution.

For a receiver to determine its position, it needs to resolve the range to at least three satellites to perform a trilateration. Tracking a fourth satellite enables the receiver to calculate the clock offset between it and the satellites and thus correct for clock errors. As mentioned earlier, differential GPS improves precision further. A reference receiver at a fixed site of accurately known position is used to calculate satellite errors by estimating the difference between the measured and the known range between it and each satellite. The necessary corrections are then either transmitted to survey receivers (real-time differential GPS) or are applied to the survey data after data collection (post-processing differential GPS). This approach allows correction for error sources that are common to both the reference receiver and the measurement station; the closer the reference station to the measurement station, the more effective is the error cancellation. Alternatively, with reference GPS (used in this study), where the positions of sites are calculated relative to a reference station, common errors are automatically subtracted without the need for correction.

Sources of error

The calculated position is subject to a number of errors: (1) orbital position errors, (2) clock errors, (3) multipath errors, (4) atmospheric errors, and (5) site-specific noise. Many of these errors can be substantially reduced with relative positioning, where a group of satellites are simultaneously observed by a network of receivers.

(1) Orbital errors result from uncertainty in the satellite position estimates. The precise orbits required for millimetre-precision positioning are generated by the IGS using 47 globally distributed sites with accurately known positions constrained by VLBI (Very Long Baseline Interferometry) and/or SLR (Satellite Laser Ranging) measurements (Beutler et al., 1999; http://igscb.jpl.nasa.gov/). The GPS satellite orbits are known with ~ 3 cm precision and ~ 5 cm accuracy.

(2) Clock errors are due to the less than perfect synchronization of the internal receiver clock with those of the satellites. They can be much reduced if a single receiver tracks at least four satellites, as mentioned above, or if two satellites are tracked by two receivers (double differencing).

(3) Multipath errors result when radio signals from the satellite do not reach the antenna directly but are reflected by nearby objects or even the ground before reaching the antenna; the distance between the satellite and antenna is thus overestimated. Multipath effects are reduced with the use of a choke-ring antenna that rejects near- or sub-horizontal waves (e.g., Tranquilla et al., 1994).

(4) Atmospheric variations, especially moisture content, significantly affect the propagation velocity of the satellite signals; signal delays arise from the ionosphere and troposphere. The ionosphere is frequency dispersive, and use of a dual-frequency receiver allows a large reduction in most of the ionospheric errors. Most of the non-dispersive atmospheric delay is associated with the troposphere and contains both "dry" (90%) and "wet" (10%) components. The dry delay arises from atmospheric molecules in hydrostatic equilibrium, whereas the wet delay is associated with water vapour out of hydrostatic equilibrium. At zenith near sea level, the dry delay is typically about 2.3 m path length, with the zenith wet delay an order of magnitude smaller; both delays are larger at other elevation angles towards horizontal for which the paths are longer. Non-dispersive atmospheric errors can be reduced by tropospheric refraction modelling.

(5) Site-specific noise may result from unfavourable conditions at the observation site. Error may arise from monument instability caused by sediment settling or an otherwise unstable set-up, inclement weather (especially snow on the antenna), wildlife or human disturbances, or user error. It is important that the user collects detailed and accurate field notes so that the cause of site-specific noise or unexplained position offsets may be identified.

CONTINUOUS GPS NETWORK

The study used data from twenty-eight continuously recording GPS stations in Yukon Territory, Northwest Territories, British Columbia, and eastern Alaska (Figure 3.1; Table 3.2). Examples of continuous GPS monuments are shown in Figure 3.2. The majority of sites are steel or concrete monuments set in bedrock or sediment to variable depths, although some antennae are attached to buildings. These stations are part of the following networks: the Alaska Deformation Array (AKDA), the British Columbia Active Control System (BCACS), the Canadian Active Control System (CACS), the US National Geodetic Survey Continuously Operating Reference Stations (CORS), and the Western Canada Deformation Array (WCDA). Previously only a small part of the available data had been processed for tectonic analysis of the northern Canadian

Table 3.2. Information on continuous GPS sites used for this study.

Site ID	Station #	Site Location	Network	LAT. (° N)	LON. (° W)	ALT. (m)	Start Date	End Date	Monument/Setting
AIS1	49998S001	Annette Island, AK	CORS[1], USCG[2]	55.0691	228.4005	32	1/19/96	-	Antenna attached to cross-brace on lattice Rohn tower encased in 6x6x4-ft concrete block, possibly buried a few ft
ATW2	49934M002	Palmer, AK	AKDA[3]	61.5982	210.8677	98	10/29/98	-	Pyramidal welded pipe structure anchored in concrete slab to 10 ft depth in sediment
BCDL[7]	594705	Dease Lake, BC	BCACS[4]	58.4256	229.9743	802	6/15/05	-	On stainless steel pillar at airport
BCFJ[8]	981274	Fort St John, BC	BCACS	56.2462	239.2506	677	2/11/05	-	On stainless steel pillar at airport
BCFN[9]	384099	Fort Nelson, BC	BCACS	58.8403	237.4151	368	2/11/05	6/28/05	On stainless steel pillar at airport
BEA2	M028001	Beaver Creek, YT	WCDA[5]	62.4078	219.1375	662	11/16/02	-	Stainless steel pin epoxied in concrete pad set in gravel - depth of pad suspected to be < 0.30 m
BIS1	49834S001	Biorka Island, AK	CORS, USCG	56.8545	224.4607	67	3/21/00	-	Antenna attached to cross-brace on lattice Rohn tower encased in 6x6x4-ft concrete block, possibly buried a few ft
CHI3	49803S003	Cape Hinchinbrook, AK	CORS, USCG	60.2375	213.3534	95	3/2/99	-	Concrete monument in concrete slab on building roof
CLGO	12722	Fairbanks, AK	AKDA	64.8739	212.1399	260	3/11/96	-	Concrete pillar with 1.5 inch rod in centre, extending to 10 ft depth into cored hole in sediment
DRAO	40105M002	Penticton, BC	WCDA	49.3226	240.3750	542	2/27/91	-	Brass plate with stainless steel bolt on 1.5 m concrete pier, anchored to bedrock with steel bars to 0.75 m depth
DSLK	771840	Dease Lake, BC	BCACS	58.4358	230.0111	819	6/1/96	11/3/04	Mast attached to north wall of building
FAIR	40408M001	Fairbanks, AK	CORS	64.9780	212.5008	319	10/17/91	-	Reinforced concrete pillar with steel tubing sheath
FNEL	602904	Fort Nelson, BC	BCACS	58.8053	237.2680	440	6/1/96	5/10/04	Mast attached to west wall of building
FTSJ	137406	Fort St John, BC	BCACS	56.2549	239.1514	706	6/1/96	2/8/05	Mast attached to NW corner of building roof
GNAA	49996S001	Glennallen, AK	CORS	62.1124	214.0298	603	7/17/97	-	Antenna attached to chain-link fence corner post, cemented in ground to 1 m depth, double-braced to adjacent posts
GRNR	49936M001	Garner, AK	AKDA	63.8356	211.0219	570	8/1/97	-	Invar rod within concrete pillar anchored to bedrock
GUS2	49802S002	Gustavus, AK	CORS, USCG	58.4178	224.3030	20	4/15/96	-	Antenna attached to cross-brace on lattice Rohn tower encased in 6x6x4-ft concrete block, possibly buried a few ft
HOLB	40130M001	Holberg, BC	CACS[6], WCDA	50.6404	231.8650	560	7/24/92	-	Brass plate with stainless steel bolt embedded on 1.0 m concrete pier, anchored to bedrock with steel bars to 0.5 m depth
HOLM	40148M001	Holman, NWT	CACS	70.7363	242.2388	40	8/28/01	-	Stainless steel plate with bolt on 1.5 m steel pillar in a rock cairn, anchored to bedrock with steel rods to 1.5 m depth
INVK	40150M001	Inuvik, NWT	CACS	68.3062	226.4731	46	7/22/01	-	Brass plate with stainless steel bolt embedded on 2.0 m concrete pier, anchored to bedrock with steel bars to 1.5 m depth
LEV1	49796S001	Level Island, AK	CORS, USCG	56.4657	226.9072	25	6/19/01	-	Antenna attached to cross-brace on lattice Rohn tower encased in 6x6x4-ft concrete block, possibly buried a few ft
PBOC	49640S002	Prudhoe Bay, AK	CORS	70.0256	211.9665	20	2/12/02	-	Antenna on mast attached to building
POT3	49801S003	Potato Point, AK	CORS, USCG	61.0563	213.3032	36	9/2/98	-	Antenna attached to cross-brace on lattice Rohn tower encased in 6x6x4-ft concrete block, possibly buried a few ft

Table 3.2. (Continued)

Site ID	Station #	Site Location	Network	LAT. (° N)	LON. (° W)	ALT. (m)	Start Date	End Date	Monument/Setting
PRDS	40124M001	Calgary, AB	CACS	50.8713	245.7065	1247	1/7/97	-	Brass plate with stainless steel bolt embedded on 2 m high concrete pier, in soil to 3 m depth
SACH	40163M001	Sachs Harbour, NWT	CACS	71.9903	234.7501	69	10/3/02	-	Brass plate with steel bolt on 1.5 m concrete pier, welded to 1.2 m platform of steel beams welded to steel casings, driven 12 m into permafrost
SELD	15621	Seldovia Airport, NWT	AKDA	59.4459	208.2933	21	10/24/00	-	Invar rod within concrete pillar anchored to bedrock
TRRC	722959	Terrace, BC	BCACS	54.5148	231.3734	62	6/1/96	-	Mast attached to south wall of building
TUKT	40165M001	Tuktoyaktuk, NWT	CACS	69.4382	227.0056	2	8/21/03	-	Brass plate with stainless steel bolt epoxied on 1.5 m high wood pole, driven ~ 6.1 m into a predrilled hole in permafrost
WHIT	40136M001	Whitehorse, YT	CACS, WCDA	60.7505	224.7779	1427	6/9/96	-	Brass plate with stainless steel bolt embedded on 1.5 m concrete pier, anchored to bedrock with steel reinforcement bars
WILL	40134M001	Williams Lake, BC	CACS, WCDA	52.2367	237.8322	1096	10/6/93	-	Brass plate with stainless steel bolt on 1.8 m high concrete pier, anchored to bedrock with steel bars to 0.5 m depth
YELL	40127M003	Yellowknife, NWT	CACS	62.4809	245.5193	181	1/21/91	-	Brass plate with stainless steel bolt on 2.3 m high concrete pier, anchored to bedrock with steel bars to 3 m depth

[1] CORS: Continuously Operating Reference Stations; [2] USCG: United States Coast Guard; [3] AKDA: Alaska Deformation Array; [4] CACS: British Columbia Active Control System; [5] WCDA: Western Canada Deformation Array; [6] CACS: Canadian Active Control System; [7] Data merged with former site DSLK; [8] Data merged with former site FTSJ; [9] Data merged with former site FNEL.

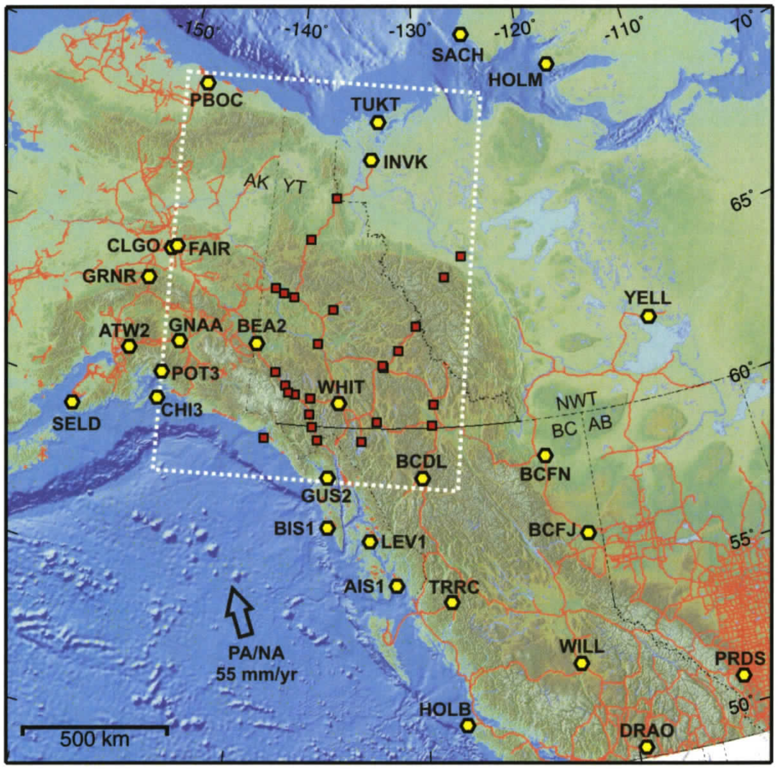

Figure 3.1. Continuous GPS stations analyzed (yellow hexagons). Analyzed campaign sites are marked by red squares. Highways are shown by red lines. Box with dotted outline defines the extent of Figure 3.3.

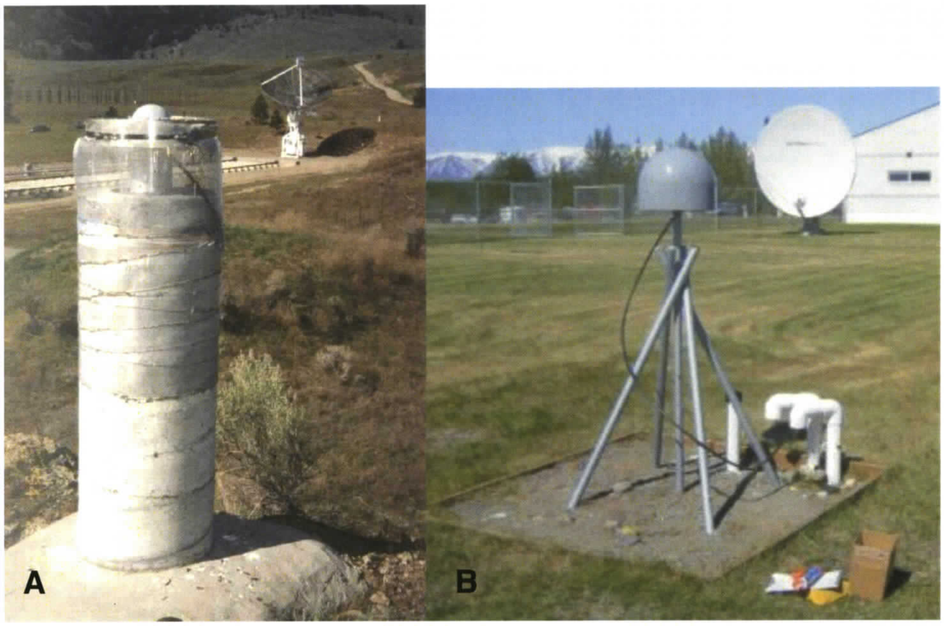

Figure 3.2. Examples of continuous GPS monuments. **A.** Concrete pier anchored to bedrock at DRAO, Penticton, British Columbia. **B.** Welded pipe structure anchored in concrete slab in sediment at ATW2, Palmer, Alaska.

Cordillera (Flück, 2003). For this study, the continuous data from January 1999 to December 2005 were collected and processed. Current data are downloaded and archived daily by the Canadian Crustal Deformation Service at the Pacific Geoscience Centre. However, the data from the four BCACS sites for 1999 to 2003 had to be retrieved from a large number of 8-mm Exabyte tapes, archived by the British Columbia Ministry of Sustainable Resources, Base Mapping and Geomatic Services. This was a very time-consuming task, but valuable data linking the northern and southern Canadian Cordillera were recovered.

CAMPAIGN GPS

The campaign sites of the Northern Cordillera Deformation Network (Figure 3.3; Table 3.3) are located in Yukon Territory, western Northwest Territories and northernmost British Columbia along the Alaska, Dempster, Klondike, Robert Campbell, and Top of the World Highways, and the Haines, North Canol and Atlin Roads. Seventeen of the campaign sites were previously occupied two to five times between

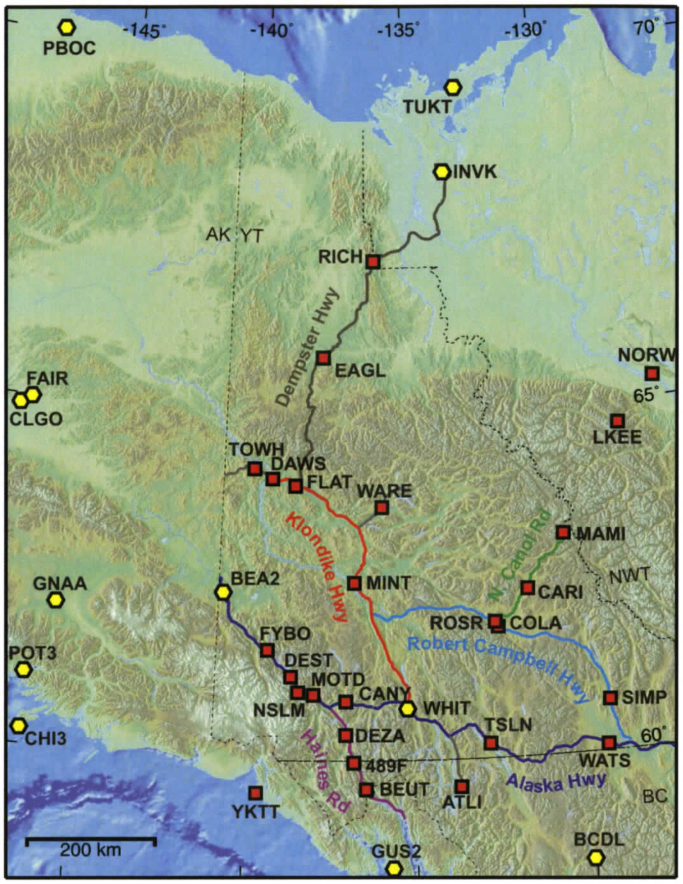

Figure 3.3. Campaign GPS sites (red squares) and the relevant Yukon highways. Continuous sites are marked by yellow hexagons.

1999 and 2002 by Geomatics Canada, the Geophysical Institute, University of Alaska Fairbanks, and the University of Victoria/PGC (Flück, 2003; Hyndman et al., 2005a).

Two GPS campaigns were carried out for the purposes of this study following the work of Flück (2003). The 2004 survey took place in the fall (September/October), similar to the late summer timing of Paul Flück's 2001 and 2002 campaigns (Flück, 2003). However, due to equipment availability, the 2005 survey took place earlier in the summer (June/July). This one to two month difference is not expected to have a significant effect. All of the surveys avoided the winter period with intermittent snow on the antenna, with the exception of the post-Denali earthquake survey of Flück (2003) in November 2002.

The 2004 survey consisted of a reoccupation of thirteen existing campaign sites, along with the establishment and occupation of seven additional sites. Six of these new

Table 3.3. Campaign GPS site information.

Site ID	Station #	Site Name	LAT. (° N)	LON. (° W)	ALT. (m)	# Occs.	Occ. Dates	# days	Occupied by	Setting
ALASKA										
YKTT	13849	Yakutat, Alaska	59.5107	220.3512	18	3	1999	4	GI	Brass marker in bedrock
							2001	7	GI	
							2002	4	GI	
ALASKA HIGHWAY										
489F	15002	489F	59.9727	223.1811	925	3	1999	1	GI	Iron rod with brass marker in sediments
							2000	3	GI	
							2004	3	GI	
CANY	43Y108	Canyon Creek	60.8592	222.9372	659	7	1999	3	GI	Brass marker in bedrock
							2000	1	GI	
							2001	2	PGC	
							2002	8	PGC	
							2004	2	PGC	
							2005	2	PGC	
DEST	43874	Destruction Bay	61.2169	221.2781	858	6	1999	2	GI	Brass marker in concrete column in sediments
							2000	2	GI	
							2001	2	PGC	
							2002	13	GI, PGC	
							2004	3	GI	
FYBO	78Y565	FYBO	61.5927	220.5551	757	3	2002	12	GI	Brass marker in concrete column in sediments
							2004	3	GI	
MOTD	M028002	Middle of the Day	60.9577	221.9595	952	7	2000	2	GI	Brass marker in bedrock
							2001	2	PGC	
							2002	6	GI, PGC	
							2004	3	GI	
							2004	2	PGC	
							2005	2	PGC	
NSLM	M008001	New Slims R.	60.9927	221.5036	806	7	2000	2	GI	Brass marker in bedrock
							2001	2	PGC	
							2002	15	GI, PGC	
							2004	3	GI	
							2004	2	PGC	
							2005	3	PGC	
TSLN	M048003	Teslin	60.2103	227.1840	1096	2	2004	4	PGC	Steel pin in bedrock
							2005	3	PGC	
WATS	77Y011	Watson Lake	60.0825	230.6313	872	2	2004	4	PGC	Brass marker in sediments
							2005	3	PGC	
ATLIN ROAD										
ATLI	987009	Atlin, BC	59.5895	226.2855	793	5	1999	4	GSD	CBN geodetic concrete pillar in bedrock
							2001	2	PGC	
							2002	4	GSD	
							2004	2	PGC	
							2005	2	PGC	
DEMPSTER HIGHWAY										
EAGL	78Y077	Eagle Plains	65.7723	222.1536	762	5	2000	3	GSD	Iron rod in bedrock
							2001	3	PGC	
							2002	3	PGC	
							2004	4	PGC	
							2005	3	PGC	
RICH	78T005	Richardson Mountains	67.0978	223.8745	713	5	2000	2	GSD	Iron rod in sediments
							2001	2	PGC	
							2002	2	PGC	
							2004	3	PGC	
							2005	2	PGC	
HAINES ROAD										
BEUT	M008003	Beauty	59.5815	223.5346	930	4	2000	2	GI	Brass marker in bedrock
							2004	3	GI	
							2004	3	PGC	
							2005	3	PGC	

Table 3.3. (Continued)

Site ID	Station #	Site Name	LAT. °N	LON. °W	ALT. m	# Occs.	Occ. Dates	# days	Occupied by	Setting
DEZA	M048000	Dezadeash Lake	60.3762	222.9458	736	4	2002	3	GI	Brass marker in bedrock
							2004	3	GI	
							2004	3	PGC	
							2005	3	PGC	
KLONDIKE HIGHWAY										
DAWS	M028000	Dawson City	64.0523	220.5654	369	3	2002	2	PGC	Steel pin in bedrock
							2004	3	PGC	
							2005	2	PGC	
FLAT	848130	Flat Creek	63.9585	221.3056	455	6	2000	1	GSD	Brass marker in concrete column in sediments
							2001	2	PGC	
							2002	6	PGC	
							2004	3	PGC	
							2005	2	PGC	
MINT	M048001	Minto	62.5761	223.2064	801	2	2004	2	PGC	Steel pin in bedrock
							2005	3	PGC	
WARE	87Y505	Wareham Dam	63.6567	224.0813	1097	2	2004	3	PGC	Brass marker in bedrock
							2005	3	PGC	
NORTH CANOL ROAD										
CARI	848123	Caribou Creek	62.4241	228.5717	895	4	2001	2	PGC	Brass marker in concrete column in sediments
							2002	4	PGC	
							2004	3	PGC	
							2005	2	PGC	
COLA	848025	Coffee Lake	61.9011	227.5890	814	5	1999	2	GSD	Aluminum cap marker on iron bar in sediments
							2001	2	PGC	
							2002	3	PGC	
							2004	6	PGC	
							2005	3	PGC	
MAMI	73Y180	MacMillan Pass	63.1751	229.7994	1179	5	1999	2	GSD	Brass marker in bedrock
							2001	2	PGC	
							2002	3	PGC	
							2004	2	PGC	
							2005	2	PGC	
ROSR	M048004	Ross River	61.9691	227.5125	838	2	2004	2	PGC	Steel pin in bedrock
							2005	3	PGC	
NORTHWEST TERRITORIES										
LKEE	789042	Little Keele R.	64.6760	231.8902		1	2004	3	PGC	Brass marker in bedrock
NORW		Norman Wells	65.2781	233.2067		1	2004	25	PGC	Aluminium plate on 1.6 m pole on roof
ROBERT CAMPBELL HIGHWAY										
SIMP	M048005	Simpson Lake	60.7353	230.7967	740	2	2004	3	PGC	Steel pin in bedrock
							2005	3	PGC	
TOP OF THE WORLD HIGHWAY										
TOWH	M048002	Top of the World Highway	64.1889	219.9704	1152	2	2004	2	PGC	Steel pin in bedrock
							2005	2	PGC	

[1] GI: Geophysical Institute, University of Alaska Fairbanks; [2] PGC: Pacific Geoscience Centre, Geological Survey of Canada; [3] GSD: Geodetic Survey Division, Geomatics Canada.

sites provide an extension of the existing network, whereas one (Ross River, ROSR) is intended to replace a marker of questionable stability at Coffee Lake (COLA). Stéphane Mazzotti of the Pacific Geoscience Centre also carried out a concurrent survey in September 2004, establishing two new sites at Norman Wells (NORW) and Little Keele River (LKEE), both in the western Northwest Territories on either side of the main mountain front. The 2005 survey entailed reoccupation of all twenty sites surveyed in 2004. However, Mazzotti's helicopter-supported two-site campaign has yet to be repeated.

The analysis included data from a further four sites that were not occupied in the 2004 and 2005 surveys. These include three sites along the Alaska Highway (489F, DEST, and FYBO), and one at Yakutat, Alaska (YKTT); campaign data were collected by the Geophysical Institute, University of Alaska (Table 3.3).

Fieldwork Logistics and Methods

The fieldwork in both 2004 and 2005 was carried out by the author, assisted by Lisa Nykolaishen. Field equipment and a 4WD vehicle were provided by the Pacific Geoscience Centre, Geological Survey of Canada (PGC-GSC), with technical support from PGC Research Engineer Mike Schmidt. Fieldwork expenses were covered by PGC-GSC and NSERC.

In each survey, sites were occupied with a GPS antenna and receiver for a minimum of 48 hours, long enough to minimize the error due to diurnal and other short-term variations and to ensure consistent satellite coverage. The antennae were Ashtech model ASH701945C_M and the receivers were Ashtech Z-Xtremes. The same units were deployed at each site in both surveys for consistency and error minimization; where possible, these were the same units deployed in the 2002 surveys of Paul Flück (2003).

Tripod set-ups (Figure 3.4A) were used for the few sites where the marker sits in consolidated sediment. The newer, more stable guyed mast set-up (Figure 3.4B) was employed for markers drilled into bedrock. Exceptions to this are (A) the Canadian Base Network (CBN) monument at Atlin, where the antenna is simply screwed into a steel spacer, in turn screwed onto a standard forced-centre concrete monument (Figure 3.4C). (B) A tripod was used for the second occupation at Minto, due to cracking of the existing mast anchor holes during the attempted set-up and the lack of rock suitable to be drilled in the small outcrop to replace them.

Figure 3.4. A. Example of a tripod set-up, at site RICH, Richardson Mountains, Northwest Territories. **B.** Example of a mast set-up, at site DAWS, Dawson City, Yukon Territory. **C.** CBN monument at site ATLI, Atlin, British Columbia.

Tripod set-ups

For a tripod set-up (Figures 3.4A; 3.5A), the tripod is centred over the centre point of the marker using the crosshairs in the eyepiece of the tribrach (a levelling device), and levelled firstly by adjusting the tripod legs and then by using the levelling bubble on the tribrach. The tripod is made as stable as possible by driving the legs into the ground and by placing heavy rocks around them. The antenna is screwed into the tribrach and adjusted so that the antenna cable connection is oriented to the north; the antenna cable is then connected to it from the receiver.

The slant height (Figure 3.5A), between the marker centre point and the lower edge of the antenna, is measured on three sides of the antenna at both the start and end of the occupation. This measurement is averaged and is used to calculate the antenna height, necessary for processing the GPS data.

Guyed mast set-ups

For a mast set-up (Figures 3.4B; 3.5B), the three sections of the TECH 2000 mast are assembled. A steel tip is then screwed into the bottom of the mast for placement in the monument; a new tip is used for each occupation as they generally become deformed during the set-up and occupation. The mast is held upright, with the tip placed in the centre point of the benchmark. Placing the tip in the centre point ensures that the antenna will be centred over the marker after levelling of the antenna. The mast is then chained to three steel anchors drilled and cemented into the bedrock, each about 50 cm from the benchmark; the bottom link of each chain is pulled to the top of the anchor to ensure that it does not slip later in the occupation and compromise the mast stability. A steel rod is slid into the top of the mast; a levelling assembly is then slid over this until it rests on the top of the mast. The mast is levelled using four levelling bubbles, one on each side of the square levelling assembly; levelling is achieved by adjusting the chain lengths using the brass turnbuckles between the chains and the mast. When all bubbles have been centred, the chains are tightened to stabilize the mast. The antenna is then screwed onto the top of the steel rod that protrudes from the mast, and is adjusted so that the antenna cable connection points towards north. The antenna cable is then connected from the receiver.

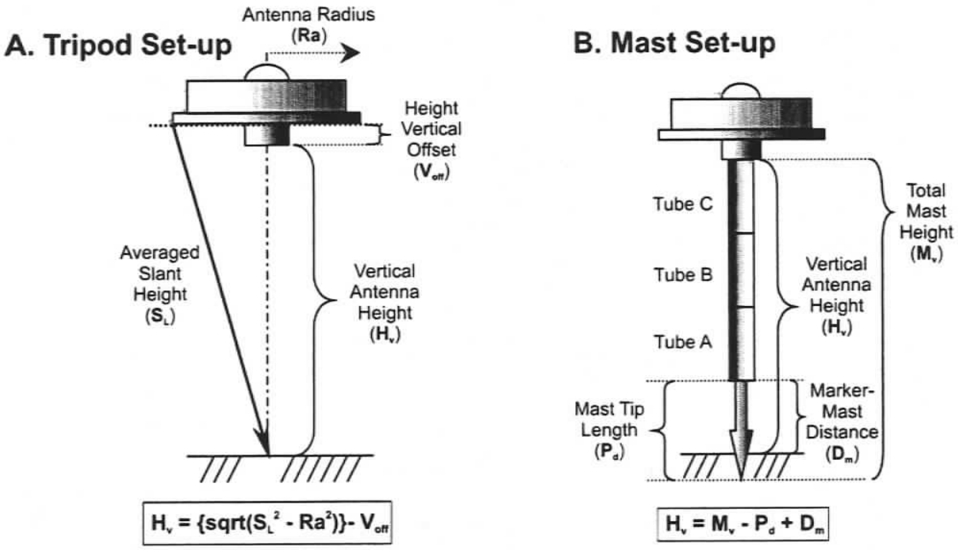

Figure 3.5. A. Calculation of antenna height using a geodetic tripod. **B.** Calculation of antenna height using a TECH 2000 GPS mast set-up.

The mast height is known; therefore, the only measurement necessary for determination of the antenna height is the distance between the bottom of the mast and the position where the tip meets the marker surface. This position is marked with a pencil while the tip is in situ to be measured after the mast has been taken down. The pencil mark is generally too high on the tip (by < 1 mm); however, at the end of an occupation the correct position is often marked by a ring of rust and possibly an indentation. In all surveys prior to the 2005 survey, this measurement was made only at the end of the occupation, while during the 2005 survey, at least three measurements were made both at the start and at the end of the survey, to achieve an average value. To facilitate the starting measurement, the set-up must be assembled, chained down, and the antenna placed on the mast; the pencil mark is then made and the mast is temporarily taken down for measurement of the tip, before being put back up again.

Procedures common to all set-ups

Before data recording can begin, there are a number of steps to be taken. While one person is setting up the mast, the other sets up the receiver. The internal battery is inserted into the receiver after ensuring that it is fully charged. The receiver is then switched on, and the internal memory checked. The external battery (a 12V gel-cell battery) is then connected to the receiver. With the receiver on, the internal battery is temporarily removed to ensure that the receiver is working off the external battery. The voltage of the external battery is then measured with a voltmeter and recorded (it should measure over 12.9 V). Next, the receiver computer is configured for the coming occupation. It is possible to do this solely using the buttons and display on the Ashtech Z-Xtreme receiver, but our procedure is to connect a laptop computer to the receiver and use the more user-friendly software "Ashtech Micromanager". The software allows specification of the site and user names, and the way that data are recorded, i.e., every thirty seconds in files that begin at 00:00:00 GMT and end at 23:59:40. This information is sent to the receiver, which is now switched off until the cable has been connected between the receiver and the antenna.

Before the receiver is turned on to start recording data, the antenna level and centering are again checked. Once the receiver has been switched on, a number of observations are recorded from the Micromanager interface. After a few minutes, the antenna should be tracking enough satellites that the receiver opens a new file and begins to record data. Recorded observations include site, start time, file size, latitude, longitude, altitude, number of satellites, and PDOP value (Position Dilution of Precision, a rough measure of position reliability based on the geometry of the observed satellites). These observations are repeated after several minutes to ensure that data are being recorded and the file is growing.

Other observations recorded in the field notes include the weather conditions, the equipment specifications and model numbers, and any other information the user considers might be useful subsequently. A sketch and written description of the horizon around the antenna is also made; it is important to know if and how the antenna's "view" of the satellites in the sky is obstructed, e.g., by buildings, trees or mountains, and possible multipath targets. Obstructions may explain why the antenna gets poor satellite coverage, and if these obstructions are close to the antenna they may cause errors due to multipath effects. Photographs are taken of the site set-up, the marker, the anchors, and of the antenna horizon, every 30°.

Before leaving a site, the Pelican$^{\text{TM}}$ weatherproof case housing the receiver and battery is locked with a combination lock, as well as being chained and locked to one of the mast anchors or tripod legs. The antenna cable connections are wrapped with electrical tape to keep out moisture. A notice is attached to the equipment, asking passers-by not to disturb the equipment and providing contact telephone numbers for anyone interested in the study to call.

In each survey, five sets of equipment were used, such that up to five sites were deployed at the same time. Where possible, each site was checked on at least once during the occupation before taking it down after at least forty-eight hours. At this time, the observations recorded are similar to those made at the start of each occupation, i.e., whether the antenna is centred and level, weather conditions, file size, latitude, longitude, altitude, number of satellites, PDOP, external battery voltage. At this time also, the data recorded thus far are downloaded to the laptop. One file is produced per site set-up per day, starting at 00:00 GMT. Downloaded files are run through a freeware program called teqc (translation, editing, quality check; Estey and Meertens, 1999) as a preliminary quality check on the data, and backed up to CD on a regular basis.

With multiple deployments, it was necessary to leave the equipment unattended at the majority of sites. Equipment set-ups at most sites are either completely out of sight to motorists and passers-by, or visible but very inconspicuous. Three sites (RICH, MAMI, and COLA) are in plain view and clearly accessible, but their locations beside relatively little-travelled highways are judged a low risk for theft/human interference. However, two sites (CANY and DAWS) are located in busy public places, where babysitting of the equipment is necessary during the day. Obviously, animal interference is possible at any of the sites; the 2004 occupation of highly-remote site CARI had to be extended after the tripod had been knocked down and the antenna cable broken, most likely by a bear.

DATA PROCESSING

The campaign and continuous GPS data were all processed using Bernese Version 4.2 software (Hugentobler et al., 2001), the standard GPS data analysis package used at the Pacific Geoscience Centre. Before processing, the raw files are first converted to RINEX (Receiver INdependent EXchange; Gurtner et al., 1989) format using teqc. The headers of the resultant RINEX files for each day include information on the site, the equipment used, and the antenna height for that day. Input files are prepared, pertaining to site names and numbers, receiver/antenna pairs, ocean tidal loading at each site, antenna heights, and the processing strategy, e.g., which sites will be processed for which days, and the reference for the site motions. Ocean tide loading corrections are made using the LOADSTP software (Pagiatakis, 1992), incorporating the FES95.2 global ocean tide model (Le Provost et al., 1998).

Bernese processes each day of data by running a series of eighteen scripts (001 to 019; there is no process 011); these are summarized in Table 3.4. When each day has been processed, the user receives a message indicating whether the processing has been successful (completed to process 019). If the processing was unsuccessful (stopping before process 019), the user can check the message for errors, e.g., the RINEX header information may not match the input files, or there may be a problem with data quality/quantity. Once the source of error has been removed, the data can be reprocessed.

Table 3.4. Summary of Bernese processes.

Process #	Script	Processes
001	PGCICOP1	Campaign directory is prepared for processing
002	PGCPOL	Standard orbit is created
003	PRETAB	(using orbits provided by the IGS)
004	ORBGEN	
005	RXOBV3	Code and phase observations are pre-processed
006	CODCHK	
007	CODSPP	
008	SNGDIF	Single difference files are created
009	MAUPRP	Cycle slips[1] are found and fixed and the data are edited
010	GPSEDT	
012	GPSQIF_1	Phase ambiguities are resolved
013	QIFXTR	
014	GPSEST	Solution for ionosphere model is run
015	GPSEST_4	Network solution is run, introducing ambiguities from process 012
016	ADDNEQ	Sinex[2] file for the day is created
017	COMPAR_2	Daily solutions for the week are compared
018	ADDNEQ_2	
019	PGCPDEL1	All relevant information is saved and copied to the archive

[1] A cycle slip is a discontinuity of a number of cycles in the measured carrier phase resulting from a loss of lock on the carrier signal;
[2] Sinex: Solution Independent EXchange format; sinex files contain position information.

Continuous GPS Data Processing

For this study, the continuous GPS data were processed using two different strategies: (1) fixed reference site, and (2) moving reference.

(1) The data were processed relative to Yellowknife (YELL), which was held fixed to its initial position throughout the time series. The resulting velocities are relative to YELL, and therefore only strictly comparable to other analyses that hold YELL fixed. The velocities can be converted to the ITRF2000 reference frame (International Terrestrial Reference Frame 2000, Altamimi et al., 2002) by addition of the estimated ITRF velocity of YELL. A drawback of this method is that for time periods of 5 years or more and survey footprints of 1000 km or more, significant network distortions due to not accounting for actual reference site motion (mostly plate rotation) can result (Mazzotti et al., 2003a; 2005).

(2) The data were processed relative to one reference site, which was constrained within 1 mm on each day, but allowed to move from day to day according to a given velocity (i.e., ITRF2000). This approach provides velocities in the ITRF2000 reference frame and avoids the potential significant network distortions of the first method. By using both methods, these distortions can be quantified. It is possible to use a number of reference stations, ideally encircling the study area. Such a strategy was considered for this study, using sites on three sides of the area of interest at Williams Lake, Whitehorse, Fairbanks and Yellowknife (Figure 3.1; Table 3.2). However, Fairbanks has undergone considerable co- and postseismic motion from the 2002 Denali earthquake and cannot be considered a stable reference. Similarly, it is of interest to determine the tectonic motion at Whitehorse, which is inside the deforming study area. Drawbacks of Williams Lake are (1) although it is a stable site, it is located relatively far south from the main area of interest, and (2) it lacks data for a significant portion of the time series of the other sites. The continuous site at Yellowknife was therefore chosen as a single reference station. YELL is close enough to the rest of the network that common systematic errors may be significantly reduced, and its location on the stable craton is sufficiently removed from the strongly-deforming study area. YELL's velocity is ~ 0.4 mm/yr to the south relative to stable North America (Altamimi et al., 2002; Table 3.5).

Successful processing provides a daily position for each site, with respect to YELL in the ITRF2000 reference frame. Plotting of the daily positions as time series allows site velocities to be determined. Best-fit velocities for the north, east and up components are obtained using weighted least-squares regression, with removal of concurrently-estimated (1-year) seasonal variations. The weighted root-mean-square (WRMS) position scatter is also calculated. Both horizontal and vertical position data are estimated; however, the errors associated with vertical position are greater as the satellites are only on one side of the antenna (above), and the estimates of vertical position and tropospheric delay are strongly correlated. The calculated ITRF velocities are transformed into a stable North America reference frame using the North America/ITRF2000 rotation vector from Altamimi et al. (2002).

Uncertainty Estimation for Continuous GPS Data

Noise in continuous GPS position time series is considered to comprise a combination of white (uncorrelated) and coloured noise (time-correlated; flicker noise and random walk noise) (e.g., Mao et al., 1999; Williams et al., 2004). Sources of coloured noise may include monument motion independent of tectonic deformation, uncertainties in the estimation of atmospheric effects and satellite orbits, and local environmental factors (Mao et al., 1999). Monument instability can be modelled as a random walk process (Langbein and Johnson, 1997); its contributory noise is expected to be larger for sediment than bedrock monument settings and for less stable set-ups, e.g., tripods versus deep-braced monuments (e.g., Williams et al., 2004).

It is important to assess the noise content of GPS time series so that realistic uncertainties can be assigned to the estimated site velocities. Mao et al. (1999) and Williams et al. (2004) used spectral analysis and Maximum Likelihood Estimation to characterize the time series noise from globally distributed continuous GPS sites. Both studies found that the noise is best described by a white plus flicker noise model, with random walk noise detectable only at time periods of several years. An assumption of purely white noise leads to underestimation of rate uncertainty by 5-11 times (Mao et al., 1999). Mao et al. (1999) defined the following equation for the estimation of rate uncertainty:

$$\sigma \cong \sqrt{\frac{12\sigma_w^2}{gT^3} + \frac{1.78\sigma_f^2}{g^{0.22}T^2} + \frac{\sigma_{rw}^2}{T}}$$

where σ_w and σ_f are respectively white and flicker noise in mm, σ_{rw} is random walk noise in mm/yr$^{1/2}$, g is the number of measurements per year, and T is the time series length in years.

Dixon et al. (2000) noted that Mao et al.'s data exhibit a strong correlation between weighted root-mean-square (WRMS) position scatter and the magnitudes of the white and coloured noise components. Mazzotti et al. (2003a) derived first-order scaling factors from these correlations in North America studies (Mao et al., 1999; Dixon et al., 2000; Miller et al. 2001). The white and flicker noise scaling factors, of 0.7 and 1.0 respectively, are consistent with those studies. The random walk noise scaling factor of 0.5 results in magnitudes consistent with estimates by Langbein and Johnson (1997) based on long (10 yr) trilateration time series, and with an upper limit on random walk noise calculated by Beavan (2005). Incorporating the scaling factors results in a modification of the above equation to the following:

$$\sigma \cong \sqrt{\frac{12(0.7 * WRMS)^2}{gT^3} + \frac{1.78(WRMS)^2}{g^{0.22}T^2} + \frac{(0.5 * WRMS)^2}{T}}$$

This equation results in calculated velocity uncertainties that are scaled not only by the data quality (as indicated by the scatter), but also by the length of the time series. This approach was adopted for the continuous GPS analysis of this study to estimate realistic velocity uncertainties.

Campaign GPS Data Processing

The campaign GPS data were processed using a strategy similar to the moving reference method employed for the continuous data. In this case it was possible to use multiple continuous reference sites, each with already-processed data spanning all the campaigns from 1999-2005. The reference sites were allowed to move from week to week, but they were constrained to their calculated weekly average position each week.

The reason for constraining the sites to their weekly average position rather than their daily average is that, on average, the weekly position is a more robust solution and minimizes the chance of data outliers biasing the results.

Reference sites BCDL, CLGO, WHIT and YELL (Table 3.2; Figure 3.1) were chosen on the basis of (1) data availability, (2) location, and (3) data quality. These sites are located on three sides of the campaign network (south, west and east); none of the potential reference sites to the north (HOLM, INVK, PBOC, SACH, TUKT) have any pre-2001 data. If a reference site is found to have a questionable solution for a particular week, the campaign data are re-processed without that site as a reference. This would obviously not be possible with only a single reference site, where a problem specific to that site would affect the campaign results. For example, inclusion of the reference site YELL for processing the campaign data of October 1st 2004 results in anomalous positions for all campaign sites analyzed that day. Solving for the position of YELL relative to another reference shows that the anomalies arise from an unknown site-specific problem at YELL; processing of the campaign data with only the other reference sites provides positions consistent with adjacent days.

Processing of the campaign GPS data provides daily positions for each site in the ITRF2000 reference frame. As described for the continuous data processing, site velocities are obtained and are transformed to a stable North American reference frame using the North America/ITRF2000 rotation vector from Altamimi et al. (2002).

Uncertainty Estimation for Campaign GPS Data

The method of uncertainty estimation used for the continuous GPS data and described above is not employed for the campaign GPS data analysis. Campaign GPS data are expected to have greater uncertainties than continuous data, partly due to the much smaller amount of data and the greater possibility of outliers affecting the estimated velocity. Campaign GPS data are also more susceptible to site survey errors due to repeated positioning of the antenna over the monument and the greater likelihood of set-up instabilities (e.g., Zhang et al., 1997). Thus, uncertainty calculations for campaign data based on a white, flicker and random walk noise model may significantly underestimate the true uncertainty.

Uncertainty on the campaign GPS velocities is estimated as the weighted standard deviation σ_w (calculated in the weighted least squares regression) normalized by the reduced chi-square misfit, χ_r^2, as shown below. The weighted standard deviation is given by:

$$\sigma_w = \sqrt{\frac{n\sum w_i (V_i - V_m)^2}{(n-1)\sum w_i}}$$

where n is the number of data points, w_i is the weight of the i^{th} data point (calculated from its uncertainty), V_i is the measured position of the i^{th} data point, and V_m is the position predicted by the regression model. The reduced chi-square misfit is given by:

$$\chi_r^2 = \frac{1}{d.f.}\sum\left[\frac{(V_i - V_m)^2}{\sigma_i^2}\right]$$

where *d.f.* is the number of degrees of freedom (the number of data points minus the number of parameters), and σ_i is the uncertainty of the observed position. Calculation of the reduced chi-square statistic allows the model to be evaluated. For a perfect fit, χ_r^2 equals one; if χ_r^2 is much greater than one, the model is too simple and/or the uncertainty is underestimated; if it is much less than one, the model is too complex and/or the uncertainty too large. Thus, the weighted standard deviation values are normalized by the reduced chi-square misfit as shown below to provide a better estimate of uncertainty σ.

$$\sigma = \sigma_w \sqrt{\chi_r^2}$$

CONTINUOUS GPS RESULTS

For each continuous GPS site, all available data between January 1st 1999 and December 31st 2005 were processed (see Table 3.2 for data availability). The resulting time series plots for each site are included in Appendix A (moving reference method, North America reference frame). Time series range in length from 2.3 to 7 years, with a mean of 5.6 years. The calculated velocities at some sites in Alaska (ATW2, CHI3, CLGO, FAIR, GNAA, GRNR, POT3) do not represent the long-term site velocity, due to co- and postseismic effects of the M 7.9 Denali earthquake in November 2002 (discussed below). For these sites, only the pre-earthquake data were used. The shortened time series (2.1 to 3.8 years in length) are long enough to provide reasonable first-order estimates of long-term site velocity. The site at Beaver Creek (BEA2) near the Alaska/Yukon border is also close enough to the Denali rupture to experience significant motion due to the earthquake. This site was only established a few weeks after the earthquake, and thus all the data are affected by a postseismic signal. The calculated velocity was corrected for postseismic motion as predicted by the finite element model of Freed et al. (2006; A. Freed, personal communication, 2005).

Comparison of Moving and Fixed Reference Methods

The results of the continuous GPS analysis (both moving and fixed reference methods) are shown as horizontal velocities in a North American reference frame in Figure 3.6. Both methods produce similar results, although they exhibit systematic differences, which generally increase in magnitude with distance from Yellowknife (see Appendix B: Figures B1, B2). The fixed reference method appears to result in a stretching of the network away from Yellowknife compared with the preferred moving reference method. This study shows that holding the reference site fixed for relatively long time periods (~ 2-7 years) and for large (2000 km) networks introduces biases on the order of 1-2 mm/yr. From this point on, only the results obtained with the moving reference method are discussed.

Comparison with Other Studies

The site velocities and their corresponding uncertainties from this study are given as north, east, and up components in both North American and ITRF2000 reference frames in Table 3.5, along with site velocities from other analyses for comparison. The horizontal velocity vectors from this and other studies are also shown relative to stable North America in Figure 3.7; velocities from other studies given in ITRF2000 are

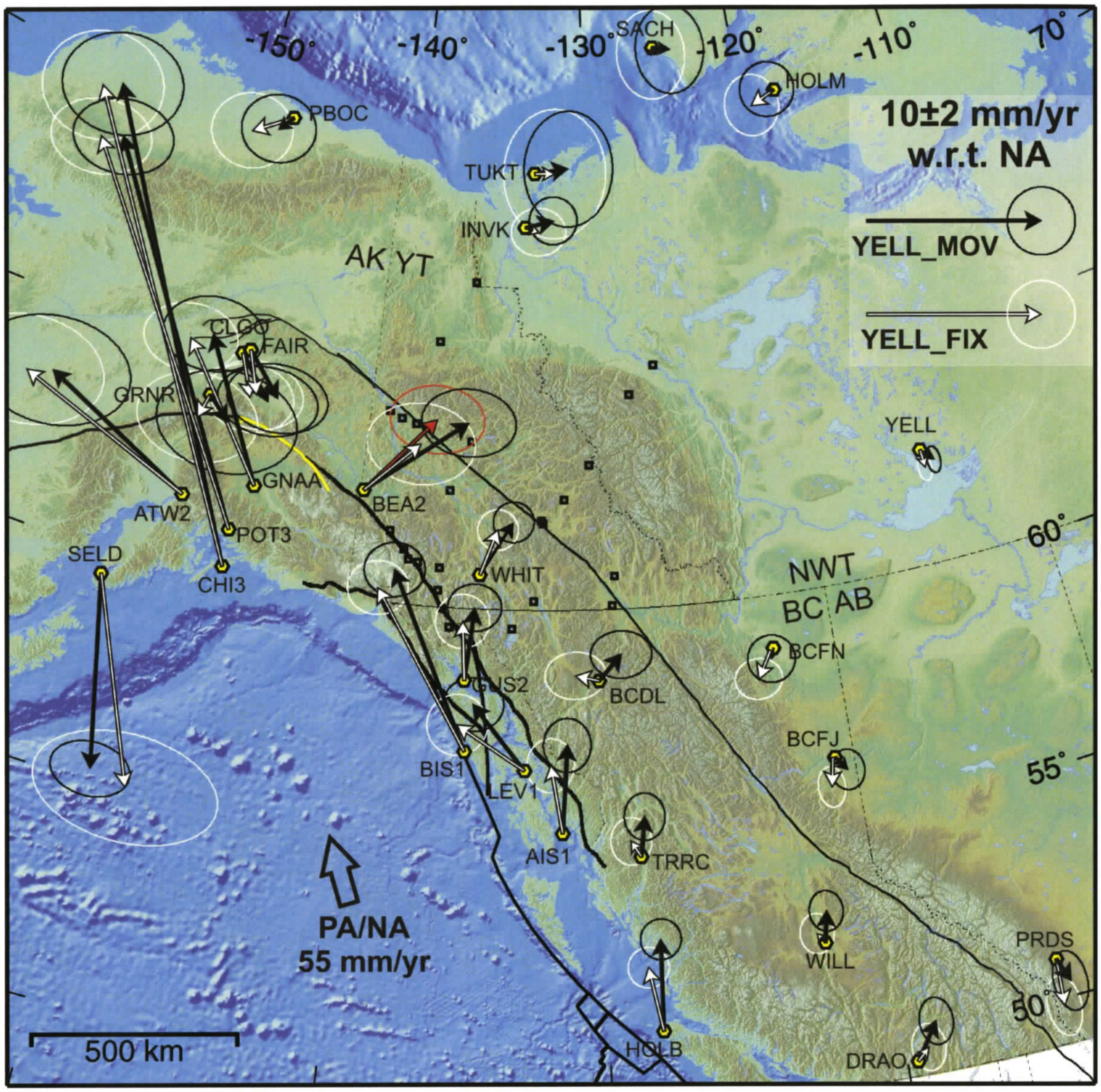

Figure 3.6. Horizontal velocity vectors for continuous GPS sites relative to stable North America. Error ellipses are at 95% confidence level. Black arrows: moving reference method. White arrows: fixed reference method. Red arrow: velocity at Beaver Creek from the moving reference method and corrected for predicted postseismic deformation.

converted to a North America reference frame using the North America/ITRF2000 rotation vector given by Altamimi et al. (2002).

The analysis of Fletcher and Freymueller (2003) provides a velocity vector at Whitehorse (yellow arrow in Figure 3.7) that is only ~ two-thirds of the magnitude of this study's vector (black arrows) and that is north- rather than NE-directed. However, the large uncertainty of their result for a shorter time interval allows for agreement of the two

Table 3.5. Continuous GPS site velocities.

Site	Source	Ref. Frame	V_N[8] (mm/yr)	σ_N[9] (mm/yr)	RMS_N[10] (mm)	V_E[11] (mm/yr)	σ_E[12] (mm/yr)	RMS_E[13] (mm)	V_U[14] (mm/yr)	σ_U[15] (mm/yr)	RMS_U[16] (mm)	T[17] (yr)
AIS1	A[1]	NA[6]	5.1	0.8	3.5	0.3	0.7	3.4	1.7	2.0	9.4	7.0
	A	ITRF[7]	-11.0	0.8	3.5	-12.5	0.7	3.4	1.7	2.0	9.4	7.0
	B[2]	ITRF	-7.9	0.7	2.1	-12.3	0.5	4.2	2.7	0.8	7.5	1.0
ATW2	A	NA	5.2	1.6	3.4	-8.9	2.3	4.8	4.2	4.6	9.4	2.1
	A	ITRF	-14.4	1.6	3.4	-17.5	2.3	4.8	4.2	4.6	9.4	2.1
	A	ITRF	-9.4	1.0	3.8	-22.8	1.2	4.8	-0.3	2.7	10.6	5.3
	B	ITRF	-10.1	0.6	2.3	-24.3	0.8	3.5	0.6	1.9	7.9	4.8
BCDL	A	NA	1.5	0.7	3.1	1.3	0.9	4.2	-1.4	2.3	10.4	6.7
	A	ITRF	-14.2	0.7	3.1	-12.2	0.9	4.2	-1.4	2.3	10.4	6.7
BCFJ	A	NA	-0.8	0.6	2.8	0.6	0.5	2.2	3.2	1.5	7.0	7.0
	A	ITRF	-13.9	0.6	2.8	-14.6	0.5	2.2	3.2	1.5	7.0	7.0
BCFN	A	NA	-0.6	0.7	3.1	-0.2	0.7	3.2	1.9	2.1	9.7	7.0
	A	ITRF	-14.2	0.7	3.1	-15.3	0.7	3.2	1.9	2.1	9.7	7.0
BEA2	A	NA	4.5	1.0	2.6	3.7	1.4	3.7	-0.4	2.8	7.7	3.1
	A	ITRF	-13.6	1.0	2.6	-7.6	1.4	3.7	-0.4	2.8	7.7	3.1
BIS1	A	NA	10.3	0.8	3.2	-4.5	0.9	3.9	2.1	2.1	8.6	5.8
	A	ITRF	-6.7	0.8	3.2	-16.5	0.9	3.9	2.1	2.1	8.6	5.8
CHI3	A	NA	26.0	1.5	4.6	-11.3	1.8	5.5	0.7	3.7	11.3	3.7
	A	ITRF	6.8	1.5	4.6	-20.5	1.8	5.5	0.7	3.7	11.3	3.7
	A	ITRF	9.3	1.2	5.4	-21.5	1.2	5.4	2.8	2.5	11.3	6.8
	B	ITRF	10.1	1.1	3.9	-25.2	0.9	4.4	2.3	1.7	7.0	4.7
CLGO	A	NA	-2.4	1.0	3.1	2.0	1.5	4.5	0.8	3.1	9.6	3.7
	A	ITRF	-21.9	1.0	3.1	-7.1	1.5	4.5	0.8	3.1	9.6	3.7
	A	ITRF	-24.6	1.0	4.4	-6.7	1.0	4.7	-1.8	2.5	11.3	6.8
	B	ITRF	-22.2	0.5	3.1	-8.0	0.6	3.1	1.5	1.5	10.4	6.9
DRAO	A	NA	2.1	0.7	3.3	1.4	0.5	2.3	0.3	2.0	9.4	7.0
	C[3]	NA	1.1	0.4	1.3	0.3	0.2	1.7	0.8	0.3	5.3	6.6
	A	ITRF	-10.7	0.7	3.3	-12.9	0.5	2.3	0.3	2.0	9.4	7.0
	B	ITRF	-11.3	0.1	2.1	-13.6	0.1	3.1	1.2	0.4	7.5	14.9
	C	ITRF	-11.7	0.3	1.3	-14.0	0.1	1.7	0.8	0.3	5.3	6.6
FAIR	A	NA	-2.4	1.0	3.1	2.1	1.5	4.8	1.0	3.6	11.3	3.8
	A	ITRF	-21.8	1.0	3.1	-7.1	1.5	4.8	1.0	3.6	11.3	3.8
	A	ITRF	-24.7	1.1	4.9	-7.1	1.1	5.0	0.8	2.4	11.0	7.0
	B	ITRF	-23.1	0.2	3.7	-8.1	0.2	3.7	3.0	0.7	14.6	15.0
GNAA	A	NA	8.1	1.1	3.5	-4.0	1.5	4.6	10.4	4.6	14.7	3.8
	A	ITRF	-11.0	1.1	3.5	-13.6	1.5	4.6	10.4	4.6	14.7	3.8
	A	ITRF	-7.0	1.2	5.7	-18.2	1.5	7.0	10.7	3.1	14.4	7.0
	B	ITRF	-7.5	1.0	2.8	-17.3	1.4	3.5	6.3	2.3	10.4	4.8
GRNR	A	NA	-1.3	1.5	3.5	1.3	2.1	4.7	4.6	4.8	10.8	2.4
	A	ITRF	-20.9	1.5	3.5	-7.4	2.1	4.7	4.6	4.8	10.8	2.4
	A	ITRF	-22.6	1.0	3.8	-8.7	1.1	4.2	9.0	2.7	10.7	5.4
	B	ITRF	-25.0	2.6	4.6	-9.6	1.2	4.2	10.4	1.9	9.7	4.4
GUS2	A	NA	4.2	0.7	3.3	0.4	0.8	3.5	18.9	2.0	9.1	7.0
	A	ITRF	-12.9	0.7	3.3	-11.7	0.8	3.5	18.9	2.0	9.1	7.0
HOLB	A	NA	5.3	0.6	2.7	0.1	0.6	2.8	1.4	2.0	9.5	7.0
	C	NA	2.8	0.5	2.3	0.7	0.5	2.3	2.2	1.4	5.7	6.6
	A	ITRF	-9.9	0.6	2.7	-12.9	0.6	2.8	1.4	2.0	9.5	7.0
	B	ITRF	-11.1	0.2	2.4	-12.6	0.3	3.5	-4.6	1.0	10.9	6.9
HOLM	A	NA	0.1	0.8	2.9	-0.4	0.8	2.7	2.0	1.9	6.4	4.3
	A	ITRF	-12.1	0.8	2.9	-17.7	0.8	2.7	2.0	1.9	6.4	4.3
	B	ITRF	-10.1	0.6	2.7	-17.6	0.8	2.9	5.3	1.8	5.8	3.2
INVK	A	NA	0.4	0.7	2.4	1.6	0.7	2.5	-8.8	3.1	10.7	4.4
	A	ITRF	-16.1	0.7	2.4	-11.8	0.7	2.5	-8.8	3.1	10.7	4.4
	B	ITRF	-12.9	0.5	3.0	-13.2	0.6	2.4	-11.5	2.0	11.7	3.2
LEV1	A	NA	3.8	0.8	2.8	-3.0	0.9	3.0	7.0	2.7	9.6	4.5
	A	ITRF	-12.6	0.8	2.8	-15.6	0.9	3.0	7.0	2.7	9.6	4.5
	B	ITRF	-11.8	0.5	2.7	-17.8	0.6	3.3	9.5	1.4	5.8	3.6
PBOC	A	NA	-0.8	1.0	3.1	-0.7	1.1	3.5	-1.3	4.4	13.4	3.7
	A	ITRF	-20.2	1.0	3.1	-9.9	1.1	3.5	-1.3	4.4	13.4	3.7
	B	ITRF	-18.6	0.5	2.0	-12.6	0.5	2.7	0.3	2.4	7.1	2.9
POT3	A	NA	20.9	1.1	3.5	-10.6	1.5	4.8	5.1	3.6	11.5	3.8
	A	ITRF	1.6	1.1	3.5	-19.9	1.5	4.8	5.1	3.6	11.5	3.8
	A	ITRF	3.1	0.8	3.6	-21.7	1.1	5.0	8.2	2.4	11.1	7.0
	B	ITRF	3.9	0.6	3.5	-23.4	0.9	4.7	13.2	1.5	7.4	4.8

Table 3.5. (Continued)

Site	Source	Ref. Frame	V_N (mm/yr)	σ_N (mm/yr)	RMS_N (mm)	V_E (mm/yr)	σ_E (mm/yr)	RMS_E (mm)	V_U (mm/yr)	σ_U (mm/yr)	RMS_U (mm)	T (yr)
PRDS	A	NA	-1.4	0.9	4.4	0.5	0.5	2.3	-2.2	2.1	9.8	7.0
	C	NA	-1.4	0.5	1.5	0.0	0.5	1.5	0.8	1.4	5.1	4.9
	A	ITRF	-12.5	0.9	4.4	-15.0	0.5	2.3	-2.2	2.1	9.8	7.0
	B	ITRF	-12.5	0.3	2.5	-14.6	0.3	3.1	-0.8	0.9	7.1	8.9
SACH	A	NA	-0.2	1.3	3.5	1.0	1.0	2.6	3.7	2.5	6.7	3.0
	A	ITRF	-14.7	1.3	3.5	-14.8	1.0	2.6	3.7	2.5	6.7	3.0
	B	ITRF	-12.4	0.6	2.9	-15.4	0.8	3.6	7.7	2.2	7.1	2.7
SELD	A	NA	-11.0	0.8	2.9	2.5	1.2	4.4	12.4	2.6	9.7	5.0
	A	ITRF	-31.0	0.8	2.9	-5.2	1.2	4.4	12.4	2.6	9.7	5.0
	B	ITRF	-31.8	0.5	2.8	-8.7	0.6	3.3	12.1	1.4	7.3	4.8
TRRC	A	NA	2.3	0.7	3.2	0.3	0.6	2.7	2.4	1.8	8.4	7.0
	A	ITRF	-13.0	0.7	3.2	-13.0	0.6	2.7	2.4	1.8	8.4	7.0
TUKT	A	NA	0.3	1.7	3.7	1.9	1.3	3.0	1.3	3.4	7.6	2.3
	A	ITRF	-16.2	1.7	3.7	-11.8	1.3	3.0	1.3	3.4	7.6	2.3
	B	ITRF	-16.5	1.0	3.6	-12.9	1.0	2.9	46.6	2.6	24.0	2.3
WHIT	A	NA	3.1	0.6	2.7	1.8	0.6	2.9	1.8	1.9	8.7	7.0
	D[4]	NA	2.3	1.1		-0.2	1.4					?
	A	ITRF	-13.9	0.6	2.7	-10.7	0.6	2.9	1.8	1.9	8.7	7.0
	B	ITRF	-14.2	0.3	3.6	-11.4	0.3	4.2	0.5	0.7	8.7	9.7
WILL	A	NA	1.8	0.6	2.8	0.3	0.5	2.2	1.7	1.8	8.4	7.0
	C	NA	0.3	0.5	1.4	-0.6	0.4	1.2	2.0	0.9	3.9	6.6
	A	ITRF	-11.7	0.6	2.8	-14.1	0.5	2.2	1.7	1.8	8.4	7.0
	B	ITRF	-12.4	0.2	2.4	-14.3	0.2	3.1	-0.1	0.5	8.4	10.6
YELL	E[5]	NA	-0.4	0.4		0.1	0.2		5.0	0.5		7.0
	E	ITRF	-11.6	0.4		-17.1	0.2		5.0	0.5		7.0
	B	ITRF	-12.7	0.2	3.5	-17.4	0.1	3.6	4.2	0.5	9.7	15.0

[1] A: This study; [2] B: SOPAC (Scripps Orbit and Permanent Array Center) Refined Model GPS Site Position Time Series, ITRF2000 (SOPAC, 2006); [3] C: Mazzotti et al. (2003a); [4] D: Fletcher and Freymueller (2003); [5] E: Altamimi et al. (2002); [6] NA: Stable North America reference frame; [7] ITRF: ITRF2000 reference frame; [8] V_N: Velocity, north component; [9] σ_N: Uncertainty, north component; [10] RMS_N: Root mean square of position scatter, north component; [11] V_E: Velocity, east component; [12] σ_E: Uncertainty, east component; [13] RMS_E: Root mean square of position scatter, east component; [14] V_U: Velocity, up component; [15] σ_U: Uncertainty, up component; [16] RMS_U: Root mean square of position scatter, up component; [17] T: Length of time series analyzed.

vectors. Part of the discrepancy may arise from differences in the realization of stable North America. The GPS site velocities of Fletcher and Freymueller (2003) were obtained in the ITRF97 reference frame (Boucher et al., 1999) rather than the updated ITRF2000 as used in this study, and were converted to a stable North America reference frame using the rotation vector of Sella et al. (2002). The vector produced by the SOPAC (Scripps Orbit and Permanent Array Center) Refined Model (SOPAC, 2006; red arrows in Figure 3.7) at WHIT is in close agreement with this study.

Mazzotti et al. (2003a) determine velocities (blue arrows in Figure 3.7) at sites that include the southernmost four sites of this analysis (DRAO, HOLB, PRDS, WILL). Their vector orientations are similar to this study at DRAO, HOLB and PRDS (within ~ 20°), but significantly more westward at WILL. Their PRDS vector has a similar magnitude, but those at the other three sites are smaller. Interestingly, Mazzotti et al.'s fixed reference (DRAO-fixed, using a different reference procedure) results at DRAO,

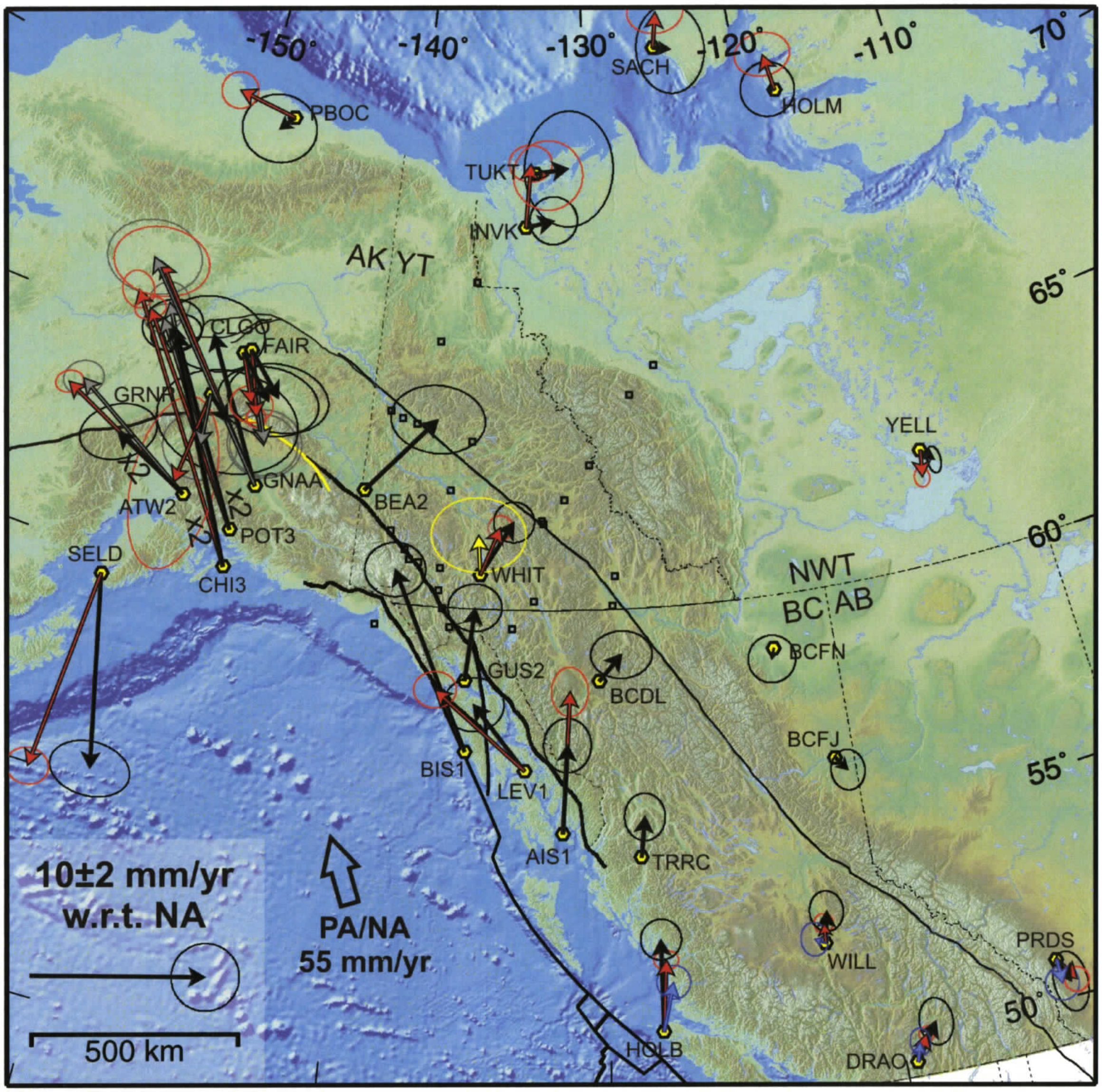

Figure 3.7. Horizontal velocity vectors for continuous GPS sites relative to stable North America. Error ellipses are at 95% confidence level. Black arrows: this study, moving reference method; pre-Denali earthquake velocities are shown for sites close to the rupture (ATW2, CHI3, CLGO, GNAA, GRNR, POT3). Grey arrows: this study, moving reference method, all data used for sites close to the Denali rupture with removal of a coseismic step, and, at ATW2, CLGO, FAIR, and GNAA, an exponential postseismic decay. Red arrows: SOPAC Refined Model (SOPAC, 2006). Blue arrows: Mazzotti et al. (2003a). Yellow arrow: Fletcher and Freymueller (2003).

HOLB and WILL are very similar to the fixed reference (YELL-fixed) results from this study (see Figure 3.6), while the SOPAC vectors at all four southern sites match the moving reference vectors from this study within the uncertainties.

Velocities are available from the SOPAC Refined Model (SOPAC, 2006) for 21 of the 28 continuous sites used in this analysis (Table 3.5; Figure 3.7). SOPAC velocities are calculated in a similar way to this study, with the removal of seasonal signals, and an uncertainty estimation that uses a white plus flicker noise model (see Nikolaidis, 2002). However, SOPAC uses different processing software (the GAMIT and GLOBK packages developed by MIT, the Scripps Institution of Oceanography, and Harvard University), and the vectors are not all directly comparable to those obtained in this study. Also, although the modelled annual seasonal trends are similar, SOPAC also solves for semi-annual variations, unlike this analysis. Often, different lengths of time series are analyzed (see last column, Table 3.5), although these differences do not generally have a large impact. The main differences are in the treatment of sites affected by the Denali earthquake (ATW2, CHI3, CLGO, FAIR, GNAA, GRNR, and POT3). While the present study (black arrows in Figure 3.7) uses only pre-Denali-earthquake data, the SOPAC velocities are calculated using all available data, corrected for coseismic offsets and, at ATW2, CLGO, FAIR, and GNAA, for an exponentially decaying postseismic term. Therefore, to facilitate a more direct comparison, another set of vectors is shown on Figure 3.7 as grey arrows. These are velocities from this study that use all available data, corrected for a coseismic Denali step at all seven sites, and for the same postseismic decay employed by SOPAC at ATW2, CLGO, FAIR, and GNAA.

As mentioned above, the SOPAC vectors at the four southernmost sites (DRAO, HOLB, PRDS, and WILL) show close agreement with this analysis. The vector orientations are very similar, but the magnitudes of the SOPAC vectors are ~ 30% smaller, except at PRDS where the SOPAC velocity is slightly larger. In the Alaskan panhandle, the SOPAC vectors at AIS1 and LEV1 show a similar direction to this study, but are about 50% larger. It is worth noting here that the SOPAC velocity at AIS1 is based on only one year's data compared to the 7-year time series of this study. As referred to above, the SOPAC vector for WHIT matches this study closely. The SOPAC velocity at YELL, while small (1.5 mm/yr), is 50% larger than the vector from this study, and is directed southwest rather then southeast.

The SOPAC vector for SELD is similar in magnitude to this study, but with a greater westward component. At the Alaskan sites most affected by the Denali earthquake, the SOPAC vectors are in closer agreement with the vectors of this study produced in a similar way (grey arrows in Figure 3.7) than with the pre-Denali earthquake vectors. The differences between these two sets of vectors indicates that either (1) the co- and postseismic corrections do not adequately remove the effects of the earthquake, or (2) the pre-Denali time series (2.1 to 3.8 years) are not long enough to deduce reliable long-term velocities. The SOPAC vectors are similar in magnitude to the grey vectors but ~ 50% bigger than the pre-Denali vectors. The directions for all three sets of vectors are similar, all within 25° except at GRNR where the pre-Denali vector is oriented ~ 60° east of the SOPAC vector.

Significant differences exist between the SOPAC solution and this analysis at the northernmost sites, with the exception of TUKT, where the vectors show fairly good agreement. At the other four northern sites (HOLM, INVK, SACH, and PBOC), the SOPAC vectors are two to five times larger, with large northward components at HOLM, INVK, and SACH, and a large westward component at PBOC, that are not evident in the present analysis. It is difficult to find an explanation for the relatively large (2-3.5 mm/yr) northward component in the SOPAC solution at HOLM, INVK, and SACH, given that the SOPAC solution for TUKT does not contain such a signal. However, the SOPAC velocities at these noisy sites are based on shorter time series (~ 3 years compared to ~ 4 years for this study; Table 3.5). Thus, the solution from this study is generally more robust and coherent than the SOPAC solution.

Vertical Continuous GPS Velocities

As mentioned earlier, vertical GPS velocities are far less accurate than horizontal velocities. The vertical position data contain more noise than both horizontal components, as evidenced by the approximately three times larger RMS scatter values in Table 3.5. The greater noise is largely a result of the difficulty in determining vertical position and other signal delay components from satellites that are only on one side of the vertical axis (up). Monument instability may also have a greater effect on vertical than horizontal velocities. For example, the weight of a heavy monument structure will increase the normal force on the substrate. If the monument is not anchored to bedrock, the substrate may deform vertically under this local force.

The vertical velocities calculated for the continuous GPS sites are included in Table 3.5 and shown in Figure 3.8, but are not considered beyond this section because of the large uncertainties. The individual values are generally smaller than the estimated uncertainty, although there are systematic trends for regional groups of stations. Although noisy, the vertical rates are generally consistent with expected deformation, as discussed below; this is further indication of the robustness of the solution.

Western Canada

In western Canada, the vertical motion data generally show small uplift (0-5 ± 2.5 mm/yr) at most sites that can be best explained by postglacial rebound (e.g., Trupin et al., 1996). A few sites exhibit subsidence; this may not be a tectonic signal, as most of these sites are either in potentially unstable sediment or on buildings. The highest rate of subsidence is found at INVK (~ 9 ± 3 mm/yr), where the monument is anchored to bedrock. Inuvik is located west of the present-day postglacial rebound zero isobase (Andrews, 1989), in a region that is inferred to be undergoing submergence due to postglacial subsidence (Forbes et al., 2004). More data are necessary to better determine the true subsidence rate at INVK; rebound model estimates are significantly lower than 9 mm/yr.

Andrews (1989) cites tide gauge data from the Canadian Hydrographic Service for current subsidence rates at Tuktoyaktuk and Sachs Harbour of 4.4 and 4.0 mm/yr, respectively. Once corrected for eustatic sea level rise of 1.8 mm/yr (Douglas, 1991; 1997), the rates become 2.6 and 2.2 mm/yr subsidence. However, the GPS data at TUKT and SACH available so far indicate low rates of uplift (~ 1-4 mm/yr), although the large uncertainties do not rule out significant subsidence. A low rate of uplift is also indicated at site HOLM (~ 2 mm/yr), consistent with its location on the eastern, uplift side of the postglacial zero isobase (Andrews, 1989).

Vertical motions determined for most continuous GPS sites in western Canada are broadly consistent with viscoelastic postglacial rebound models (Trupin et al., 1996; Tarasov and Peltier, 2004). Both modelled and GPS-estimated rebound is highest at Yellowknife (~ 5 mm/yr) diminishing to between 0 and 3 mm/yr at most BC and Yukon sites. Discrepancies occur at BCDL, and at PRDS, Alberta, where the GPS data indicate

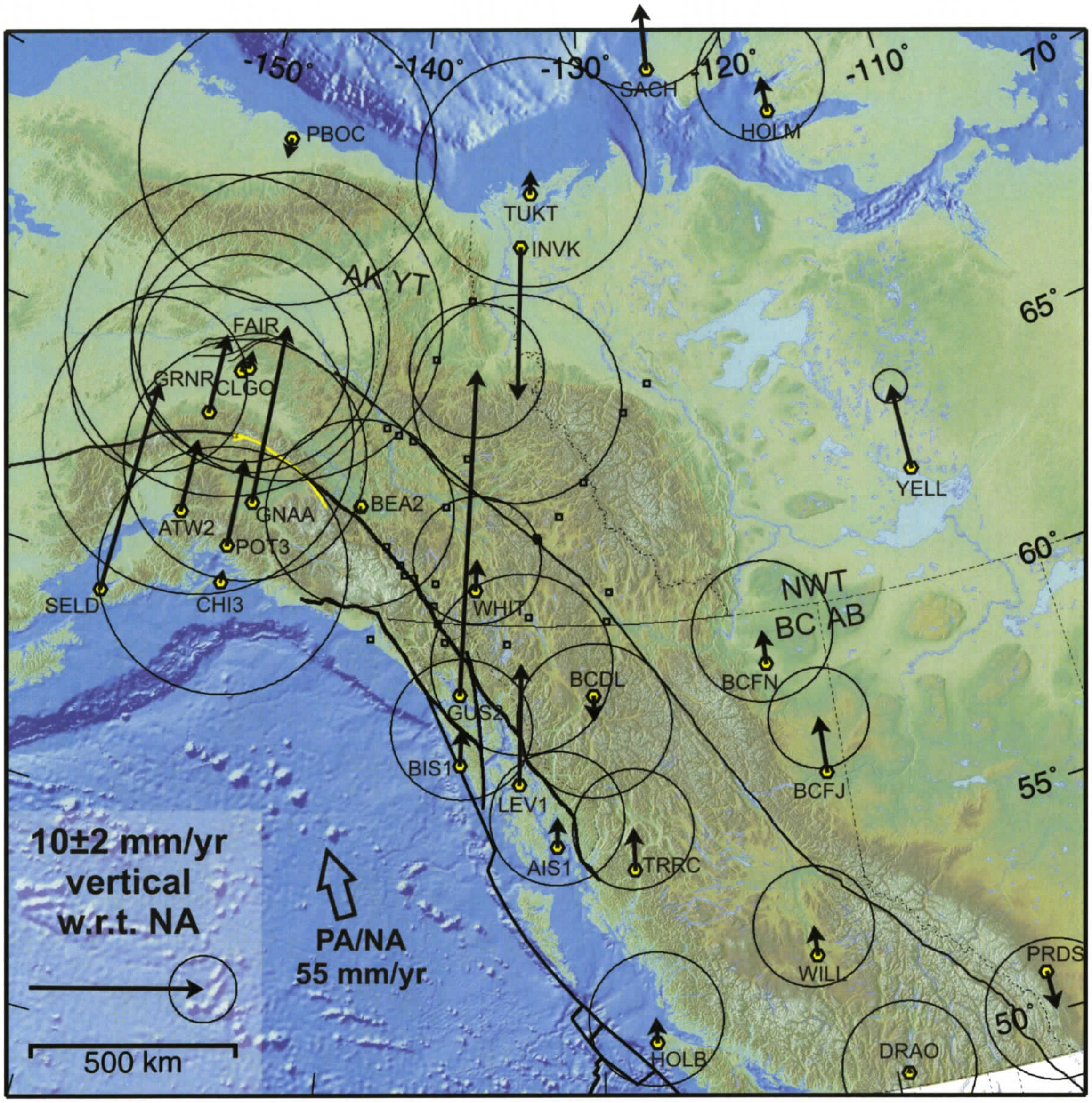

Figure 3.8. Vertical velocity vectors for continuous GPS sites relative to stable North America. North is up; south is down. Errors, shown as circular ellipses for convenience, are at 95% confidence level.

slight subsidence in contrast to the slight uplift indicated by the models. The subsidence is insignificant at BCDL, (zero within the uncertainties), and is barely significant at PRDS. Subsidence at PRDS could be explained if the postglacial forebulge extended a little further north than current models suggest (T. James, personal communication, 2006). Similarly, the Glacier Bay postglacial rebound model of Larsen et al. (2005; Freymueller, 2006) suggests that BCDL may be located in the forebulge region; subsidence is thus expected.

Alaskan Panhandle

A very high uplift rate (19 ± 2 mm/yr) is estimated at GUS2, located in Glacier Bay in the Alaskan panhandle. The Glacier Bay region has been undergoing high rates of viscoelastic uplift (peak of 32 mm/yr over the Yakutat icefield) for the last ~ 250 years due to rapid post-Little Ice Age glacial retreat (Larsen et al., 2004; 2005). Glacio-isostatic rebound may also account for the relatively high uplift rate (7 ± 3 mm/yr) at LEV1 and the lower uplift rates at nearby sites BIS1, AIS1, and TRRC (Trupin et al., 1996).

Southern Alaska

Vertical velocities at GPS sites in southern Alaska have very large uncertainties, but neighbouring sites are generally consistent with each other. The highest uplift rate is at SELD (12.4 ± 2.6 mm/yr) on the western Kenai Peninsula. This rate is in good agreement with that determined at Seldovia (11.3 ± 0.8 mm/yr) from the tide gauge analysis of Cohen and Freymueller (2001). The western Kenai Peninsula is located above the subducting slab, down-dip of a low-slip segment in the middle of the coseismic rupture zone of the 1964 great Alaska earthquake (e.g., Holdahl and Sauber, 1994), and has therefore been affected by postseismic deformation. Seldovia shows no decrease in its uplift rate since the earthquake, implying a localized long-lived postseismic transient that has yet to decay (Cohen and Freymueller, 2001). The postseismic signal is also strongly apparent in the horizontal velocity vector at SELD, as discussed below.

Sites ATW2, CHI3, POT3 are also located above or landward of the 1964 coseismic rupture (e.g., Holdahl and Sauber, 1994; Johnson et al., 1996). However, this region experienced higher coseismic slip and more rapid postseismic decay than the western Kenai Peninsula; Cohen and Freymueller (2001) infer that the postseismic deformation process is essentially complete in this region and attribute the small uplift rate at Anchorage (near site ATW2) to interseismic elastic strain accumulation. Thus, the uplift rates of ~ 4-5 ± 4 mm/yr at ATW2 and POT3 are likely also at least partly the result of interseismic loading due to locking of the subduction megathrust. The near-zero uplift rate at CHI3 is consistent with its location in the zone of coseismic uplift rather than subsidence (Plafker, 1965; 1966); near-zero tectonic uplift rates are predicted for coastal sites in the region (e.g., Sauber and Molnia, 2004).

Cohen and Freymueller (2001) observe that areas down-dip of high coseismic rupture experience rapid postseismic decay and those areas down-dip of low-slip segments undergo slower decay. This may explain the high uplift rate (10.4 ± 4.6 mm/yr) at GNAA, located down-dip of the easternmost end of the 1964 rupture, which experienced relatively small coseismic slip. However, unlike at SELD, a postseismic signal is not obvious in the horizontal velocity vector for GNAA; the main cause of uplift may instead be postglacial rebound, as discussed below.

Glaciers in Alaska (and NW Canada) are currently undergoing rapid wastage and are estimated to constitute the largest glaciological contribution to current sea level rise (~ 0.3 mm/yr; Arendt et al., 2002). The ice melt model of Trupin et al. (1996) predicts postglacial rebound uplift rates that are lowest at sites CLGO and FAIR, consistent with the ~ 1 mm/yr uplift determined there, ~ 3-5 mm/yr at sites SELD and CHI3, ~ 5-8 mm/yr at ATW2, POT3, and GRNR, and ~ 10 mm/yr at GNAA. The high mantle temperatures and low-viscosity shallow asthenosphere in this region may result in much faster rebound than for cratonic regions (e.g., Wahr and Wyss, 1980; James et al., 2000; Hyndman et al., 2005a,b). Thus, postglacial rebound may have a larger contribution to uplift rates in the area than tectonic strain accumulation, with the exception of SELD, where postseismic uplift dominates. At CHI3, the near-zero uplift rate may result from interseismic subsidence offsetting the postglacial rebound.

TECTONIC INTERPRETATION OF HORIZONTAL CONTINUOUS GPS VELOCITIES

Low-velocity Stable North America Sites

A number of sites in the continuous GPS analysis exhibit near-zero horizontal velocities with respect to stable North America (up to ~ 1.5 mm/yr, but zero within the uncertainties). These include PRDS, BCFN, BCFJ, YELL, INVK, PBOC, SACH, and HOLM (Figure 3.7). These sites are all located far from active plate boundaries, landward of the Cordilleran mountain fronts, and are therefore not expected to experience significant active tectonic deformation. Small horizontal motions are expected due to postglacial rebound. The slightly larger estimated velocity at TUKT (1.9 ± 1.5 mm/yr), located ~ 330 km north of INVK, has a large uncertainty due to the short time series (2.3 years). It is also possible that there is a small transient elastic deformation associated with large locked faults to the west. TUKT is very close to the Eskimo Lakes fault zone (see Figure 2.6, Chapter 2) that has been active recently (see Figure 4.7, Chapter 4); INVK is just on the craton side.

Southern British Columbia

The velocities of the three southern British Columbia sites reflect a landward-decreasing influence of the plate boundary to the west (Figure 3.7). DRAO is located a few hundred kilometres inboard of the northern Cascadia subduction zone; its northeastward motion of ~ 2.5 mm/yr is normal to the plate margin and is likely a viscoelastic response to the earthquake cycle (e.g., Wang et al., 2001). Further north, HOLB and WILL are situated inboard of the plate boundary, near where a transition occurs from oblique subduction to the south (Cascadia subduction zone) to oblique strike-slip motion to the north (Queen Charlotte transform) (e.g., Ristau, 2004). The small margin-oblique motion of HOLB, and possibly that of WILL, probably result from locking of the plate boundary where strain is partitioned into convergent and transform components. WILL's velocity is three times as small as HOLB's, reflecting its far greater distance from the plate margin.

Northern British Columbia and Alaskan Panhandle

Sites in northern coastal BC and the Alaskan Panhandle are also strongly influenced by the Pacific/North America plate boundary to the west: the Queen Charlotte-Fairweather transform fault system. This influence is strongest at coastal site BIS1, which is moving northwest, sub-parallel to the locked Queen Charlotte-Fairweather fault, at ~ 20% of the fault slip rate. The influence of the transcurrent fault locking decreases inland away from the margin, as evidenced by the decrease in site velocities. Along with the dominant margin-parallel motion, sites AIS1, TRRC, GUS2, and BCDL also show a significant margin-normal component indicative of an oblique convergent element of strain and/or block motion. Further south, oblique convergence at 10-20° to the margin is recognized for the Queen Charlotte Islands, from plate motions and GPS measurements (Hyndman and Hamilton, 1993; Mazzotti et al., 2003b; Bustin, 2006).

Southwestern Yukon

The only two continuous GPS sites in Yukon, BEA2 and WHIT are located inboard of the Yakutat collision zone. Their motion is approximately normal to the plate boundary, directed northeast, and greater than would be expected if all plate boundary deformation was taken up in a narrow zone at the margin itself or the adjacent Saint Elias Mountains. This indicates that a portion of the collisional strain is being transferred further inland to the northeast. This conclusion is further discussed with the inclusion of campaign GPS results below and with calculated seismic strain rates (Chapters 4, 5).

South-central Alaska

Crustal motion at GPS sites in south-central Alaska is dominated by the influence of the Alaska subduction zone, as shown by other GPS analyses (e.g., Cohen et al., 1995; Cohen and Freymueller, 1997; Sauber et al., 1997, 2006; Freymueller et al., 2000; Fletcher, 2002; Zweck et al., 2002a; Hreinsdóttir et al., 2006). Locking of the megathrust should produce a pattern of interseismic loading that is landward, approximately orthogonal to the margin. However, SELD, located directly inboard of the subduction zone on the western Kenai Peninsula, exhibits a large southward velocity in the opposite direction (~ 11.5 mm/yr) that is explained in terms of ongoing postseismic deformation from the 1964 great Alaska earthquake. As mentioned above, SELD is located above the subducting slab down-dip of a low-slip segment of the 1964 coseismic rupture (e.g., Christensen and Beck, 1994; Holdahl and Sauber, 1994; Cohen and Freymueller, 2004). GPS studies show that the western Kenai Peninsula and adjacent Cook Inlet are moving trenchward, in contrast to the adjacent parts of the subduction zone to the NE and SW, the eastern Kenai Peninsula and Kodiak Island respectively, which are moving landward, reflecting interseismic strain accumulation due to locking (e.g., Freymueller et al., 2000; Zweck et al., 2002a). Forty years after the great earthquake, the western Kenai Peninsula and Cook Inlet are still experiencing a long-lived postseismic transient that likely results from afterslip and/or viscoelastic relaxation (Zweck et al., 2002b).

The other sites in south-central Alaska are located inboard of the eastern end of the subduction zone and are less influenced by postseismic deformation from the 1964 event, although a small component of postseismic deformation is thought to continue along almost the entire length of the 1964 rupture (Freymueller et al., 2000). At least at CHI3, POT3, ATW2, and GNAA, interseismic loading from plate boundary locking is more dominant, resulting in NW-directed (pre-Denali-earthquake) vectors that decrease inland away from the margin, from almost 30 mm/yr at CHI3 to ~ 9 mm/yr at GNAA.

Crossing the Denali fault, the GPS vectors switch from NW-directed south of the fault to SE-directed north of the fault at GRNR, CLGO, and FAIR. Larger SE-directed vectors at CLGO and FAIR than at GRNR may be due to their greater distance from the subduction zone and therefore a smaller degree of interseismic loading. However, the influence of the locked Denali fault itself must also be taken into account, especially as the vectors are sub-parallel to this major right-lateral strike-slip fault that accommodates some of the Pacific-North America relative motion. Although none of the sites are within the ~ 50 km-wide interseismic strain accumulation zone expected for locking of the Denali fault to ~ 25 km depth (e.g., Freed et al., 2006), the velocities are indicative of a broad region of long-term right-lateral shear approximately centred on the Denali fault. The relative velocities of CLGO, FAIR and GRNR may also be interpreted as indicating clockwise rotation of blocks to accommodate dextral shear between the Denali and Tintina-Kaltag fault systems, as proposed by Page et al. (1995). Clockwise rotations are facilitated by sinistral strike-slip on NE-striking faults (see Chapter 4). Such ambiguities highlight the difficulties of deciphering the driving forces and crustal responses behind ongoing crustal motions detected with GPS.

CAMPAIGN GPS RESULTS

The campaign GPS data provide lower precision, but much better spatial distribution compared to the few continuous stations in the region. This section begins with discussion of the measured velocities, followed by the corrections for the coseismic and postseismic deformation due to the 2002 Denali earthquake that are required prior to interpretation in terms of ongoing tectonic processes.

Raw Results

The campaign GPS data were processed as described above. The resulting site position time series relative to stable North America are included in Appendix C (first plot for each site), with velocity vectors shown in Figure 3.9. These vectors result from the best-fit line through the actual site positions over time. However, these velocities do not accurately reflect the long-term motion of most of the campaign sites due to the M_w 7.9 Denali earthquake on 3 November 2002, which caused significant co- and postseismic motion over a large surrounding area (e.g., Freed et al., 2006).

The Denali earthquake occurred in the middle of the time series for most of the campaign sites, and was preceded by a maximum of four occupations since 1999 (Table 3.3), insufficient to establish reliable long-term site velocities for most stations prior to the event. Similarly, a maximum of four occupations in the three years after the earthquake is not enough to independently constrain long-term site velocity, and the post-event positions may also be affected by cumulative postseismic motion. Therefore, the post-Denali campaign GPS site positions must be corrected for their predicted co- and postseismic displacements in order to obtain a better estimate of long-term average velocities. These corrections, described below, are the greatest source of uncertainty for the campaign site velocities at this time. As more data are collected in the future, effects of the earthquake will be less important, and eventually the earlier data can be discarded and the corrections will no longer be necessary, as long as another large earthquake does not occur in the area in the near future.

The campaign GPS data are not corrected for interseismic strain build-up on the Denali fault. As described below, the sites near Dawson City were most affected by the Denali earthquake, with ~ 60 mm combined co- and postseismic offset predicted by models (Figure 3.10). Assuming (1) that strain accumulates linearly and is proportional to the co- and postseismic displacements, and (2) a recurrence interval of 550 years (the penultimate event on the 2002 rupture segment occurred ~ 450-650 years ago; Schwartz et al., 2005), the interseismic strain rate is only ~ 0.1 mm/yr at these sites. Elastic strain

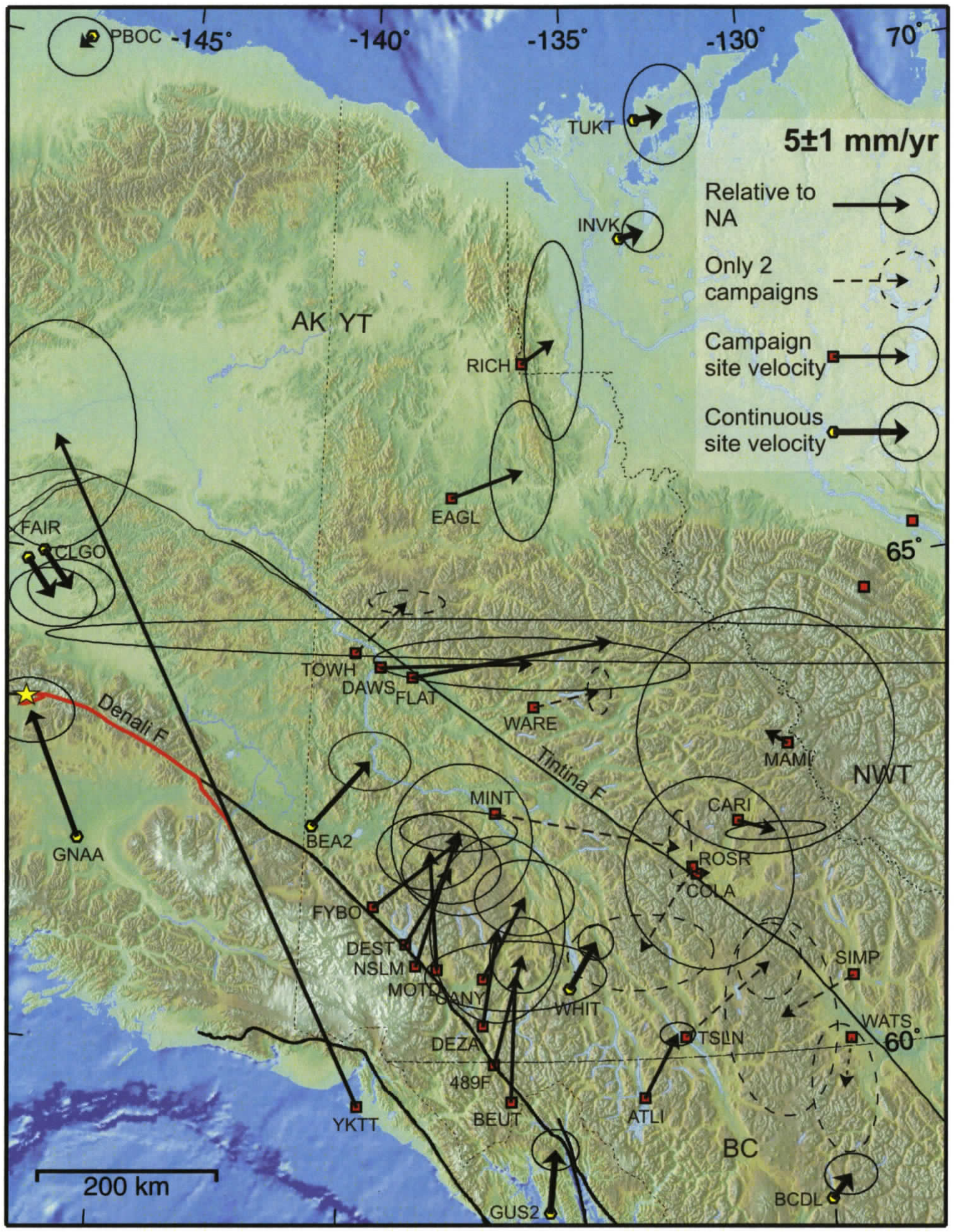

Figure 3.9. Horizontal velocity vectors for campaign (thin arrows) and adjacent continuous (thicker arrows) GPS sites relative to stable North America. Error ellipses are at 95% confidence level. Red line and yellow star mark the surface rupture and epicentre of the Denali earthquake, respectively. Dashed vectors and error ellipses have only two occupations and have very low precision.

build-up may occur at the SW Yukon sites along the Canadian extension of the Denali fault, but is likely also negligible, as low slip rates are estimated for this segment (see Chapter 4).

Data Corrections: 2002 M_w 7.9 Denali Earthquake

The Denali earthquake, described in greater detail in Chapter 4, involved ~ 340 km of surface rupture that began in the northwest as south-directed thrusting on the previously unrecognized Susitna Glacier fault. Rupture continued to the southeast as predominantly right-lateral strike-slip (with a component of vertical northside-up dip slip) on the Denali fault, followed by motion on the Totschunda fault that splays to the southeast from the main mapped Denali fault (Eberhart-Phillips et al., 2003a; Hreinsdóttir et al., 2006; Figure 3.10).

Coseismic slip

Hreinsdóttir et al. (2006) used GPS data along with surface offset data to invert for the coseismic slip distribution of the Denali earthquake, improving on an earlier model by Hreinsdóttir et al. (2003) based on a more limited dataset. Their estimated horizontal coseismic offsets show a typical right-lateral displacement pattern: sites north of the NW-trending rupture moved eastwards and those to the south moved westwards; sites to the NW and SE moved towards the fault, while those to the NE and SW moved away from it. The largest GPS site horizontal displacements (up to 3.25 m sub-parallel to the rupture) were measured at sites close to the surface rupture; coseismic offset magnitude generally decreased with distance from the surface rupture.

Hreinsdóttir et al. (2006) produced a coseismic slip distribution model by inversion of the displacement data on a three-dimensional (11-plane) fault model in an elastic half-space. Their results show that slip magnitudes increased from west to east along the Denali fault, with four localized areas of higher slip extending to the base of the model (18 km). The modelled surface offsets are generally in good agreement with the measured surface displacements, although misfits up to tens of millimetres are common. Freed et al. (2006) find a better fit of their layered-Earth calculated coseismic offsets to observed displacements by adding deep slip (to 24 km) to the Hreinsdóttir et al. (2006) model.

Coseismic corrections

S. Hreinsdóttir (personal communication, 2005) provided predictions of coseismic

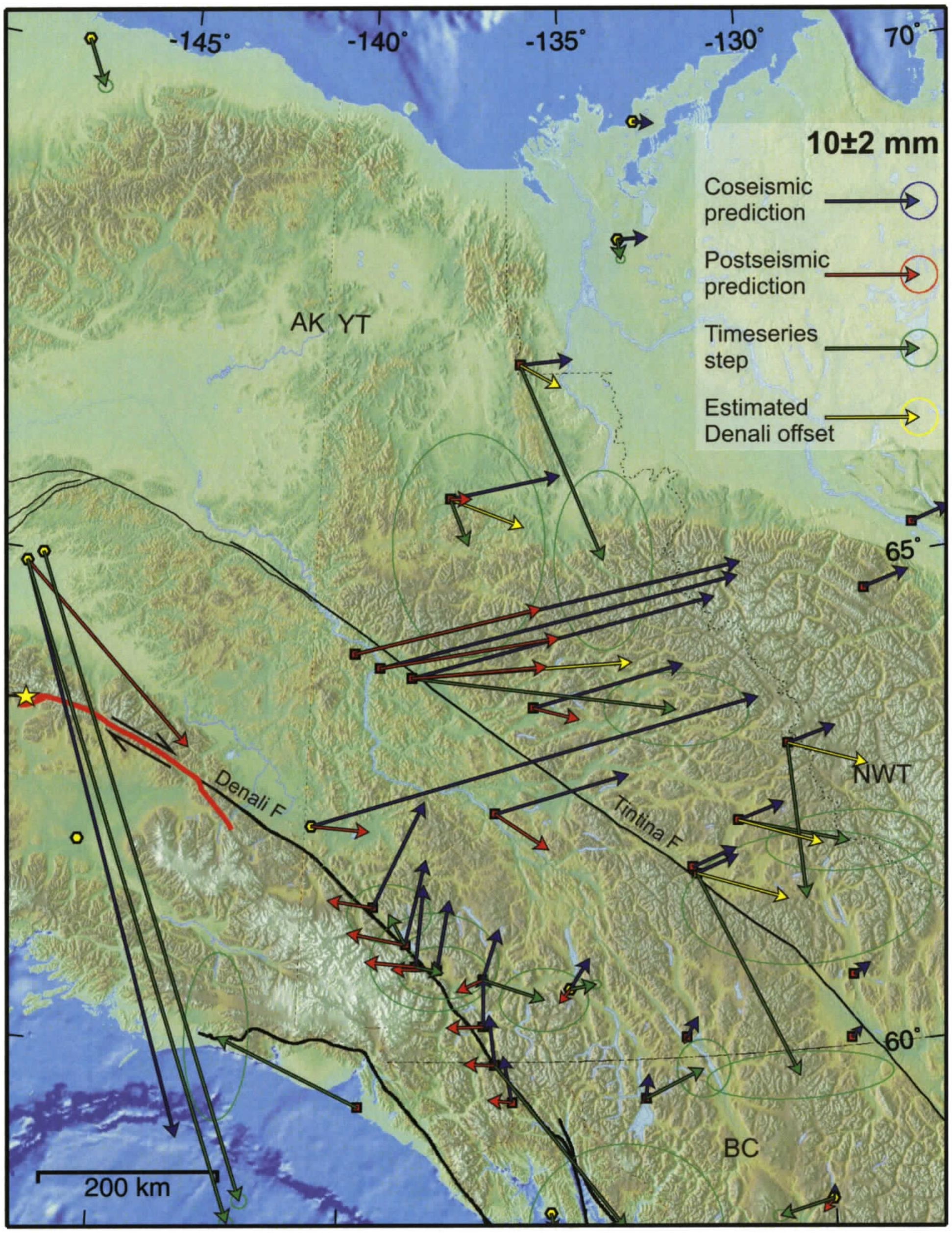

Figure 3.10. Horizontal GPS site displacements due to the 2002 M_w 7.9 Denali earthquake. Blue arrows: coseismic model prediction (S. Hreinsdóttir, personal communication, 2005). Red arrows: postseismic model prediction (A. Freed, personal communication, 2005). Green arrows: observed step in site position time series between pre- and post-Denali data. Error ellipses are at 95% confidence level. Yellow arrows: estimated site offset due to the Denali earthquake, calculated as a compromise between predicted and observed displacements. Thick red line and yellow star mark the surface rupture and epicentre of the Denali earthquake, respectively.

displacement due to the Denali earthquake at each campaign site of this study, based on the elastic half-space model of Hreinsdóttir et al. (2006). These model predictions are shown as blue arrows in Figure 3.10. All sites to the east and northeast of the surface rupture have modelled coseismic motions directed ENE away from the rupture, magnitude decreasing with distance, from ~ 40 mm at ~ 240 km (Dawson City), to ~ 5 mm at ~ 600 km (Richardson Mts. and MacMillan Pass). Sites southeast along strike of the surface rupture have small modelled coseismic motions (~ 5-12 mm) directed to the north or northeast. The campaign site positions were corrected for the model-predicted coseismic motion by subtraction of the model coseismic step from all post-Denali data. The time series corrected for coseismic offsets are shown in Appendix C as the second plot for each site.

Postseismic deformation

Postseismic deformation occurs in order to relieve stress concentrations in the lithosphere after large earthquakes. Such stress relaxation is thought to be accommodated by some combination of the processes of (1) afterslip, (2) poroelastic rebound and (3) viscoelastic relaxation (e.g., Freed et al., 2006).

(1) Afterslip is the process whereby areas close to the coseismic rupture "catch up" to the rupture via aseismic slip induced by the coseismic stress changes; afterslip may occur within the original rupture surface or on a down-dip extension of the ruptured fault (e.g., Heki et al., 1997; Bürgmann et al., 2002; Hsu et al., 2002).

(2) Large earthquakes cause pore fluid pressure to increase in areas of coseismic compression and decrease in coseismic dilational zones (Nur and Booker, 1972). The relaxation of these pressure gradients by fluid flow in the near-field crust produces poroelastic rebound over a few months following the earthquake, which may induce significant postseismic deformation and stress changes (e.g., Peltzer et al., 1998; Jónsson et al., 2003; Freed, 2005). The importance of poroelastic rebound increases with higher moisture content and permeability.

(3) Viscoelastic relaxation occurs in the lower crust and/or upper mantle in response to coseismic stress changes that cannot be sustained at the higher temperatures found at depth. Viscous flow over years/decades transfers the stress laterally and

upwards, resulting in postseismic deformation of the surface (e.g., Nur and Mavko, 1974; Thatcher et al., 1980; Freed, 2005).

The relative contribution of the three processes to the postseismic displacement field depends on the fault, earthquake and lithospheric properties, and is difficult to accurately define. Nearly the same pattern of surface deformation may result from different processes (e.g., Thatcher et al., 1980; Hearn, 2003).

Freed et al. (2006) used GPS data to assess the near-field (within 50 km of the surface rupture) and far-field postseismic deformation over the two years following the Denali earthquake and to investigate the contributory processes. The pattern of postseismic displacements is similar to the coseismic deformation pattern, but total postseismic magnitudes after 2 years are smaller. Maximum postseismic displacements are almost 0.2 m in the near-field region, decaying to less than 10 mm, 300 km north of the rupture (Freed et al., 2006). For the five continuous and twenty campaign sites for which both co- and postseismic measured horizontal displacements are available (Freed et al., 2006; Hreinsdóttir et al., 2006), the postseismic signal is on average ~ 45% of the coseismic motion. However, the ratio is quite variable. At the campaign sites with the highest measured coseismic offsets (~ 3.1 m for MEN, and ~ 1.5 m for ATT), the measured postseismic displacement is only a fraction (~ 5%) of the coseismic motion. These sites are located very close to the surface rupture and their coseismic motions likely resulted from nearby patches of high slip on the fault. The overall pattern of postseismic surface deformation appears to be a smaller and decaying continuation of shear motion that is similar to, but smoother than, the coseismic pattern. This is expected for surface displacements caused mainly by processes occurring at depth beneath the coseismic rupture and over a broad area.

Freed et al. (2006) used the postseismic horizontal GPS displacement data to constrain a three-dimensional viscoelastic finite element layered-Earth model in which the curved Denali fault is approximated by part of a circle bounding a counter-clockwise-rotating half-cylindrical block to the south. Their preferred model indicates that postseismic deformation following the Denali earthquake is due to a combination of: (1) viscoelastic upper mantle flow; (2) afterslip adjustment in the upper crust, neighbouring regions of high coseismic slip; (3) poroelastic rebound in the crust; and (4) afterslip on the down-dip extension of the Denali fault in the lower crust-uppermost mantle (~ 30-60 km depth). In the lower crust, the model equally favours viscoelastic flow and afterslip, but the existence of seismic velocity discontinuities across the Denali fault to at least 65 km (Eberhart-Phillips et al., 2003b) leads Freed et al. (2006) to prefer the mechanism of afterslip.

The implications of Freed et al.'s model are at variance with the conclusion of Pollitz (2005) that viscoelastic relaxation of the lower crust and upper mantle is the sole significant contributor to the Denali earthquake postseismic deformation field. However, Pollitz's model results in significant misfits in the early part of the postseismic period; Freed et al. (2006) suggest that the better fit of their model is due to large afterslip occurring in the first several months after the earthquake.

Postseismic corrections

A. Freed (personal communication, 2005) provided predictions of horizontal postseismic displacement for various time intervals after the Denali earthquake for the campaign GPS sites in the southwestern part of this study, based on the postseismic viscoelastic finite element model of Freed et al. (2006). No model predictions of postseismic motion are available for the Dempster Highway and North Canol Road campaign sites, which fall outside the half-cylinder of Freed et al.'s model. Located at distances of ~ 450-650 km from the Denali surface rupture, these sites are not expected to have experienced large postseismic displacements; however, neglecting motion of only a few millimetres could significantly impact the estimated long-term vectors of these relatively slow-moving sites.

The total modelled postseismic displacements three years after the Denali earthquake are shown (for sites within the model area) as red arrows in Figure 3.10. Model-predicted postseismic motions for sites to the northeast of the surface rupture (TOWH, DAWS, FLAT, WARE) are directed ENE away from the rupture in a direction close to the modelled coseismic motion but less than half the magnitude. At the other sites, while the magnitude of modelled three-year postseismic motion is also generally a little less than half the coseismic model prediction, the directions differ. At MINT, located directly east of the southeastern end of the surface rupture, the model-predicted postseismic motion is SE- rather than ENE-directed. At the Alaska Highway and Haines Road sites, located along strike southeast of the surface rupture, modelled postseismic motion is to the west or west-northwest in contrast to the north/northeast coseismic model predictions. These differences may result from minor differences in the coseismic slip distributions of the two models, which would have greatest effect close to along-strike projections of the fault plane.

The predictions provided by A. Freed (personal communication, 2005) for the total postseismic motion expected 1.5, 2, 2.5, and 3 years after the earthquake show that approximately two-thirds of the 3-year total motion happens in the first 1.5 years. The campaign GPS data from this study, already corrected for a coseismic step, were further corrected for the postseismic motion predicted for the time between the earthquake and each occupation, using linear interpolation between the 6-month model predictions. The assumption of linear interpolation is not expected to introduce significant errors (A. Freed, personal communication, 2005). The time series corrected for both co- and postseismic model-predicted motion are included in Appendix C as the third plot for each site (for those sites with postseismic predictions). Also, the resulting horizontal velocity vectors are shown in Figures 3.11 and 3.12 in comparison with the raw vectors.

Raw data versus data corrected for modelled Denali motion

The data corrected for model-predicted Denali motion should be a better approximation to the true long-term velocities than the raw data. If so, the RMS scatter should be smaller for the corrected than the raw data. Figure 3.13A-B shows a comparison of the raw data RMS (y-axis) versus the corrected data RMS (x-axis) for the Dempster Highway and North Canol Road sites (A) and the Alaska Highway sites (including the Haines Road sites and ATLI) (B). For the former, the RMS of the latitudinal component is either the same or slightly worse after correcting the data, while the longitudinal RMS is either the same or slightly improved, with one site (FLAT) showing a dramatic decrease in RMS after data correction. Thus, with the exception of site FLAT, the Denali corrections do not significantly improve the RMS of the residual. For the Alaska Highway sites, correcting the data results in slightly increased RMS

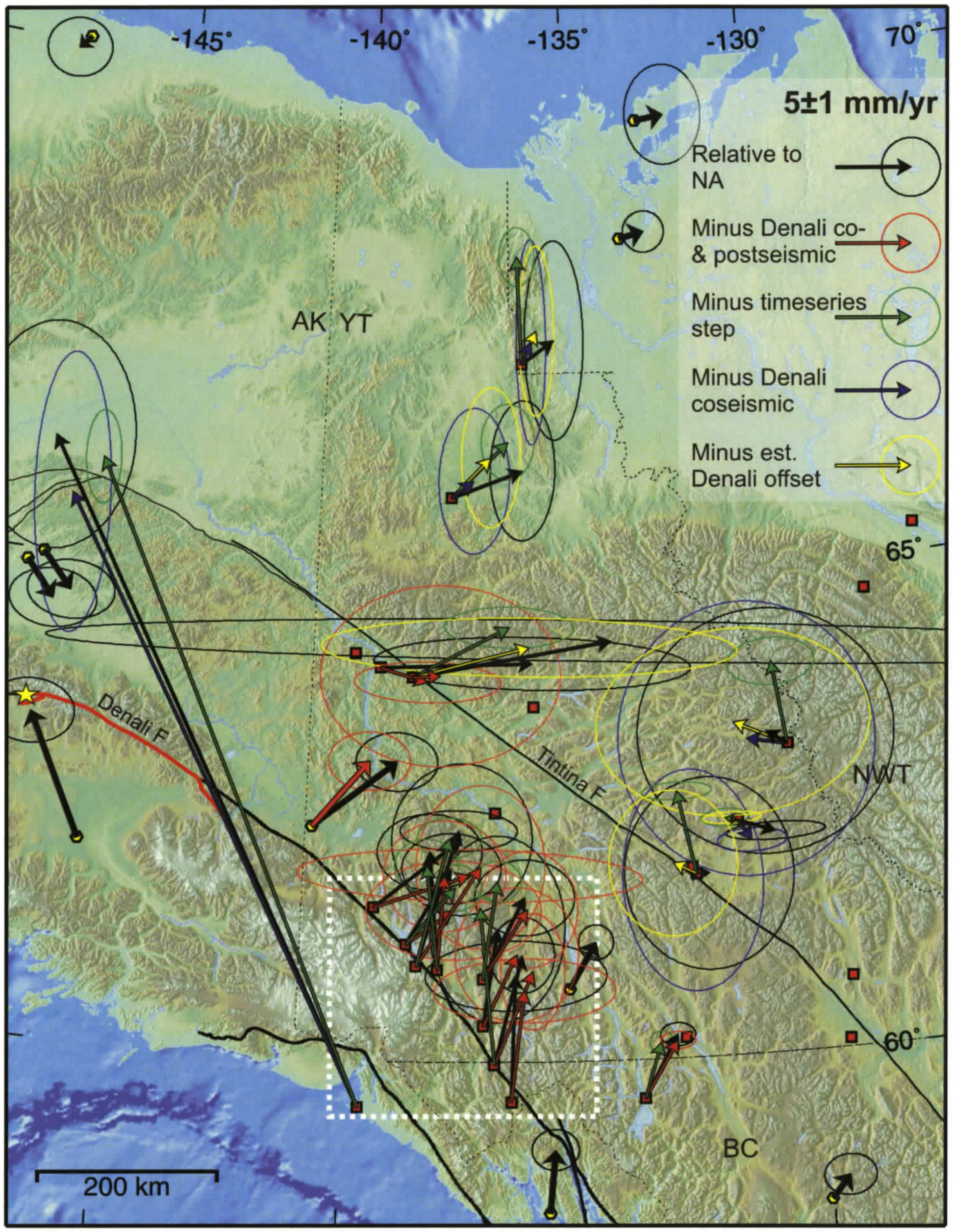

Figure 3.11. Horizontal velocity vectors for campaign and adjacent continuous GPS sites relative to stable North America. Black arrows: raw, uncorrected data. Blue arrows: data corrected for Denali coseismic motion from the model of Hreinsdóttir et al. (2006). Red arrows: data corrected for Denali co- and postseismic motion from the models of Hreinsdóttir et al. (2006) and Freed et al. (2006). Green arrows: data corrected for an estimated step in the site position time series between the pre- and post-Denali data. Yellow arrows: data corrected for the estimated Denali displacements, calculated as a compromise between the observed and model-predicted motions. Error ellipses are at 95% confidence level. Dotted box shows extent of Figure 3.12, which is a zoomed-in picture of the Alaska Highway site velocity vectors. Red line and yellow star mark the surface rupture and epicentre of the Denali earthquake, respectively.

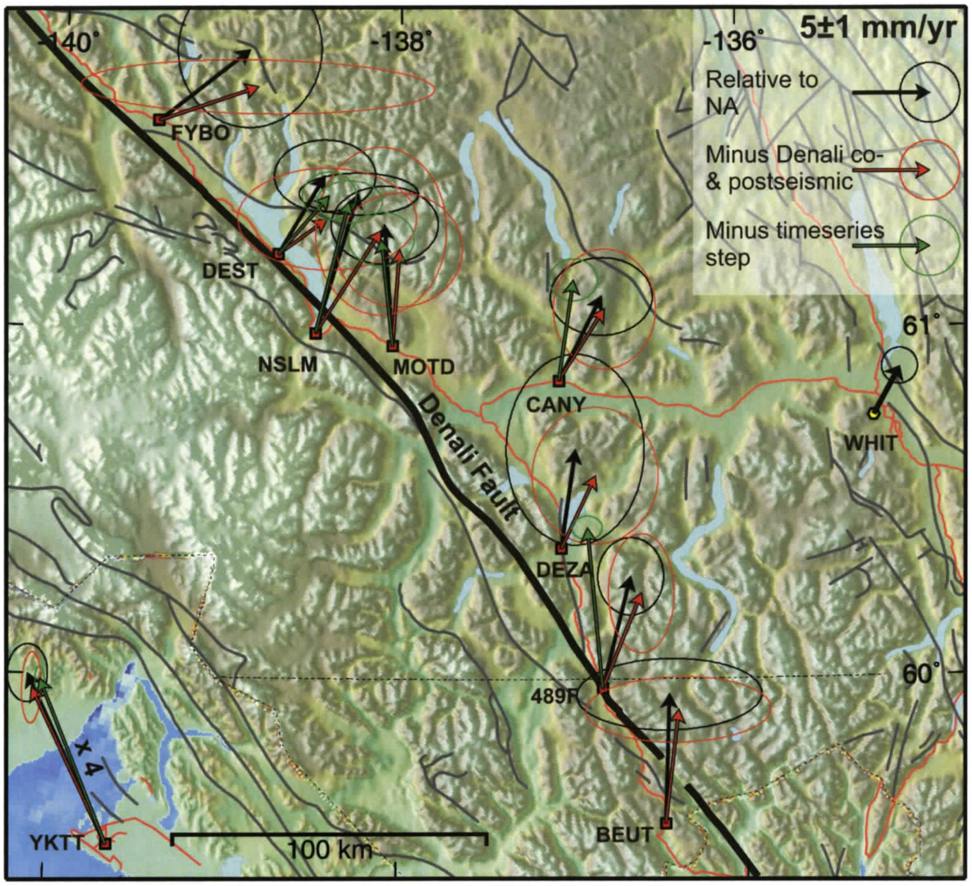

Figure 3.12. Horizontal velocity vectors for campaign and adjacent continuous GPS sites in southwestern Yukon relative to stable North America. Extent of figure is shown as box in Figure 3.11. Arrows and error ellipses as explained in Figure 3.11. Note scale difference for vectors at YKTT.

values for both latitudinal and longitudinal components, suggesting limitations in the modelled Denali displacements.

Observed time series offsets

Neither the raw data nor the data corrected for modelled Denali offsets provide an entirely satisfactory approximation of the long-term horizontal velocity pattern in Yukon. One other approach is possible: a Denali offset can be calculated and removed for each site, based on the actual campaign data. If the data were perfect, such an approach would be ideal; however, noise may play a large role in influencing the estimation of such offsets and caution is necessary.

For each site, an offset is calculated between the pre- and post-Denali positions,

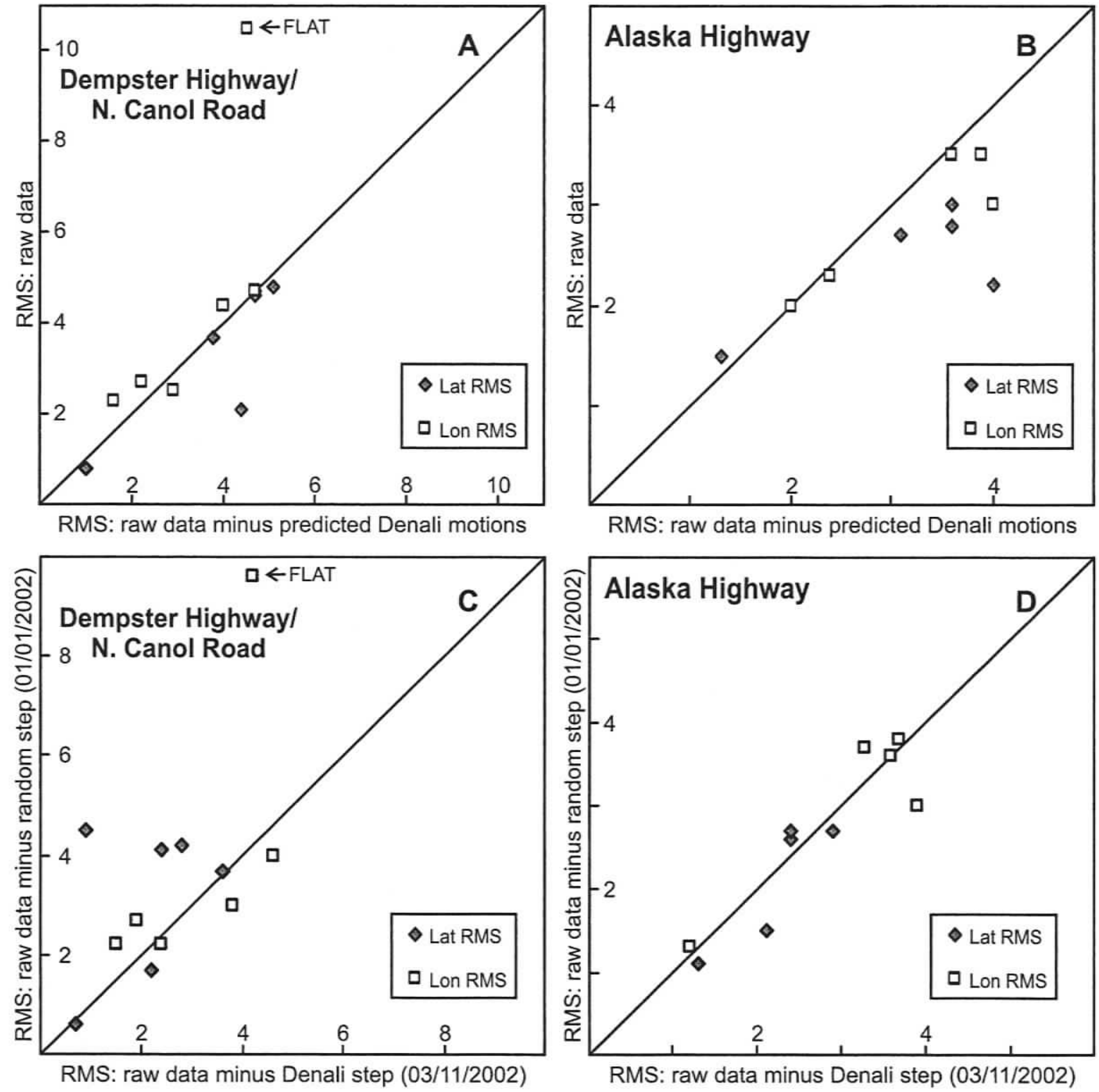

Figure 3.13. Comparison of campaign GPS latitude and longitude time series RMS scatter for the Dempster Highway/North Canol Road sites (A, C, E, G) and the Alaska Highway area sites (B, D, F, H). **A, B.** Data corrected for model-predicted co- and postseismic Denali motions versus the raw data. **C, D.** Data corrected for a Denali time series step versus a random time series step. **E, F.** Data corrected for a Denali time series step versus the raw data. **G, H.** Data corrected for a Denali time series step versus data corrected for model-predicted co- and postseismic Denali motions.

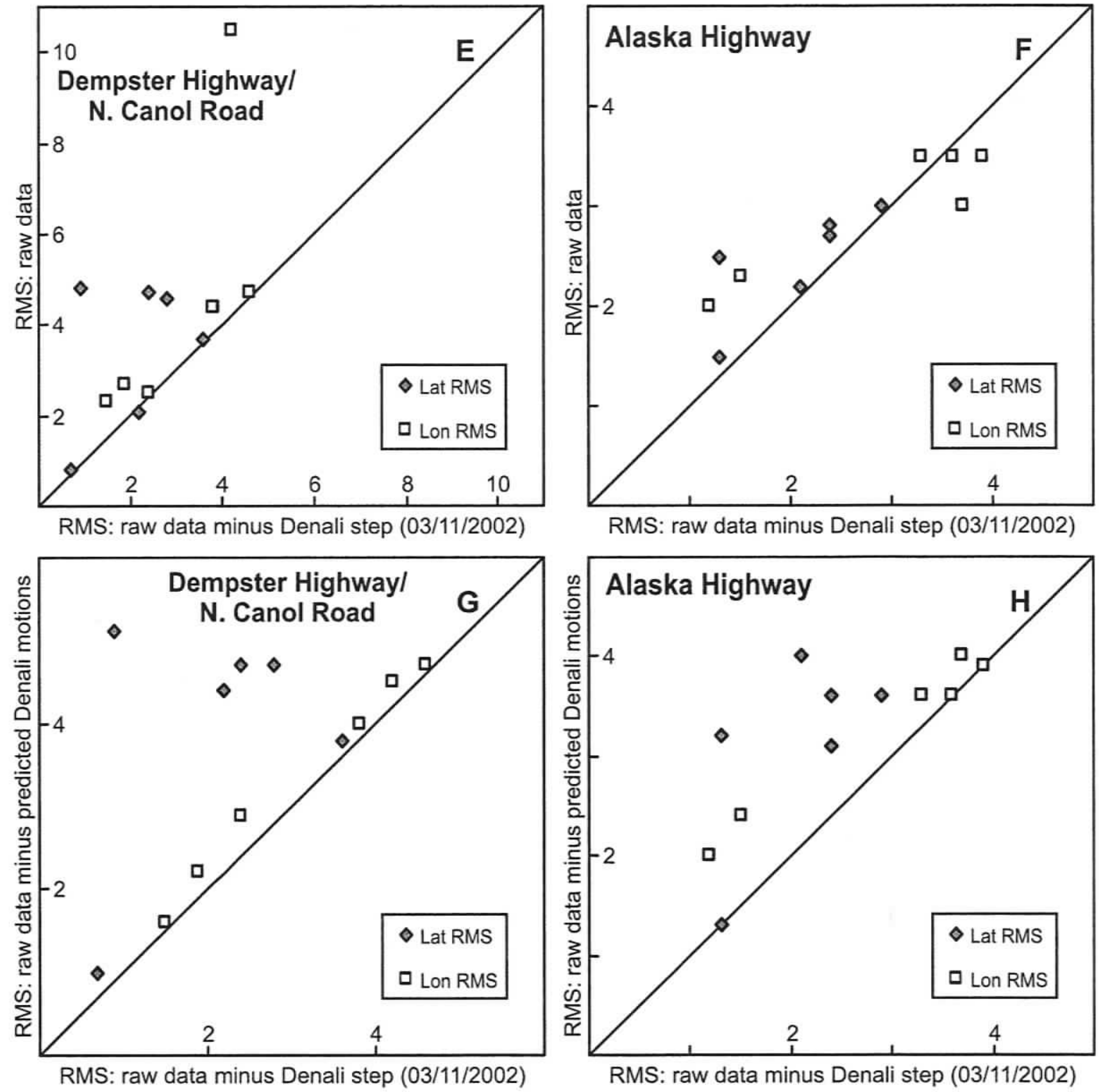

Figure 3.13. (Continued)

so as to maximize the fit of a line through the data after removal of the offset. Assuming no noise contribution, the calculated offsets are equivalent to the coseismic offset plus some fraction of the postseismic deformation at each site, depending on the timing of the first post-Denali campaign (almost 2 years after the earthquake for most sites).

First, it is important to assess the validity of a step coinciding with the Denali earthquake. Can the data justify the existence of a step at the time of the earthquake or is such a step no more significant than a step at some other random time? Figure 3.13C-D shows a comparison of the best-fit velocity RMS for the data corrected for an estimated step at the time of the Denali earthquake (03/11/2002; x-axis) versus an estimated step at a random time (01/01/2002; y-axis). For the Dempster Highway/North Canol Road sites, the Denali step is more significant than the random step. However, the Alaska Highway data show no clear preference between the two steps, indicating that no significant step can be defined at the time of the Denali earthquake.

The time series steps calculated in this way are shown as green arrows in Figure 3.10. Large differences exist between these offsets estimated from the data time series and the modelled Denali coseismic and postseismic displacements; these differences are illustrated as residuals in Figure B3 (Appendix B). Despite the large uncertainties of the estimated time series offsets (Figure 3.10), there is clearly a southward component of motion experienced by most of the campaign sites that is not accounted for by the Hreinsdóttir et al. (2006) and Freed et al. (2006) models. The consistency of this pattern, particularly for the Dempster Highway sites, suggests that the time series steps do have some significance and may not be solely due to random noise. However, as discussed below, the time series steps cannot simply be removed from the time series without a proper explanation for their size and pattern.

Time series step correction versus Denali model predictions

Before further consideration of the most appropriate way to deal with the effects of the Denali earthquake on the campaign site velocities, the goodness of fit for the different sets of results are compared. The RMS values are compared for the data corrected for an estimated Denali time series step versus the raw data in Figure 3.13E-F and versus the data corrected for modelled Denali offsets in Figure 3.13G-H.

The Dempster Highway/North Canol Road sites show RMS values that are better for the time series step-corrected data than both the raw data and the Denali model-corrected data. RMS values for the Alaska Highway sites are also lower for the step-corrected data than either the raw or the model-corrected data, although the picture is not quite as clear. As mentioned earlier, the Alaska Highway data could accommodate a random step equally as well as a Denali earthquake step, which therefore may be insignificant. For these sites, the best approach may be to make no corrections at all to the data, given that the model predictions do not improve the fit compared to the raw data, and any offset due to the Denali earthquake is statistically insignificant.

Data from the Dempster Highway and North Canol Road sites, on the other hand, show a significant offset between the pre- and post-Denali campaigns that needs to be addressed. The time series step corrections do a better job of improving the RMS of the data than the model predictions; however, the deformation pattern suggested by these steps (green arrows in Figure 3.10) cannot be entirely accounted for in terms of co- and postseismic deformation, i.e., the steps do not simply decrease with increased distance from the Denali surface rupture.

The Dempster Highway sites exhibit southeastward displacements that are similar in magnitude to the model predictions and decrease with distance from the Denali surface rupture from site FLAT to Inuvik, with the exception of RICH, which has an exceptionally large offset (~ 20 mm). Less than half of the SSE-directed step at RICH could conceivably result from co- and postseismic deformation. The remainder of the offset is unexplained: at least part of it is probably data noise, but an unknown local phenomenon such as permafrost creep may be partly responsible for offsetting the sediment in which the monument sits. Future campaign data collection is necessary to determine the authenticity of the observed offset at RICH; for now, it is assumed that the unexplained offset results from noise.

The Dempster Highway and North Canol Road data are corrected for Denali effects using a compromise between the observed and the model-predicted offsets. Coseismic offsets predicted by the model of Hreinsdóttir et al. (2006) exhibit a power-law decay with distance from the Denali surface rupture (Figure 3.14). The Denali offset magnitudes at the campaign sites are estimated by shifting the power-law coseismic offset curve to better match the observed time series offsets, such that the estimated displacements show a realistic decay with distance. Similarly, the direction of displacement is estimated as a compromise between the model and observed offsets (Figure 3.15). The resulting offsets estimated for the Dempster Highway and North Canol Road sites are shown as yellow arrows in Figure 3.10. The time series resulting from correction of the post-Denali data are shown in Appendix C as the final plot for sites

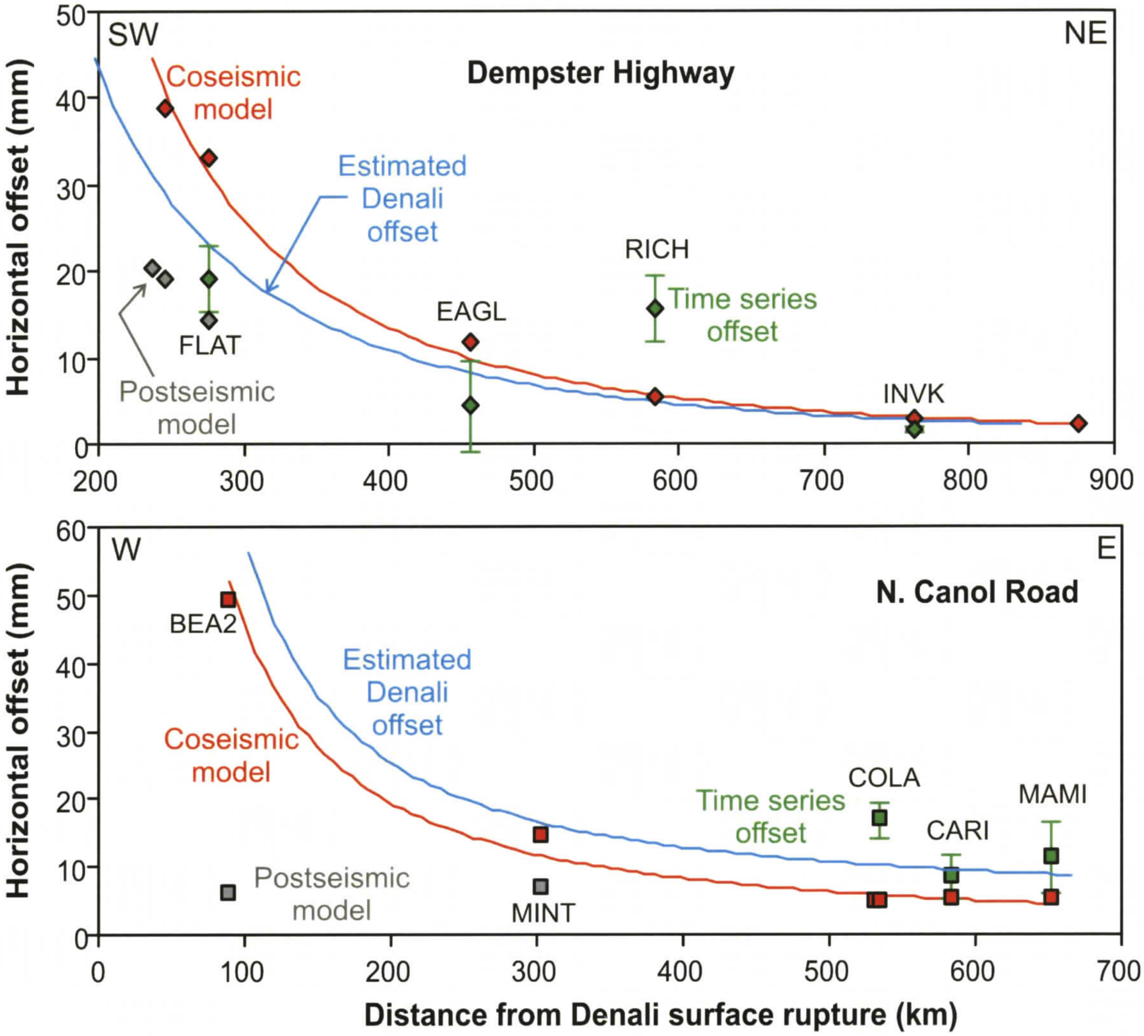

Figure 3.14. Profiles of displacement due to the Denali earthquake. Red symbols and lines: coseismic offsets predicted by the model of Hreinsdóttir et al. (2006); grey symbols: postseismic offsets predicted by the model of Freed et al. (2006); green symbols: offsets present in site time series; blue lines: estimated Denali offset magnitude, obtained by shifting the power-law decay curve of the coseismic model to better fit the observed time series offsets.

CARI, COLA, EAGL, FLAT, MAMI and RICH. The resulting horizontal velocity vectors are shown as yellow arrows in Figure 3.11.

An RMS comparison (Figure B4, Appendix B) shows that the Dempster Highway/North Canol Road data corrected with the estimated Denali offsets are an improvement on both the raw data and the data corrected for modelled displacements. As expected, the RMS values are greater than for the less realistic time series step-corrected data.

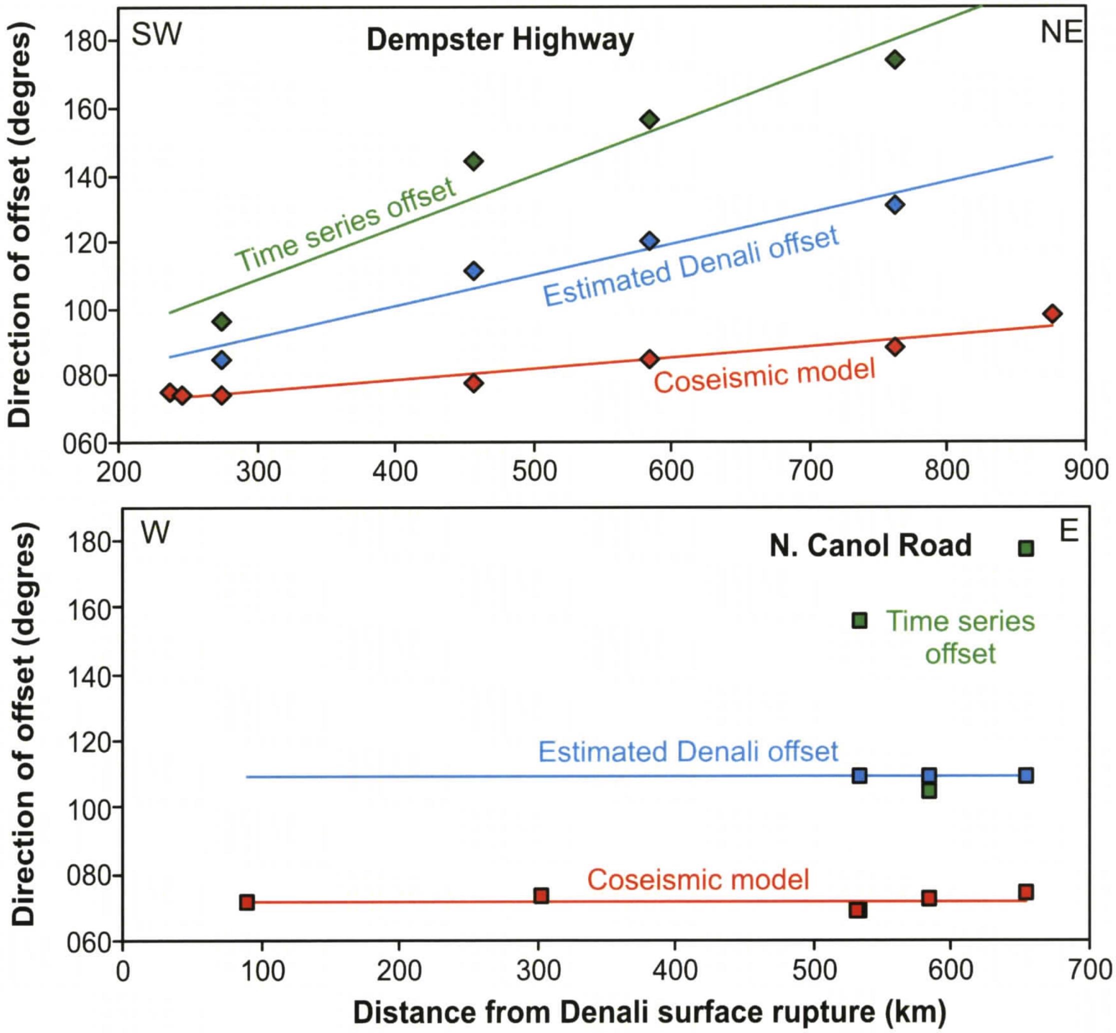

Figure 3.15. Profiles of direction of displacement due to the Denali earthquake. Red symbols and lines: coseismic offset direction predicted by the model of Hreinsdóttir et al. (2006); green symbols and line: offset direction from the site time series steps; blue symbols and lines: estimated Denali offset directions, obtained by averaging the coseismic model and time series step offset directions.

Preferred Campaign GPS Solution

The preferred solution for the long-term velocity vectors of the campaign GPS sites is shown in Figure 3.16, with the corresponding velocities given in Table 3.6. Only the horizontal site velocities are included; the vertical velocities have uncertainties that are an order of magnitude larger. Also excluded are the estimated velocities of sites MINT, ROSR, SIMP, TOWH, TSLN, WARE, and WATS, which have been occupied only twice, with time series of less than one year. The raw vectors of these sites,

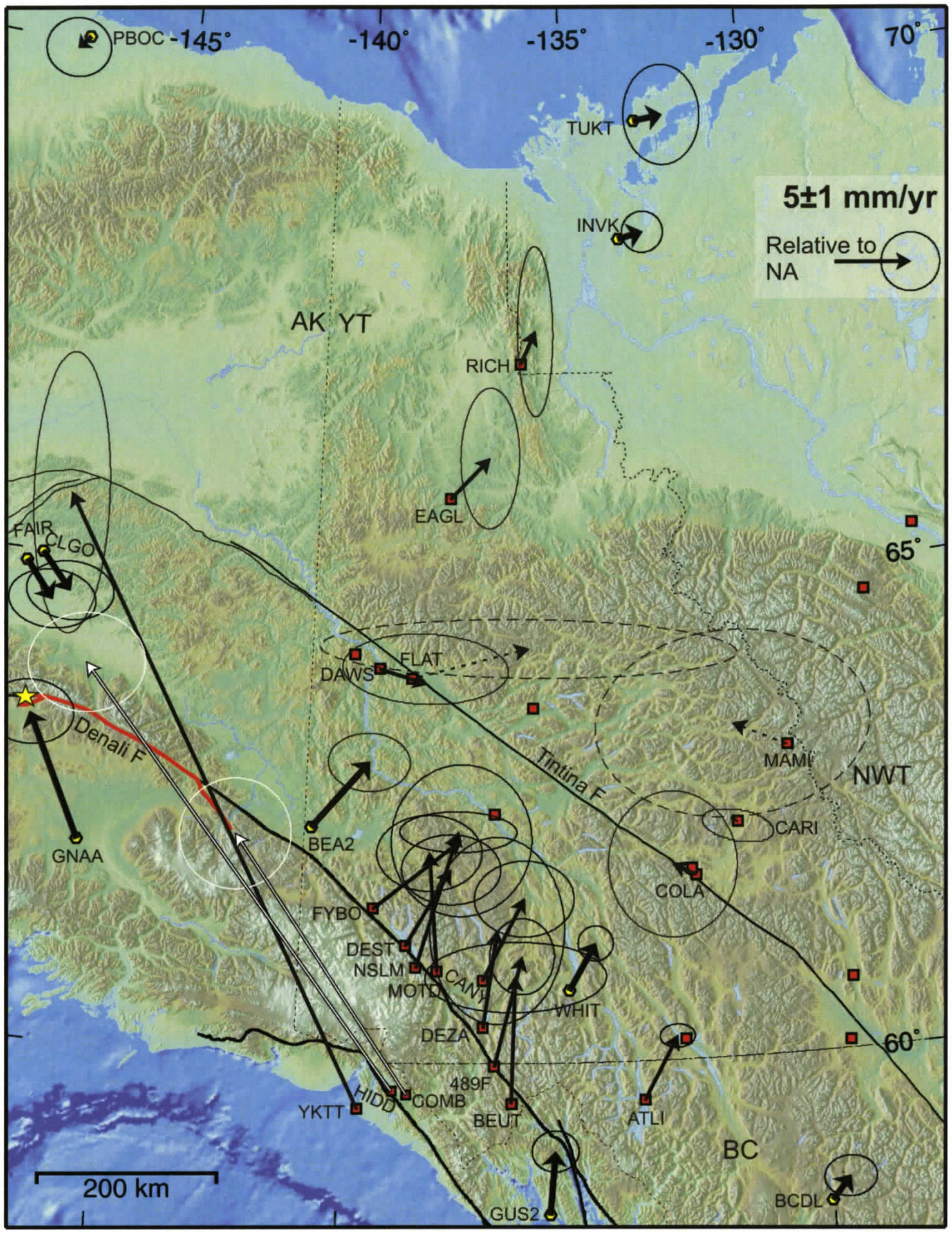

Figure 3.16. Preferred horizontal velocity vectors for campaign and adjacent continuous GPS sites relative to stable North America. White arrows are horizontal velocity vectors for sites HIDD and COMB in the Alaska Panhandle, from the analysis of Fletcher and Freymueller (2003). Error ellipses are at 95% confidence level. Red line and yellow star mark the surface rupture and epicentre of the Denali earthquake, respectively.

shown in Figure 3.9 as dashed arrows, likely have underestimated uncertainties; with only two occupations, the RMS values are deceivingly small. At least one more campaign is needed at these sites to attain velocities with useful precision.

Table 3.6. Campaign GPS horizontal site velocities with respect to stable North America.

Site	Source	V_N[10] (mm/yr)	σ_N[11] (mm/yr)	RMS_N[12] (mm)	V_E[13] (mm/yr)	σ_E[14] (mm/yr)	RMS_E[15] (mm)	T[16] (yr)	# Occs.	Site Rank[17]
489F	A[1,6]	7.3	1.3	2.5	1.9	1.1	2.3	6.3	4	B
ATLI	A[6]	4.2	0.4	1.5	2.3	0.6	2.0	6.0	5	A
BEUT	A[6]	8.5	1.2	2.1	0.3	3.1	3.8	5.3	5	A
CANY[3]	A[6]	5.5	1.3	2.8	2.8	1.7	3.5	6.1	7	A
	B[2]	3.7	1.7		0.4	2.6		8.0	3	
CARI	A[7]	0.2	0.6	0.7	-0.4	1.0	2.0	3.9	4	C
COLA	A[7]	0.8	2.5	4.1	-1.5	2.2	3.8	5.8	5	C
COMB[4]	B	17.3	1.9		-11.7	1.9		7.0	2	
DAWS	A[7]	-0.9	1.2	1.2	3.1	2.5	2.3	2.6	3	B
DEST	A[6]	5.1	1.2	2.7	3.0	1.7	3.0	5.1	6	B
	B	2.8	1.6		0.7	2.3		3.0	3	
DEZA	A[6]	6.5	3.2	3.7	0.9	2.3	3.3	3.4	5	B
EAGL	A[7]	2.7	2.4	3.6	2.6	1.0	2.5	4.8	5	B
FLAT	A[7]	2.1	1.0	2.4	7.7	7.1	6.2	4.8	6	C
FYBO	A[6]	4.7	2.6	3.1	5.8	2.4	3.0	3.4	4	C
HIDD[5]	B	28.3	1.7		-20.9	2.0		7.0	2	
MAMI	A[7]	1.7	3.2	4.1	-3.5	4.7	5.0	5.8	5	B
MOTD	A[6]	7.8	1.3	3.0	-0.6	1.8	3.5	5.3	8	A
NSLM	A[6]	9.1	0.7	2.2	2.7	2.0	3.5	5.1	7	A
	B	3.3	1.6		-0.4	2.4		3.0	4	
RICH	A[7]	2.2	2.9	4.3	1.0	0.6	1.8	4.8	5	B
YKTT	A[9]	40.6	4.8	5.4	-20.2	1.3	2.9	5.1	6	B
	B	41.3	1.3		-22.9	1.2		9.0	6	

[1] A: This study; [2] B: Fletcher and Freymueller (2003); [3] CANY: site X7 in Fletcher and Freymueller (2003); [4] COMB location: 59.6998°N 221.3607°W (Fletcher and Freymueller, 2003); [5] HIDD location: 59.7055°N 221.0545°W (Fletcher and Freymueller, 2003); [6] Raw solution; [7] Raw data minus estimated Denali displacement (see text); [8] Raw data minus Denali postseismic displacement from the Freed et al. (2006) model; [9] Raw data minus Denali coseismic displacement from the Hreinsdóttir et al. (2006) model; [10] V_N: Velocity, north component; [11] σ_N: Uncertainty, north component; [12] RMS_N: Root mean square of position scatter, east component; [13] V_E: Velocity, east component; [14] σ_U: Uncertainty, east component; [15] RMS_E: Root mean square of position scatter, east component; [16] T: Length of time series analyzed; [17] Site rank: Site solutions are ranked from A to C with decreasing reliability, according to criteria that include monument stability, time series length, number of occupations, and solution RMS (see Table B1, Appendix B).

The raw data provide the preferred solution for the Alaska Highway and Haines Road sites, as well as Atlin. As described above, the time series at these sites do not indicate a significant offset at the time of the Denali earthquake, so there is no justification for applying data corrections.

In contrast, a significant offset occurs at the Dempster Highway and North Canol Road sites. The preferred solution for these sites incorporates a correction for the Denali earthquake that is a compromise between the observed time series offsets and the displacements predicted from the co- and postseismic models of Hreinsdóttir et al. (2006) and Freed et al. (2006).

A significant offset is also apparent at site Yakutat in the Alaskan panhandle. Here, the preferred solution is the data corrected for the model-predicted coseismic motion, which provide lower RMS values than the raw data.

Site DAWS, at Dawson City, was established after the Denali earthquake. Therefore, no coseismic correction needs to be made to the data, and no time series step can be estimated. The preferred solution comes from the data corrected for the model-predicted postseismic motion, which exhibit lower RMS values. However, at nearby site FLAT, the observed time series step is directed significantly further south than both the co- and postseismic model predictions. Therefore, it is possible that the true long-term motion at DAWS has a northward component that is not evident in the chosen solution. A new campaign site (TOWH) was established in 2004, ~ 40 km west of DAWS. This site has data from only two occupations over a short time series (< 1 year), and thus its velocity is not included in the final solution. The preliminary velocity indicates northeastward motion (Figure 3.9), consistent with the Dempster Highway sites to the north.

The uncertainties for the campaign GPS velocities are estimated as the standard error normalized by the reduced χ^2 misfit, as described above. At the Dempster Highway and North Canol Road sites, where the raw data were corrected for the estimated Denali offset, the resulting error ellipses are generally large enough to include the possibility that either the model prediction or the time series step may be correct. However, at site CARI, the error ellipse must be expanded to the south to include the possibility that the Denali coseismic model is correct. Similarly, the error ellipse at DAWS is expanded to the north to include the possibility that the postseismic motion has a larger southward component than predicted by the Freed et al. (2006) model, as discussed above.

Ranking of site solutions

The campaign GPS sites are ranked according to the reliability of their solutions. Grades from A (most reliable) to C (least reliable) are included as the final column of Table 3.6. These grades were determined using several criteria shown in Table B1 (Appendix B): (1) monument stability; (2) number of occupations; (3) time series length; and (4) mean latitude/longitude RMS of the preferred solution.

The resulting ranks generally correspond to the estimated uncertainties, with the main exception of site CARI, which has a small estimated uncertainty but is ranked low (C). In general, the best-ranked sites are those in the Alaska Highway area, whereas the sediment-based monuments of the Dempster Highway and North Canol Road are ranked lowest.

Comparison with other studies

Previous analyses of the campaign GPS data were carried out by Flück (2003; Hyndman et al., 2005a) and by Fletcher and Freymueller (2003). Flück's analysis involved all the 1999-2002 campaign data included here, and also used the processing software (Bernese version 4.2) at PGC-GSC, but with a single reference site (Yellowknife) held fixed. As the present study builds and improves on that analysis, the earlier results are not included for comparison. The few previously well-defined sites are not significantly changed.

The analysis of Fletcher and Freymueller (2003) includes data from three Alaska Highway sites (CANY, DEST, and NSLM), along with YKTT. They also present the velocities of two sites inland of Yakutat, COMB and HIDD, that were not processed as part of the present analysis. Their horizontal velocity vectors for all these sites are listed in Table 3.6 and shown in Figure B5 (Appendix B) in comparison to the results of the present study.

Fletcher and Freymueller's result for YKTT is similar to its velocity vector determined in this study (within the uncertainties). However, the vectors for the Alaska Highway sites show significantly lower rates (35-60%), and directions that are rotated slightly counterclockwise (up to 34°) compared to the results of the present analysis. However, the uncertainties are large enough to permit agreement at CANY and DEST, although not at NSLM, where Fletcher and Freymueller's velocity is only a third of the magnitude of this study's vector.

The most likely explanation for the differences between the two analyses is in the amount of data analyzed; Fletcher and Freymueller had data from only 3-4 campaigns at those sites, compared to the 6-7 occupations now available and analyzed here. Discrepancies may also result from the differences in processing software (Bernese version 4.2, this study, versus GIPSY/OASIS II, Fletcher and Freymueller, 2003), or in the reference frame definition. Fletcher and Freymueller (2003) obtained GPS position data in the ITRF97 reference frame (Boucher et al., 1999) rather than the updated ITRF2000 as used for the present analysis, and they converted the velocities to a stable North America reference frame using the rotation vector of Sella et al. (2002). With the differences in available data and processing, the differences in vectors seem reasonable.

TECTONIC INTERPRETATION OF CAMPAIGN GPS VELOCITIES

Yakutat Collision Zone

The three campaign GPS sites near the coast and closest to the Yakutat collision zone, YKTT (Yakutat), COMB, and HIDD, experience the greatest velocities of any of the GPS sites in this study (Figure 3.16). Yakutat is moving to the northwest at ~ 45 mm/yr, which is similar to the motion of the Pacific plate relative to North America (~ 51 mm/yr; DeMets and Dixon, 1999), but ~ 90% of the rate and in a slightly more westerly direction. As noted by Fletcher and Freymueller (1999; 2003), Yakutat's motion therefore suggests that the Yakutat block is essentially moving with the Pacific plate, but is rotating slowly counter-clockwise relative to it, consistent with its resistance to subduction and with motion around the several arcuate transcurrent faults inland. The high velocity of YKTT indicates that most of the plate boundary deformation occurs inboard of Yakutat.

Sites COMB and HIDD are located east and inland of Yakutat, just to the northeast and southwest, respectively, of the Fairweather fault, which acts almost as the Pacific/North America plate boundary in the area. Both sites exhibit horizontal velocity vectors that are directed to the northwest, sub-parallel to the Fairweather fault, consistent with locking of the fault, an influence that decreases with distance from ~ 35 mm/yr at HIDD, 4 km from the fault, to ~ 21 mm/yr at COMB, 7 km from the fault (Fletcher and Freymueller, 2003).

Southwestern Yukon

In the southwestern part of the campaign network, the sites along the Alaska and Haines highways, northeast of the Saint Elias Mountains, are moving to the north or northeast at velocities of ~ 6-10 mm/yr (Figure 3.16). These sites are all located close to the eastern Denali fault, but the vectors do not show significant differences in either rate or direction across the fault, indicating that deformation associated with locking is small or has a long wavelength (i.e., deep locking) along this part of the Denali fault. The absence of associated deformation is consistent with the relative inactivity/slow motion on the Denali fault system in Canada compared to central-eastern Alaska, as shown from

Holocene offsets and recent seismicity (e.g., Richter and Matson, 1971; Cassidy et al., 2005; Chapter 4). Instead, the vectors appear to be strongly influenced by the collision zone to the south, indicating the north-/northeastward transfer of a portion of the collisional deformation from the plate boundary. This is further borne out by the motion of Atlin and the continuous site Whitehorse, both located further inboard, northeastward at slightly lower velocities than the Alaska Highway sites (~ 5 and 3.5 mm/yr, respectively). There is some indication that the Alaska Highway site vectors are converging systematically rather than diverging as might be expected for a "point" deformation source (Yakutat collision).

Recent work by Chris Larsen of the University of Alaska, Fairbanks, suggests that the measured horizontal velocities of the Alaska Highway GPS sites may include a significant component of glacio-isostatic adjustment (Freymueller, 2006). This adjustment is in response to rapid post-Little Ice Age glacial retreat in the Glacier Bay area to the south, as mentioned earlier. After correcting his estimated Alaska Highway site velocities for postglacial motion with the model of Larsen et al. (2005), C. Larsen (personal communication, 2006) finds a residual northeast-directed motion of ~ 5 mm/yr (see Figure B6, Appendix B). The site velocities presented above have not been corrected for the predicted postglacial motion. It appears that such corrections would produce a slight decrease in estimated site velocity, and a more northeasterly direction.

Dempster Highway

The Dempster Highway sites, in the northern part of the campaign GPS network, have large errors that result from uncertainties associated with the Denali earthquake and with limited occupations. However, it is clear that the northeastward motion seen in the southwestern part of the network continues to the north at a decreasing rate (Figure 3.16). The preferred solution for sites DAWS and FLAT shows ESE to ENE motion at rates of ~ 3-8 mm/yr; however, the significant eastward component of motion is not required by the large uncertainties. EAGL and RICH appear to be moving to the northeast at ~ 2.5-4 ± 1.7 mm/yr, consistent with the NE-SW principal stress direction calculated from a moment tensor analysis of earthquakes in the Richardson Mountains (Ristau, 2004; Hyndman et al., 2005a; Ristau et al., 2006; Figure 4.3, Chapter 4).

North Canol Road

The North Canol Road GPS sites, in the eastern part of the network, also have especially large uncertainties. After more data have been collected and analyzed, there may be justification for removing outlier data points. Removal of a suspected outlier at MAMI (the only 1999 data point) would significantly reduce the uncertainty without greatly affecting the velocity. However, in other cases, the presence of outliers is less clear and depends on the data treatment. Therefore, only data points with very large uncertainty (generally short data files) were removed for the analysis.

The results suggest motion of the North Canol Road sites to the northwest at rates of ~ 0.5-4 mm/yr, although the uncertainties do not exclude near-zero velocities (Figure 3.16). The northward component of motion of these sites is consistent with northward strain transfer as indicated by the sites to the southwest and to the north, and with the NNE-SSW principal stress orientation determined from moment tensor inversion (Ristau, 2004; Ristau et al., 2006; see Figure 4.3, Chapter 4). However, the westward component of motion is surprising, given the northeastward motion of the SW Yukon sites, and the ~ NNE-directed thrusting suggested by focal mechanisms in the Mackenzie Mountains (Figure 4.6, Chapter 4). However, NW-trending dextral strike-slip faulting is also suggested by some nearby mechanisms. It is possible that this area is accommodating distributed dextral shear on NW- to NNW-striking faults between the Tintina fault and the Mackenzie Mountains.

CHAPTER 4

Seismic Deformation of the Northern Canadian Cordillera

HISTORICAL SEISMICITY OF THE NORTHERN CANADIAN CORDILLERA

Historical seismicity is an important indicator of the current tectonics of the northern Canadian Cordillera and surrounding regions. However, the usefulness of the seismic record is limited by its relatively short history and sparse network. The short history means that locked faults with a long recurrence interval may be erroneously perceived as inactive. The sparse network (Figure 4.1) results in fairly large location errors, particularly in the north. In general, errors for recent earthquakes (post ~ 1971) are estimated at ± 5-10 km horizontally, with focal depths not routinely determined (Cassidy et al., 2005). Older events are generally less well located. However, better accuracy locations and focal depth determinations are available from a number of detailed studies (e.g., Horner, 1983; Wetmiller et al., 1988; Horner et al., 1990; Cassidy and Bent, 1993; Doser and Lomas, 2000; Ratchkovski and Hansen, 2002; Ristau, 2004). In most areas, earthquakes as small as magnitude 3.0 have been detected since 1979.

The distribution of seismicity in the vicinity of the Yakutat collision and the northern Canadian Cordillera is shown in Figure 4.2. Intense seismicity occurs at the collision zone itself, but considerable activity also occurs in other areas far inland from the plate boundary. The pattern and nature of seismicity is described for each distinct area below, using information from the earthquake distribution and the available earthquake focal mechanisms.

The earthquake mechanisms plotted in Figures 4.3-4.7 come from a number of sources (listed below) and consist of moment tensor solutions, *P*-wave first motion solutions, and mechanisms calculated by body- and surface-wave modelling. (1) Harvard centroid moment tensor solutions have been calculated for earthquakes larger than ~ M 5.0 since 1979 (e.g., Dziewonski et al., 1981). (2) Regional moment tensor solutions calculated for events larger than ~ M 4.0 since 1995 have been calculated by J. Ristau

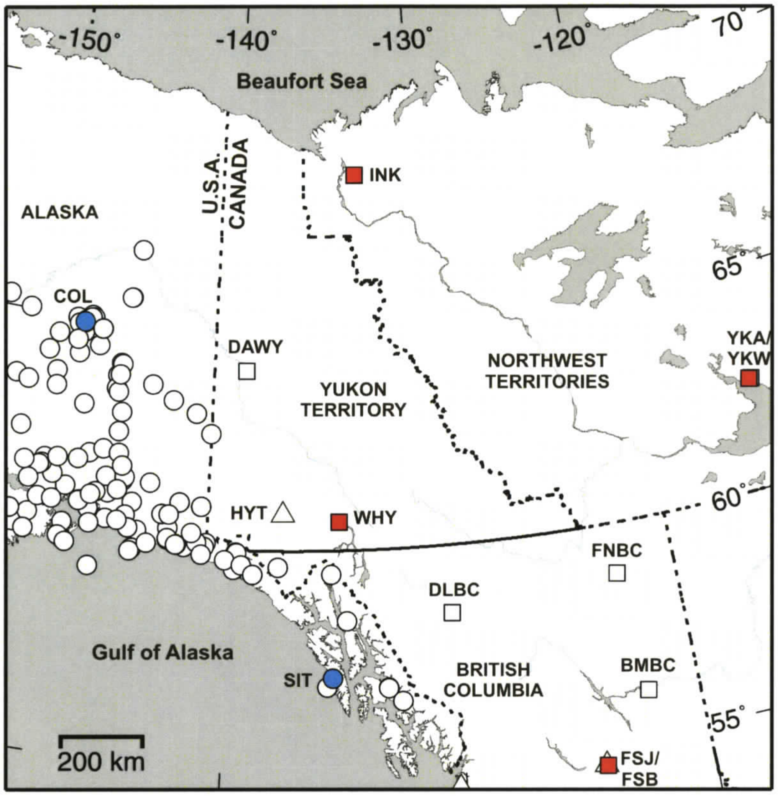

Figure 4.1. The seismic network in the northern Cordillera as of 2004 (after Cassidy et al., 2005). Squares: three-component broadband stations of the Canadian National Seismograph Network (CNSN); triangles: single-component short-period stations of the CNSN; circles: Alaska seismic stations (principally single-component short-period). Blue symbols: 1951 station distribution; red and blue symbols: 1971 distribution. BMBC: Bull Mountain; COL: College; DAWY: Dawson; DLBC: Dease Lake; FNBC: Fort Nelson; FSB and FSJ: Fort St. John; HYT: Haines Junction; INK: Inuvik; SIT: Sitka; WHY: Whitehorse; YKA and YKW: Yellowknife.

(Ristau, 2004; Hyndman et al., 2005a). (3) Regional moment tensor solutions have been calculated since 2003 by the Alaska Earthquake Information Center (AEIC). Solutions for events in interior Alaska are provided by Ratchkovski and Hansen (2002). (4) The polarity of *P*-wave first motions has been used to calculate focal mechanisms for a number of larger events (Stauder and Bollinger, 1966; Wickens and Hodgson, 1967; Gedney, 1970; Hasegawa et al., 1979; Perez and Jacob, 1980; Huang and Biswas, 1983; Biswas et al., 1986; Estabrook et al., 1988; Wetmiller et al., 1988; Horner et al., 1990). (5) Finally, other mechanisms have been produced by modelling of surface and body waves (Estabrook et al., 1992; Cassidy and Bent, 1993; Fletcher and Christensen, 1996; Doser and Lomas, 2000).

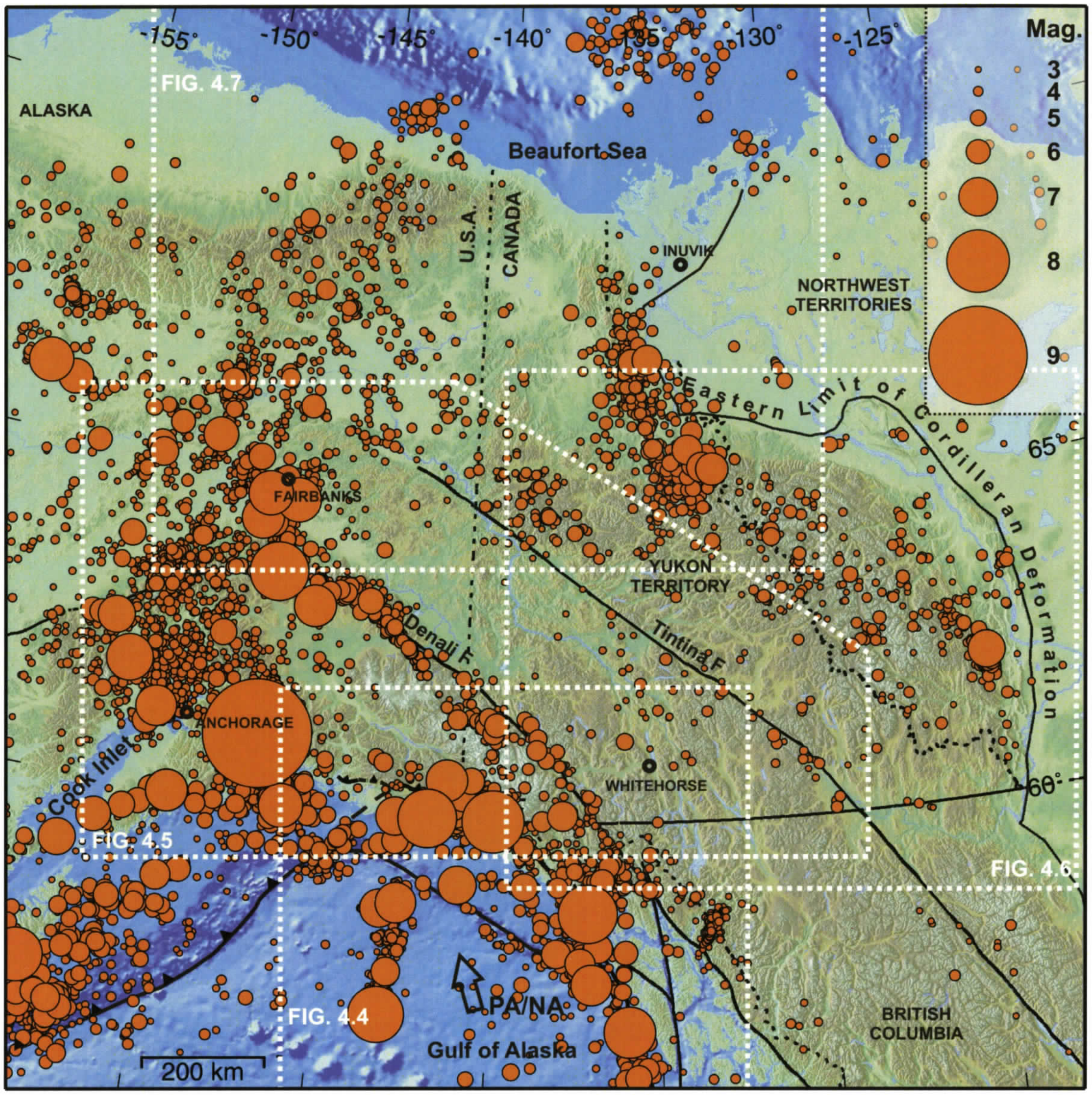

Figure 4.2. The distribution of earthquakes of magnitude 3 and greater from 1899 to 2004 in the northern Canadian Cordillera and eastern Alaska. Alaskan events with focal depths > 25 km that are probably in the subducted oceanic plate are excluded. Size of circles is proportional to magnitude, as shown at upper right. Data are sourced from the Geological Survey of Canada National Earthquake Database and the Alaska Earthquake Information Centre (AEIC) Database (2005). Boxes show extent of subsequent figures.

Composite stress directions have been determined from stress inversion of moment tensor and first-motion solutions for several areas of the northern Cordillera: the Yakutat region, the Mackenzie and Richardson Mountains (Ristau, 2004; Hyndman et al.,

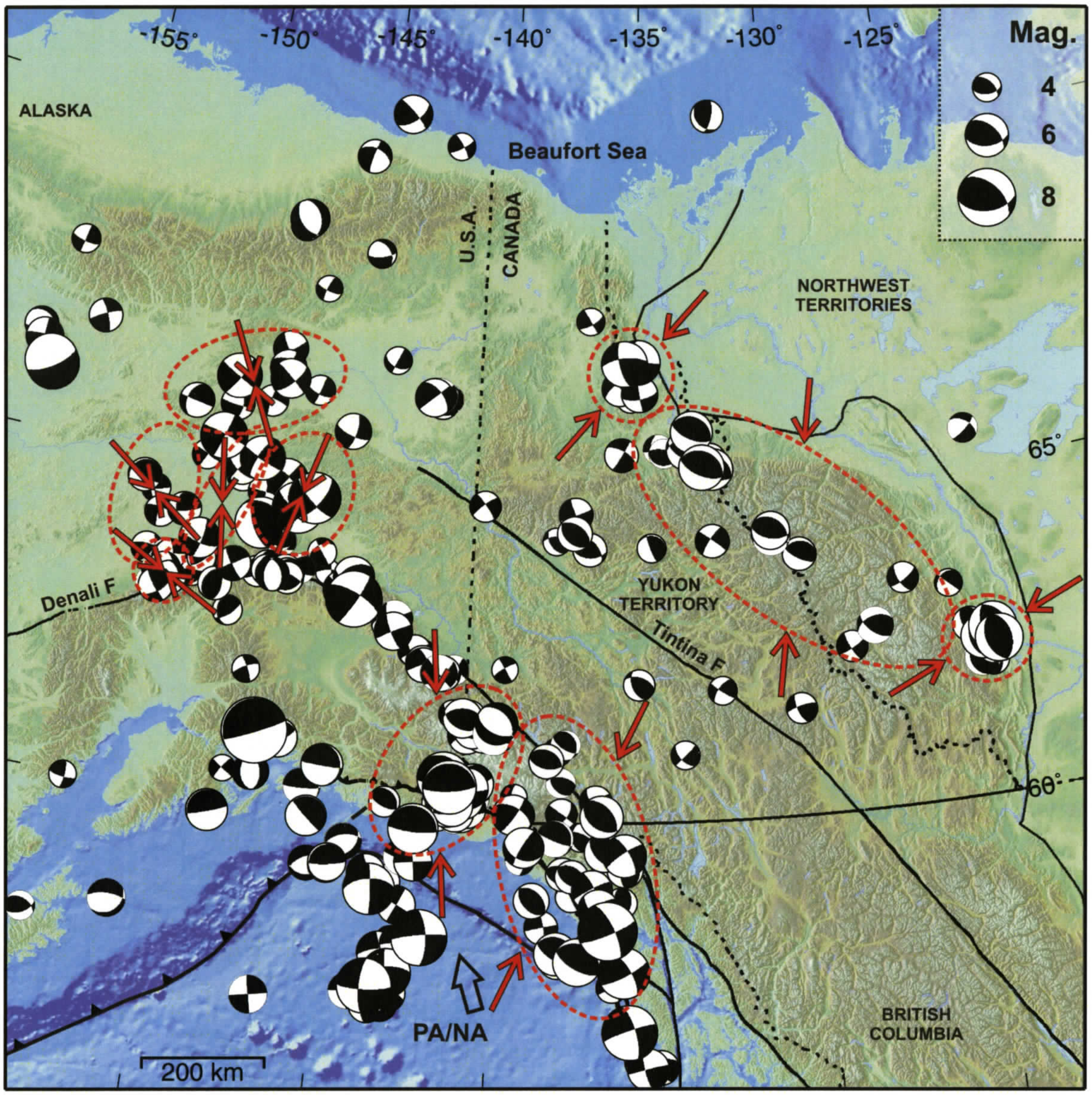

Figure 4.3. Earthquake focal mechanisms and composite stress directions for various regions in the northern Cordillera determined from stress inversion, after Ristau (2004), Hyndman et al., (2005a), Ristau et al., (2006), and Ratchkovski and Hansen (2002).

2005a; Ristau et al., 2006), and interior Alaska (Ratchkovski and Hansen, 2002). These stress orientations are shown in Figure 4.3 and are further discussed in the relevant sections below.

Yakutat-Saint Elias Region

The pattern of very intense seismicity in the Yakutat-Saint Elias region is shown in Figure 4.4. The earthquakes are concentrated in the main Yakutat collision zone to the

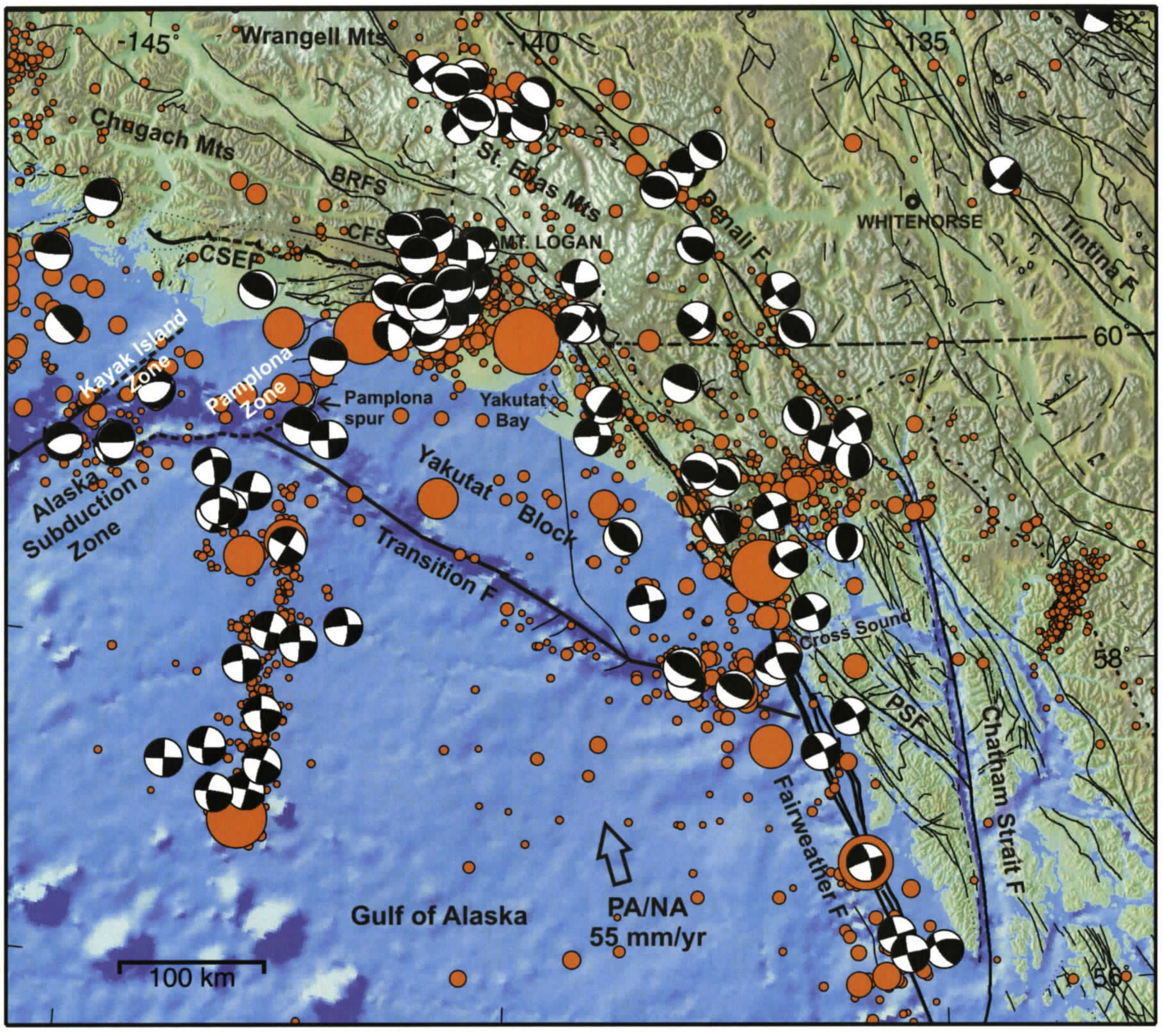

Figure 4.4. Fault traces, seismicity and earthquake mechanisms in the Yakutat region. Earthquake magnitude scale as in Figure 4.2. CSEF: Chugach-St. Elias fault; CFS: Contact fault system; BRFS: Border Ranges fault system; PSF: Peril Strait fault.

southwest of the Saint Elias Mountains, with a second concentration inboard of the southeastern end of the Yakutat block in the Alaskan panhandle. There have been several M ~ 8 earthquakes recorded and eight events over M 7.0 since 1899. The Saint Elias Mountains themselves appear to exhibit lower seismicity, with higher seismicity again to the northeast.

Available earthquake focal mechanisms indicate a mixture of thrust and strike-slip faulting. Dextral displacement along the Fairweather fault accommodates most of the Pacific-North America differential motion; a series of large historic dextral strike-slip earthquakes have ruptured the entire length of the fault (e.g., Cassidy et al., 2005). Intense seismicity occurs in the zone of collision between the Yakutat block and the North America plate. Here, earthquake mechanisms indicate thrust faulting along and above the plate interface, representing deformation within the North America plate and the Yakutat block (Doser and Lomas, 2000). Relatively little seismicity occurs in the interior of the Yakutat block, with the exception of the western portion, the Pamplona zone, where oblique thrusting is indicated (e.g., Doser et al., 1997). A linear band of seismicity occurs in the Pacific plate south of the Pamplona zone; focal mechanisms indicate north-south dextral strike-slip faulting that appears to be rupturing into the Pacific plate (e.g., Pegler and Das, 1996).

The composite stress orientation (Figure 4.3; Ristau et al., 2006) is NE-SW for the eastern Yakutat block and northern Fairweather fault, an area dominated by dextral strike-slip faulting. This orientation is well constrained by a variety of earthquake mechanisms. To the northwest in the Saint Elias Mountains where thrust mechanisms dominate, the stress direction changes to NNW-SSE. However, the prevalence of thrust mechanisms in that area makes the latter direction less well constrained. A variety of fault orientations and mechanisms are necessary for a reliable stress inversion (Michael, 1984).

Fairweather fault

The Fairweather strike-slip fault (Figure 4.4) is the northern extension of the Queen Charlotte transform boundary between the Pacific and North America plates; it also forms the eastern and northeastern boundaries of the Yakutat block. Right-lateral strike-slip motion along the northwest-trending Fairweather fault is close to the direction of, and accommodates most of, the Pacific-North America differential motion. At its northern end, the strike-slip motion is probably transferred to the E- to SE-trending thrust/oblique thrust faults of the Chugach-Saint Elias fault system (Plafker et al., 1978).

The Fairweather fault has ruptured throughout its length in a series of earthquakes in 1927, 1949, 1958, and 1972. The southernmost portion ruptured in the 1949 M_w (moment magnitude) 8.1 Queen Charlotte event, with a further M_w 6.8 event in 2004; the 1927 and 1972 Sitka events (M_w 7.0 and 7.6 respectively) ruptured the southern and central sections of the fault, while slip on the northern section occurred in the 1958 M_w 8.2 Lituya Bay earthquake (e.g., Nishenko and Jacob, 1990; Doser and Lomas, 2000; Bufe, 2005). The focal mechanisms of these events indicate dextral strike-slip motion on near-vertical NW-trending planes (Stauder, 1960; Plafker et al., 1978; Doser and Lomas, 2000; Bufe, 2005).

The rupture length of the 1949 event was ~ 490 km; the rupture may have extended as far north as 56°N, but the aftershock distribution is not well determined for the northern portion (Rogers, 1986). The 1927 event occurred near the junction of the Fairweather fault with the Transition fault zone; the focal depth was ~ 16 km, and the rupture length ~ 35 km (Doser and Lomas, 2000). The 1972 earthquake initiated at a depth of ~ 10 km and ruptured ~ 180 km of the Fairweather fault; the northernmost rupture extent coincides with the southernmost rupture of the 1927 event (Doser and Lomas, 2000). Inferred slip of ~ 7 m occurred in the epicentral region (Schell and Ruff, 1989). The epicentre of the 1958 event was located in Cross Sound, close to a bend in the Fairweather fault where it merges with the Peril Strait fault. The focal depth was ~ 16 km and the rupture length was at least 250 km (Doser and Lomas, 2000). Most of the 1958 rupture involved strike-slip motion along the fault; as much as 6.6 m of dextral slip was measured onshore (Tocher, 1960). However, some aftershocks at the northern end delineate an east-west trend that borders on the rupture zone of the 1979 St. Elias thrust earthquake described below (e.g., McCann et al., 1980).

Southeastern Alaska: inland of the Fairweather fault

A broad swath of seismicity in the Alaskan panhandle between the Fairweather and Denali faults at ~ 59°N may represent a tectonic link between these fault systems (Figure 4.4; e.g., Rogers, 1976; Horner, 1983). Focal mechanisms suggest that both thrust and strike-slip faulting on NW- to NNW-striking planes is accommodating dextral transpression across this zone.

Almost no seismicity is associated with the Chatham Strait fault, a NNW-striking transform fault to the east of the Fairweather fault that has accommodated ~ 100 km of Cenozoic (post ~ 25 Ma) dextral displacement (Hudson et al., 1982). It appears that the vast majority of relative right-lateral motion between the Pacific and North America plates in this region is currently taken up by the Fairweather fault. However, a few M 5+ events have occurred in the vicinity of the northern end of the fault (Figure 4.4).

Inland of the Chatham Strait fault, earthquake swarm activity (M < 4) defines a NE-SW 100-km-long trend across the border between British Columbia and SE Alaska just north of 58°N (Figure 4.4). These events have not been linked to mapped faults in the region, and show a seasonal trend that is likely related to glacial processes (Rogers, 1976), although Horner (1983) also suggests a volcanic source as an alternative.

Pamplona zone, western Yakutat terrane

Within its boundaries, the Yakutat block (the surface expression of the Yakutat terrane that likely extends beneath the margin) is largely undeformed, with the exception of the Pamplona zone to the west (Figure 4.4). The Pamplona zone is a broad region of complex deformation in the form of an onshore-offshore thin-skinned fold and thrust belt developed in Tertiary sedimentary cover. The Pamplona zone fold and thrust belt extends from the Pamplona spur (Figures 2.3, 4.4) in the east to the southern (Transition fault zone), western (Kayak Island zone) and northern boundaries of the Yakutat terrane. Structures of the Pamplona zone trend primarily E-W to SW-NE and dip to the north and northwest (e.g., Plafker et al., 1978; Doser et al., 1997). The eastern margin is marked by a 25-km-long, 650-m high bathymetric ridge, the Pamplona spur, interpreted to have formed by repeated motion on a system of high-angle reverse faults and a tightly folded anticline (Bruns, 1985; Doser et al., 1997).

The Pamplona zone has been the site of moderately intense historical seismicity, with five events over M_w 6.0 since 1900. One of these occurred in 1958 (M_w 6.1); the others were part of an earthquake sequence in 1970, with magnitudes up to M_w 6.7 (Doser et al., 1997). Focal mechanisms determined by Perez and Jacob (1980a) and Doser et al. (1997) suggest that the eastern Pamplona zone is dominated by low-angle thrusting, with higher-angle oblique thrusting occurring in the western part of the zone. Focal depths typically lie between ~ 5 and 15 km; the largest event, in the northern Pamplona zone, may have ruptured part of the megathrust boundary, while most of the events occurred well above it (Doser et al., 1997). An exceptionally deep event (~ 35 km) occurred at the southern edge of the Pamplona zone in 1964 and was likely a stress accommodation after the great Alaska earthquake (M_w 9.2) that occurred 2 months previous; this m_b (body-wave magnitude) 5.1 event involved low-angle dextral-oblique thrusting on a NW-trending fault (Stauder and Bollinger, 1966) and may have been associated with the Transition fault rather than faults of the Pamplona zone (Doser et al., 1997).

The Pamplona zone is thought to represent the main locus of the current Pacific-North American plate boundary, as it links subduction along the Aleutian megathrust with thrusting along the Chugach-St. Elias fault system to the north, and the Pamplona spur marks the eastern limit of post-Miocene deformation within the Yakutat terrane (Plafker et al., 1978; Perez and Jacob, 1980a; Plafker, 1987; Estabrook et al., 1992; Doser et al., 1997). The Kayak Island thrust zone, located to the west of the Pamplona zone, marks the easternmost extent of rupture in the M_w 9.2 Alaska megathrust earthquake of 1964 (e.g., Stauder and Bollinger, 1966; Estabrook et al., 1992), while the westernmost rupture extent in the 1979 M_w 7.3 St. Elias plate boundary earthquake coincides with the onshore extension of the Pamplona zone, the Malaspina fault system (Horner, 1983; Estabrook et al., 1992). The plate boundary between the rupture extents of the 1964 great Alaskan earthquake and the 1958 Fairweather event was identified as the Yakataga seismic gap due to its seismic quiescence relative to adjoining regions (e.g., Tobin and Sykes, 1968). The eastern part of the seismic gap was ruptured in the 1979 M_w 7.3 St. Elias earthquake, but the western part has not ruptured since a pair of great earthquakes in 1899 (e.g., Lahr and Plafker, 1980).

Historical seismicity in the Pamplona zone likely reflects compression and transpression of sediments offscraped from the underthrusting Yakutat basement, and possibly some relative Yakutat-Pacific motion. As discussed below, the Pamplona spur aligns with, and may be controlled by, a N-S-striking dextral fault zone in the Pacific plate that probably developed in response to greater subduction resistance of the eastern Yakutat terrane compared with the western part. One or more megathrust earthquakes may be expected in the near future on the Pacific-North American plate boundary beneath or down-dip of the Pamplona zone to relieve the strain built up in the Yakataga seismic gap since the great earthquakes of 1899.

Saint Elias region

The Saint Elias orogen marks the northern boundary of the Yakutat terrane with North America, and also represents the Pacific-North America plate boundary between the Aleutian subduction zone and the Fairweather transform (the Yakataga seismic gap mentioned above). Collision of the Yakutat block with North America drives high uplift rates in the coastal mountains, where many peaks rise to elevations over 5000 m. The terrane is underthrusting and accreting to North America along the Chugach-Saint Elias thrust fault system and, seaward, a wide foreland fold and thrust belt, both of which trend approximately east-west (Figure 4.4).

The Saint Elias region has been the site of intense historical seismicity, including two M ~ 8 events in September 1899 that are thought to have ruptured most or all of the Yakataga seismic gap on the Pacific-North America plate interface (e.g., Thatcher and Plafker, 1977; McCann et al., 1980). The eastern part of the gap ruptured again in the 1979 M_w 7.3 St. Elias earthquake (e.g., Lahr et al., 1979).

The surface-wave magnitudes (M_s) of the 1899 events have been estimated from interpretations of modified Mercalli intensities (McCann et al., 1980). The first event (M_s 8.5) was most strongly felt from west of Kayak Island to Yakataga (Figure 2.3), a distance of approximately 180 km across the western half of the Yakataga seismic gap. Coseismic uplift of 1 m was reported at Yakataga (Tarr and Martin, 1912), inferring several metres of slip on the plate boundary. The second event (M_s 8.4), preceded by an M_s 7.8 foreshock, was most strongly felt in Yakutat Bay, where up to 15 m of coseismic uplift occurred; deformation may have extended west of Yakutat Bay to encompass the eastern half of the Yakataga seismic gap (McCann et al., 1980).

The February 28 1979 M_w 7.3 St. Elias earthquake was initially interpreted as involving thrusting on a low-angle NNW-dipping fault plane below the Saint Elias Mountains (Lahr et al., 1979; Hasegawa et al., 1980; Perez and Jacob. 1980b). Reanalysis by Estabrook et al. (1992) reveals a complex rupture with two subevents: slip propagated to the east-southeast as a shallow N-dipping thrust, changing to a more steeply NE-dipping thrust with a large dextral strike-slip component. The strike-slip component is consistent with a change to the dextral strike-slip regime of the Fairweather fault to the east and southeast, and with an east-west trending zone of aftershocks of the 1958

Fairweather event that borders on the 1979 St. Elias rupture zone. The second subevent nucleated in a region coinciding with the largest concentration of aftershocks (~ 50 km southeast of the mainshock) and with the onshore extension of the Pamplona zone (Horner, 1983; Estabrook et al., 1992). Estabrook et al. (1992) suggest that this region represents the northernmost boundary of the Yakutat terrane, which may have acted as a barrier to continuous rupture.

The St. Elias earthquake is interpreted as having ruptured the Pacific-North America plate boundary (e.g., Hasegawa et al., 1980; Estabrook et al., 1990; 1992). The event had an estimated focal depth of ~ 20 km, a rupture length of 50-80 km, and an average fault displacement of ~ 2 m (Hasegawa et al., 1980; Perez and Jacob, 1980b; Page et al., 1982; Estabrook et al., 1992). Aftershocks occurred at shallow depths over a broad region extending ~ 115 km to the southeast of the mainshock epicentre (Stephens et al., 1980). The aftershock zone is consistent with the low-angle thrust mechanism and with the southeastward rupture propagation inferred from body- and surface-wave analysis (Hasegawa et al., 1980; Boatwright, 1980). The aftershock zone does not appear to extend to the surface (Stephens et al., 1980), consistent with the lack of detected surface rupture (Lahr and Plafker, 1980).

Transition fault zone

The Transition fault zone forms the southwestern, seaward boundary of the Yakutat block with the main Pacific plate, and marks the base of the continental slope (Figure 4.4). Although described as inactive by Bruns (1983), a sequence of earthquakes in Cross Sound in 1973 (mainshock M_w 6.4) show that at least the southernmost portion of the Transition zone is seismically active. Plafker (1987) also cites local deformation of Quaternary sediments as evidence that the Transition fault remains active. Tentative evidence for seismic activity along the western portion of the zone comes from the 1964 occurrence of a deep (35 km) thrust earthquake (m_b 5.1) on a NW-trending plane beneath the eastern Pamplona zone (Doser et al., 1997). This event was interpreted as an aftershock of the 1964 great Alaska earthquake (Stauder and Bollinger, 1966).

P-wave first-motion studies (Perez and Jacob, 1980a) and waveform modelling (Doser and Lomas, 2000) of the 1973 Cross Sound events indicate faulting on a series of low-angle, NW-trending thrusts. Focal depths of ~ 20 km for the mainshock and first aftershock suggest thrusting of the Pacific plate beneath the Yakutat block; a shallower depth (5-10 km) for the second aftershock places it in the upper part of the Pacific plate (Doser and Lomas, 2000). No right-lateral motion along the Transition fault in this region is indicated by these events, although dextral oblique motion has been suggested by some authors (e.g., Lahr and Plafker, 1980; Plafker, 1987; Plafker et al., 1994), and the Transition fault may have originated as a dextral transform fault (Bruns, 1985; see Chapter 2).

Fletcher and Freymueller (1999) argue that as much as 20 mm/yr sinistral-oblique convergence must be occurring across the Transition fault and/or other unrecognized structures offshore to account for the more westward motion of the Yakutat block compared to Pacific/North America motion, as shown by their GPS data. The buoyant continental crust in the eastern part of the Yakutat block resists subduction, and the oblique convergence results in the block being forced to the west.

This counter-clockwise rotation of the Yakutat block is facilitated by dextral motion along the Fairweather fault to the east, and by dextral oblique convergence to the north along the Chugach-St. Elias fault system. To the south, the Transition fault is an obvious candidate to take up relative Pacific-Yakutat motion, but appears to be seismically active only at its southeastern end, accommodating thrusting of the Pacific plate beneath the Yakutat block. If no slip occurs along the western Transition fault, the Pacific-Yakutat relative motion in that region may be accommodated by a combination of E-W to NE-SW convergence within the western Yakutat block (Pamplona fold and thrust belt) and sinistral slip along faults within the Pacific plate sub-parallel to, and outboard of, the Transition fault, for example, the first event in a sequence of earthquakes in the Gulf of Alaska between 1987 and 1992 (Pegler and Das, 1996).

Gulf of Alaska plate-tear earthquakes

A strong linear earthquake sequence ~ 250 km long occurred in the Gulf of Alaska within the Pacific plate starting in 1987. This region had not previously exhibited significant historical seismicity (Figure 4.4). The sequence involved three mainshocks of M_w 7.2, 7.8, and 7.7, respectively, within three months of each other in 1987-1988, and a further M_w 6.8 event in 1992 (Pegler and Das, 1996). These events are among the largest oceanic intraplate earthquakes ever recorded (e.g., Page et al., 1991). The first, smaller event of the sequence involved left-lateral strike-slip motion on an ENE-WSW-trending fault zone; the rupture zone was ~ 40 km long, and the focal depth was ~ 12 km (Pegler and Das, 1996). The later earthquakes of the sequence involved right-lateral strike-slip rupture on a N-S-trending fault zone with a composite length of ~ 250 km; focal depths were ~ 6-13 km (Pegler and Das, 1996).

The N-S trending fault zone corresponds to a magnetic anomaly (13) within the Pacific plate, suggesting the presence of a pre-existing zone of weakness related to the process of plate formation at the ridge (Lahr et al., 1988). The N-S fault zone also aligns with the Pamplona spur at the eastern margin of the Pamplona zone, ~ 50 km to the north (Doser et al., 1997). If the location of the Pamplona spur is controlled by the N-S trending fault zone that produced the Gulf of Alaska earthquakes, this fault zone has likely also been active in the past (Pegler and Das, 1996; Doser et al., 1997). Dextral slip along the N-S zone likely occurs due to the contrast in buoyancy between the westernmost and main eastern Yakutat block, causing more subduction resistance to the east and leading to fragmentation of the Pacific plate in the form of a north-south tear. The 1987-1992 Gulf of Alaska earthquakes may have been triggered by changes in stress seaward of the trench in the wake of the landward Pacific plate motion of the 1964 megathrust earthquake (Lahr et al., 1988; Hwang and Kanamori, 1990).

Southern Alaska Range

A broad swath of seismicity trends north-northeast from northern Cook Inlet to the Denali fault (Figure 4.5). Most events are less than M 5.0, but an M_s 7.3 earthquake in 1943 was located within this band. Seismic-waveform and first-motion analysis of this event along with composite focal mechanisms for a few shallow microearthquakes in 1980 infer thrust faulting with W- to NW-trending P-axes (Page et al., 1991, and references therein).

The ENE-trending Castle Mountain fault passes 40 km north of Anchorage in the southern part of the area (e.g., Labay and Haeussler, 2001; Figure 4.5). This ~ 200-km-long fault was likely the source of an M_s 6.9 event in 1933 (e.g., Page et al., 1991). The

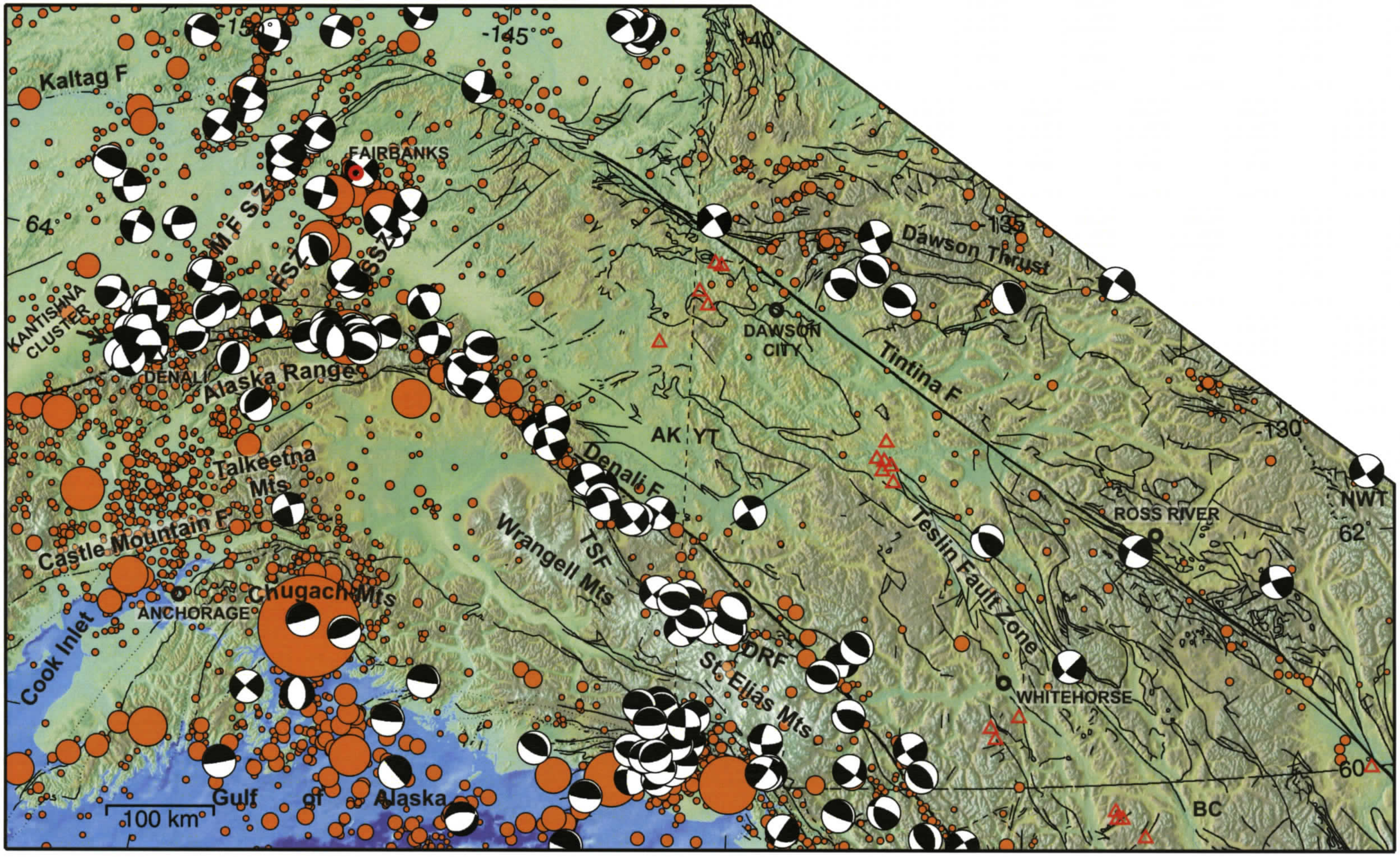

Figure 4.5. Fault traces, seismicity and earthquake mechanisms in the region of the Denali and Tintina fault systems. Earthquake magnitude scale as in Figure 4.2. MFSZ, FSZ, SSZ: Minto Flats, Fairbanks, and Salcha seismic zones; DRF: Duke River fault; TSF: Totschunda fault. Red triangles: location of Neogene-Recent Northern Volcanic Province centres from Edwards and Russell (2000).

1984 M_s 5.2 Sutton earthquake involved dextral slip at 13-20 km depth along a 10-km-long buried segment of the eastern, Talkeetna section of the fault (Lahr et al., 1986). Dextral slip along an ENE-trending fault plane is also inferred by an AEIC moment tensor solution close to the eastern trace of the fault (Figure 4.5). Holocene dextral and northside-up offsets have been documented for the western part of the Castle Mountain fault, and a fault-cored anticline to the north indicates contraction (Haeussler et al., 2000). Right-lateral transpression of this forearc region appears to be accommodating lateral escape to the west and southwest in response to the Yakutat collision (Haeussler et al., 2000).

Wadati-Benioff zone seismicity

The primary focus of this chapter is the crustal seismicity of the North America plate in eastern Alaska and northwestern Canada, generally excluding the Alaska-Aleutian subduction zone. Thus, deep (> 25 km) earthquakes beneath Alaska are excluded from Figures 4.2-4.7, as most of these are associated with the Wadati-Benioff zone of the underthrusting Pacific plate.

Wadati-Benioff zone (WBZ) earthquakes (events within the subducting slab) are associated with both the NE- to N–trending Aleutian volcanic arc and the shorter E-SE trending Wrangell arc to the east (Page et al., 1989; 1991). The Aleutian volcanoes are far more active than the Wrangell volcanoes, which have not been highly eruptive in the past 3 m.y. Wrangell volcanism is believed to have been produced by subduction of the oceanic northwestern part of the Yakutat terrane (Richter et al., 1990; Plafker et al., 1994). Similarly, the Aleutian WBZ is about a hundred times more seismically active than the Wrangell WBZ (Page et al., 1989).

The intense seismicity associated with the Aleutian WBZ shows eastward-shallowing dips and ends abruptly to the east beneath the central Alaska Range along a NNW-trending zone that approximately aligns with the western edge of the Yakutat block. The weaker Wrangell WBZ dips to the NNE below the Wrangell Mountains (Figure 4.4; Stephens et al., 1984). Its geometry is poorly constrained due to a lack of hypocentre locations, but it extends at least 150 km along strike and to depths of at least 100 km (Page et al., 1989). A receiver function analysis by Ferris et al. (2003) beneath the central Alaska Range imaged a 15-km-thick zone that may represent thickened oceanic crust of the Yakutat terrane, which would therefore have a down-dip extent of at least 500 km. Seismicity in the 20-45 km depth range appears to be continuous from the Aleutian WBZ to the Wrangell WBZ, which may represent adjacent limbs of a buckle in the subducted plate (Page et al., 1989). It is uncertain whether the limbs remain continuous at depth, but the apex of the buckle would approximately underlie the apex of the Denali fault through the Alaska Range, and the space problem at depth must contribute to the intense crustal transpression and mountain building in this region.

Denali and Tintina Fault Systems

Denali fault system

Inland of the coast of the Gulf of Alaska, seismicity is concentrated along the Denali fault, a major dextral strike-slip fault that forms a wide arc from a northwesterly trend in SW Yukon and SE Alaska changing through the Alaska Range to an easterly to northeasterly strike in western Alaska (Figure 4.5). Most seismicity occurs along the portion of the fault in eastern Alaska, where slip rates have been estimated at 8-13 mm/yr from dextral offsets of Quaternary deposits (Plafker et al., 1977; Schwartz et al., 2005; Matmon et al., 2006) and GPS data (Fletcher, 2002). The M_w 7.9 dextral strike-slip Denali earthquake (described in more detail below) occurred on this part of the Denali fault and also involved rupture on two subsidiary faults including the Totschunda fault.

Seismicity and Holocene slip rates on the Denali fault decrease to the west (W. Alaska) and to the southeast (Yukon). It appears that the majority of deformation along the main Alaskan portion of the Denali fault is transferred to the Totschunda fault system rather than the eastern portion of the Denali fault in Yukon Territory (e.g., Cassidy et al., 2005). The estimated Holocene slip rate on the Totschunda fault system, which splays to the southeast off the Denali fault, is similar to that on the main part of the Denali fault (~ 9 mm/yr (Schwartz et al., 2005); ~ 6 mm/yr (Matmon et al., 2006)), whereas much lower rates (< 3 mm/yr) are estimated for the Denali fault in Yukon and in easternmost Alaska east of the junction with the Totschunda fault (e.g., Richter and Matson, 1971; Horner, 1983; Plafker et al., 1994).

Prior to the 2002 Denali earthquake, only a low level of seismicity was recorded along the Denali fault (e.g., Ratchkovski et al., 2003). The largest event attributed to the fault was the M ~ 7.2 event in July 1912, discussed below (Doser, 2002). Earthquake focal mechanisms for events along the fault system in interior Alaska indicate dextral slip (Figure 4.5). However, adjacent events to the south and some to the north in the Alaska Range have thrust faulting mechanisms, consistent with a compensating thrust system (positive flower structure) developed in response to the change in fault strike and intense transpression at the apex of the Denali fault (e.g., Ratchkovski and Hansen, 2002; Fisher et al., 2004). For example, moment tensor and aftershock analysis of an M_w 5.8 earthquake in 1996 located ~ 10 km north of the Denali fault in the eastern Alaska Range infers shallow (0-5 km) sinistral-oblique thrust faulting on a low-angle, NW-dipping, NE-trending fault plane ~ 7 km long (Ratchkovski and Hansen, 2002).

One of the largest continental strike-slip earthquakes ever recorded, the M_w 7.9 Denali fault earthquake occurred on 3 November 2002 (e.g., Eberhart-Phillips et al., 2003a). The earthquake triggered landslides along a 30-km-wide zone, caused liquefaction at greater distances, and generated seiches and caused buildings to sway up to 2400 km from the epicentre (Eberhart-Phillips et al., 2003a; Cassidy and Rogers, 2004). Rupture intersected the main 1.2-m-diameter trans-Alaska pipeline from Prudhoe Bay, but the pipeline survived due to its earthquake-resistant design. The earthquake also produced substantial coseismic and postseismic displacements in the surrounding region up to distances of several hundred kilometres, as discussed in Chapter 3 (see Figure 3.10). The mainshock was preceded by the M_w 6.7 Nenana Mountain earthquake on 23 October 2002, which occurred ~ 55 km to the west of the Denali epicentre, with aftershocks extending to within 10 km (Eberhart-Phillips et al., 2003a). The focal mechanism for this foreshock infers pure dextral strike-slip motion along the trace of the Denali fault. Ratchkovski et al. (2003) estimate a focal depth of ~ 8 km for the Nenana Mountain earthquake.

The 3 November event involved a complex sequence comprising three subevents and resulting in 341 km of surface rupture (Eberhart-Phillips et al., 2003a; Figure 3.10, Chapter 3). The Denali earthquake nucleated on one of the compensating thrust faults mentioned above, the previously unrecognized Susitna Glacier fault (e.g., Crone et al., 2005). The *P*-wave first-motion solution for the initial M_w 7.2 subevent indicates slightly dextral-oblique thrusting on a north-dipping ENE-trending plane. The 48° dip of the preferred nodal plane is steeper than the 10-25° surface dip of the fault, suggesting flattening of the fault plane near the surface (Eberhart-Phillips et al., 2003a). Total dip slip on the fault was ~ 3.3 m; 48 km of surface rupture occurred, with vertical displacements up to 5.4 m measured on the main south-directed thrust, and up to 4 m or more on north-directed backthrusts (Eberhart-Phillips et al., 2003a; Crone et al., 2005).

Earthquake slip passed from the Susitna Glacier fault to continue as an eastward-propagating right-lateral rupture along 218 km of the Denali fault, before stepping southeastward, via a 14-km-wide transfer zone of en-echelon fault segments linked by N-striking normal faults, onto the Totschunda fault, where a 66-km-long section of dextral slip followed (Eberhart-Phillips et al., 2003a; Haeussler et al., 2004). Mechanisms for the second and third subevents, both located on the Denali fault, infer pure right-lateral motion on near-vertical planes, although coseismic displacements record a component of northside-up vertical dip slip in some areas (e.g., Hreinsdóttir et al., 2006). Offset across the Denali fault increased from west to east, up to a maximum of 8.8 m dextral slip; maximum slip on the Totschunda fault was 2.1 m (Eberhart-Phillips et al., 2003a; Hreinsdóttir et al., 2006).

The Denali earthquake had a shallow focal depth (4.2 km; Ratchkovski et al., 2003); most coseismic slip was concentrated from the surface to 9 km depth, but rupture may have extended as deep as 24 km (Hreinsdóttir et al., 2006; Freed et al., 2006). The majority of aftershocks occurred at depths shallower than 11 km (Ratchkovski et al., 2003). Most aftershocks are strike-slip events, many mechanisms infer thrust faulting, and a few normal-faulting events are located in the November 3 epicentral region and the Denali-Totschunda transfer zone (Ratchkovski, 2003).

The western, lower-slip part of the 2002 Denali fault rupture may have last ruptured in the M_w 7.2-7.4 Delta River earthquake of 1912 (Page et al., 1991; Doser, 2002; Carver et al., 2004). Trees that sustained damage due to surface rupture in 2002 showed evidence of similar previous damage that was tree-ring-dated to 1912 (Carver et al., 2004). Felt intensity reports from the 1912 earthquake suggest westward rupture propagation (Carver et al., 2004).

Paleoseismic studies by Schwartz et al. (2005) reveal two large pre-2002 events on the Totschunda fault and the main 2002 Denali rupture segment, the most recent of which is dated at 450-650 years ago. Their work also documents three or four paleo-events on the Denali fault segment just to the east of the Totschunda junction; the most recent shows an offset of 1.5 m and probably occurred after the penultimate event on the fault segment to the west. Offsets of up to 4 m are documented for the most recent event on the Denali fault segment located west of the western end of the 2002 rupture (Schwartz et al., 2005). Preliminary paleoseismic studies along the Susitna Glacier fault suggest that recurrence times are an order of magnitude greater than those on the Denali fault (Crone et al., 2005).

As mentioned above and in Chapter 2, Holocene dextral displacements on the Denali fault decrease east of the intersection with the Totschunda fault to near-zero in Yukon (e.g., Richter and Matson, 1971), although Clague (1979) found evidence for limited Holocene dip-slip motion. The lack of Holocene activity is reflected in the lack of historical earthquakes on the northwesternmost 100-km section of the Denali fault in Yukon (Figure 4.5). Only a few events greater than M 3.0, and none over M 4.0, have been located along this segment. However, seismicity increases further to the southeast in the region where the Duke River fault is closest to the Denali fault, and to the northeast of that region (Figure 4.5). Several M 5+ earthquakes have been located in this area. A composite mechanism of microseismicity in this region infers either dextral strike-slip on a N-S-oriented plane or sinistral motion on an E-W-trending plane, neither of which align with the Denali fault (Horner, 1983). Focal mechanisms to the north and south of the Denali fault trace infer low-angle thrusting on WNW- to NW-trending planes. These solutions are consistent with NNE- to NE-directed transpression across the Denali fault in SW Yukon.

A concentration of seismicity, with earthquakes up to M 6+, occurs in the vicinity of the westernmost extent of the Duke River fault and the southeasternmost extent of the Totschunda fault (Figure 4.5). This seismic cluster appears to be linked to the most active portion of the Denali fault system in Yukon Territory mentioned above (Figure 4.5). Earthquake mechanisms are dominated by thrusting on WNW- to NW-trending planes and probable dextral slip on NW- to NNW-trending planes. The Totschunda fault between this cluster and the southernmost extent of the 2002 Denali earthquake rupture has little recorded historical seismicity, but a N-S trending band of seismicity along the Yukon/Alaska border appears to link the southern cluster with the easternmost Alaskan segment of the Denali fault. Likewise, a diffuse band of seismicity across the Saint Elias Mountains may provide a link to the Fairweather fault and the collision zone to the south (e.g., Lahr and Plafker, 1980).

Tintina fault

The NW-trending Tintina fault in Yukon Territory and easternmost Alaska is characterized by a slight linear concentration of low-level seismicity (up to ~ M 5.0; Figures 4.2, 4.5). Two moment tensor solutions have been determined along the fault in Yukon and one *P*-wave first-motion solution is available along its apparent extension in eastern Alaska (Figure 4.5). The two Yukon events have estimated focal depths of ~ 12 km.

All three focal mechanisms are similar and imply strike-slip motion along near-vertical fault planes. Either right-lateral motion along NW-SE-oriented planes or left-lateral motion on NE-SW-trending planes is inferred. The dextral mechanisms are consistent with both the strike of the Tintina fault and its inferred historical motion (e.g., Gabrielse, 1985). However, sinistral motion on the NE-SW-trending planes may be equally plausible, at least for the two northern events. The Alaskan event aligns with a NE-SW-trending sinistral fault zone in the Fairbanks region to the southwest, while the Yukon/Alaska border event is located in a region where late-stage NE-SW-trending lineaments have been found to cross-cut the Tintina fault zone (Mortensen and Von Gaza, 1992). However, the southernmost event (near Ross River; Figure 4.5) occurred in an area dominated by NW-SE-trending strands of the Tintina fault system that do not appear to be cross-cut by orthogonal faults; dextral motion is thus more likely here.

West- and south-central Yukon and easternmost interior Alaska

The region between the Denali and Tintina faults in Yukon and easternmost Alaska is characterized by sparse seismicity (Figure 4.5). The largest recorded earthquake was an M_w 5.2 northwest of Whitehorse in 1990, but catalogue events do not generally exceed M 4.0. Moment tensor solutions are available for two events east and north of Whitehorse, with estimated focal depths of 6 and 9 km, respectively (Ristau, 2006). Strike-slip faulting is indicated for the southern event: either dextral slip on a NW-SE-trending plane or sinistral motion on a NE-SW-striking fault plane. The mechanism for the earthquake north of Whitehorse infers low-angle oblique thrust faulting on either a NE- or SW-dipping plane.

The epicentres of these two events, along with others nearby, appear to align on the NW-SE-trending Teslin fault zone (Figure 4.5), which was active as a terrane-bounding, right-lateral, west-over-east transpressive fault during the Late Triassic to mid-Jurassic (Hansen, 1986). NNW-trending surface metamorphic foliation dips steeply to the west in the western part of the fault zone, flattening eastwards (Hansen, 1986), but seismic reflection data suggest that the fault dips to the northeast and soles into a mid-crustal detachment (Snyder et al., 2005). Based on the fault history, the preferred mechanisms are NE-directed dextral-oblique thrusting for the northern event, and NW-SE dextral strike-slip for the southern earthquake. It is likely that the Teslin fault zone has been reactivated under the current stress regime, which has exploited its favourable alignment for NE-SW transpression.

An AEIC moment tensor solution is available for an earthquake near the Yukon/Alaska border ~ 50 km NE of the Denali fault. Strike-slip faulting on a near-vertical NE- or NW-striking plane is inferred. The NE-trending nodal plane aligns with a NE-trending mapped fault on which the epicentre appears to lie; thus NE-SW right-lateral motion is inferred. This mechanism is different from any others nearby. Further to the northwest in Alaska, similar mapped and inferred NE-trending faults show evidence of NE-SW left-lateral strike-slip faulting; the Yukon mechanism thus shows opposite motion.

A number of Neogene to Recent volcanic centres of the Northern Cordilleran Volcanic Province (NCVP; Edwards and Russell, 1999) are found between the Denali and Tintina faults in Yukon and easternmost Alaska (red triangles in Figure 4.5; see Chapter 2). These centres do not appear to have any associated detectable seismicity. A region of unusually hot asthenosphere has been detected by seismic tomography beneath the area (Frederiksen et al., 1998). The possibility of particularly high crustal heat flow in the volcanic centre localities could explain the conspicuous absence of even low-level seismicity. Heat flow measurements have been made at several nearby sites (Lewis et al., 2003). One measurement in the direct vicinity of the northern BC volcanic centres records high heat flow (98 mW/m^2). Heat flow data are not available in the immediate localities of the other centres, but measurements ~ 40 km north of the southern Yukon group and ~ 70 km west of the west-central Yukon (Fort Selkirk) volcanics infer lower heat flow (60 and 86 mW/m^2, respectively). A 3-month microseismicity study of Mount Edziza, an NCVP centre in northwestern British Columbia (~ 58°N), measured only ~ 20 small earthquakes in the vicinity of the volcano (Milne et al., 1970).

East-central Alaska

In contrast to the low seismicity of west-central Yukon and easternmost Alaska described above, the area between the Denali and Tintina-Kaltag fault systems in east-central Alaska is highly seismically active, with at least three M 7+ earthquakes in the 20th century (Figure 4.2).

Seismicity in the region defines a series of NNE-trending lineations, from west to east: the Minto Flats (MFSZ), Fairbanks (FSZ) and Salcha (SSZ) seismic zones (Figure 4.5; e.g., Biswas and Tytgat, 1988). These lineaments have not been associated with mapped faults, mostly due to the surface cover of loess and vegetation (e.g., Page et al., 1995). However, several NE-striking faults have been mapped further to the southeast, and show evidence of late Cenozoic, possibly Holocene displacement (Page et al., 1995). Seismicity in the vicinity of the seismic zones is fairly diffuse, suggesting the presence of overlapping sub-parallel faults and splays (e.g., Ratchkovski and Hansen, 2002).

An M_s 7.3 earthquake in 1904 and a pair of M_s 6.3-6.5 earthquakes in 1929 have been located in the general region between the Tintina and Denali fault systems in Alaska, but cannot be linked to specific seismic zones due to their large location uncertainties (Page et al., 1995). The first seismograph in mainland Alaska (College, Figure 4.1) was not installed until 1935.

The Salcha seismic zone is characterized by a ~ 60-km-long NNE-trending band of epicentres. An M_s 7.3 event occurred within this zone in July 1937. A *P*-wave first-motion solution from Wickens and Hodgson (1967) infers left-lateral strike-slip motion on a steep NNE-trending fault. This is in agreement with the mechanism determined from body-wave modelling by Fletcher and Christensen (1996), who calculated that the event had a moment magnitude of M_w 7.2, a shallow focal depth (1-10 km), and a displacement of ~ 3 m, and that it may have ruptured the whole extent of the SSZ.

Three earthquakes (M_s 5.5-5.9) occurred within several minutes in June 1967 in the Fairbanks seismic zone ~ 20 km SE of Fairbanks. A *P*-wave first-motion solution for the first event (M_s 5.6; Gedney, 1970) indicates nearly pure strike-slip faulting on either a NE- or NW-striking steep fault plane. The pattern of aftershock hypocentres, which extend to ~ 20 km depth, provides the preferred mechanism of sinistral strike-slip motion on a NE-trending plane (Matumoto et al., 1968). An M_s 7.2 (M_w 7.1) event in October 1947 has also been linked to the FSZ (e.g., Page et al., 1995; Fletcher and Christensen, 1996); a poorly-constrained focal mechanism solution indicates low-angle thrusting on a NW-striking, NE-dipping plane (Wickens and Hodgson, 1967). A similar focal mechanism was determined from body-wave modelling, which allowed estimation of the focal depth (1-10 km), displacement (up to 5 m), and rupture length (~ 30 km) (Fletcher and Christensen, 1996). Approximately 5-6 felt earthquakes occur per year in the FSZ, along with periodic swarms of intense, migratory microearthquake activity (Biswas and Tytgat, 1988).

The Minto Flats seismic zone is the longest and most coherent of the three zones, extending from the Kantishna seismic cluster in the south to the Kaltag fault system in the north (Figures 4.2, 4.5; Ratchkovski and Hansen, 2002). The most active part of the MFSZ coincides with a 20-km-long zone of scarps that have been interpreted as a fault that was active as late as the Holocene, but may represent terraces of the Nenana River rather than paleoseismic features (Page et al., 1991; 1995).

An earthquake of M_w 6.0 occurred in October 1995 in the northern part of the MFSZ, ~ 50 km NW of Fairbanks. A moment tensor solution for the event and the aftershock distribution imply left-lateral motion on a high-angle NNE-trending plane (Ratchkovski and Hansen, 2002). The focal depth for the mainshock is estimated at ~ 12 km, while the aftershocks extended from the surface to ~ 20 km depth (Ratchkovski and Hansen, 2002). A pair of earthquakes (M_w 5.6 and 5.3) occurred in the southern part of the MFSZ within 40 seconds of each other in November 2000. The preferred mechanisms for both events indicate sinistral strike-slip motion on a N-trending plane; Ratchkovski and Hansen (2002) note a change in fault plane orientations along the MFSZ from NNE-SSW north of 64° to N-S to the south. The estimated mainshock focal depth is ~ 20 km, with the aftershock zone extending from 5 to 45 km depth, although few earthquakes in the source region had been located below 20 km prior to the 2000 sequence (Ratchkovski and Hansen, 2002).

Page et al. (1995) propose a block rotation model whereby the set of NE-trending seismic zones and sub-parallel Cenozoic faults bound a number of crustal blocks up to 250 km long and ~ 20-50 km wide between the Denali and Tintina fault systems in east-central Alaska. Sinistral slip between the blocks ("bookshelf" faulting) facilitates clockwise rotation of the blocks to accommodate transpressional shortening across a broad dextral shear zone in response to NNW-directed compression transmitted from the Yakutat collision zone.

As mentioned in Chapter 2, apparent sinistral offsets of the frontal eastern Alaska Range are possible evidence that such block faulting has occurred on the mapped faults to the southeast of the currently active seismic zones. However, very little seismicity is currently associated with these mapped faults. It is possible that the apex of the Denali fault (and therefore of the Alaskan orocline) has migrated northwestwards to its current position as crustal material has been transferred along the Denali fault system from the collision zone to the southeast (e.g., Redfield and Fitzgerald, 1993). Thus, the blocks in easternmost central Alaska may have been formerly located within the orocline apex, and therefore the focus of intense transpression across the Denali-Tintina dextral shear zone at that time, a focus that has since shifted to the northwest. An implication of this idea is that the presently active seismic zones may be relatively new features.

The Kantishna seismic cluster, located just north of the Denali fault on the northwestern side of the apex, is the most active crustal seismic source in interior Alaska (Figure 4.5). The analysis of Ratchkovski and Hansen (2002) provides detailed characterization of Kantishna seismicity as follows. Most earthquakes in the cluster are located within the upper 20 km of the crust; however, a vertical lineation of events in the western part appears to extend to ~ 50 km depth, greater than the presumed 40-km crustal thickness in the area. Events in the northern part of the Kantishna cluster define a NE-SW band of seismicity, where focal mechanisms indicate both thrust faulting on NE-trending planes and strike-slip faulting with a significant reverse component. Seismicity in the southern Kantishna cluster is aligned WNW-ESE and most earthquake mechanisms are consistent with right-lateral slip on a NW-trending fault.

Composite stress directions calculated by Ratchkovski and Hansen (2002) show that the principal stress orientation within east-central Alaska rotates around the bend in the Denali fault (Figure 4.3). The principal stress across the Kantishna seismic cluster is oriented WNW-ESE to NW-SE. Within the area between the Denali and Tintina/Kaltag faults west of the Minto Flats seismic zone (between ~ 150 and 154°W), the composite stress direction is NW-SE. For the MFSZ, it becomes N-S, and for the area east of the MFSZ (between ~ 145 and 148°W), the composite stress is oriented NNE-SSW. The composite stress direction thus remains approximately orthogonal to the trend of the Denali fault around its apex, consistent with crustal material to the south of the bend in the Denali fault acting as a local point source indenter.

Eastern Foldbelt

Mackenzie and Selwyn Mountains

On the northeastern side of the Canadian Cordillera, significant seismicity occurs in the Mackenzie Mountains, concentrated 50 to 150 km west of the main thrust deformation front (Figure 4.6). Most earthquakes exhibit thrust mechanisms, although some strike-slip events have also occurred (e.g., Horner et al., 1990). Nodal planes are parallel to local geological structures, oriented N-S in the southern Mackenzie Mountains and NW-SE in the north (e.g., Cassidy et al., 2005). This change in orientation of structures and earthquake mechanisms is reflected in the composite stress orientation, which changes from ENE-WSW in the south (Nahanni region; poorly constrained) to NNE-SSW in the central and northern Mackenzie Mountains (Figure 4.3; Ristau, 2004; Hyndman et al., 2005a; Ristau et al., 2006).

The southern Mackenzie Mountains were the site of two of the largest recorded earthquakes in the northern Canadian Cordillera, the M_w 6.6 and 6.8 Nahanni earthquakes of October and December 1985, respectively (Weichert et al., 1986; Wetmiller et al., 1988; Horner et al., 1990). These earthquakes were felt at distances of over 1500 km, and

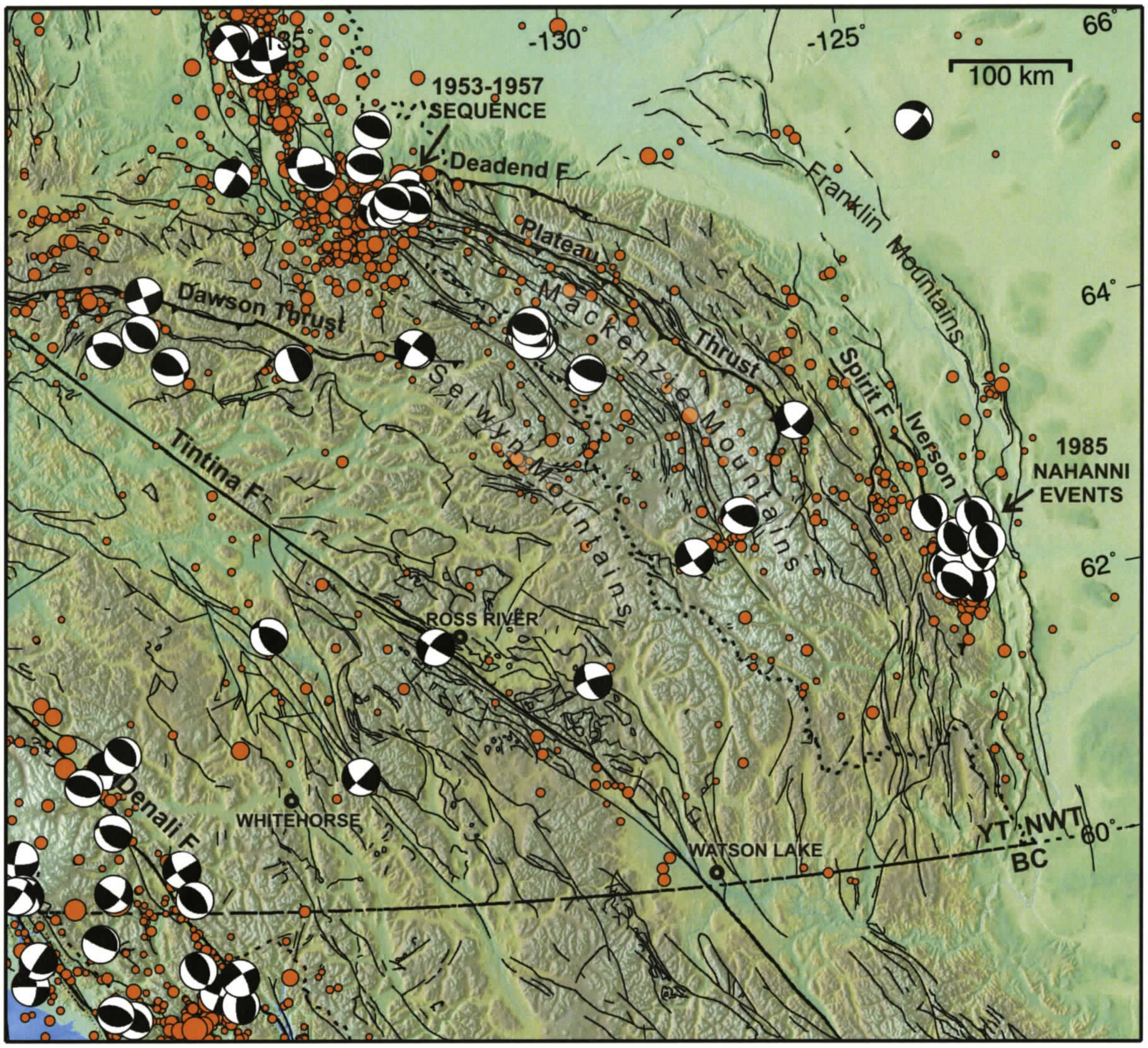

Figure 4.6. Fault traces, seismicity, and earthquake mechanisms in the eastern foreland belt (Mackenzie Mountains). Earthquake magnitude scale as in Figure 4.2.

were followed by thousands of aftershocks, some of which were recorded with temporary deployments of portable instruments (Wetmiller et al., 1988; Horner et al., 1990).

The two main events occurred within ~ 3 km of each other; both show pure thrust mechanisms on low-angle (25-35°), W-dipping planes (Wetmiller et al., 1988). Focal depths of both mainshocks are estimated at 6 km, with aftershocks between 4 and 10 km depth (Horner et al., 1990). Local mapped faults, including the Iverson thrust (Figure 4.6), do not appear to have been involved in aftershock activity, and no surface rupture was found; the Nahanni events are interpreted as occurring on a blind thrust fault of Late

Cretaceous/Early Tertiary age within the Proterozoic and Paleozoic sedimentary rocks above the crystalline basement (Wetmiller et al., 1988; Horner et al., 1990). Most aftershocks show thrust mechanisms similar to those of the mainshocks; however, some aftershocks to the south of the December event exhibit strike-slip mechanisms, with both left- and right-lateral motion on NW-SE-striking nodal planes (Horner et al., 1990). These strike-slip aftershocks appear to have occurred on subsidiary high-angle rupture zones that developed during or after the December mainshock (Horner et al., 1990).

Large earthquakes have also been recorded in the northern Mackenzie Mountains. A large concentration of seismicity occurs in the northwesternmost part of the Mackenzie Mountains, where the intersection of the Richardson fault array with the fold and thrust belt is reflected in a mixture of thrust and strike-slip focal mechanisms (Figure 4.6). Five events of magnitude 5.5-6.5 occurred between 1953 and 1957 (Cassidy et al., 2002; 2005). Focal mechanisms determined from body-wave modelling indicate thrust faulting on low-angle (30-40°) NNE-dipping planes; focal depths are estimated at 9 to 15 km (Cassidy et al., 2002). The epicentres are distributed over a distance of ~ 45 km; the first events occurred in the ESE, with activity then migrating to the WNW (Cassidy et al., 2002).

Seismicity extends westwards from the Mackenzie Mountains into the northern Selwyn Mountains, but is very sparse in the southern Selwyn Mountains and almost completely dies out south of the Mackenzie Mountains into northern British Columbia (Figures 4.2, 4.6). The only two focal mechanisms available in the northern Selwyn Mountains, from a pair of closely-located events in November 1997 (M_w 4.4 and 4.7), indicate near-vertical strike-slip faulting. These events are located just north of the surface trace of the Dawson thrust fault at its eastern mapped extent and are discussed in the section below.

Dawson thrust fault

Seismicity (up to ~ M 5.0 in the catalogue) occurs both to the north and south of the Dawson thrust fault in west-central Yukon Territory (Figure 4.7). No focal mechanisms have been determined for the southern Ogilvie Mountains north of the Dawson thrust. Four moment tensor solutions to the south of the surface fault trace

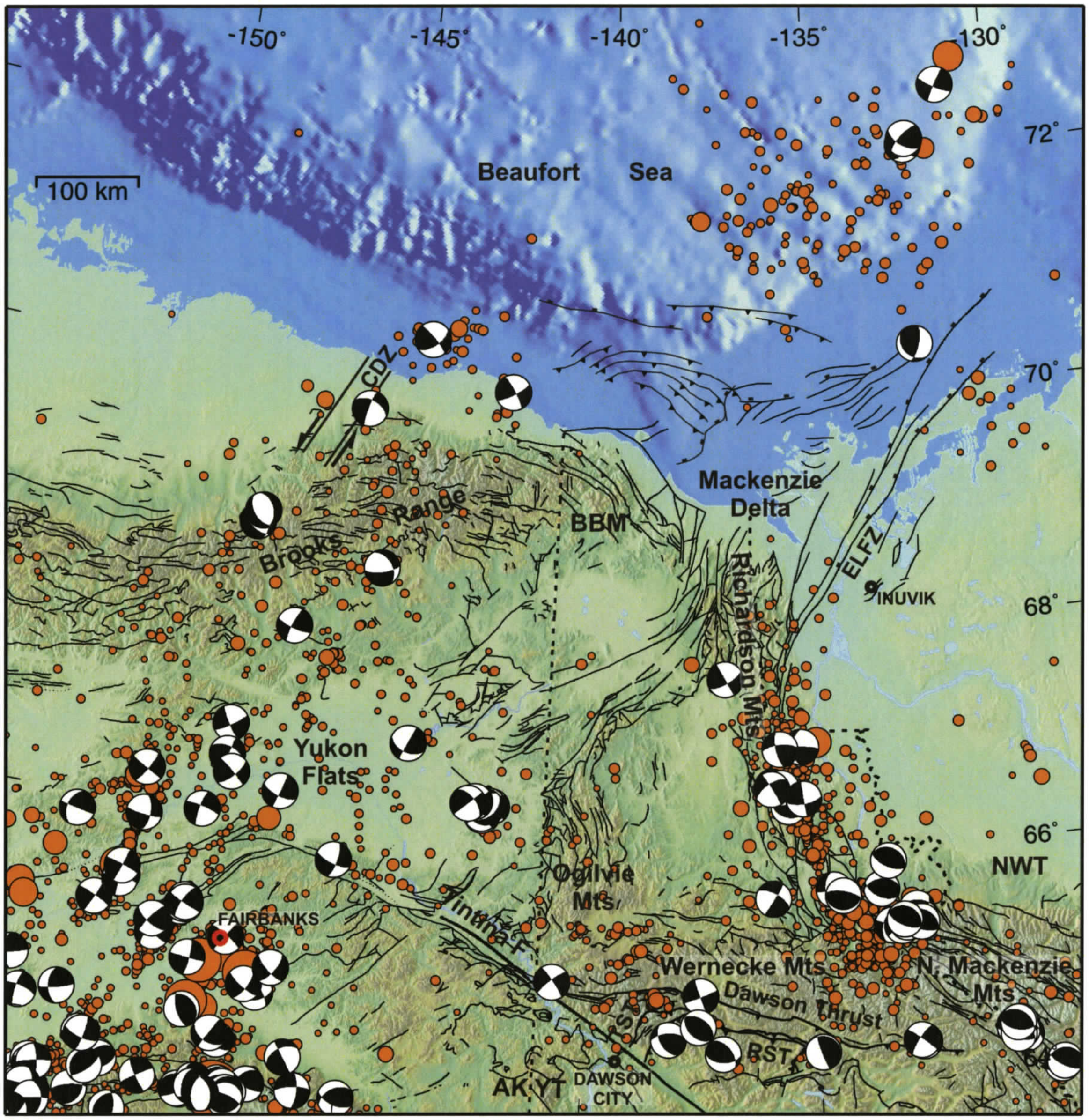

Figure 4.7. Fault traces, seismicity and earthquake mechanisms in the northernmost Cordillera, including the Richardson Mountains, the Beaufort-Mackenzie foldbelt, and the Brooks Range. BBM: British-Barn Mountains; CDZ: Canning displacement zone, from Grantz et al. (1983); ELFZ: Eskimo Lakes fault zone; RST: Robert Service thrust; TST: Tombstone thrust.

indicate thrust faulting on E-W to NW-SE-oriented planes, and four solutions close to the surface trace indicate either NW-SE dextral motion or NE-SW sinistral motion on near-vertical fault planes (Figure 4.7). All eight events have estimated focal depths between 3 and 12 km.

The low-angle thrust mechanisms likely imply NE-directed motion on the Dawson, Tombstone or Robert Service thrust faults, or on a basal detachment; post-91 Ma tilting and northward displacement is inferred by paleomagnetic data from a pluton within the Dawson thrust sheet (Symons et al., 2006). The two easternmost strike-slip earthquakes are located in the northern Selwyn Mountains. The preferred mechanism is right-lateral motion on NW-SE-striking planes due to the dominant NW-SE structural grain in the area and the location of the events south of similar inferred mechanisms in the Richardson Mountains (Figure 4.7). The westernmost strike-slip event is located close to the Tintina fault and may reflect NE-SW dextral strike-slip motion on the Tintina fault system itself. Alternatively, left-lateral motion on a NE-SW-trending fault plane is possible; late-stage NE-SW-trending lineaments cut across the Tintina fault in that region (Mortensen and Von Gaza, 1992).

Northernmost Cordillera

Richardson Mountains

North of the Mackenzie Mountains, the composite stress direction changes to NE-SW in the Richardson Mountains, where a N-S-trending belt of seismicity is characterized by mechanisms with probable right-lateral strike-slip motion on N-S-trending fault planes (Figures 4.3, 4.7). The highest concentration of seismicity occurs in the southern Richardson Mountains (south of ~ 67°N), decreasing to the north. Some minor seismicity appears to follow part of the Eskimo Lakes fault zone to the northeast.

The two largest recorded earthquakes in the Richardson Mountains, M_w 6.3 and 6.6, occurred in May and June 1940, respectively. Teleseismic- and body-wave modelling by Cassidy and Bent (1993) reveals that both earthquakes involved a complex rupture consisting of two to three subevents. In each case, rupture appears to have propagated upwards, from 14.5 to 11 km in the May event, and from 10 to 7 km in the June event. Focal mechanisms for both events determined from body-wave modelling are interpreted as right-lateral strike-slip motion on steeply W-dipping, N-S-trending planes (Cassidy and Bent, 1993). The June event occurred ~ 20 km west of the May event, and the second and third June subevents show an east-west separation of ~ 15 km; rupture may have been triggered on nearby strands of the fault system (Cassidy and Bent, 1993).

A microearthquake study of the Richardson Mountains region involving six seismograph stations was carried out over six weeks in 1972 (Leblanc and Wetmiller, 1974). Focal depths for the 27 located events (local magnitude $M_L > 1.2$) are poorly constrained, but most events were estimated to occur in the upper 20 km of the crust, with a few up to 26 km depth. The occurrence of a larger earthquake (m_b 4.8) during the survey in July 1972 allowed the estimation of a poorly-constrained focal mechanism solution from *P*-wave first motions; right-lateral motion on a near-vertical NNW-trending plane is implied (Leblanc and Wetmiller, 1974), consistent with the 1940 event mechanisms. The focal depth was estimated at 26 km, with subsequent aftershocks showing an apparent shallowing trend implying upward-propagating rupture as interpreted for the 1940 events (Leblanc and Wetmiller, 1974; Cassidy and Bent, 1993).

Beaufort-Mackenzie region and eastern Brooks Range

A large concentration of seismicity occurs beneath the continental slope of the Beaufort Sea (Figure 4.7), coinciding with a positive free-air gravity anomaly on the seaward side of the transition from continental to oceanic crust (e.g., Basham et al., 1977; Stephenson et al., 1994). The Beaufort Sea earthquakes have poorly-constrained hypocentres, especially depth, due to sparse network coverage, but are thought to occur in the lower crust or upper mantle, at depths of ~ 40 km (Hasegawa et al., 1979). The three largest recorded events have magnitudes of 6.5 (1920), 5.5 (1937) and 5.1 (1975). The few focal mechanisms available from first-motion studies indicate both normal and strike-slip components of motion on steeply-dipping faults (Figure 4.7; Hasegawa et al., 1979). Near-horizontal tension axes lead to the interpretation that the events are caused by tension normal to the margin, probably due to flexure in response to loading under the thick pile of Mackenzie Delta sediments (Hasegawa et al., 1979; Hyndman et al., 2005c).

Such margin-normal tension is in contrast to the ~ N-S compressional seismicity further to the south in northern Yukon, which suggests northward strain transfer of a few mm/yr, as also indicated by campaign GPS results (Chapter 3). A gap in seismicity occurs in the Mackenzie Delta region between the Richardson Mountain earthquakes and the Beaufort Sea cluster. Hyndman et al. (2005c) suggest that N-S shortening in this region is probably taken up aseismically; ductile deformation is expected within the relatively incompetent deltaic sediments and at the probable high temperatures of the thickly sediment-covered basement beneath. However, they also state that the possibility of infrequent large thrust earthquakes cannot be excluded.

The eastern Brooks Range of northern Alaska is characterized by evenly-distributed, relatively weak seismicity that extends to the Fairbanks region in the south and slightly offshore to the north (cluster described below), but appears to be abruptly truncated to the east about 50 km west of the Yukon border (Figure 4.7). Thus, the British-Barn Mountains of northern Yukon are practically historically aseismic. Two focal mechanisms are available for events on the southern margin of the Brooks Range. A *P*-wave first-motion solution from Estabrook et al. (1988) infers oblique normal faulting on an E-W-striking, steeply-dipping fault plane. An alternate solution for this event indicates either SE- or WSW-directed oblique shallow thrusting, but Estabrook et al. (1988) favour the E-W plane of the normal solution as it mirrors the local structural grain. An AEIC moment tensor solution for a 2004 M_w 4.0 event further to the southwest infers strike-slip faulting on a NNE- or WNW-trending plane at ~ 5 km depth. The preferred mechanism is left-lateral strike-slip motion on the NNE-trending plane, similar to a number of events further to the south in the Yukon Flats region (discussed below).

Three AEIC moment tensor solutions are also available for events on the northern margin of the eastern Brooks Range (Figure 4.7). In August 2003, an M_w 5.3 earthquake occurred at ~ 10 km depth, and was followed 25 hours later by another M_w 5.3 event at approximately the same location and depth. Focal mechanisms for both events indicate low-angle extensional faulting on a NE- or SW-dipping, NW-striking plane. The moment tensor solution for a February 2006 M_w 4.6 earthquake located further to the northeast is consistent with strike-slip faulting on either a vertical NNE-trending or a N-dipping WNW-trending plane.

A small cluster of earthquakes occurs along the eastern Alaskan Beaufort Sea coastline, both onshore and offshore, as an extension of the NE Brooks Range seismicity (Figure 4.7). Estabrook et al. (1988) provide two *P*-wave first-motion solutions, one of which indicates strike-slip faulting on either a NE- or a NW-striking fault plane. The other mechanism (further offshore) for an M_s 4.9 event in January 1968 has both strike-slip and normal components, with a P-axis that is rotated 90° from the former event

(Estabrook et al., 1988). However, Biswas et al. (1986) determined a different focal mechanism for this earthquake, which they interpret as left-lateral strike-slip on a NE-SW-oriented plane with a significant dip-slip component.

Biswas and Tytgat (1988) note that the latter mechanism is consistent with both the orientation and the sense of displacement inferred for the Canning displacement zone, identified by Grantz et al. (1983; Figure 4.7). Page et al. (1991) note that the broad band of seismicity that runs offshore from the NE Brooks Range appears to be bounded on the west by the Canning displacement zone, a young, mainly sinistral strike-slip shear zone that facilitates northward and upward movement of the NE Brooks Range relative to the lowland to the west. The 2006 event on the northern margin of the Brooks Range also aligns with this zone, and its NNE-trending nodal plane is consistent with left-lateral motion. The mixture of extensional and strike-slip earthquake mechanisms suggests that this region is undergoing ~ NE-SW transtension, in contrast to the region to the south (east-central Alaska), where the seismicity implies transpression. A transtensional regime is also indicated to the southwest in west-central Alaska, as discussed below.

North-central Alaska: Yukon Flats

The Yukon Flats lowland area, south of the Brooks Range and north of the Yukon-Tanana upland, is the site of generally dispersed seismicity with events up to magnitude 6.5 (Figures 4.2, 4.7). The composite stress direction for events in this region is oriented NNW-SSE (Figure 4.3; Ratchkovski and Hansen, 2002).

The M_s 6.5 October 1968 Rampart earthquake occurred in the southern part of the area in the vicinity of the Kaltag fault, causing landslides and ground fissures (Biswas and Tytgat, 1988). A *P*-wave first-motion solution by Huang and Biswas (1983) infers strike-slip motion on a near-vertical plane trending either WNW or NNE. Aftershocks delineate a 50-km-long NNE-trending near-vertical plane extending from the surface to ~ 35 km depth, with most events concentrated in the upper 15 km (Biswas and Tytgat, 1988). Thus, left-lateral motion on a NNE-trending plane is inferred.

The 1985 Dall City earthquakes occurred ~ 100 km north of the Rampart event. An earthquake of M_s 5.4 in February 1985 was followed 3 weeks later by an M_s 6.0 event. The aftershocks define an elongate near-vertical zone sub-parallel to the Rampart aftershock zone and extending from 0 to 20 km depth (e.g., Biswas and Tytgat, 1983). A *P*-wave first-motion solution for the second event infers a sinistral mechanism on a NNE-trending plane similar to that of the Rampart earthquake and to other nearby events (Estabrook et al., 1988). It appears that the left-lateral strike-slip regime between the Denali and Tintina-Kaltag faults continues to the north.

A moment tensor solution is available for an M_w 4.3 earthquake that occurred in May 1997 at ~ 3 km depth in the eastern part of the Yukon flats area ~ 60 km west of the Yukon border (Ristau, 2004). Strike-slip motion on a near-vertical NW- or NE-trending plane is indicated. The preferred mechanism is left-lateral slip on the NE-trending nodal plane, consistent with the strike of mapped faults to the north and south and with the Rampart and Dall City mechanisms 200 km to the west (Figure 4.7). An M_w 5.4 earthquake occurred at almost the same location in February 2006, followed several hours later by an event of M_w 5.1. AEIC moment tensor solutions for these events, and for an M_w 4.0 aftershock two days later, are almost identical to that for the 1997 event. Focal depths are estimated at 5-10 km.

West-central Alaska

Dispersed seismicity continues to the west of the Yukon Flats region between the Kaltag fault and the Brooks Range, generally with magnitudes $\leq$ 5.0. However, ~ 300 km to the west of the Rampart-Dall City area, a series of larger events occurred in 1958. The April 7 M_s 7.3 Huslia earthquake was followed by two M 6+ aftershocks within a week, including the M_s 6.8 event of April 13. Body-wave modelling of the mainshock confirmed an earlier focal mechanism indicating extensional faulting on a NE-trending plane (Fletcher and Christensen, 1996). The mechanism has a near-vertical compressional (P-) axis and a near-horizontal NW-SE-oriented tensional (T-) axis. The most severe damage from the earthquake occurred over a 16-km-wide 64-km-long NE-trending zone (Davis, 1960). Fletcher and Christensen (1996) estimate the focal depth of the event at 2-8 km. Other focal mechanisms in the area indicate either normal or strike-slip faulting. The overall stress regime in this part of western Alaska is apparently one of NW-SE-oriented transtension.

SEISMIC DEFORMATION RATES

Current crustal deformation rates can be calculated from seismicity statistics, assuming that most of the deformation is taken up seismically, and that the frequency of earthquakes does not change with time (e.g., Hyndman et al., 2003). In this study, seismic deformation rates are calculated for various parts of the region in Yukon and adjacent Northwest Territories and Alaska. Since the calculated deformation rate is averaged over the zone, each zone selected is assumed to be characterized by a similar rate of seismicity and by a similar set of faulting mechanisms. It is also assumed that there are no "characteristic earthquakes", i.e., no infrequent large events where no or little ongoing smaller-magnitude seismicity occurs. The method used to estimate the deformation rate of each zone is described below, and is based on studies by Hyndman and Weichert (1983), Mazzotti and Hyndman (2002), Hyndman et al. (2003), Mazzotti and Adams (2005), and Willoughby and Hyndman (2005).

Seismic Deformation Rate Estimation

The catalogue seismicity from the area of interest is plotted as magnitude versus cumulative frequency of occurrence. It is assumed that (1) the seismicity follows the Gutenberg-Richter recurrence relation (e.g., Anderson, 1979) up to an estimated maximum magnitude, (2) the recurrence relation is a valid representation of the observed seismicity, and (3) the seismicity statistics of the area are constant over time. The density recurrence function is:

$$\begin{aligned} n(M) &= N_0 \exp(-\beta M)\,[1-\exp(-\beta(M_x - M))] && M < M_x \\ n(M) &= 0 && M \geq M_x \end{aligned}$$

where β is the density recurrence coefficient and M_x is the maximum magnitude (e.g., Mazzotti and Adams, 2005)).

The magnitude-frequency of occurrence incorporates the magnitude intervals of completeness (Weichert, 1980). Larger magnitude earthquakes can be included from a longer time period than smaller ones, and a larger magnitude completeness cut-off must be applied for earlier time periods when there were fewer seismic stations, as only some of the events at smaller magnitudes will be detected.

The maximum magnitude, M_x, and the form of the recurrence curve approaching it, must be estimated. This is important, as the majority of the moment is contributed by the larger magnitude events. In this study, M_x is taken to be an abrupt truncation in the density function, and the cumulative recurrence curve falls off smoothly towards M_x (Hyndman and Weichert, 1983). The catalogue seismicity must be extrapolated to a maximum expected magnitude using the statistics of the smaller earthquakes. The largest earthquakes have a large recurrence interval and thus the average occurrence is poorly constrained at larger magnitudes for which there are few, if any, events in the catalogue. M_x may be predicted by calculating the magnitude of an earthquake on the largest fault in the area; M_x is estimated from the fault area, and an empirical relation between fault area and magnitude determined by Wells and Coppersmith (1994):

$$\mathrm{M} = x + y \log A$$

where x and y are constants, and A is the rupture area. From their data compilation, for strike-slip faults, x is 3.98 and y is 1.02; for reverse faults, x is 4.33 and y is 0.9, and for all faults in general, x is 4.07 and y is 0.98.

Seismic moment rate

The seismic moment contributions for each magnitude are integrated up to the assumed maximum magnitude M_x. This requires that the magnitudes be converted to seismic moments. The moment-magnitude relation is assumed to be deterministic, with moment M_o given by the relation:

$$\log \mathrm{M_o} = c + d\,\mathrm{M}$$

where c and d are constants defined by the M-M_o relation (e.g., Hanks and Kanamori, 1979). Figure 4.8 shows the M_L-M_o relation determined for events in the region (Ristau, 2004; Hyndman et al., 2005a). Within the confidence limits, this relation agrees with the

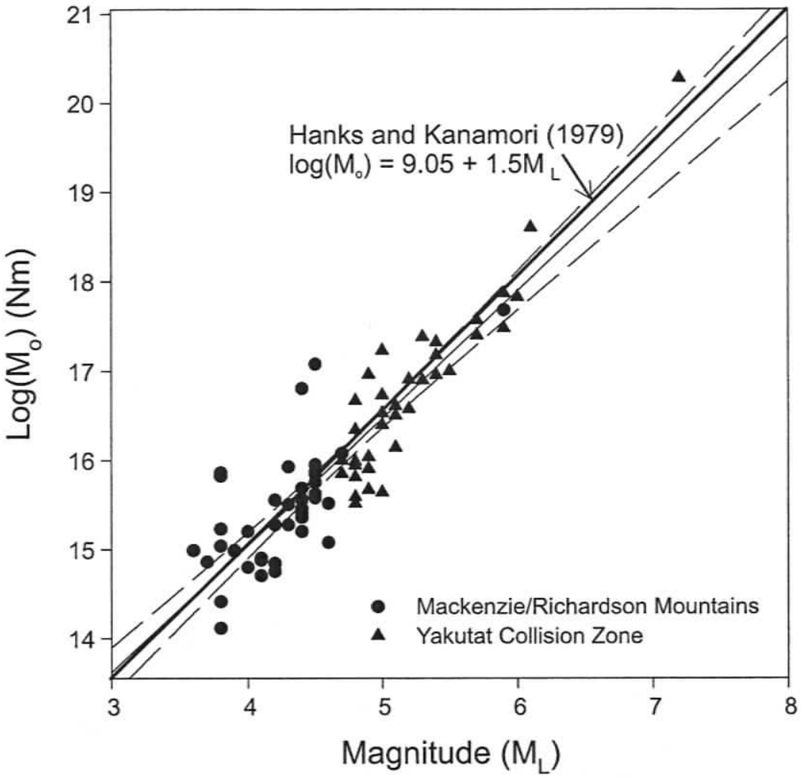

Figure 4.8. The relation between local magnitude M_L and seismic moment M_o for earthquakes in the region. The thin solid line and dashed lines are the least-squares fit and the 95% confidence limits. From Ristau (2004) and Hyndman et al. (2005a).

equation derived by Hanks and Kanamori (1979), where $c \sim 9.05$ and d is 1.5. These coefficients are used in this study.

The total seismic moment rate M_o' of the incremental or density function is calculated using the following equation:

$$M_o' = \varphi\, b\, \frac{10^{[(d-b)M_x + a + c]}}{d-b}$$

where a and b are the cumulative recurrence coefficients, and φ is the asymmetry correction factor. The intercept (a) and the slope (b) are defined as:

$$a = \log_{10}(N_0)$$
$$b = \beta / \ln 10$$

The asymmetry factor, φ, corrects for the asymmetry of the logarithmic moment-magnitude relation; for a calculated root-mean-square scatter of about 2 in the M_o distribution, φ is given a value of 1.27 (Hyndman and Weichert, 1983).

Seismic deformation rate

The seismic moment M_o released by rupture of an individual fault is given by:

$$M_o = \mu\, A\, s$$

where μ, the shear modulus, is taken to be 3.0×10^{10} Nm^{-2} , a typical value for crustal rocks (Turcotte and Schubert, 2002). A, the fault area, is the fault length times the estimated down-dip seismogenic extent, and s is the slip magnitude. The slip rate s' on the fault is given by:

$$s' = M_o' / (\mu A)$$

This equation can be used to calculate the relative motion between two adjacent blocks separated by the fault (Mazzotti and Adams, 2005). The slip can be broken down into vertical and horizontal (both fault-normal and fault-parallel) components.

In order to estimate the vertical and horizontal deformation rates of a broadly-deforming region, the zone is assumed to take up the relative motion between two blocks. It is also assumed that the entire zone is characterized by the same earthquake recurrence statistics and by a characteristic fault style described by a dip (δ) and a rake (ϕ). The dip is the angle of faulting (0° for a horizontal fault to 90° for a vertical fault), while the rake is the orientation of slip relative to the strike of the fault (0° for pure strike-slip motion to 90° for pure dip-slip motion). The dip and rake chosen to represent each particular zone are estimated from the available earthquake focal mechanisms and geological constraints. The vertical (s_v'), normal (s_n') and strike-slip (s_s') components of relative block motion are given by:

$$s_v' = \frac{\sin(\phi)\sin^2(\delta)M_o'}{\mu L h}$$

$$s_n' = \frac{\sin(\phi)\cos(\delta)\sin(\delta)\mathrm{M_o}'}{\mu L h}$$

$$s_s' = \frac{\cos(\phi)\sin(\delta)\mathrm{M_o}'}{\mu L h}$$

where L is the length of the seismic zone parallel to the strike of the characteristic faulting, and h is the seismogenic thickness of the zone (the estimated vertical extent over which the majority of deformation occurs seismically). The seismogenic thickness is estimated using available information on focal depth ranges from moment tensor solutions and detailed regional studies.

Uncertainty estimation

Estimation of the seismic moment and deformation rates involves numerous parameters, each of which contributes an uncertainty to the estimates. Some of these parameters (a, b, and φ) have uncertainties that are derived from the data analysis and can be described formally as the standard deviation about the mean. Other parameters are selected more subjectively (especially δ, ϕ, h, and $\mathrm{M_x}$); their uncertainties depend largely on the availability and reliability of constraining data, which vary from zone to zone. These parameters cannot be assumed to follow a normal probability distribution; thus, a standard deviation uncertainty estimation is inappropriate for the overall estimate. Instead, the analysis uses the logic tree approach commonly used in earthquake hazard analysis and described for this purpose by Mazzotti and Adams (2005).

Each parameter is assigned three values: the central value represents the best estimate, while the lower and upper values represent the estimated uncertainty. For parameters a and b, the central value is the mean, while the lower and upper values are the mean minus and plus the standard deviation respectively. Each parameter value is assigned a weight, with most weight given to the central value. Parameter d, one of the M-$\mathrm{M_o}$ conversion factors, is given a value of 1.5 for all cases and a weight of one. Similarly, parameter L, the strike-parallel length of the seismic zone is weighted one as it is a direct measurement, but its value will obviously vary from zone to zone. For those parameters assumed to have a normal probability distribution (a, b, c, φ, and μ), the central value is given a weight of 0.45, and equal weights of 0.275 are assigned to the lower and upper values (Tables 4.1, 4.2). Weighting of the other parameters (δ, ϕ, h, and M_x) varies depending on the information available, and may be skewed (see Table 4.2).

For each region, the logic tree analysis computes every possible combination of lower, central, and upper parameter values, and the associated uncertainties resulting from the weighting. As the seismic moment rate estimates involve four parameter sets (φ, a & b, c & d, and M_x), with three possible values each, 81 (3^4) estimates are produced. The deformation rate calculations involve a further four parameter sets, of which three (μ, δ & ϕ, and h) each have three possible values (L has just one possibility). This results in 2187 (3^7) deformation rate estimates for each zone. The results are plotted as probability distributions of the moment rate and deformation rate (e.g., Figure 4.9), from which the 16, 50, and 84 percentile values are extracted, representing the median value and 66% confidence interval.

Data

Earthquake catalogue

A file was prepared containing the locations and magnitudes of all earthquakes in the study region up until the end of 2004. The Geological Survey of Canada (GSC) catalogue was used for all events east of -145°E, and the Alaska Earthquake Information Center (AEIC) catalogue for all events to the west of that longitude. The majority of events in both catalogues are listed as local magnitude M_L, which has been found to be closely equivalent to M_w for this region, with an uncertainty of ~ 0.2 magnitude units (Ristau et al., 2005). A number of events in both catalogues are listed only as body-wave magnitude (m_b). Plots of events for which both M_L and m_b values are provided (Figure D1, Appendix D) show that m_b is approximately equivalent to M_L in the magnitude range of most of these events. In addition, some events in the GSC catalogue are listed only by Nuttli magnitude M_n, and one only by surface-wave magnitude M_s. Plotting of M_L versus M_n and M_s (Figure D2, D3, Appendix D) provides the relations:

$$M_L \sim M_n + 0.4$$

$$M_L \sim 0.66\, M_s + 2$$

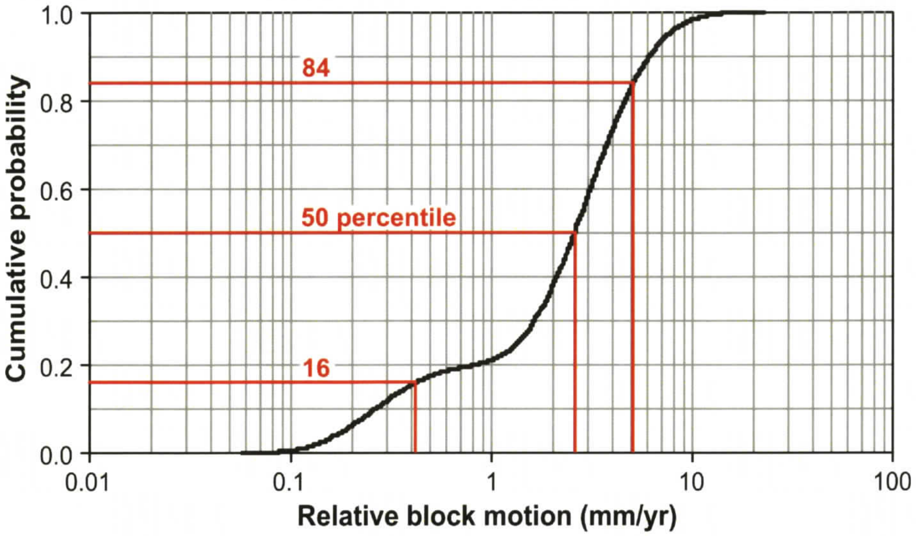

Figure 4.9. Cumulative probability distribution of block motion rate, and the extraction of the 16, 50, and 84 percentile values (mean and 66% confidence interval). Example is normal deformation rate for the N. Mackenzie Mountains region (Figure 4.10; Tables 4.2, 4.3).

The numbers of m_b, M_s, and M_n events are small and should not have a significant effect on the moment statistics. Once all events had been converted to M_L, sub-files were extracted from the complete earthquake file containing all events that occurred within each selected zone (zone boundaries are shown in Figure 4.10).

Magnitude intervals of completeness

Due to changes and improvements in the seismic station network with time (e.g., Figure 4.1), the lower magnitude limit of detected earthquakes has decreased over time. Thus, earthquakes of larger magnitudes have been completely detected for longer time periods than those of smaller magnitudes. These minimum magnitudes for completeness vary from region to region. The magnitude intervals of completeness used for each zone of this study are shown in Table D1 (Appendix D). For the Canadian regions and the Saint Elias region, the completeness intervals used were as determined by Adams and Halchuk (2003) for the fourth generation seismic hazard map of Canada. For the zones in Alaska, the completeness intervals determined for the adjacent areas of Canada were used. This approach is a source of uncertainty, although it is conservative given the much greater seismic station network density in Alaska, at least presently (Figure 4.1).

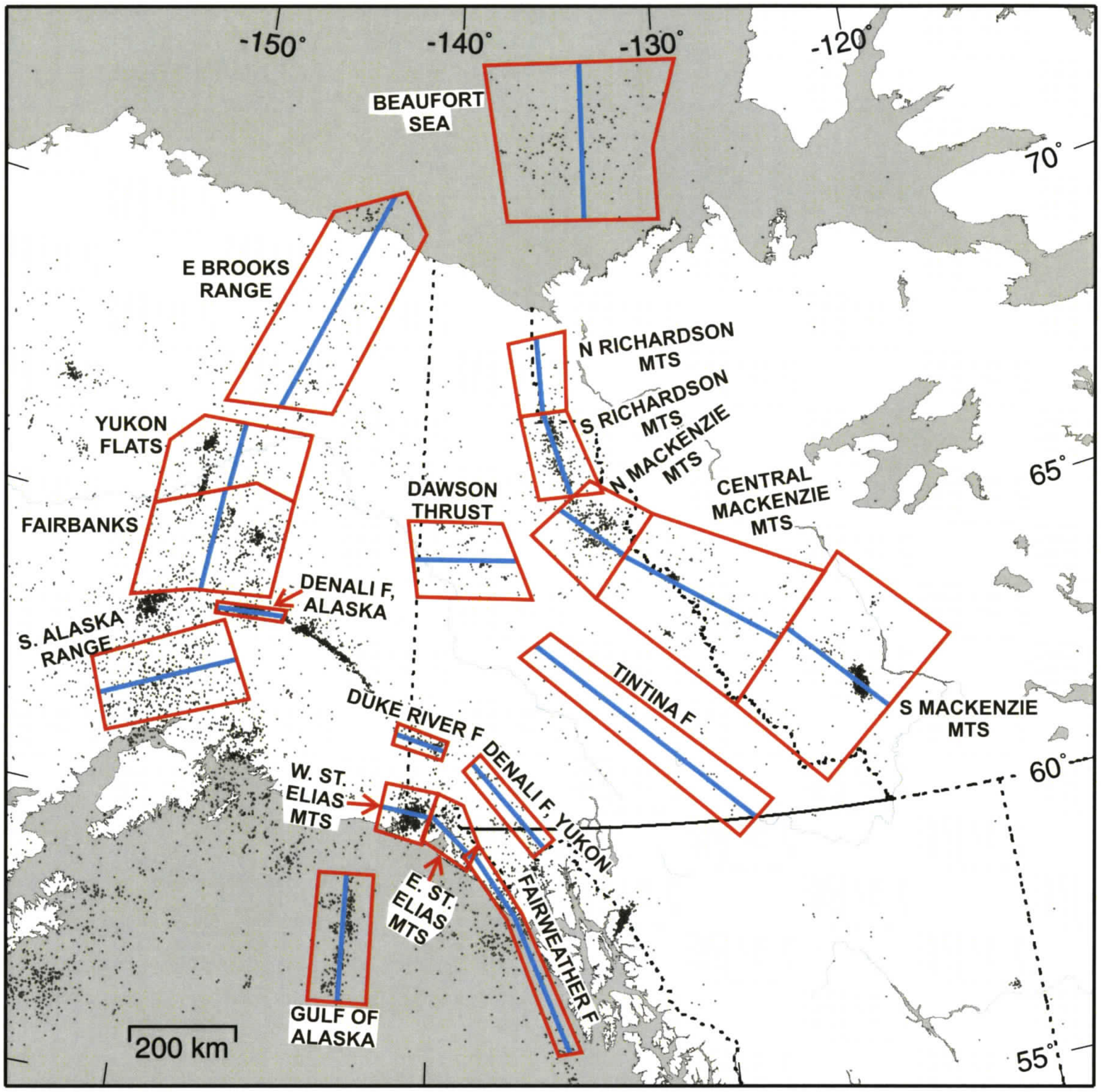

Figure 4.10. Seismicity distribution (black dots), seismic zones (red boxes), and assumed fault orientations (blue lines) for which seismic deformation rates were estimated.

An additional constraint was applied to zones close to the 2002 Denali fault rupture zone, that only pre-November-2002 data were used. This was to avoid the impact of short-term aftershock activity on the estimates of long-term seismic deformation. Aftershocks from other large earthquakes in the region may also affect the estimates. However, except for the aftershocks of the 1985 Nahanni events in the southern Mackenzie Mountains (discussed below), such events have not been systematically removed from the earthquake files, but are considered an additional source of uncertainty.

Parameter selection

The regions shown in Figure 4.10 were selected on the basis of a relatively even distribution of seismicity along the length of the zone, a similar set of earthquake mechanisms, where available, and a similar inferred tectonic regime. The information discussed in the historical seismicity section of this chapter was used both to aid in the zone selection and to estimate parameter values for each zone. The parameter values common to all areas are shown in Table 4.1 with their associated weights; Table 4.2 lists the lower, central and upper values determined (parameters a and b) or chosen (h, δ, ϕ, and M_x) for each zone, along with their weights.

Table 4.2 also lists the chosen values for the minimum magnitude cut-off (M_{min}) for each region. The minimum magnitude used for each time interval for each zone is controlled first by the magnitude intervals of completeness, as shown in Table D1 (Appendix D). The lower-magnitude earthquakes are therefore only used for the more recent time intervals. The completeness of these small-magnitude events is crucial, because the form of the recurrence curve is determined primarily by the large number of these events. Thus, the low-magnitude completeness is re-analyzed; for each region, the effect of the minimum magnitude allowable (at any time) on the recurrence statistics is examined. Values for a and b show large variations for minimum magnitudes that are too low or too high; M_{min} is chosen as a value that results in stable a- and b-values.

Results

Recurrence statistics

The Gutenberg-Richter cumulative recurrence coefficients (a and b) determined for each area are listed in Table 4.2. Values for a (frequency at $M = 0$) are generally in the range 2.2 to 4.8, while most b-values lie between 0.75 and 1.00. However, the Fairweather fault region has an exceptionally low b-value of 0.58 ± 0.05. This is lower than the b-value obtained for the Queen Charlotte fault further to the south (0.73; Bustin, 2006) and suggests that this part of the fault may show atypical behaviour. If b is constrained to a more common slope of ~ 0.8, the computed deformation rate would be lower. The deformation rate calculated for this zone is therefore viewed with caution.

Magnitude-frequency plots for each zone are included in Appendix D (Figures D4-D23). Examples for the Beaufort Sea and western St. Elias zones are shown in Figure 4.11.

Table 4.1. Parameter values for all regions.

	μ^1 (10^{10} Nm^{-2}) lower,central,upper	φ^2 lower,central,upper	c^3 lower,central,upper	d^3
Value	2.3,3.0,3.7	1.11,1.27,1.53	8.95,9.05,9.15	1.5
Weight	0.275,0.45,0.275	0.275,0.45,0.275	0.275,0.45,0.275	1

[1] Shear modulus; [2] Asymmetry factor; [3] M-M_o conversion factors.

Table 4.2. Input parameters (lower, central, upper values) and their assigned weights (below) for the seismic deformation rate estimation of each region.

Region[1]	$h^{2,3}$ **(km)**	**Dip δ (°)**	**Rake ϕ (°)**	a^3	b^3	$M_x{}^3$	$M_{min}{}^4$
Beaufort Sea	10,15,20	40,60,80 0.25,0.5,0.25	80,45,10 0.25,0.5,0.25	3.58,4.04,4.51	0.92,1.04,1.16	7.2,7.5,7.8	3.8
E Brooks Range	8,10,12	30,60,90 0.25,0.5,0.25	80,45,10 0.25,0.5,0.25	2.23,2.56,2.89	0.67,0.77,0.87	7.2,7.5,7.7	3.8
N Richardson Mts	10,12,15	90 1	0 1	1.68,2.30,2.92	0.63,0.81,1.00	7.4,7.7,7.9	3.4
S Richardson Mts	12,16,23	90 1	0 1	3.45,3.70,3.95	0.87,0.95,1.02	7.4,7.7,7.9	3.4
N Mackenzie Mts	10,15,18	30,60,80 0.3,0.5,0.2	90,45,10 0.3,0.5,0.2	3.50,3.82,4.14	0.82,0.90,0.98	7.5, 7.7, 7.9	3.9
Cen. Mackenzie Mts	10,12,15	30,40,70 0.3,0.5,0.2	90,60,20 0.3,0.5,0.2	3.05,3.48,3.92	0.78,0.89,1.00	7.5, 7.7, 7.9	3.9
S. Mackenzie Mts	8,10,12	30,40,70 0.3,0.5,0.2	90,80,20 0.3,0.5,0.2	4.59,4.79,4.99	0.96,1.02,1.07	7.3,7.5,7.7	3.9
S. Mackenzie Mts 2[5]	8,10,12	30,40,70 0.3,0.5,0.2	90,80,20 0.3,0.5,0.2	3.78,4.12,4.45	0.89,0.97,1.06	7.3,7.5,7.7	3.9
Yukon Flats	12,16,20	30,85,90 0.25,0.5,0.25	70,10,0 0.25,0.5,0.25	3.59,3.81,4.03	0.85,0.92,0.98	7.5,7.7,7.9	3.5
Dawson Thrust	10,12,15	30,60,80 0.3,0.5,0.2	90,80,20 0.3,0.5,0.2	2.52,2.77,3.03	0.70,0.78,0.86	7.4,7.6,7.8	3.2
Tintina F	8,10,12	90 1	0 1	1.96,2.34,2.73	0.68,0.81,0.94	7.5,7.8,8.0	3.0
Fairbanks	15,20,25	30,85,90 0.25,0.5,0.25	70,10,0 0.25,0.5,0.25	3.11,3.25,3.39	0.72,0.77,0.81	7.5,7.7,7.9	3.2
Denali F, Alaska	12,15,18	30,70,85 0.25,0.5,0.25	70,30,0 0.25,0.5,0.25	1.68,2.31,2.95	0.58,0.75,0.92	7.9,8.0,8.1	3.7
Denali F, SE Yukon	10,12,15	30,60,80 0.25,0.5,0.25	70,45,10 0.25,0.5,0.25	2.33,2.76,3.20	0.74,0.88,1.02	7.7,7.9,8.0	3.2
Duke River F	10,12,15	30,60,80 0.25,0.5,0.25	70,45,10 0.25,0.5,0.25	3.03,3.27,3.51	0.80,0.88,0.95	7.4,7.6,7.8	3.2
S Alaska Range	12,15,20	30,60,80 0.25,0.5,0.25	70,45,10 0.25,0.5,0.25	3.59,4.06,4.52	0.93,1.06,1.18	7.4,7.5,7.6	3.7
W St. Elias Mts	15,20,23	40,30,20 0.2,0.5,0.3	60,70,90 0.2,0.5,0.3	3.97,4.14,4.31	0.88,0.93,0.98	8.2,8.5,8.8	3.5
E St. Elias Mts	14,16,18	50,70,90 0.2,0.5,0.3	50,20,0 0.2,0.5,0.3	2.84,3.05,3.26	0.76,0.83,0.90	8.3,8.5,8.8	3.1
Gulf of Alaska	12,15,18	90 1	0 1	3.94,4.07,4.20	0.85,0.89,0.93	7.8,7.9,8.0	3.4
Fairweather F	12,15,18	80,85,90 0.2,0.5,0.3	10,5,0 0.2,0.5,0.3	2.06,2.22,2.39	0.53,0.58,0.64	8.2,8.3,8.4	3.2

[1] Region extents shown in Figure 4.10; [2] Estimated seismogenic thickness; [3] Weights of lower, central, upper values: 0.275, 0.45, 0.275; [4] Minimum magnitude cut-off (for earthquakes $\geq M_{min}$, event selection for each time period depends on the magnitude intervals of completeness, as shown in Table D1, Appendix D); [5] Aftershocks of 1985 Nahanni earthquakes removed.

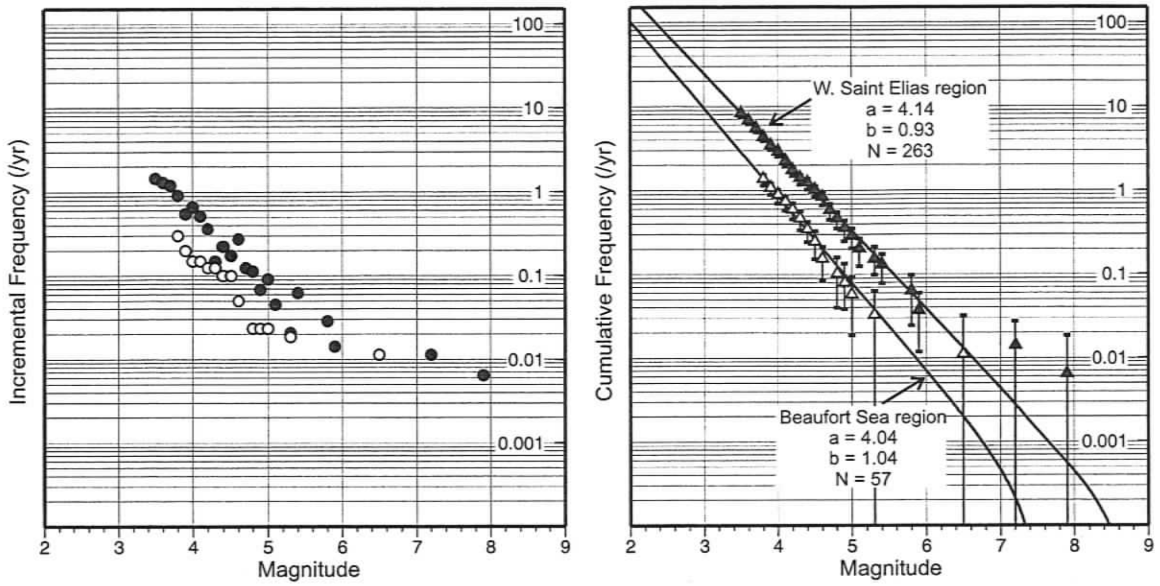

Figure 4.11. Example of earthquake recurrence statistics: incremental and cumulative frequency distribution for the Beaufort Sea region (open symbols) and the western St. Elias region (grey symbols). The error bars assume Poissonian statistics. Zone extents are shown in Figure 4.10.

Seismic deformation rates

The seismic moment rates and vertical, normal, and strike deformation rates determined for each region are listed in Table 4.3. Normal and strike directions are relative to the assumed fault orientations shown in Figure 4.10. Rates are listed as a median ("best") value (50 percentile) with 66% confidence limits represented by the range between the 16 and 84 percentile values (see Figure 4.9). Two sets of results are given for the S. Mackenzie Mountains zone; the first set is influenced by a large number of aftershocks of the 1985 Nahanni earthquakes, which affect the recurrence relations (as discussed below; Figures D10, D11, Appendix D). The second set of results is preferred, where the aftershocks are removed. The main results are also shown in Figure 4.12, where the given deformation rates refer to the dominant style of deformation across each fault zone (shortening, strike-slip, transpression, or transtension). Figure 4.13 shows an example of the parameter contribution to the final uncertainty.

Table 4.3. Seismic moment and deformation rates determined for each seismic zone.

Region	Moment rate (10^{17} Nm/yr)			Relative block motion (mm/yr)								
				Up			Normal[1]			Strike[1]		
	16%	50%	84%	16%	50%	84%	16%	50%	84%	16%	50%	84%
Beaufort Sea	0.561	0.974	1.91	0.2	0.4	0.8	0.0	0.3	0.6	0.1	0.5	1.2
E. Brooks Range	0.435	0.773	1.47	0.1	0.2	0.5	0.0	0.2[2]	0.4	0.1	0.3	0.8
N. Richardson Mts	0.179	0.678	2.06	0.0	0.0	0.0	0.0	0.0	0.0	0.4	1.3	4.3
S. Richardson Mts	1.28	2.12	3.66	0.0	0.0	0.0	0.0	0.0	0.0	1.7	3.0	5.8
N. Mackenzie Mts	3.73	5.81	9.35	1.4	3.1	6.3	0.4	2.6	5.0	0.0	4.4	9.6
Cen. Mackenzie Mts	1.68	3.07	5.81	0.4	0.8	1.6	0.4	1.0	2.0	0.0	0.7	2.1
S. Mackenzie Mts	5.3	7.48	11.2	2.0	3.3	5.4	1.6	4.0	6.7	0.0	1.0	6.2
S. Mackenzie Mts[3]	1.98	3.24	4.94	0.8	1.3	2.3	0.6	1.6	2.9	0.0	0.4	2.3
Yukon Flats	2.87	4.28	7.02	0.0	1.1	2.2	0.0	0.1	2.5	1.5	5.8	11.3
Dawson Thrust	1.54	2.65	4.92	0.8	1.8	4.0	0.4	1.4	2.9	0.0	0.5	2.3
Tintina F	0.309	0.872	2.31	0.0	0.0	0.0	0.0	0.0	0.0	0.3	0.9	2.5
Fairbanks	7.75	11.6	17.7	0.0	1.6	3.0	0.0	0.2	3.5	2.1	8.2	15.3
Denali F, Alaska	0.958	2.8	9.44	0.0	1.1	4.4	0.0	0.7	2.7	0.9	3.3	11.3
Denali F, SE Yukon	0.3	0.915	2.62	0.1	0.4	1.1	0.0	0.3	1.0	0.2	0.6	2.0
Duke River F	1.19	1.89	3.49	0.8	1.8	3.9	0.2	1.4	2.9	1.1	3.0	6.3
S. Alaska Range	0.465	0.784	1.63	0.1	0.2	0.5	0.0	0.2	0.4	0.1	0.4	0.9
W. St. Elias Mts	14.3	22.1	36.7	4.3	8.8	17.5	9.1	15.9	28.2	0.0	5.9	13.6
E. St. Elias Mts	5.37	9.77	19.7	0.0	4.5	11.8	0.0	1.8	6.2	7.9	16.4	35.0
Gulf of Alaska	11.5	16.1	22.7	0.0	0.0	0.0	0.0	0.0	0.0	9.5	14.3	21.7
Fairweather F	36.9	64.3	99.9	0.0	2.3	5.2	0.0	0.2	0.6	17.7	31.3	51.3

[1] Direction relative to assumed fault orientations shown in Figure 4.10; [2] Extensional deformation inferred rather than shortening; [3] Aftershocks of 1985 Nahanni earthquakes removed.

Discussion

The zones with the highest seismic moment release and corresponding highest deformation rates are those that represent most directly the boundaries between the North America plate and the Pacific plate and/or Yakutat block: the Fairweather fault zone (~ 31 mm/yr), and the Saint Elias Mountains zones (both ~ 16 mm/yr). However, high deformation rates are also indicated for the Gulf of Alaska dextral strike-slip zone within the Pacific plate (~ 14 mm/yr) and the Fairbanks and Yukon Flats sinistral strike-slip regions to the north of the Denali fault (~ 6-8 mm/yr). Substantial moment release and deformation rates of ~ 1-5 mm/yr occur in the foreland belt to the northeast of the plate boundary, the Mackenzie and Richardson Mountains. Slip rates of approximately the same magnitude also occur along the analyzed segment of the Denali fault in Alaska, the Duke River fault zone, and the Dawson thrust zone. The lowest estimated deformation rates (< 1 mm/yr) occur to the north in the Beaufort Sea and eastern Brooks Range regions, along the Tintina fault and the Yukon portion of the Denali fault, and in the southern Alaska Range between Cook Inlet and the Denali fault.

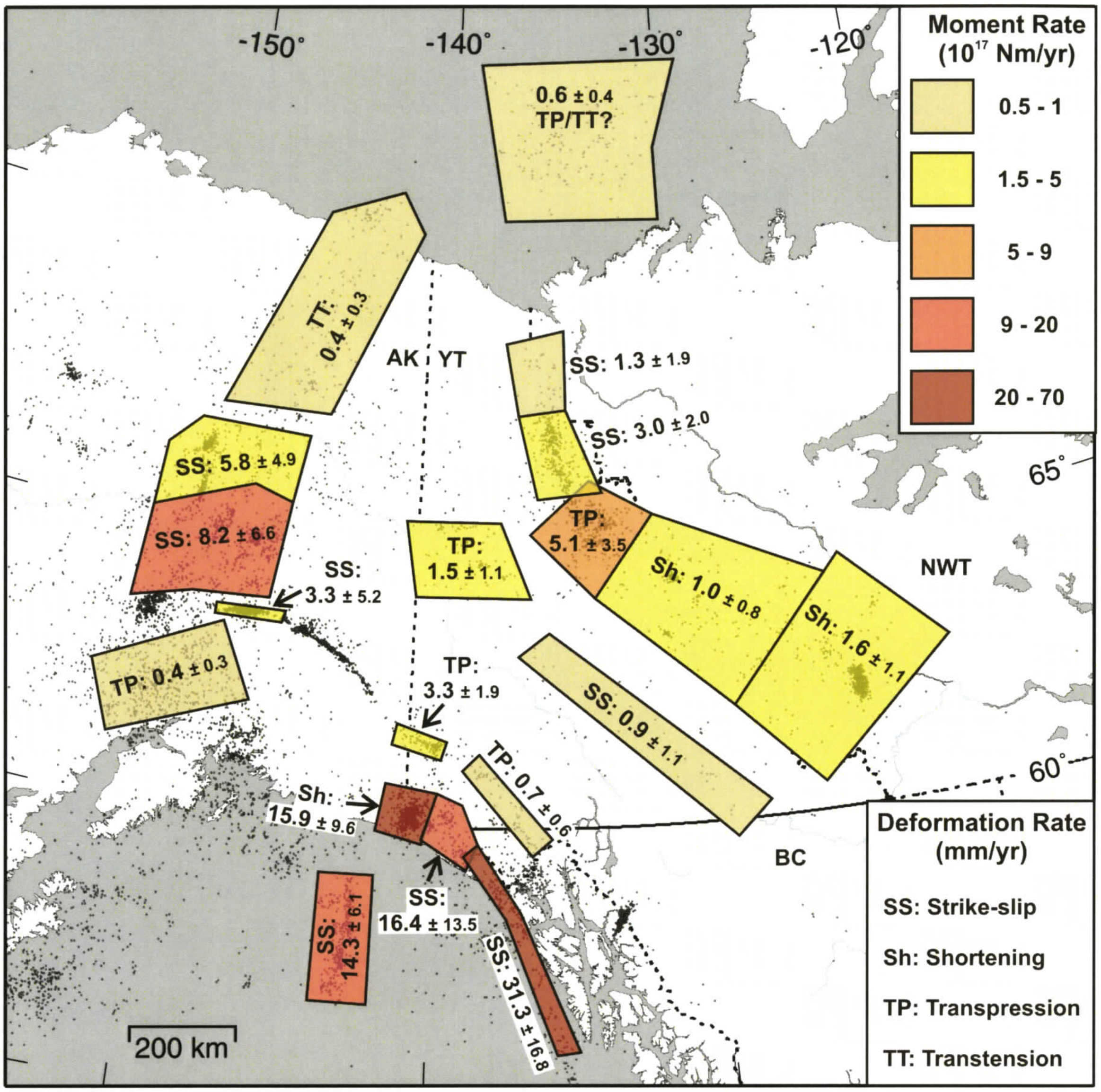

Figure 4.12. Seismic moment rates (shading) and deformation rates (numbers) determined for each seismic zone. Deformation rates refer to the dominant style of deformation across each fault zone (fault orientations shown in Figure 4.10). Deformation rates are the median value (50 percentile) plus or minus half the range of the 66% confidence interval.

The Fairweather fault zone shows a strike-slip deformation rate of ~ 31 mm/yr. This is less than, but within the uncertainties of the ~ 46 mm/yr slip rate estimated for the fault from GPS data inversion (Fletcher and Freymueller, 2003), and the ~ 48 mm/yr slip rate estimated from seismicity rates for the Queen Charlotte fault to the south (Bustin, 2006). The recurrence statistics for the Fairweather fault are characterized by an exceptionally low *b*-value, suggesting that the earthquake catalogue does not adequately represent the long-term slip on the fault.

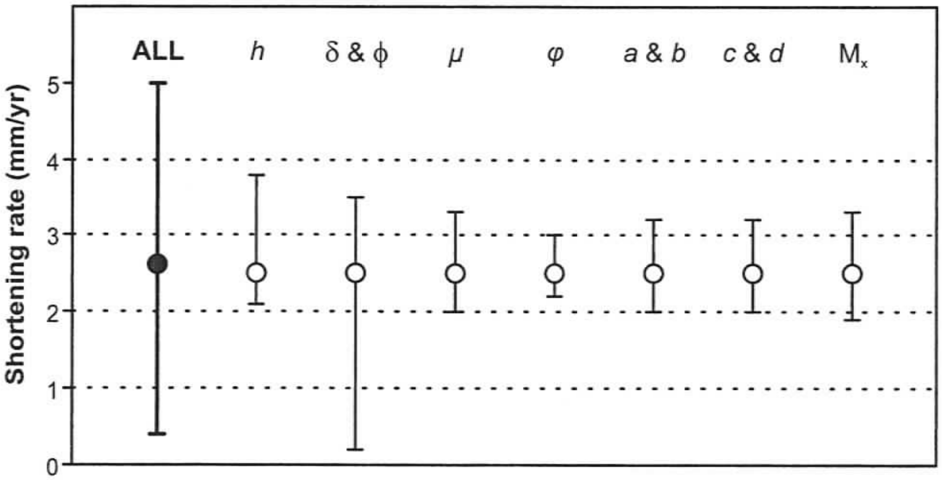

Figure 4.13. Parameter contribution to the final deformation rate uncertainty. Example is normal deformation rate for the N. Mackenzie Mountains region. Solid data point labelled "ALL" represents the final median rate and 66% confidence interval. h: seismogenic thickness; δ & ϕ: dip and rake; μ: shear modulus; φ: asymmetry correction factor; a & b: cumulative recurrence coefficients; c & d: M-M_o conversion factors; M_x: maximum magnitude.

The western Saint Elias Mountains zone, where thrust faulting mechanisms dominate, is characterized by a shortening rate from seismicity of ~ 16 mm/yr, and a dextral strike-slip rate of ~ 6 mm/yr. In contrast, the eastern Saint Elias zone is dominated by dextral strike-slip faulting associated with the Fairweather fault system. A dextral strike-slip rate of ~ 16 mm/yr is indicated, with minor shortening.

The high rate of dextral slip determined for the Gulf of Alaska Pacific plate tear (~ 14 mm/yr) may be misleading, as little seismicity occurred in this region prior to the 1987-1992 earthquake sequence. Some authors suggest that this sequence was triggered by stress changes after the 1964 great Alaska earthquake on the plate boundary to the west. However, the alignment of the epicentres with the Pamplona spur, a bathymetric feature at the eastern margin of the Pamplona zone of the Yakutat block, suggests that the strike-slip zone may have been active in the past, and the high determined deformation rate may represent the longer-term rate.

The segment of the Denali fault system analyzed in Alaska has a median dextral transpressional rate of 3.4 mm/yr from seismicity, but the uncertainties allow for strike-slip deformation of up to 11 mm/yr. Holocene slip rates on this section of the fault suggest 8-13 mm/yr of motion (Plafker et al., 1977; Schwartz et al., 2005). The easternmost Alaskan and westernmost Yukon segment of the Denali fault did not have enough historical seismicity data to adequately define recurrence statistics. The southeastern Yukon portion of the fault shows a dextral transpressional rate estimate of ~ 0.7 mm/yr (0.2-2.0), similar to the low slip rate on the Tintina fault in Yukon (0.9 mm/yr; 0.3-2.5). However, a higher rate of dextral transpression (1-7 mm/yr) is indicated for the western Duke River-eastern Totschunda region, suggesting that strain may be transferred from the collision zone to the Alaskan Denali fault principally via this area rather than the eastern portion of the Denali fault.

Low rates (~ 0.4 mm/yr) of seismic deformation are recorded by the southern Alaska Range south of the Denali fault. This suggests block-like motion of this forearc region, with little internal deformation between the plate boundary to the south and the Denali fault system to the north. Westward escape of this region along the Denali fault system has been suggested by several authors (e.g., Redfield and Fitzgerald, 1993; Haeussler et al., 2000).

The Fairbanks/Yukon Flats regions are characterized by high seismic slip rates; median values are 8.2 and 5.8 mm/yr, respectively. The slip is assumed to occur along a system of NE-SW-striking sinistral faults; the rates thus indicate N-S left-lateral relative motion between two blocks, and near-zero N-S shortening rates are indicated. However, as discussed in the first part of this chapter, the sinistral fault system is likely accommodating ~ E-W dextral transpression via clockwise rotation of a number of fault-bounded blocks in a dextral shear zone between the Denali and Tintina-Kaltag fault zones and extending a little further north (e.g., Page et al., 1995). Thus, the slip values more likely imply E-W transpression of ~ 5-10 mm/yr. To the north of the Yukon Flats region, slip rates decrease dramatically in the eastern Brooks Range. Here, earthquake mechanisms suggest a change from a NE-SW sinistral transpressional regime to NE-SW sinistral transtension. Slip rates are small (~ 0.4 mm/yr), but still significant.

Northeast of the Yakutat-North America collision zone, low slip rates (< 1 mm/yr) are indicated for the Denali and Tintina faults in Yukon. However, substantial moment release and deformation rates of ~ 1-5 mm/yr or more occur in the foreland belt to the northeast of the plate boundary, the Mackenzie and Richardson Mountains. These rates are similar to the deformation rates determined earlier by Mazzotti and Hyndman

(2002) of 2.5-5.5 mm/yr in the Mackenzie Mountains, and 2.5-7.5 mm/yr in the Richardson Mountains. Earthquake mechanisms range from pure thrusting through dextral-oblique thrusting to pure dextral strike-slip. The strike-slip component appears to increase to the north; no thrust mechanisms have been determined for the Richardson Mountains. This may be a symptom of the nature of pre-existing structures along the edge of the strong craton that are being reactivated under the current stress regime. The pre-existing steep N-S-trending faults of the Richardson Mountains are more likely to undergo strike-slip than dip-slip reactivation under the NE-SW-oriented stress, while the lower-angle structures of the Mackenzie Mountains can better facilitate shortening.

Deformation rates in the mountain front are highest in the northern Mackenzie Mountains. This area is the location of a swing in strike of geological structures and earthquake nodal planes from NW-SE in the south to N-S in the north, and a corresponding northward change in principal stress orientation from NNE-SSW to NE-SW (Figures 4.3, 4.6). The bend in the deformation front in this region and the divergence of the principal stress direction suggest a component of passive indenter tectonics, where the stronger, undeforming older crust to the east acts as a protruding backstop to the encroaching foreland belt, resulting in a focussing of strain.

The two sets of results for the southern Mackenzie Mountains show the large effect of aftershocks on the recurrence relations. Two earthquakes of M_w 6.6-6.8 occurred in 1985, and temporary arrays recorded thousands of aftershocks (Wetmiller et al., 1988; Horner et al., 1990). Tens of these aftershocks are greater than the 3.9 minimum magnitude cut-off and are thus included in the earthquake file for this region (for the first set of results). Aftershocks tend to have a very well-defined Gutenberg-Richter recurrence relation and a *b*-value close to 1.0 (e.g., Shcherbakov et al., 2004); thus the recurrence statistics of the overall catalogue seismicity are influenced by these events. The region was re-analyzed after removal of all events for a year after the first mainshock in October 1985 (excepting the second mainshock in December 1985). The removal of the aftershocks results in lower *a*- and *b*-values (Table 4.2), closer to those for the other Mackenzie Mountains zones, and much lower (approximately half) moment and deformation rates (Table 4.3).

The region around the Dawson thrust fault is the westward continuation of the foreland fold and thrust belt. This zone is calculated to accommodate 0.4-2.9 mm/yr of shortening, along with up to 2.3 mm/yr of strike-slip motion. As discussed in Chapter 5, such shortening approximately accounts for the decrease in northward velocity determined from campaign GPS measurements (Chapter 3).

Strain in the Richardson Mountains is inferred to be pure dextral strike-slip, as suggested by the earthquake mechanisms and geological structures. Calculated seismic moment and slip rates are higher in the southern zone (1.7-5.8 mm/yr) than to the north (0.4-4.3mm/yr), but the difference is not significant. A gap in seismicity occurs north of the Richardson Mountains in the Mackenzie Delta region. Deformation in this region is probably aseismic, but infrequent large earthquakes are possible (Hyndman et al., 2005c). Seismic activity further to the north in the offshore Beaufort Sea region allows determination of seismic deformation rates of ~ 0.6 mm/yr. The Beaufort Sea seismicity is poorly understood, but the few available mechanisms suggest a different regime than occurs in the Richardson Mountains to the south.

CHAPTER 5

Conclusions

SYNTHESIS OF DEFORMATION CONSTRAINTS

The synthesis of strain rates determined from GPS and earthquake statistics with geological constraints provides an improved picture of the deformation field of northwestern Canada and eastern Alaska. As long as there is no elastic component of strain associated with large faults, GPS velocities are indicative of the long-term deformation, and should be in line with rates inferred from recent geological data. Strain rates calculated from earthquake statistics, on the other hand, refer only to the deformation that is taken up seismically. If these rates are lower than the long-term rates, some aseismic deformation may be inferred. Similar comparisons have been made for the Andes, where it was found that shortening rates inferred from GPS and geological data (via cross-section balancing) are in agreement (at least for the last ~ 10 Ma; Hindle and Kley, 2002; Hindle et al., 2002), whereas seismic strain rates are an order of magnitude lower, indicating that aseismic deformation is likely occurring (Klosko et al., 2002).

Current deformation of the northern Canadian Cordillera and eastern Alaska is believed to result from the collision of the Yakutat block with North America in the corner of the Gulf of Alaska. This collision began only ~ 5-6 Ma, and thus the current tectonic situation is young. However, geological structures in the region have a long history, last culminating in Cenozoic Cordilleran orogenesis. The reactivation of faults and deformation zones implies that either earlier faulting weakened the lithosphere or both earlier and current faulting are concentrated where the lithosphere has long-term weakness. The current motion along many of these reactivated structures appears to be similar to the Cenozoic sense of motion, probably as a consequence of earlier terrane collisions. Also, known Quaternary-age deposits that could provide information on surface offsets due to the current motion are generally lacking across much of the region (with the notable exception of the Denali fault). Thus, it is difficult to differentiate current from earlier Cenozoic motions in the geological data. However, the geological data provide important constraints on the orientation and sense of recent faulting throughout the region.

Figure 5.1 shows a comparison of the current tectonic motions determined from GPS data analysis (Chapter 3) with the distribution of seismicity and mapped faults. Some of the GPS vectors in the Aleutian forearc and Alaskan panhandle are not representative of long-term strain due to the influence of fault locking on the Aleutian megathrust and Fairweather transcurrent fault respectively. This information is also included in Figure 5.2, along with the seismic deformation rates determined for selected high-seismicity zones from the earthquake catalogue (Chapter 4). The calculation of these rates is largely dependent on constraints on the nature and areal extent of faulting from: earthquake focal mechanisms, the geometry of geological structures, and detailed analyses of large and microseismic earthquakes. This comparison provides important information as to where and how crustal strain is accommodated within the region.

The following sections provide a summary and discussion of the main constraints on deformation throughout the region. These constraints are also summarized in Figure 5.3, a schematic map that shows the approximate tectonic motions of various areas with respect to stable North America.

Yakutat Boundaries

The Yakutat block (the unsubducted part of the Yakutat terrane) is colliding obliquely with North America in the corner of the Gulf of Alaska (Figure 5.3). The Yakutat terrane likely originated further to the south as a piece of the North American continental margin and adjacent oceanic crust that was sliced off when the transform plate margin jumped inboard to the present-day Queen Charlotte-Fairweather system (Bruns, 1983). The older transform fault may be represented by the Transition fault that currently bounds the Yakutat block to the southwest. After the plate boundary jump, the terrane moved northwards with the Pacific plate, and the oceanic northern part of the terrane subducted beneath North America, resulting in andesitic volcanism along the Wrangell arc (e.g., Plafker et al., 1989) and the formation of a fold and thrust belt along

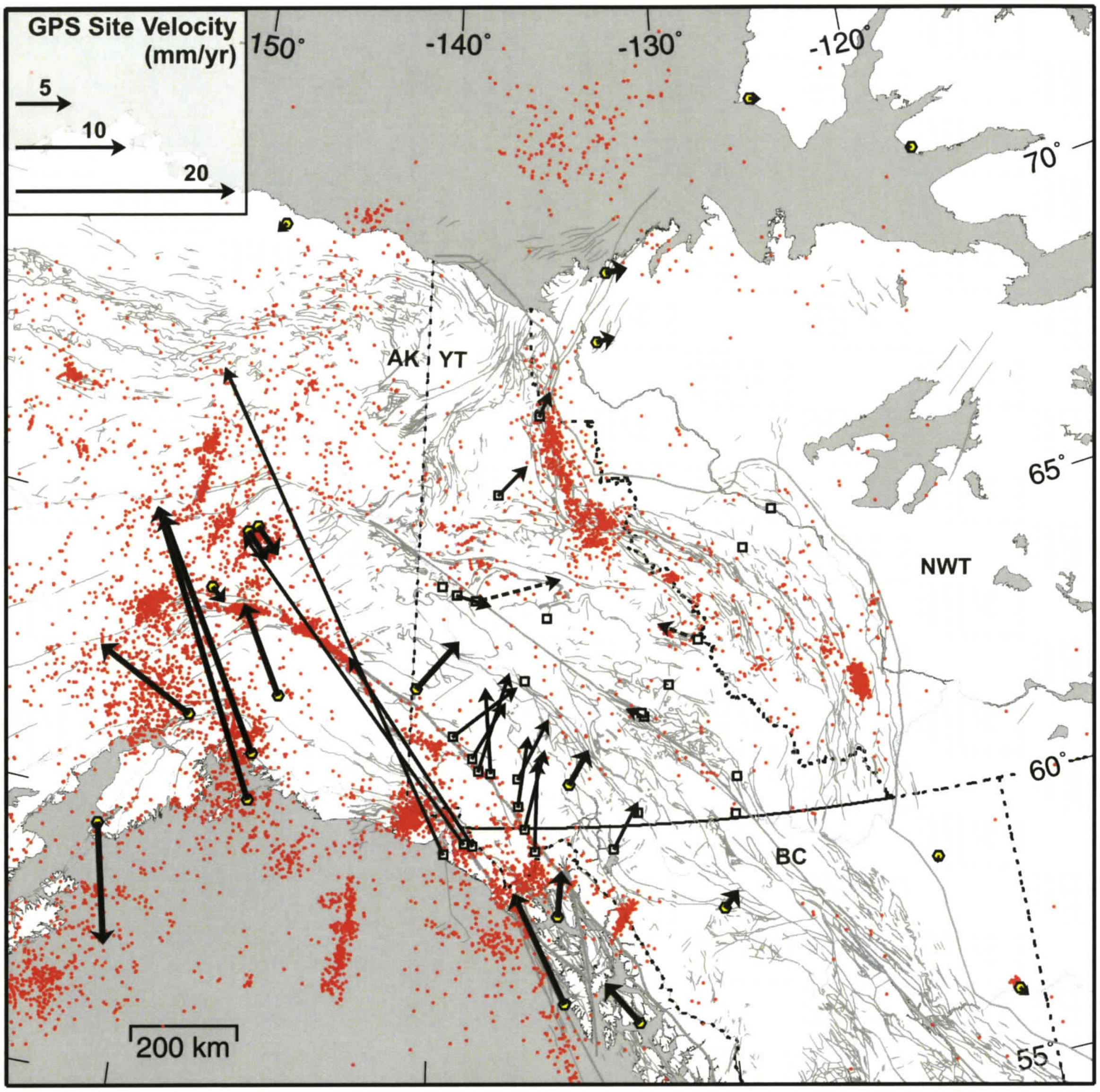

Figure 5.1. Comparison of the preferred GPS solution (black arrows) with the distribution of seismicity (red dots) and mapped faults (grey lines). Error ellipses are omitted for clarity (see Chapter 3).

the Chugach-Saint Elias fault system. Uplift rates in the Saint Elias Mountains and central Alaska Range show an acceleration beginning ~ 5-6 Ma (Fitzgerald et al., 1995; O'Sullivan and Currie, 1996) that may represent the start of the Yakutat collision, i.e., the time when the continental part of the terrane reached the subduction zone and began to resist subduction.

Assuming that the Transition fault was originally sub-parallel to the Fairweather fault, its current orientation implies counter-clockwise rotation of the Yakutat block

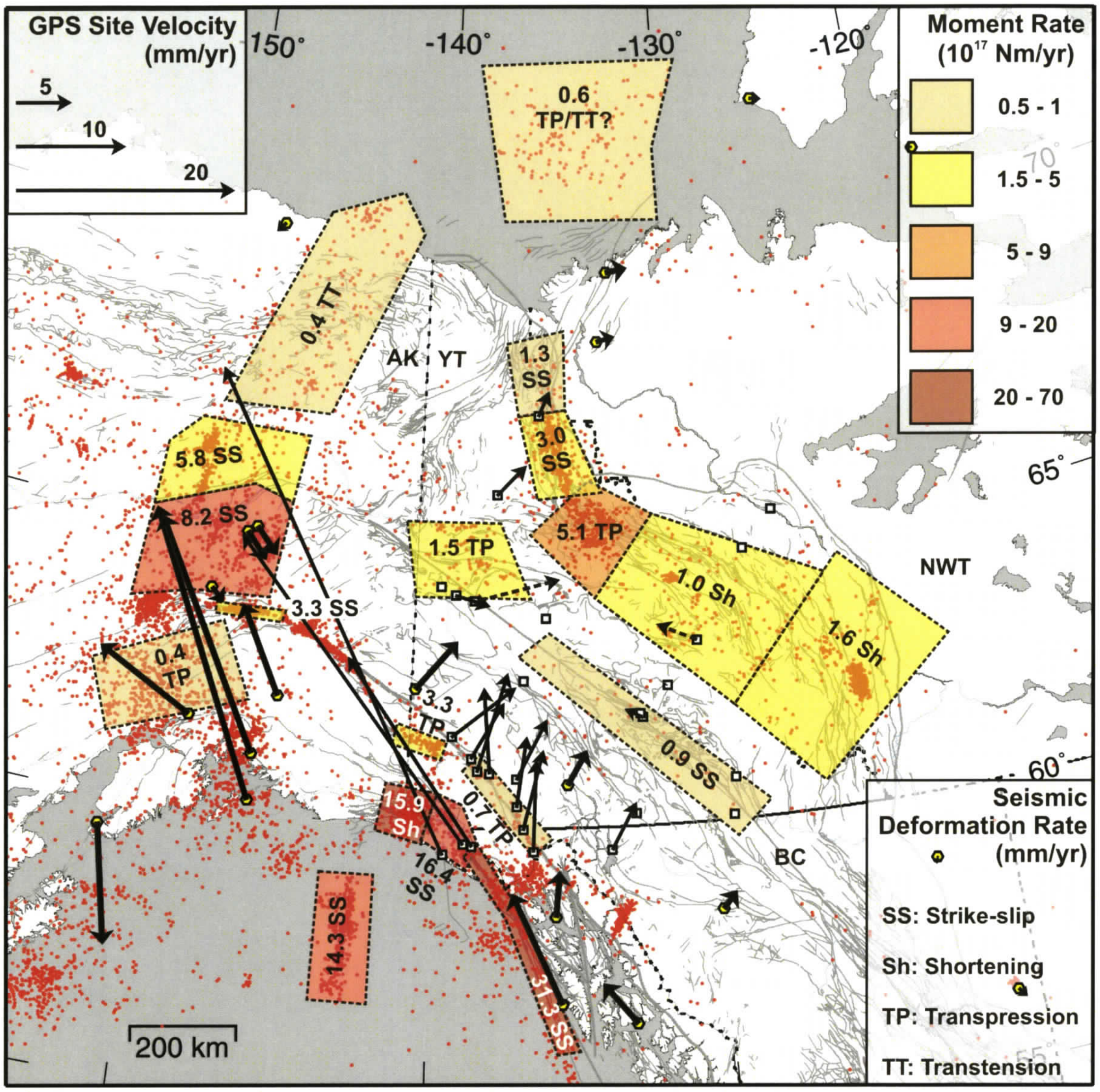

Figure 5.2. Comparison of the preferred GPS solution (black arrows) with seismic deformation rates (see Chapter 4), and the distribution of seismicity and faults. GPS error ellipses and deformation rate uncertainties are omitted for clarity (see Chapters 3 and 4).

around the corner of the plate margin. This is supported by the velocity of the campaign GPS site at Yakutat, which shows a motion that is a little slower and more westward compared to the relative Pacific-North America motion. The Transition fault does not appear to be active along most of its length, evidenced by a lack of both Holocene offsets in seismic reflection data and current seismicity. However, both seismicity and Quaternary deformation suggest ongoing thrusting at the southeastern end. This part of the fault is at a high angle to the motion of the Pacific plate and is adjacent to the eastern,

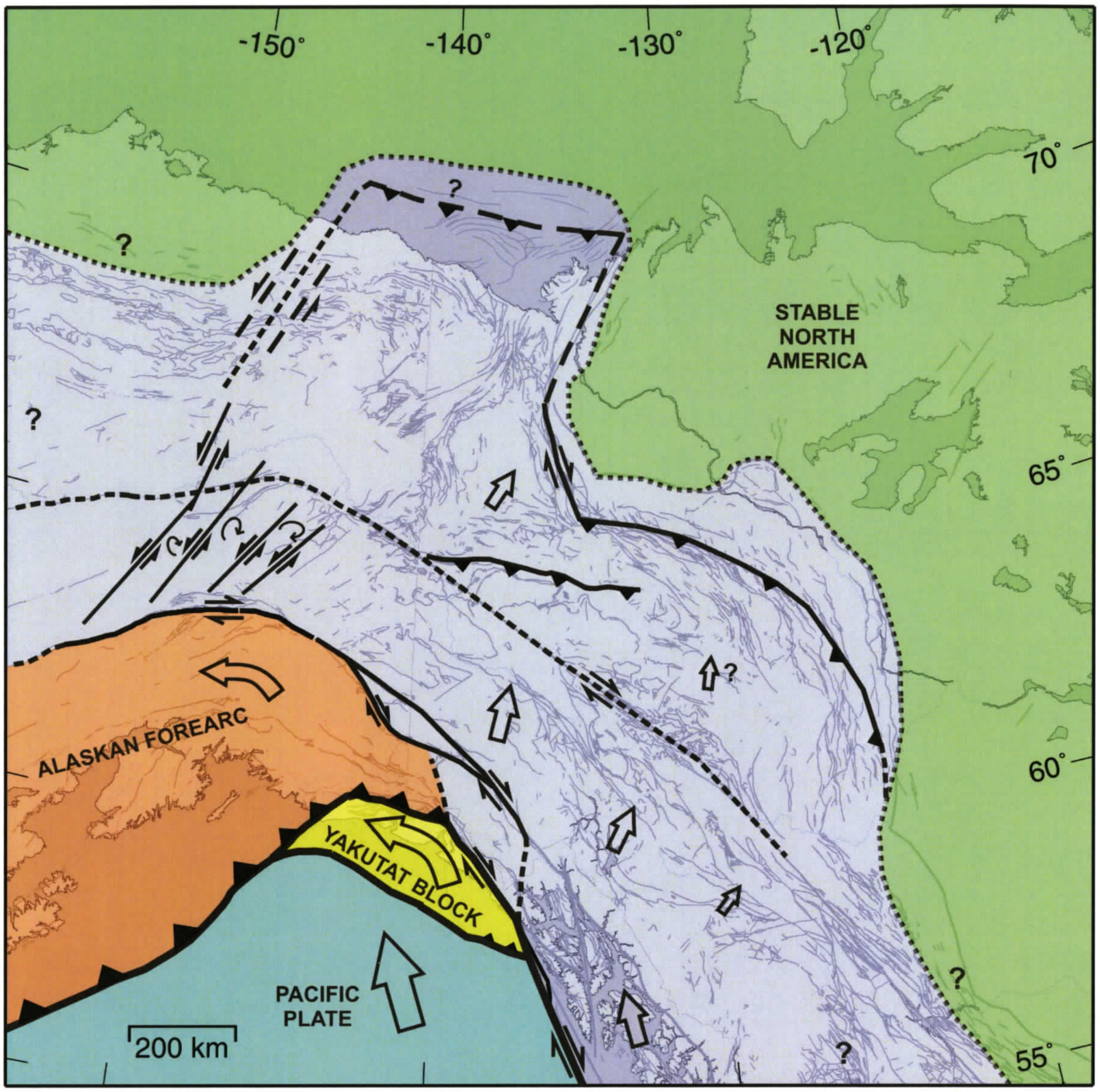

Figure 5.3. Schematic diagram, showing a simplified picture of the current tectonics of the northern Canadian Cordillera and eastern Alaska. Blue: Pacific plate; Green: stable North America plate; Yellow: Yakutat block; Orange: southern Alaska forearc; Grey: zone of continuous deformation in the North America crust affected by the Yakutat collision. Large arrows show the approximate tectonic motion relative to stable North America. Arrow pairs show the sense of motion on faults. Triangles show the down-dip side of thrust boundaries. Little-constrained areas are indicated by question marks.

continental part of the Yakutat block; incipient subduction of the Pacific plate is possible here. At least the continental part of the Yakutat block will likely be accreted to the continental margin in the future, and the Pacific-North America subduction boundary will then be localized along the southern margin of the block in this area.

The subduction resistance of the Yakutat block, in contrast to the Aleutian subduction zone to the west, is also the apparent cause of a N-S sequence of dextral strike-slip earthquakes within the Pacific plate in the Gulf of Alaska (Figures 5.1, 5.2). To the west, the oceanic crust is pulled into the subduction zone by the subducted slab, whereas the Pacific oceanic crust to the east is held up by the collision of the Yakutat block. Deformation rates calculated from the recent seismicity statistics of the Gulf of Alaska plate tear suggest right-lateral slip of 10-20 mm/yr (Chapter 4). It is not clear how this relative motion will be accommodated in the Pacific plate in the long term. The seismicity could be a transient associated with the 1964 great earthquake on the Aleutian megathrust to the west.

Some continued subduction of the oceanic, western part of the Yakutat block occurs to the northwest beneath the Kayak Island zone. The Yakutat block shows little internal deformation, except for the seismically-active Pamplona zone fold and thrust belt to the west, where mostly Quaternary-Recent deformation has propagated southeastwards and likely represents offscraping of Yakutat block sediments above the subducting oceanic basement.

The eastern margin of the Yakutat block is formed by the Fairweather right-lateral transform fault, and the northern margin occurs along the Chugach-Saint Elias thrust fault system. Intense seismicity occurs in the Saint Elias region, the northern boundary of the Yakutat block with North America. Earthquake mechanisms indicate mostly thrust faulting in the western region (e.g., 1979 M_w 7.3 event), and mostly dextral strike-slip faulting in the east (e.g., 1958 M_w 8.2), consistent with motion along the northernmost extent of the Fairweather fault. Along most of its length, the Fairweather fault is moving at close to the Pacific-North America rate (~ 45 mm/yr), but at its northernmost end in the eastern Saint Elias region, seismic deformation rates are only ~ 16 mm/yr, comparable to the shortening rate calculated from the seismicity catalogue for the western Saint Elias region (Chapter 4). Thus, although some aseismic deformation may occur, a substantial amount of strain related to the Yakutat collision is not accommodated locally within the main collision deformation zone.

Denali Fault

Part of the oblique collision is accommodated by dextral motion along the Denali fault, a continental-scale strike-slip fault that arcs northwest through SW Yukon and eastern Alaska and continues southwest through western Alaska, with a northern apex in the central Alaska Range. Seismicity and Holocene offsets suggest that the most active part of the fault is in eastern Alaska in the region of the apex. High rates of uplift in this area have produced the highest mountain in North America (Denali/Mount McKinley at over 6000 m). Intense transpression across this zone has produced a positive flower structure evidenced by hypocentre distributions that dip towards the Denali fault (e.g., Fisher et al., 2004). The 2002 M_w 7.9 event ruptured ~ 340 km of the Denali and splaying faults in this region. Holocene dextral slip rates are estimated at ~ 10 mm/yr, decreasing to zero along the western part of the fault and the eastern segment in western Yukon (Richter and Matson, 1971; Plafker et al., 1977; Clague, 1979). Seismic deformation rates (calculated from the pre-Denali earthquake catalogue to avoid aftershocks) suggest dextral slip of only ~ 3.5 mm/yr near the apex (Figure 5.2), although motion of up to 11 mm/yr is allowed by the uncertainties (Chapter 4). Low rates of seismicity occur along the Denali fault in easternmost Alaska and SW Yukon. Current right-lateral motion appears to splay off the Denali fault onto the Totschunda fault (as it did during the 2002 rupture), linking to the Duke River fault in westernmost Yukon, where a transpressional deformation rate of ~ 3.3 mm/yr was calculated (Chapter 4). It is unclear exactly how this deformation connects to the collision zone to the south; sparse seismicity occurs southwards through the Saint Elias Mountains, and a seismic deformation rate of only ~ 0.7 mm/yr was calculated for the southernmost portion of the Denali fault.

Alaskan Forearc

The forearc region south of the Denali fault in Alaska experiences a low rate of crustal seismic deformation (~ 0.4 mm/yr; Chapter 4). The motion of continuous GPS sites in the region is dominated by interseismic strain accumulation due to locking of the Aleutian megathrust, so crustal deformation cannot be readily resolved. However, there is some indication of a counter-clockwise rotation, as previously noted by Fletcher (2002).

This is consistent with westward motion of the forearc, facilitated partly by dextral motion along the curved Denali fault to the north.

Eastern Alaska

North of the Denali fault in Alaska, the Fairbanks region exhibits high rates of seismicity. Earthquakes occur mainly along NE-trending seismic zones; left-lateral strike-slip focal mechanisms are consistent with the inferred motion on sub-parallel faults to the southeast that were active during the Tertiary. Page et al. (1995) propose that sinistral slip occurs between NE-trending crustal blocks to facilitate their clockwise rotation, which, in turn, accommodates dextral transpression between the Denali and Tintina-Kaltag fault systems. Such rotation appears to be supported by the southeastward motion of the three continuous GPS sites in the region, the two sites to the northeast moving at higher rates than one to the southwest (Figure 5.1). Seismic slip rates of ~ 8 mm/yr were calculated from the earthquake catalogue (Figure 5.2); this left-lateral motion is shared between the NE-trending zones and implies a similar rate of ~ E-W dextral shear across the whole zone.

The system of NE-trending sinistral strike-slip seismic zones extends north of the Tintina-Kaltag system into the Yukon Flats region of eastern Alaska. This suggests that dextral shear is accommodated over a wider region than the Denali-Tintina-Kaltag systems in this area. Calculated seismic deformation rates of ~ 6 mm/yr suggest that deformation decreases northwards (Figure 5.2).

Distributed seismicity occurs over a NE-trending band through the NE Brooks Range of Alaska and extends slightly offshore. This trend is approximately parallel to the left-lateral Canning displacement zone identified by Grantz et al. (1983) as having facilitated northward and upward motion of the NE Brooks Range relative to the lowland to the west. Strike-slip earthquake focal mechanisms in the area are consistent with left-lateral motion on NE-striking planes. Normal faulting is also indicated by focal mechanisms, implying that transtension is occurring in this region. Seismic deformation rates determined from the earthquake catalogue indicate only ~ 0.4 mm/yr of slip. Only one GPS site is located nearby: the continuous site at Prudhoe Bay on the North Slope, west of the zone of seismicity. The site horizontal velocity is zero within the uncertainties, but suggests a small motion to the southwest (~ 1 mm/yr) that is consistent with a low rate of sinistral slip on a NE-trending zone to the east. Thus, northern Yukon and northeasternmost Alaska appear to be moving north relative to both the craton to the east and the stable north coast of Alaska to the west (Figure 5.3).

Southwestern Yukon

The region to the northeast of the Yakutat collision zone in SW Yukon and northwesternmost British Columbia has a relatively dense GPS network, at least compared to the rest of the area. Eight campaign GPS sites are located close to the trace of the Denali fault (due to the coincident highways), with another campaign site and two continuous stations inland of the fault. The velocities of all these sites indicate north or northeastward motion at rates of ~ 6-10 mm/yr (Figure 5.1). Recent work by C. Larsen suggests that the motion of most of these sites includes a component of glacio-isostatic adjustment in response to rapid post-Little Ice Age glacial retreat in the Glacier Bay region to the south (C. Larsen, personal communication, 2006). Subtraction of this postglacial motion from the velocities of the sites in this region still results in a northeastward motion of ~ 5 mm/yr. Earthquake mechanisms in this area indicate a combination of dextral strike-slip and NE-SW thrusting consistent with partitioning of strain into strike-slip and convergent components.

The region between the Denali and Tintina faults in Yukon is characterized by a low rate of seismicity. However, epicentres show a slight alignment along the NW-trending Teslin fault zone, and focal mechanisms suggest that dextral transpressional reactivation of this Triassic-Jurassic fault may be occurring. The generally sparse seismicity between the Denali and Tintina faults in Yukon and in easternmost Alaska suggests that little seismic strain is accommodated in this region, in contrast to the high strain rates in the Fairbanks zone further to the northwest. The area is characterized by high heat flow (e.g., Lewis et al., 2003) and coincides with the northern extent of the Northern Cordilleran Volcanic Province (e.g., Edwards and Russell, 1999), a group of Neogene to Recent alkaline volcanic centres. This volcanism may result from decompression melting due to either the presence of a slab window (subducted spreading ridge; e.g., Thorkelson and Taylor, 1989) or to incipient rifting of the crust (e.g., Edwards and Russell, 1999; 2000). Perhaps the most likely scenario is the presence of extensional transfer zones between the Denali and Tintina faults, which are exploited by slab window magmatism (e.g., Lowe and Cassidy, 1995; Hart and Villeneuve, 1999).

Seismic deformation rates calculated from the earthquake catalogue along the Tintina fault in Yukon reveal a low rate of implied dextral motion (~ 1 mm/yr; Figure 5.2). The campaign GPS site at Coffee Lake, along the Tintina fault near Ross River, shows a northwestward motion of ~ 2 mm/yr, i.e., sub-parallel to the Tintina fault zone, which comprises several strands in this region (e.g., Snyder et al., 2005). However, inferences about possible fault locking cannot be made due to the large uncertainties of the GPS vector, mostly resulting from unsatisfactory corrections for co- and postseismic motions related to the 2002 M_w 7.9 Denali fault earthquake.

Campaign GPS data are also provided for two sites on the southern side of the Tintina fault near Dawson City in westernmost Yukon (Figure 5.1). The motion of these sites appears to be dominated by an eastward component, although large uncertainties also occur here due to the Denali earthquake. Coseismic modelling (Hreinsdóttir et al., 2006) suggests that these sites moved eastward during the earthquake, and it is possible that some residual eastward motion has not been accounted for. Also, the site data suggest a possible southward component that is not accounted for in the co- and postseismic model predictions. Thus, a more northward motion of these sites is possible; more data are crucial. A northeastward preliminary velocity is suggested for a new site located a little further west (TOWH). The data at this site should be relatively unaffected by Denali postseismic motion as it was established almost two years after the event; however, the vector from this and other new sites are omitted from the final solution as they represent only two occupations over a short time series (< 1 year).

The E-W-trending Dawson, Robert Service and Tombstone thrust faults are located on the northeastern side of the Tintina fault in western Yukon. The latter two faults may have accommodated as much as 100 km of ~ N-S shortening during Cordilleran orogenesis (Mair et al., 2006). Earthquake focal mechanisms indicate a combination of thrust and strike-slip faulting in the area, for which a seismic deformation rate of ~ 1.5 mm/yr (of inferred transpressional slip) is estimated (Figure 5.2; Chapter 4). Minor shortening across this zone may account for the reduction in northward motion from the GPS sites in SW Yukon to those in the northeast, described below (Eagle Plains and Richardson Mountains).

The two easternmost campaign GPS sites in Yukon are located in the Selwyn Mountains just west of the Mackenzie Mountains, and have inferred motions that are difficult to explain. These vectors have large uncertainties due to the difficulty of correcting their motion for co- and postseismic effects of the Denali earthquake. The easternmost site (MAMI), at the border of the Northwest Territories, appears to be moving to the northwest at ~ 4 mm/yr, while the other North Canol Road site (CARI) to the southwest shows near-zero motion with respect to stable North America. Although the estimated uncertainty at CARI is lower than that at MAMI, its solution has a lower ranking, mostly due to its setting in sediments, compared to bedrock for MAMI. A northward component of motion is expected for this area, given the northeastward motion of sites to the southwest, with little intervening strain indicated by seismicity. The apparent lack of an eastward component of motion is surprising. The Mackenzie Mountains to the east are characterized by generally NE-SW thrusting, with some NW-SE dextral shear also apparent from earthquake focal mechanisms. A northeastward or even pure northward motion of the North Canol Road sites could be partitioned into the observed transform and convergent strain observed in the Mackenzie Mountains. More data will be crucial to determining reliable velocities for these sites.

Mackenzie and Richardson Mountains

Seismic strain rates calculated for the Mackenzie Mountains indicate that ~ 1-2 mm/yr of shortening is accommodated in the southern and central regions, while a much higher deformation rate (~ 5 mm/yr) was determined for the northern Mackenzie Mountains (Figure 5.2; Chapter 4). This region represents a change in the strike of geological structures (from NW-SE in the central Mackenzie Mountains to ~ N-S in the Richardson Mountains) and a corresponding change in the style of deformation. Earthquake mechanisms indicate that the Mackenzie Mountains are dominated by thrust faulting, whereas only strike-slip mechanisms have been determined for the Richardson Mountains. Both thrusting and strike-slip mechanisms occur in the northern Mackenzie Mountains. Calculated seismic deformation rates decrease to the north through the

Richardson Mountains, with a rate of ~ 3 mm/yr determined for the southern region, and ~ 1.3 mm/yr in the north (Figure 5.2). The concentration of strain in the northern Mackenzie Mountains may be a consequence of the convex (to the west) shape of the shallow edge of the older, stronger crust to the east of the deformation front. The principal stress orientation determined from moment tensor inversion also changes around this bend, from NNE-SSW in the south to NE-SW in the north, remaining approximately orthogonal to the deformation front. The stronger crust to the east appears to act as a passive indenter, a backstop to the encroaching foreland belt, and thus strain is focussed here.

Northern Yukon, Northwesternmost NWT, and Mackenzie Delta

Campaign GPS sites in northern Yukon (EAGL and RICH) exhibit northeastward motion (Figure 5.1), consistent with the NE-SW principal stress orientation. Again, these vectors are uncertain due to the Denali earthquake, and more data will improve this constraint. The northward decrease in motion from EAGL (~ 4 mm/yr) to RICH (~ 2.5 mm/yr) is consistent with strain accommodation within the Richardson Mountains. The motion at RICH is comparable to the estimated seismic strain rate in the region, suggesting that strain is not transferred east of the deformation front (Figure 5.2). This is generally supported by the small velocities of continuous GPS sites INVK and TUKT, located to the northeast. However, these sites are not far from the deformation front and are not considered part of the stable craton. The eastward motion of ~ 1.5-2 mm/yr at these sites may be influenced by locking of the Eskimo Lakes fault zone, which has little historical seismicity, but has inferred extensional Cenozoic motion and may be active.

A gap in seismicity occurs to the north in the region of the Mackenzie Delta. However, a concentration of earthquakes occurs further north beneath the continental slope of the Beaufort Sea (Figures 5.1, 5.2). The depths and mechanisms of these events are poorly constrained, but both normal and strike-slip faulting within the lower crust is suggested (e.g., Hasegawa et al., 1979). A seismic deformation rate of ~ 0.6 mm/yr was calculated for this region. The seismicity may result from flexure of the crust in response to loading beneath the thick pile of Mackenzie Delta sediments. Horizontal tension axes suggest that the area is not affected by northward-directed compressional stress.

Important questions are: (1) is the strain transferred from the Yakutat collision completely expended in the region south of the Beaufort coast, or is there a residual northward motion that occurs in the Mackenzie Delta region? (2) If northward strain transfer occurs, is it accommodated aseismically within the Mackenzie Delta, or is there potential for large infrequent earthquakes on a locked thrust fault, and perhaps associated tsunamis (e.g., Hyndman et al., 2005c)?

SUGGESTIONS FOR FUTURE WORK

GPS Measurements

Reoccupation and more reliable vectors are critically needed for the central and eastern Yukon GPS sites. A densification of both the continuous and campaign GPS networks would yield greatly improved constraints on the regional deformation. However, logistics are difficult. The road network in Yukon and Northwest Territories is extremely limited, and many potential site locations in areas of interest require expensive access by air. Ideally, more sites should be established in the eastern and northern parts of the area, encompassing the Mackenzie Mountains (helicopter access), Ogilvie, and Richardson Mountains (Dempster Highway). Sites in the northeastern Brooks Range of Alaska and close to the northern Yukon coast would also provide important constraints.

Reoccupation of the existing campaign GPS sites is planned in 2006, with the unfortunate exception of the two easternmost sites in the Northwest Territories (NORW and LKEE, which requires helicopter access). These sites have only been occupied for one campaign (2004) and thus have yet to provide velocity data. The seven other sites that were newly established in 2004 were reoccupied in 2005, but the time series are too short to yield reliable data. The 2006 occupation will provide preliminary velocities for these sites, adding to the available constraints.

Expansion of Seismic Network

The sparse existing network of seismic stations in the northern Cordillera leads to large errors in earthquake hypocentral locations, as mentioned in Chapter 4. Earthquakes are particularly poorly constrained in the northern part of the region. Additional permanent seismic stations and/or temporary deployments would much improve location accuracy and allow for better-constrained earthquake mechanisms and crustal velocity models. In turn, better association of seismicity with mapped faults would greatly improve constraints on the current tectonics and seismic hazard of the region.

Paleoseismicity

Little work on the neotectonics of faults in the northern Cordillera has been carried out to date. As mentioned earlier, this is partly due to difficult access and partly to the problems of differentiating recent from earlier motions on faults where young sediments are lacking. However, the apparent association of seismicity with mapped faults, and consistency of earthquake mechanisms with inferred historical motions, suggest the possibility of recent surface offsets. Paleoseismic analyses of the Denali fault in Alaska reveal as much as 350 m of Holocene dextral motion (e.g., Richter and Matson, 1971), and an analysis of the Tintina fault from Landsat imagery (Mortensen and Von Gaza, 1992) suggests relatively recent activity. Other areas to focus on could include the southern Yukon portion of the Denali fault, the Duke River fault, the Teslin fault zone, the Dawson thrust zone, as well as seismically-active regions of the Mackenzie and Richardson Mountains of Yukon and Northwest Territories and the NE Brooks Range of Alaska.

Low-Temperature Thermochronology

GPS and seismicity studies in the northern Canadian Cordillera and eastern Alaska provide estimates of current deformation, which are generally related to the collision of the Yakutat block with North America in the corner of the Gulf of Alaska. The Chugach-Saint Elias fold and thrust belt was initiated ~ 20 Ma due to this convergence; the latest phase of uplift started ~ 5 Ma and may relate to a change to a more collisional tectonic regime (e.g., Fitzgerald et al., 1995; O'Sullivan and Currie, 1996, and references therein). An important question is how the deformation in the foreland compares with that in the collision zone. Low-temperature thermochronology could provide constraints on the timing and rates of this far-field deformation.

Apatite fission track analysis and apatite U-Th/He thermochronometry provide detailed information on the low-temperature thermal history of rocks. Exhumation is often controlled by the interplay between tectonic processes and erosion; thus where tectonic processes lead to exhumation, apatite fission track and He ages have the potential to constrain the timing and rates of deformation (e.g., Fitzgerald et al., 1995; Wolf et al., 1997). The relatively low closure temperatures of these systems (~ 110°C for apatite fission track analysis, e.g., Gallagher et al., 1998, and ~ 70°C for U-Th/He thermochronometry, Wolf et al., 1996) allow documentation of the latest cooling stages of rocks as they pass through the uppermost crust, i.e., as they are exhumed. The latest documented stage of rapid cooling represents the latest episode of tectonic denudation, but only if it was sufficient to exhume rocks from below the closure temperature.

Apatite fission track analyses from the region reveal young ages in the Saint Elias Mountains and the central Alaska Range, documenting rapid uplift and exhumation since ~ 5-6 Ma (Fitzgerald et al., 1995; O'Sullivan and Currie, 1996). To the north, the latest cooling recorded by fission track data occurred ~ 35-40 Ma in the Yukon-Tanana Upland (Dusel-Bacon and Murphy, 2001), ~ 24 Ma in the central Brooks Range and North Slope (O'Sullivan et al., 1997), and ~ 56 Ma in the onshore Beaufort-Mackenzie region (O'Sullivan and Lane, 1997). With a lower closure temperature, U-Th/He thermochronometry has greater potential to document the youngest denudational episode (e.g., Ehlers and Farley, 2003). A recent study of the Fairweather Range (McAleer and Spotila, 2005) reveals young U-Th/He ages (< 5 Ma), documenting Pliocene exhumation, in agreement with the young fission track ages in the nearby Saint Elias Mountains.

Low-temperature thermochronological data has the potential to provide improved constraints on deformation in the foreland belt. Target areas for such a study should include areas of the foreland that display current deformation, e.g., the Mackenzie and Richardson Mountains, and the NE Brooks Range.

Modelling

The deformation estimates provided by this thesis can be used to constrain numerical kinematic models that attempt to explain the observed deformation pattern. The region could be modelled as a number of rigid blocks, which rotate with respect to each other, as has been done in the case of the India-Eurasia collision (e.g., Avouac and Tapponnier, 1993). Perhaps more suitable is the finite element method, which considers deformable blocks and allows more complex patterns of deformation (e.g., Lundgren et al., 1995). One approach is the inversion of strain rate and/or fault slip data to solve for a smooth velocity field (e.g., Holt et al., 1995). The other main approach is to use forward models, which solve equations of stress equilibrium and conservation of mass with assumed rheologies and densities in order to predict velocities, stresses and strain rates that can then be compared with those observed (e.g., Houseman and England, 1986; Bird, 1999).

Finite element modelling of crustal deformation in Alaska was carried out by Lundgren et al. (1995) and by Bird (1996). The thin-shell model of Lundgren et al. (1995) is constrained by very long baseline interferometry (VLBI) data and by fault slip data, with boundary conditions defined by Pacific-North America plate motions. Their preferred model produces displacement of the northern Cordilleran crust to the northeast at ~ 10 mm/yr; this motion is absorbed in the Mackenzie Mountains. These results are in approximate agreement with geologic observations, except that the rate is higher than inferred by GPS and seismic deformation rates and the model produces no deformation in the Richardson Mountains, where earthquake statistics tell us that dextral strike-slip motion is occurring at rates of ~ 3 mm/yr (Figure 5.2; Chapter 4).

Input data for the thin-plate models of Bird (1996) include variable crust and lithospheric thickness, heat flow, elevation, and active fault traces and dips, with boundary conditions imposed by plate motions. The models predict anelastic strain rate, stress and velocity fields, which were compared with available strain information including fault slip rates, and geodimeter and VLBI data in order to choose a best-fit model. This model also predicts northeastward motion of the northern Cordillera, and appears to produce deformation in the Richardson Mountains as well as the Mackenzies. The modelling code used by Bird, along with other variations, is available as free software (ftp://element.ess.ucla.edu), with the model assumptions and basic instructions given by Bird (1999). The improved constraints on crustal deformation in the northern Cordillera arising from this thesis should allow for a model that more accurately explains the regional kinematics.

ADDITIONAL STUDY: CHAPTER 6

Coseismic Subsidence in great Cascadia Earthquakes: Coastal Estimates versus Elastic Dislocation Models

INTRODUCTION

This chapter on coastal constraints on great earthquake subsidence is based on our published article for the 1700 event (Leonard et al., 2004) and on an unpublished report to the U.S. Geological Survey (Hyndman et al., 2004) that presented subsidence data for pre-1700 events and additional modelling. The study is presented here to include all research carried out during the PhD program.

Despite the lack of great megathrust earthquakes at the Cascadia subduction zone (Figure 6.1) in historical time (the last 200 years), their occurrence approximately every 500 years is well supported by several lines of evidence. Japanese records of wave heights from a far-field tsunami in January 1700 are consistent with a magnitude 9 earthquake on the Cascadia megathrust (Satake et al., 1996). This occurrence is compatible with Native American oral records from Cascadia (e.g., Ludwin, 2002), the deep-sea turbidite record (Adams, 1990; Goldfinger et al., 2003), and with coastal subsidence evidenced by buried soils and submerged trees where the time of submergence can in some cases be dated to lie between the 1699 and 1700 growing seasons (Yamaguchi et al., 1997; Jacoby et al., 1997).

Geodetic measurements (e.g., Savage and Lisowski, 1991; Dragert et al., 1994; Mitchell et al., 1994; Hyndman and Wang, 1995; McCaffrey et al., 2000; Miller et al., 2001; Mazzotti et al., 2003a) indicate that the Cascadia subduction thrust is presently almost fully locked and that interseismic elastic strain accumulation is causing uplift and shortening along much of the coast. Figure 6.2 shows the schematic interseismic and coseismic deformation expected with such a subduction thrust fault. Close to the deformation front, there is interseismic subsidence and coseismic uplift, whereas farther

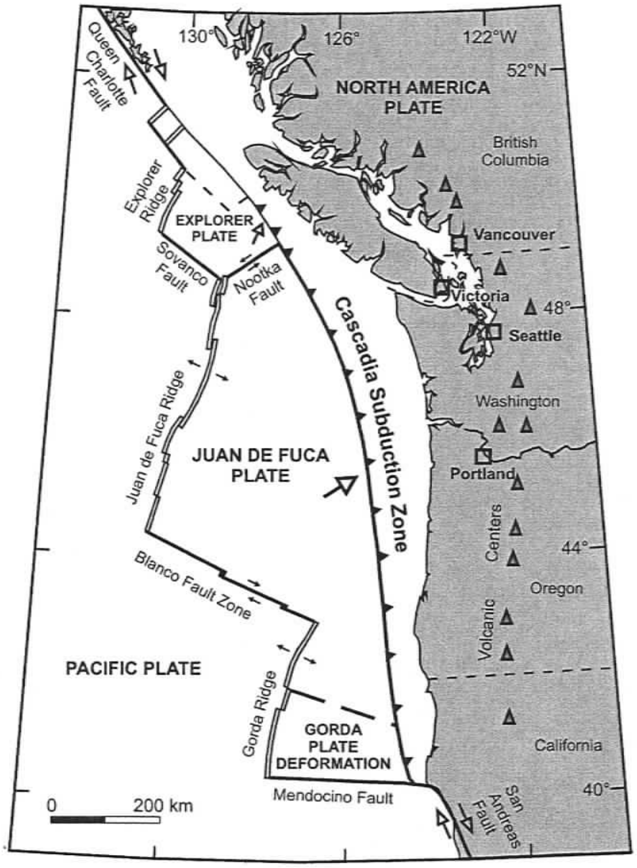

Figure 6.1. The plate tectonic setting of the Cascadia subduction zone.

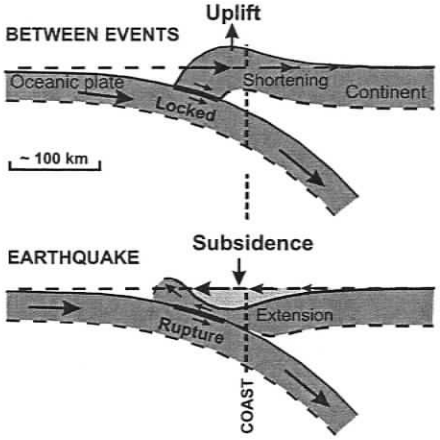

Figure 6.2. The pattern of interseismic and coseismic deformation expected with a subduction thrust fault (modified from Dragert et al., 1994). Much of the Cascadia coast is currently undergoing interseismic uplift; during a great earthquake this area is subject to coseismic subsidence.

landward, coinciding with much of the Cascadia coast, a pattern of interseismic uplift and coseismic subsidence prevails. Such patterns of interseismic and inverse coseismic vertical motions have been observed at other subduction zones that have experienced historical great earthquakes, including Chile (Plafker and Savage, 1970), Alaska (e.g., Plafker, 1972), southwest Japan (e.g., Thatcher, 1984; Savage and Thatcher, 1992; Hyndman and Wang, 1995), and Sumatra (e.g., Gahalaut et al., 2006; Subarya et al., 2006).

The determination of the amount of coseismic slip in the 1700 and previous events is crucial to our understanding of seismic hazard in the region. Estimates of coastal coseismic subsidence provide an important constraint on the rupture extent and slip. Current hazard assessments for great earthquakes are largely based on the predictions of elastic dislocation models, which are constrained by recent geodetic strain measurements and by thermal estimates.

The main objective of this study is to compare the magnitude of coseismic subsidence estimated from coastal marsh studies for the 1700 event with that predicted by elastic dislocation models. The need for this comparison has been stressed previously (Flück et al., 1997; Long and Shennan, 1998). The coastal marsh data perpendicular to the margin (east-west) are too limited to significantly constrain the rupture area. However, the coastal data along the Cascadia margin do provide a strong constraint to the rupture area, especially the critical landward limit.

The coastal subsidence data for great Cascadia earthquakes prior to the 1700 event are very limited, but indicate that although the magnitude of subsidence has varied it is generally similar (e.g., Peterson et al., 1997). We also examine coastal coseismic subsidence for pre-1700 events, but the event dating is not yet adequate to correlate individual pre-1700 events along the margin. Future studies may allow comparisons for individual events similar to our work on the 1700 earthquake.

COSEISMIC SUBSIDENCE IN MEGATHRUST EARTHQUAKES

Coastal coseismic subsidence and uplift in historical subduction zone earthquakes have been documented in Alaska, Chile, Japan, and Sumatra. In a more subtropical environment along the coast of Sumatra, the great earthquake of 2004 resulted in diagnostic uplifted or submerged coral (e.g., Subarya et al., 2006). In the case of the M ~ 9 1960 Chile and 1964 Alaska great earthquakes, coseismic subsidence converted some vegetated coastal lowlands to barren estuarine mudflats (e.g., Plafker and Savage, 1970; Ovenshine et al., 1976). At the head of Cook Inlet near Portage, Alaska, aggradation and uplift have since permitted the re-establishment of lowland trees and shrubs (Ovenshine et al., 1976; Brown et al., 1977; Atwater et al., 2001). Therefore, in a stratigraphic sequence, a layer of peat overlain by intertidal mud ("peat-mud couplet") that grades upwards into another peat layer may represent a cycle of coseismic subsidence and interseismic shoaling (Atwater, 1987) as shown in Figure 6.3. Peat-mud couplets have also been cited as evidence of ancient subduction earthquakes in Chile and Alaska (e.g., Wright and Mella, 1963; Ovenshine et al., 1976; Combellick, 1986).

Atwater (1987) was the first to describe buried soils at Cascadia in detail and attribute them to past subduction megathrust earthquakes. They have since been found to occur at many estuaries along the coast in northern California, Oregon, Washington, and southern Vancouver Island, British Columbia (Figure 6.4). Figure 6.5 shows a typical peat-mud couplet in Cascadia, where the peat is capped by a tsunami-deposited sand layer. These sequences, as in Chile and Alaska, have also been attributed to ancient subduction earthquakes.

However, peat-mud couplets are not uniquely a product of large earthquakes; similar stratigraphic sequences are observed at mid-latitude passive margin coasts, and may be caused by a range of local and regional aseismic processes that result in relative sea-level changes (e.g., Nelson et al., 1996a). Thus, criteria are necessary to distinguish peat-mud couplets that result from great earthquake subsidence from those that are produced by other processes. The 1700 buried soil fulfils the criteria established by Nelson et al. (1996a): (1) subsidence was sudden, as evidenced by the preservation of growth-position macrofossils, and (2) it amounted to at least 0.5 m along the majority of

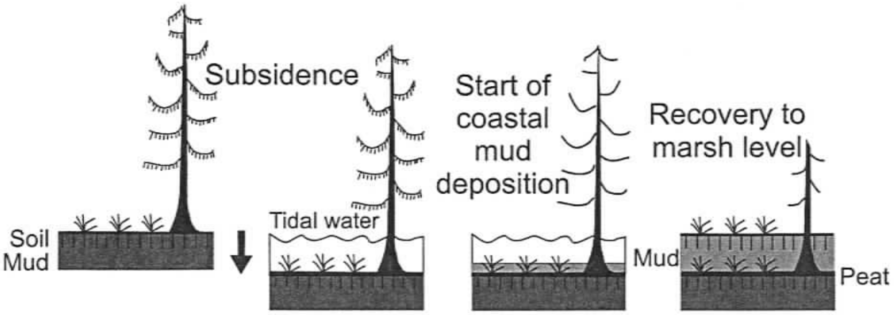

Figure 6.3. The formation of peat-mud couplets as a result of coseismic subsidence during megathrust earthquakes (modified from Atwater et al., 1995).

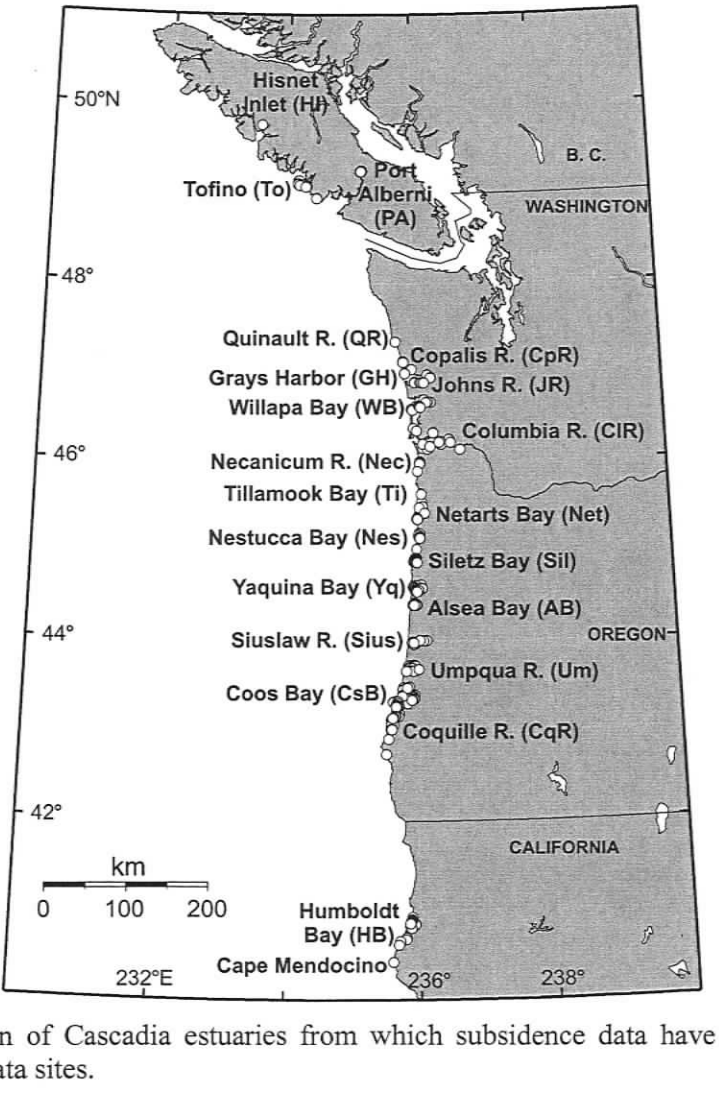

Figure 6.4. Location of Cascadia estuaries from which subsidence data have been extracted. Open circles mark data sites.

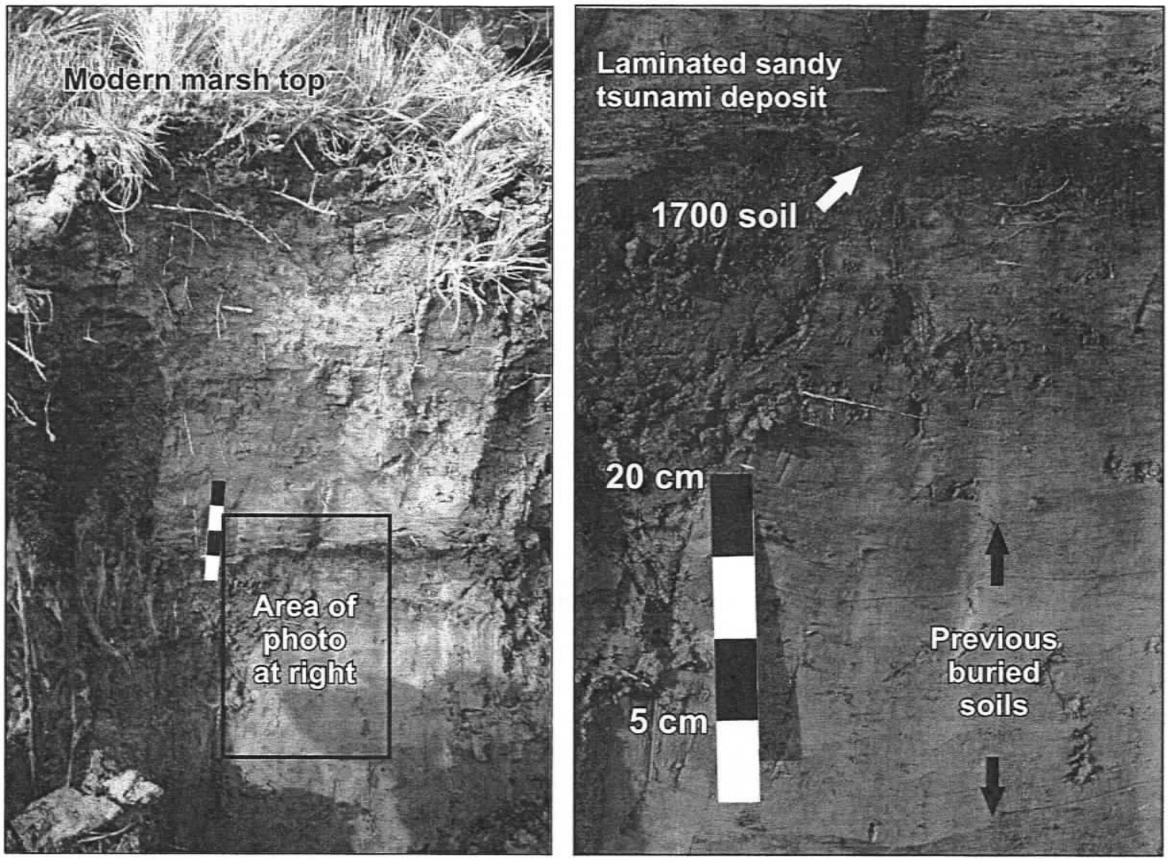

Figure 6.5. The 1700 buried soil, as exposed in a cutbank section of the Niawiakum River, Willapa Bay, Washington. The 1700 peat is overlain by sandy layers interpreted to have been deposited by a tsunami coincident with the earthquake; the sand is in turn overlain by intertidal mud, grading up to the present marsh surface. Previous megathrust earthquakes are suggested by older buried soils below the 1700 horizon. (Photo by author)

the coast; (3) lasting submergence is shown by a long-term switch to lower intertidal zones above the 1700 horizon; (4) the 1700 soil is widely correlated, and (5) it is often covered by a laminated sandy deposit (e.g., Figure 6.5) inferred as the product of a tsunami generated in the event, that rushed into the subsided coastal area.

There are two methods available to determine the coseismic subsidence from coastal marshes (described in detail in sections below): (1) a technique that finds, by comparison with elevations of the different zones of the modern marsh, the paleoelevation difference between the 1700 horizon and overlying sediments, (2) the depth interval between the modern marsh top and the buried marsh, corrected for global sea level change, postglacial rebound, and interseismic land uplift. Method 1 and its results, which are primarily a compilation of previously published work, are presented first. We then describe our elastic dislocation models, and compare the model predictions of subsidence with the results of method 1. Then we discuss method 2 and its results, which are original to this study. Finally, a compilation of coseismic subsidence estimates for pre-1700 events are presented for comparison with the 1700 coseismic subsidence.

METHOD 1: ESTIMATING COSEISMIC SUBSIDENCE USING INTERTIDAL ELEVATION INDICATORS ABOVE AND BELOW BURIED MARSH TOP

The magnitude of coseismic subsidence is the difference in paleoelevation between the 1700 marsh top horizon and the sediments that either directly overlie it or that overlie an intervening tsunami sand cap; in the case of the latter, coseismic subsidence amounts to the thickness of the sand deposit added to the paleoelevation difference. Such a definition assumes that (1) the overlying sediment records the time immediately after the earthquake (i.e., prior to any large postseismic deformation) and (2) the sediments are unaffected by compaction or other subsequent disturbance (discussed below).

Paleoelevation is determined by calibration of elevation indicators in the buried sediment with the depth indicators in the zones of the modern marsh surface. Modern intertidal elevational zones may be defined by the distribution of: (1) organic content, (2) vascular plants, (3) foraminiferal assemblages, (4) diatom assemblages, and (5) pollen assemblages. Although the distribution of estuarine organisms is controlled by many biologic and ecologic factors, most of these are directly related to elevation relative to average sea level (e.g., Frey and Basan, 1985; Jennings and Nelson, 1992); it is primarily the amount and duration of subaerial exposure that limits organisms to a particular elevation range (Scott and Medioli, 1980).

In this study we review and analyze published reports on Cascadia marsh subsidence. In some cases we have slightly revised the published subsidence in an effort to use consistent methods along the whole margin. We have also added subsidence estimates to the database based on our interpretation of other published coastal stratigraphic and sedimentological data.

Survey of Modern Marsh

Ideally, the modern marsh reference sites are surveyed in close proximity and a similar environment to the site of fossil data collection; this was done in the studies of Darienzo and Peterson (1990), Hemphill-Haley (1995b), Guilbault et al. (1996), Shennan et al. (1996; 1998), Barnett (1997), Peterson et al. (1997), and Hughes et al. (2002). In estuaries where no modern reference survey has been done, we compare the fossil data to surveys of nearby estuaries, generally combining the data from several localities in order to reduce miscorrelation due to site differences. Averaging reference site data results in an increase in the calculated subsidence errors. A typical modern survey is carried out as follows. One or more surface transects of the modern marsh from the forest edge to the water are sampled at short intervals, for example at every 10-cm change in elevation; relative elevations are tied into local benchmarks to give absolute elevation with respect to tide level. A number of intertidal zones defined by elevation can be determined from analysis of surface and near-surface sediment, plants and micro-organisms. Sampling methods and processing are described for analysis of foraminifera by Guilbault et al. (1995); diatoms by Nelson and Kashima (1993) and Hemphill-Haley (1995a); and pollen by Hughes et al. (2002).

Organic Content and Plant Macrofossils

Organic content of estuarine sediment generally increases with elevation in the intertidal zone (e.g., Peterson and Darienzo, 1991). Modern Cascadia marshes generally exhibit a continuous vertical transition from mud at low elevations, through rooted mud, peaty mud and muddy peat, to peat at higher elevations (for definitions see Peterson and Darienzo, 1991, p. 5). The elevational limits of each of these modern zones may be compared with the buried sediment types to allow paleoelevation to be estimated to a first order. Organic content is estimated visually or by loss on ignition. However, because relative peat development varies considerably among sites, the zoning may not be robust, and estimates based on this property alone are found to be less reliable than those based on fossil assemblages (Nelson et al., 1996a).

Plant macrofossils provide valuable clues to the paleoelevation of buried sediment, although often few if any are preserved. An indicator species in the buried marsh is taken to represent a paleoelevation within the elevation range of that species in the modern marsh; the narrower that modern range, the more precise the paleoelevation estimate. For example: (1) Spruce trees will grow no lower than the forest edge (no high-tide inundation); (2) typical high marsh plants are *Potentilla*, *Grindelia* and *Juncus*; (3) *Salicornia*, *Distichlis* and *Triglochin* characterize the low marsh; (4) *Triglochin*, *Carex* and *Scirpus* may colonize the upper tidal flats (e.g., Peterson et al., 1997).

Microfossils: Statistical Methods

At Cascadia, pollen data have been used in only one detailed study: coseismic subsidence was estimated for Tofino, Vancouver Island, by Hughes et al. (2002). Zoning of modern pollen data is achieved by classification with optimal splitting. Determination of indicator taxa (pollen that are good indicators of elevation), and analogue matching between current surface and fossil pollen samples, allow the development of a transfer function calibration of fossil pollen samples to elevation (for details see Hughes et al., 2002).

Elsewhere, marine microfossils usually provide the most precise paleoelevation estimates. In foraminiferal and diatom studies, Q-mode factor analysis may be used to cluster the modern data into groups defined by elevation (for details of statistics see Hemphill-Haley, 1992; 1995a; Guilbault et al., 1995; 1996). Paleoelevation of subsurface horizons is calculated by application of transfer functions (derived from the factor analysis) to factored fossil data. Discriminant function analysis (e.g., Jennings and Nelson, 1992; Nelson and Kashima, 1993; Nelson et al., 1996b) determines how well the modern data are grouped, i.e., whether the selected zones are statistically significantly distinct. Discriminant functions derived from the modern data are applied to the fossil data for paleoelevation determination. Visual comparison of fossil and modern data usually yield paleoelevation estimates very comparable to those derived from statistical methods (e.g., Guilbault et al., 1995).

Sources of Error

The correlation of a buried sediment horizon with a modern intertidal zone elevation is a relatively precise way of determining its paleoelevation; however the accuracy of the methods described above depends on a number of factors: (1) the width and thus elevation range of intertidal zones are functions of the local tidal range; intertidal zones at Cascadia are typically broad and have gradational boundaries (e.g., Jennings and Nelson, 1992; Hemphill-Haley, 1995a). These factors reduce the resolution of coseismic subsidence estimates. Use of a combination of elevation indicators that differ in their zonation narrows the acceptable paleoelevation range.

(2) The elevations of upland and mudflat zones are only defined at the lower and upper ends respectively. Thus, in a stratigraphic sequence, only the minimum change to or from either of these zones can be estimated with useful accuracy (e.g., Jennings and Nelson, 1992).

(3) A modern marsh survey should be carried out in as close proximity as possible to the fossil sample site in order that it represents the best possible calibration analogue. Neighbouring estuaries may have different tidal ranges, and within an estuary local site differences such as the presence of streams may increase error (e.g., Guilbault et al., 1996). At most Cascadia estuaries it is probably a safe assumption that tidal conditions within an individual estuary have not changed significantly in the last 300 years (e.g., Peterson and Darienzo, 1991; Nelson et al., 1996a). However, there is no modern analogue at Cascadia for the sediments immediately above the 1700 horizon and tsunami sand; the estuarine environment in the aftermath of coseismic subsidence is little understood (e.g., Shennan et al., 1998; Hughes et al., 2002).

(4) If the sediment section was affected by compaction due to shaking at the time of the earthquake, coseismic subsidence will be overestimated. Compaction accounted for a significant proportion of subsidence in some areas for the 1964 Alaska earthquake (0.8 m of 2.4 m subsidence in the Portage area) (Ovenshine et al., 1976). However, the Portage area is underlain by ~ 300 m of unconsolidated sediment, and compaction does not appear to have played a significant role in subsidence at Cascadia, where unconsolidated sediments are usually thin. The 1700 soil can be traced in outcrop onto indurated Pleistocene deposits at the Copalis River and Willapa Bay, Washington

(Atwater, 1987; 1992; Atwater and Hemphill-Haley, 1997); at Tofino, Vancouver Island, the Holocene sequence (< 2 m thick) overlies compact glaciomarine clay and shows no systematic difference in unit thickness for sites close to bedrock and those further away with thicker recent sediments (Clague and Bobrowsky, 1994a; Guilbault et al., 1995). In cores from Alsea Bay, Oregon, Peterson and Darienzo (1991) found relatively small changes in bulk density downcore, suggesting compaction has not been a major factor.

(5) Another concern is whether the sediments overlying the 1700 horizon were deposited quickly enough that they predate significant postseismic deformation associated with deep creep on the fault or viscoelastic rebound of the mantle. The postseismic vertical deformation could produce either uplift or extra subsidence in the zone of coseismic subsidence. Postseismic uplift of up to 0.55 m in one area had occurred in 12 years following the 1964 Alaska earthquake (Brown et al., 1977). The buried peat near Tofino is overlain by an undisturbed layer of tsunami sand; the fact that this was not washed away while exposed in the intertidal zone suggests that sedimentation resumed almost immediately after the 1700 quake (Guilbault et al., 1996). At Tofino, paleoelevation studies (pollen and foraminifera) indicate that the sediment between 1 and 7 cm above the tsunami sand represents about 40 cm of uplift; the difference (34 ± 30 cm) is attributed to postseismic rebound (Guilbault et al., 1996; Hughes et al., 2002). Higher than 7 cm, sedimentation has kept pace with elevation change (20 cm uplift in 17 cm sediment), suggesting that postseismic rebound had practically ceased after 7 cm of sedimentation. Guilbault et al. (1996) suggest that this sediment thickness represents a few to several decades. Discriminating the rate of sedimentation in interseismic sediments has yet to accomplished (Shennan et al., 1998). Studies in the aftermath of the 2004 Sumatra megathrust earthquake may aid our understanding of postseismic motion (e.g., Hashimoto et al., 2006).

An important question is whether populations had time to colonize the post-1700 sediments before much rebound occurred and therefore to record the full amount of coseismic subsidence. Diatom populations can establish within days to weeks in shallow water, and therefore fossil assemblages in post-1700 sediments should record mainly coseismic subsidence (Hemphill-Haley, 1995b).

(6) There may be a bias in the microfossil record due to differential preservation or transport that increases the error of coseismic subsidence estimates. For example, finely silicified diatom species such as *Gyrosigma* spp. are vulnerable to dissolution, whereas the marine-brackish water benthic species *Paralia sulcata* is very resistant. Because the latter forms long chains easily entrained into the plankton, its abundance is readily enhanced in estuarine deposits as allochthonous (transported) valves (Hemphill-Haley, 1995b).

1700 Cascadia Earthquake Coseismic Subsidence Estimates

A compilation of coseismic subsidence estimates (Table E1, Appendix E; summary in Table 6.1) is shown plotted against latitude in Figure 6.6, and against longitude in Figure 6.7. There are two large gaps in data along the Cascadia coast, one extending between central Washington and central Vancouver Island, the other between southern Oregon (Coquille) and Humboldt Bay, northern California. These areas lack large tidal marshes (Peterson et al., 1997). Some of the compiled estimates have previously been published, others are interpretations of published core logs or reinterpretations of published estimates based on comparison with modern surveys of intertidal zones in nearby estuaries, for example as described by Peterson et al. (1997) for a number of Washington and Oregon estuaries, Shennan et al. (1998) for Netarts Bay, Oregon, Jennings and Nelson (1992) and Nelson and Kashima (1993) for Coos Bay and Siuslaw River, Oregon, and Shennan et al. (1996) for Johns River, Washington.

The plotted uncertainty on the coseismic subsidence estimates (± 0.25 to 0.8 m; Figures 6.6 and 6.7) results mainly from the width of intertidal zones, which control the size of the paleoelevation ranges used to calculate coseismic subsidence. For sites where the modern marsh has not been surveyed, uncertainty is increased as previously described. Errors are greater in the event that unrecognized compaction, postseismic rebound or bias in the fossil record, as discussed above, were significant.

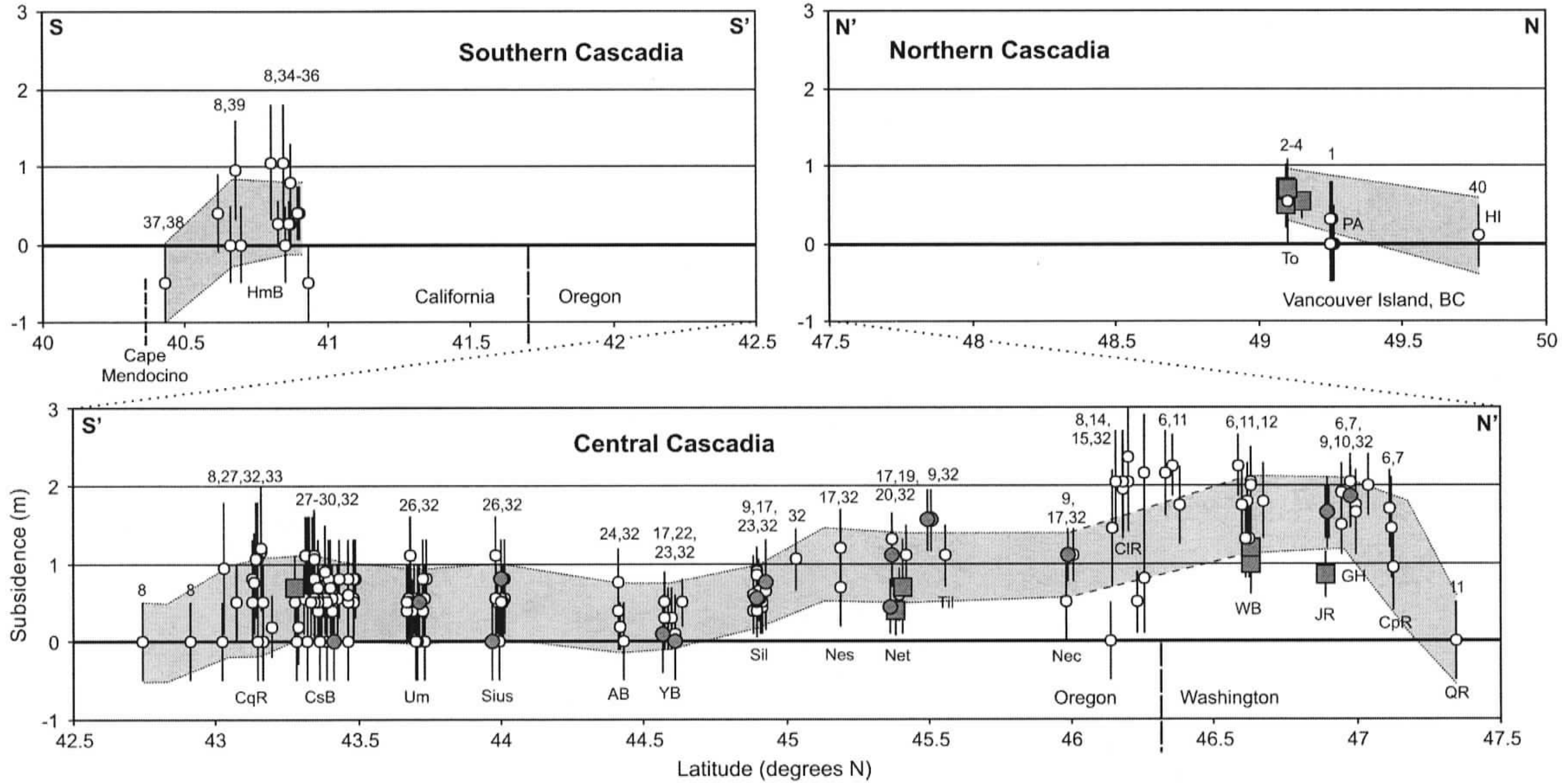

Figure 6.6. Compilation of coseismic subsidence estimates made using method 1, plotted against latitude. Individual error bars represent the uncertainty due to a range of possible paleoelevations above and below the 1700 horizon. Grey shading represents the weighted mean plus or minus weighted standard deviation of groups of points; the Columbia River and Port Alberni data are excluded from this shading, the former due to unreliability as discussed in the text, the latter due to a location significantly inland. Grey squares are estimates made via detailed microfossil studies; grey circles represent estimates made using organic content and relative percentage of freshwater/brackish diatoms plus or minus plant macrofossils; open circles are estimates made using organic content plus or minus plant macrofossils. Locations and abbreviations shown in Figure 6.5. Numbers above data points reference the data sources (see Table 6.1).

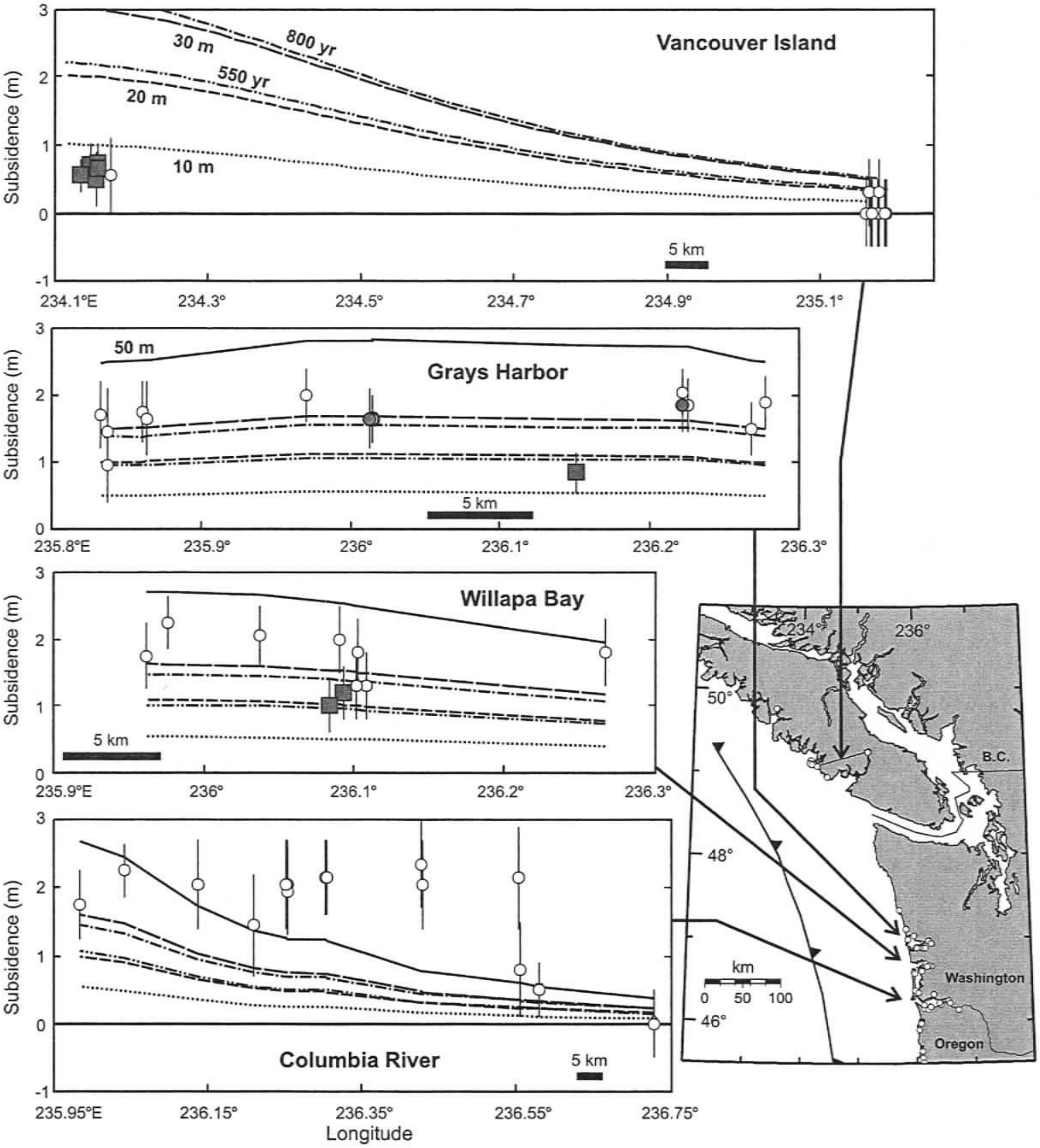

Figure 6.7. Transverse sections of the Cascadia coastal subsidence data plotted against longitude, in comparison with the subsidence predictions (for the same sites) of elastic dislocation models described in the text. Error bars and symbols as explained in Figure 6.6. Notches apparent in the model curves are due to north-south variations in site locations.

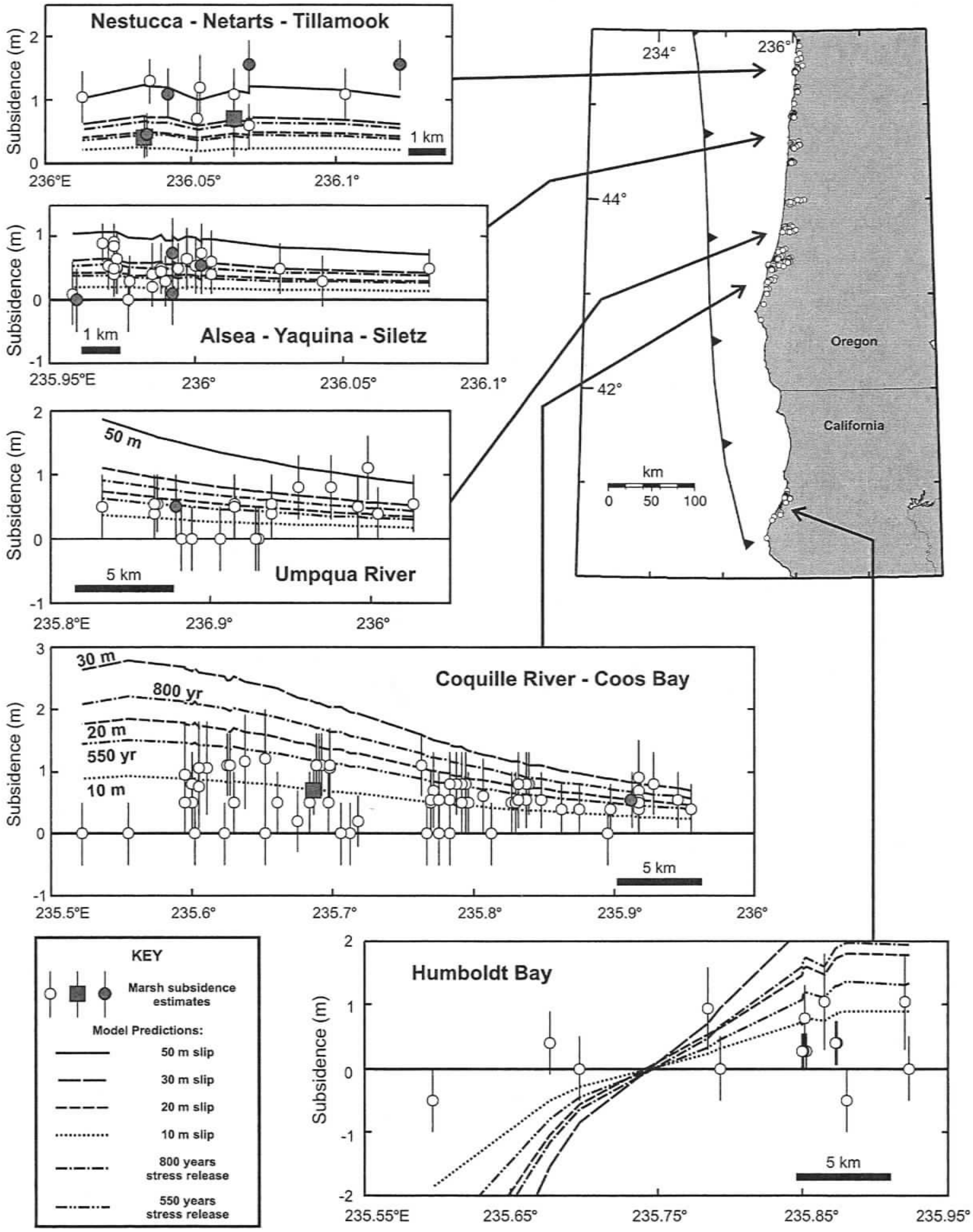

Figure 6.7. (Continued)

Table 6.1. Summary of estimated Cascadia coseismic subsidence: 1700 and pre-1700 events.

Marsh location	Buried soils	Mean depth of 1700 soil (m)	Range of estimated subsidence (m)	Coseismic subsidence: mean ± std. deviation (m)	Max. # soils; Total # ests.	Data Sources[1]
Port Alberni	1700	0.46	0 ± 0.5 to 0.3 ± 0.5	0.07 ± 0.13	1;9	1
Tofino	1700	0.28	0.5 ± 0.3 to 0.72 ± 0.3	0.62 ± 0.09	1;6	2-5
Copalis	1700	1.18	0.95 ± 0.55 to 1.7 ± 0.5	1.37 ± 0.38	1;3	6,7
River	pre-1700		0.6 ± 0.5 to 1.7 ± 0.5	1.03 ± 0.59	3;3	6,7
Grays	1700	0.59	0.85 ± 0.3 to 2.05 ± 0.35	1.7 ± 0.31	1;12	6,8-10
Harbor	pre-1700		0.1 ± 0.5 to 1.9 ± 0.4	1.0 ± 0.66	7; 18	6, 10
Willapa	1700	0.83	1 ± 0.4 to 2.25 ± 0.4	1.7 ± 0.42	1;12	6,11-13
Bay	pre-1700		0.1 ± 0.5 to 2.25 ± 0.4	1.33 ± 0.70	7; 17	6
Columbia R.	1700	1	0 ± 0.5 to 2.35 ± 0.65	1.67 ± 0.75	1;13	6,8,14-16
Necanicum	1700	0.61	0.5 ± 0.5 to 1.1 ± 0.35	0.9 ± 0.35	1;3	8,9,17,18
River	pre-1700		0.1 ± 0.5 to 1.0 ± 0.5	0.58 ± 0.51	3;5	9,30
Tillamook	1700	0.51	1.1 ± 0.4 to 1.55 ± 0.4	1.4 ± 0.26	1;3	8,15
Bay	pre-1700		0.85 ± 0.4	0.85 ± 0.4	1;1	9
Netarts	1700	0.61	0.4 ± 0.32 to 1.1 ± 0.4	0.81 ± 0.36	1;7	8,17,19-21
Bay	pre-1700		0.4 ± 0.4 to 1.3 ± 0.5	0.80 ± 0.39	6;9	19, 20
Nestucca	1700	0.69	0.7 ± 0.5 to 1.2 ± 0.5	0.95 ± 0.35	1;3	8,17
Bay	pre-1700		0.1 ± 0.4 to 1.3 ± 0.5	0.55 ± 0.31	9;45	41
Siletz	1700	0.6	0.4 ± 0.35 to 0.9 ± 0.3	0.58 ± 0.15	1;21	8,9,17,19
Bay	pre-1700		0.3 ± 0.3 to 0.82 ± 0.45	0.50 ± 0.45	5;24	23
Yaquina	1700	0.58	0 ± 0.5 to 0.5 ± 0.4	0.29 ± 0.19	1;8	8,17,22,23
Bay	pre-1700		0.2 ± 0.5 to 0.85 ± 0.4	0.48 ± 0.16	8;34	22, 41
Alsea	1700	0.51	0 ± 0.5 to 0.75 ± 0.45	0.34 ± 0.32	1;4	8,17,24,25
Bay	pre-1700		0.2 ± 0.3 to 1.35 ± 0.45	0.45 ± 0.28	9;71	25
Siuslaw	1700	0.88	0 ± 0.5 to 1.1 ± 0.5	0.53 ± 0.31	1;12	8,26
	pre-1700		0.5 ± 0.4 to 1.2 ± 0.6	0.67 ± 0.22	7;43	26,27
Umpqua	1700	0.95	0 ± 0.5 to 1.1 ± 0.5	0.46 ± 0.31	1;23	8,26
	pre-1700		0.4 ± 0.4 to 1.2 ± 0.6	0.56 ± 0.14	6;49	26,27
Coos	1700	0.72	0 ± 0.5 to 1.1 ± 0.6	0.61 ± 0.32	1;52	8,26-31
Bay	pre-1700		0 ± 0.5 to 1.2 ± 0.6	0.72 ± 0.26	10;151	26-28,30
Coquille	1700	0.77	0 ± 0.5 to 1.2 ± 0.8	0.51 ± 0.45	1;18	8,27,32,33
	pre-1700		0.4 ± 0.4 to 2.0 ± 1.0	0.91 ± 0.39	6;37	32,42
Humboldt	1700	1.1	0 ± 0.5 to 1.05 ± 0.75	0.44 ± 0.37	1;14	34-36
Bay	pre-1700		0.55 ± 0.45 to 1.05 ± 0.75	0.76 ± 0.22	7;55	39

[1] Data sources: 1, Clague and Bobrowsky, 1994b; 2, Hughes et al., 2002; 3, Guilbault et al., 1996; 4, Clague and Bobrowsky, 1994a; 5, Guilbault et al., 1995; 6, Atwater, 1988; 7, Atwater, 1992; 8, Peterson et al., 1997; 9, Barnett, 1997; 10, Shennan et al., 1996; 11, Peterson et al., 2000; 12, Hemphill-Haley, 1995b; 13, Atwater and Hemphill-Haley, 1997; 14, Atwater, 1994; 15, Peterson et al., 1993; 16, Peterson and Madin, 1997; 17, Darienzo, 1991; 18, Gallaway et al., 1992; 19, Shennan et al., 1998; 20, Darienzo and Peterson, 1990; 21, Peterson and Darienzo, 1988; 22, Peterson and Priest, 1995; 23, Peterson et al., 1996; 24, Peterson and Darienzo, 1996; 25, Peterson and Darienzo, 1991; 26, Briggs, 1994; 27, Nelson, 1992; ; 28, Nelson et al., 1996b; 29, Peterson and Darienzo, 1989; 30, Darienzo and Peterson, 1995; 31, Nelson et al., 1998; 32, Briggs and Peterson, 1993; 33, Witter et al., 1997; 34, Vick, 1988; 35, Carver and Burke, 1989; 36, Jacoby et al., 1995; 37, Carver et al., 1994; 38, Merritts, 1996; 39, Li, 1992; 40, Hutchinson et al., 2000; 41, Darienzo et al., 1994; 42, Witter et al., 2003.

ELASTIC DISLOCATION MODEL

The model coseismic subsidence predictions are from the 3-D elastic dislocation fault model developed for the Cascadia subduction zone by Flück et al. (1997). The model is based on the point source solution by Okada (1985); deformation at each location on the earth's surface is calculated by numerical integration of point source dislocations over the fault plane (details in Flück et al., 1997). The model assumes elastic behaviour, i.e., all of the strain accumulated over the earthquake cycle is released in the earthquake. It also assumes that strain accumulation occurs at the present rate throughout the earthquake cycle.

The geometry of the subduction thrust fault is constrained by Benioff-Wadati seismicity, seismic reflection, seismic refraction, seismic tomography, and teleseismic waveform analysis (Hyndman and Wang, 1995; Flück et al., 1997). The thrust fault consists of a locked zone and a transition zone (Figure 6.8). The entire locked zone ruptures in an earthquake and is locked between events; its up-dip and down-dip limits may be thermally controlled (e.g., Hyndman and Wang, 1993; 1995). In the simple model for the transition zone, fault rupture is assumed to decrease linearly down-dip to zero; continuous aseismic slip is assumed to occur down-dip of this zone. A recently recognized complexity involves semi-periodic slow-slip events that probably occur on the thrust down-dip of the main megathrust rupture zone (e.g., Rogers and Dragert, 2003; Dragert et al., 2004; Kao et al., 2006).

The model is constrained by geodetic data including repeated levelling, repeated gravity, tide-gauge data, triangulation-trilateration laser ranging, and GPS data (cf. references in Hyndman and Wang (1995) and Flück et al. (1997)). Some minor model refinements have been suggested based on recent horizontal GPS data (McCaffrey et al., 2000; Miller et al., 2001; Svarc et al., 2002; Mazzotti et al., 2002), but deformation of the Cascadia forearc makes horizontal data more complex compared to the mainly vertical data used by Flück et al. (1997). In this study, we use an updated Flück et al. model, but the coastal data may be readily compared to other model variations. The convergence direction and rate between the Juan de Fuca (and Gorda) and North America plates vary along the margin, due to clockwise rotation of the Juan de Fuca plate with respect to

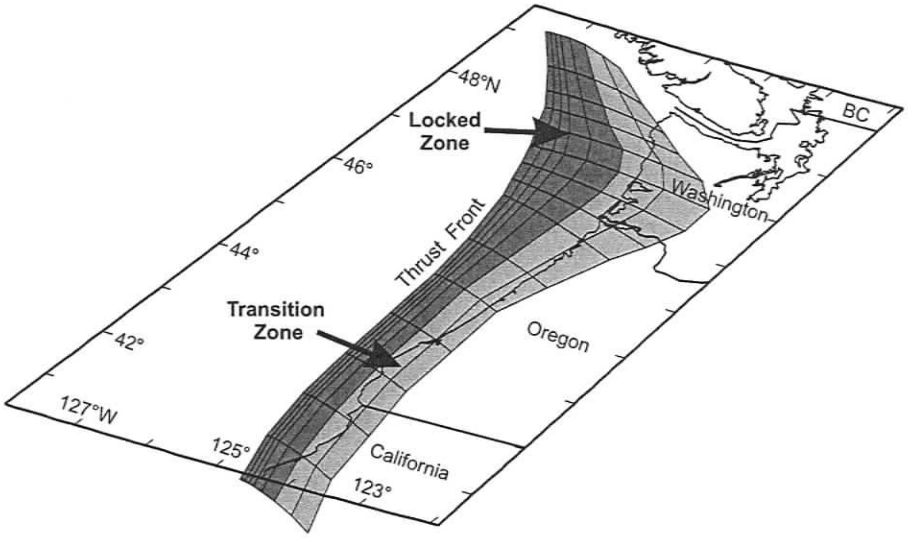

Figure 6.8. The locked and transition zones of the Cascadia megathrust (based on thermal constraints and geodetic data) used in the elastic dislocation model (after Flück et al., 1997).

North America (Wilson, 1993). The convergence increases continuously northward from 27 mm/yr toward 042° at the southern end of the subduction zone to 45 mm/yr toward 056° at the northern end. More margin-normal and higher rates of convergence result in greater coseismic slip, and thus it is critical to incorporate these variations into the model. In our model we have ignored the small effect of the motion of the Cascadia forearc relative to North America.

MODEL PREDICTIONS AND COMPARISON WITH COASTAL MARSH ESTIMATES

The elastic dislocation model is used in two ways to predict the coseismic subsidence that occurred in 1700. Our first approach is to predict the amount of subsidence expected upon release of all the strain built up as a result of convergence over a particular time period. We use strain buildup for two different time intervals. The first uses the ~ 800 years (600-1000) between the previous megathrust earthquake and the 1700 event (Atwater and Hemphill-Haley, 1997), and the second uses an average recurrence interval of 550 years (500-540 years over the last 3500 years from marshes, Atwater and Hemphill-Haley, 1997; 590 years over 7770 years from deep sea turbidites, Adams, 1990). For 800 years of convergence the slip increases from 21.6 m in the south to 36 m in the north, and for 550 years there is 14.9 m slip in the south increasing to 24.8 m in the north. Model coseismic subsidence is calculated for each of the coastal marsh sites. Figure 6.9A shows a comparison between the model coseismic subsidence predictions and the marsh estimates.

The second approach is to use models with a constant slip magnitude along the margin (but allowing for the varying direction of slip along the margin). The predictions for 10, 20, 30, and 50 m slip on the megathrust (and corresponding transition) are shown against latitude in Figure 6.9B in comparison with the coseismic subsidence estimates obtained through coastal marsh studies. The marsh estimates are the weighted mean and standard deviation of groups of points that are close in latitude and longitude. The results of all models are also shown, plotted against longitude, in comparison with the marsh estimates in Figure 6.7.

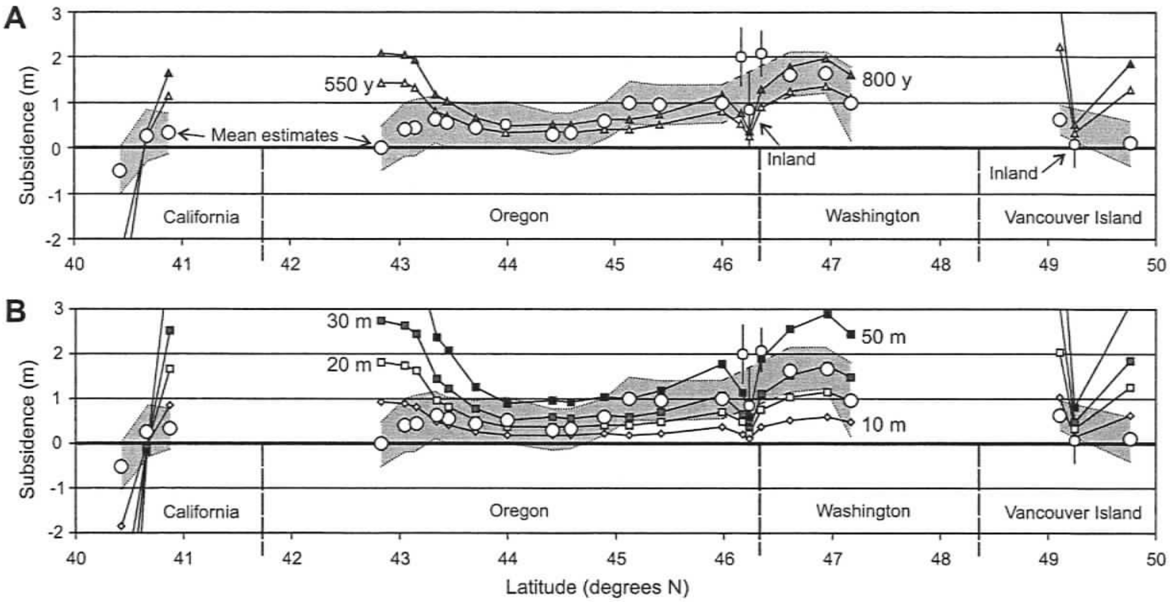

Figure 6.9. Mean subsidence estimates (from Figure 6.6) at averaged locations (see Figure 6.10), compared with the predictions of elastic dislocation models for the same sites. Mean estimates are the weighted mean (circles) plus or minus the weighted standard deviation (shading) of subsidence estimated at closely spaced sites (the Columbia River and Port Alberni data are excluded from the shading). The model predicts the subsidence expected: **(A)** after (i) 800 and (ii) 550 years of plate convergence; **(B)** for uniform slip on the megathrust of 10, 20, 30, and 50 m.

The coastal marsh data are better fit by the models with full release of the strain built up over 550 and 800 years respectively (see also Figure 6.10 for map view of contoured subsidence predicted after 800 years). This agreement supports the conclusion that the convergence varies in rate and direction along the margin. The 550- and 800-year models both produce a similar reasonable agreement with the observed north-south trend of coastal subsidence, fitting within the error of the coastal estimates for much of the margin between south-central Oregon and central Washington. Model time intervals of much less than 550 or greater than 800 years do not provide a satisfactory agreement. None of the models provide a good fit at either end of the subduction zone.

In the south, misfit may be due to break-up of the Gorda Plate and complex subduction tectonics near the Mendocino triple junction (e.g., Chaytor et al., 2002). A greater frequency of events implied from the seafloor turbidite record (Goldfinger et al., 1999; Goldfinger et al., 2003) results in a smaller coseismic displacement per event. Displacement on upper plate structures, probably synchronous with megathrust dislocation, may be responsible for the subsidence experienced at some sites in southern Oregon and northern California (e.g., Carver and Burke, 1989; Goldfinger et al., 1992). Our study cannot resolve the relative contributions of the two sources of subsidence; however, we note that the fit between the dislocation model predictions and the subsidence data would be improved in southern Oregon with a narrower locked zone in that area. A narrower locked zone would cause a seaward shift in the model profiles shown in Figure 6.7.

At the northern, Vancouver Island end of the subduction zone, coseismic subsidence is significantly over-predicted, indicating that the model is a poor representation there. According to uniform slip models, the estimated 1700 coastal subsidence results from less than 10 m of slip on the megathrust. Recent geodetic measurements indicate interseismic uplift rates of ~ 3 mm/yr on western Vancouver Island (2.6 ± 0.6 from repeated levelling, after Dragert et al., 1994; 3.8 ± 2 from absolute gravity measurements, Lambert et al., 2001). This rate is consistent with the average rate for the last 300 years (Figure 6.10). If this uplift rate was sustained over the ~ 800 years since the previous event, one would expect ~ 2.4 m subsidence, approximately the same as predicted by the simple dislocation model, but significantly greater than the 0.65 m

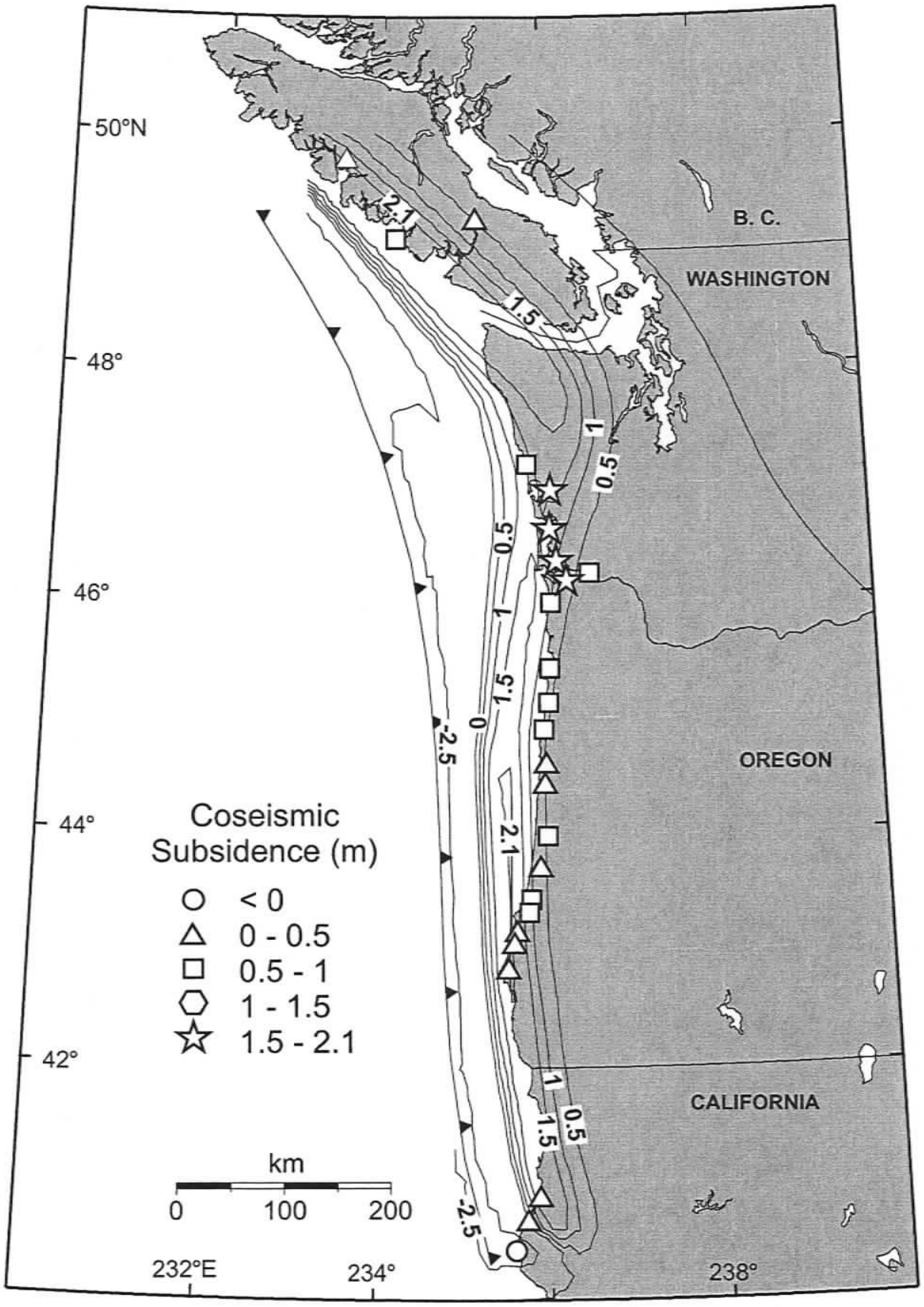

Figure 6.10. Mean subsidence estimates (symbols) of Figure 6.6 in comparison with the predictions of the simple elastic dislocation model (contoured) for the elastic release of 800 years of strain accumulation (Figure 6.9 A).

observed (Hughes et al., 2002). If the 0.65 m of subsidence in 1700 represented release of all the interseismic strain since the previous earthquake, an average interseismic uplift rate of only 0.8 mm/yr over 800 years is implied. An additional complexity in this area is the lack of buried soils older than the 1700 event on western Vancouver Island, in contrast to the rest of the subduction zone. This absence suggests that there is long-term coastal uplift at a rate faster than the sea level rise of ~ 1.8 mm/yr. Postglacial rebound after retreat of the southern Cordilleran ice-sheet can only account for approximately one third of this long-term uplift (estimated at ~ 0.55 mm/yr on western Vancouver Island; Figure 13(c) in Clague and James, 2002). It is possible that the 1700 event released only some fraction of the strain accumulated over the previous ~ 800 years, and that future earthquakes will cause greater subsidence, i.e., the interseismic and coseismic deformation will balance out over a number of earthquake cycles.

Comparisons of the results of uniform slip modelling with subsidence estimates can provide estimates of the magnitude of slip that occurred at different parts of the margin. We have used a simple visual comparison to assign a best-fit uniform slip model for each part of the margin (Figure 6.11). Our results indicate a surprisingly smooth variation of rupture slip along the margin in 1700, but some variability among great earthquakes is expected. The dislocation model suggests that greatest slip in 1700 occurred in northern Oregon/southern Washington (30-50 m), and that slip decreased to the north and south to less than 10 m. Slip along most of the margin is consistent with the expected maximum slip in a magnitude 9 earthquake of ~ 20-30 m (20-25m, 1964 Alaska, Johnson et al., 1996; 20-40 m, 1960 Chile, Barrientos and Ward, 1990; average slip was around 10 m in both events). These slip values indicate a seismic moment release (Brune, 1968) of ~ 5.6×10^{29} to 7×10^{29} N-m, corresponding to a moment magnitude (Hanks and Kanamori, 1979) of 9.1 to 9.2, depending on the tapering of slip towards the ends of the subduction zone. Our result is in agreement with the 1700 event of magnitude 9 suggested from Japanese tsunami wave heights, which require rupture of almost the entire length of the subduction zone (Satake et al., 1996).

The main model anomaly is the Columbia River area, where slip of at least 50 m is suggested. Either this is evidence for significant postseismic creep on the seismogenic fault, or there are problems with the subsidence data. The subsidence data from the more inland Columbia River sites may be biased. Fully saline marine conditions extend only as far upstream as river mile 7 (11.3 km); beyond mile 23 (37 km) the river is fully freshwater (e.g., Pruter and Alverson, 1972). In less saline conditions the elevation zoning relationship may break down, for example, plants usually restricted to higher elevations due to saltwater intolerance may be found at lower elevations.

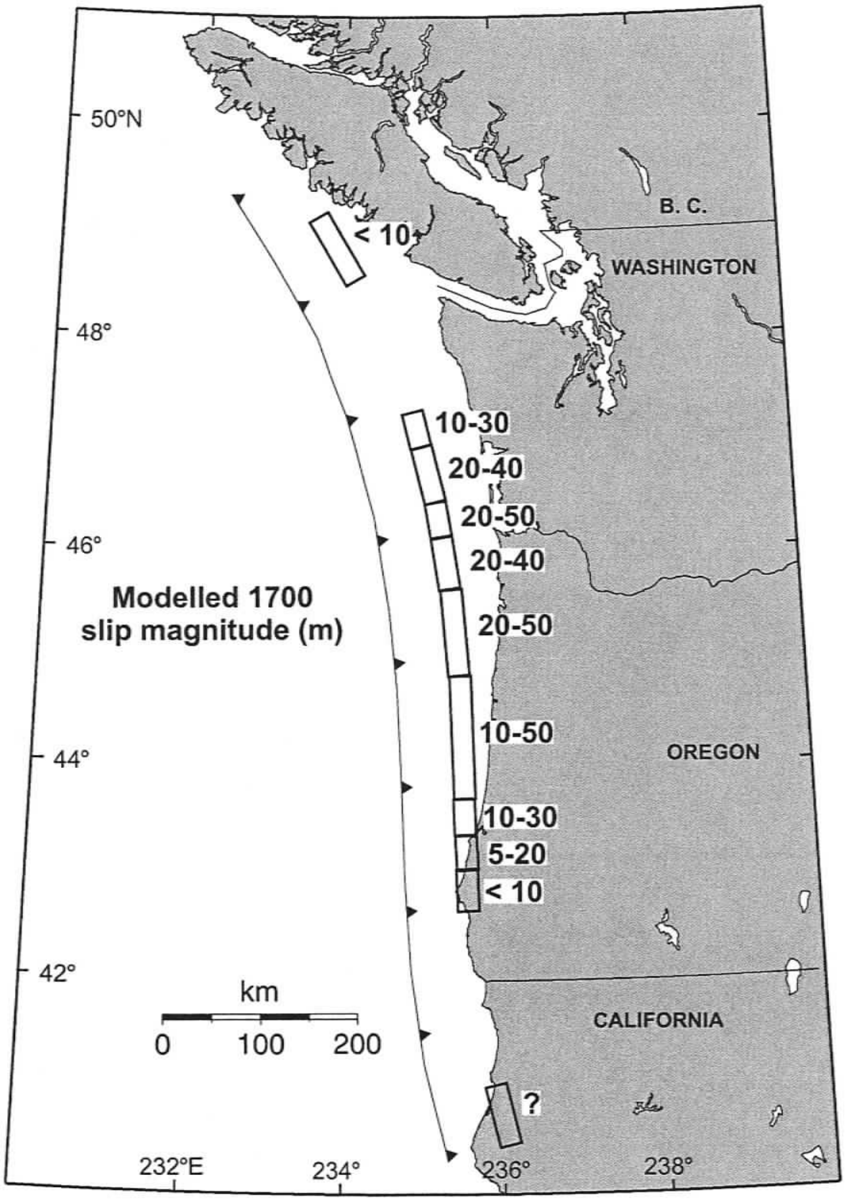

Figure 6.11. Along-coast variations in slip magnitude for the 1700 earthquake, from comparisons of the predictions of the elastic dislocation uniform slip models with geological subsidence estimates (Figure 6.9B). The plate convergence over 800 years ranges, north to south, from 22 to 36 m.

METHOD 2: ESTIMATING COSEISMIC SUBSIDENCE USING 1700 HORIZON DEPTH

A second method of estimating coseismic subsidence is illustrated in Figure 6.12, which also shows how interseismic uplift can be deduced (discussed below). The subsurface depth of the buried soil is measured relative to the current marsh elevation, and this figure is corrected for other processes that have affected its vertical position since the 1700 event. These processes include postglacial rebound, eustatic sea-level change, and interseismic uplift (e.g., Hyndman and Wang, 1995). Postglacial rebound is most significant at the northern end of the subduction zone (up to ~ 0.55 mm/yr), and decreases southwards to zero by ~ 45°N at the coast (Figure 13(c) in Clague and James, 2002); corrections of 0 to + 0.55 mm/yr are accordingly applied to the depth data for the northern half of the subduction zone. Eustatic sea level has risen by approximately 1.8 mm/yr over the last 100 years (Douglas, 1991; 1997); a correction of -1.8 mm/yr from 1700 to the year of measurement is applied.

Total interseismic uplift is more difficult to quantify. In this study we use an elastic dislocation model (constrained mainly by levelling and tide gauge data and using current convergence directions and rates) to predict the interseismic uplift at each site. The convergence rate between the Juan de Fuca plate and the Cascadia forearc is based on recent (~ 1 Myr) plate motion models and integrates separate Explorer, Gorda, and Oregon forearc micro-blocks (see Mazzotti et al., 2002 for description). The resultant interseismic uplift correction, and therefore the subsidence estimates (Figure 6.13), are dependent on the details of the input fault slip geometry, i.e., whether one uses (a) the transition zone with linear down-dip slip decay of Flück et al. (1997), or (b) the larger "effective" transition zone with exponential down-dip decay of Wang et al. (2003).

This method for estimating coseismic subsidence assumes that sediment supply has kept pace with the available vertical accommodation, and that the sediments at the modern surface lie at an elevation equal to the paleoelevation of the pre-earthquake surface, i.e., that the modern and 1700 marsh surfaces at a particular site formed in the same intertidal zone.

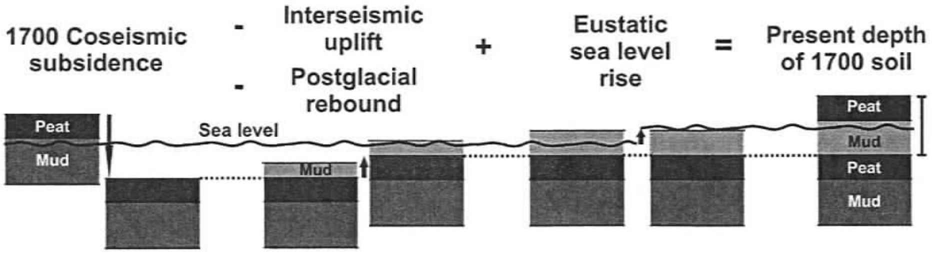

1700 Coseismic subsidence = Present depth of 1700 soil + Interseismic uplift + Postglacial rebound - Eustatic sea level rise

1700 Coseismic subsidence - Present depth of 1700 soil - Postglacial rebound + Eustatic sea level rise = Interseismic uplift since 1700

Figure 6.12. Method 2: the method for estimating coseismic subsidence using the depth of the 1700 peat horizon below the modern marsh top (results in Figure 6.13). Also shown is an independent method of estimating interseismic uplift since 1700, using marsh coseismic subsidence estimates, the depth of the 1700 horizon, postglacial rebound, and eustatic sea level rise (results in Figure 6.14).

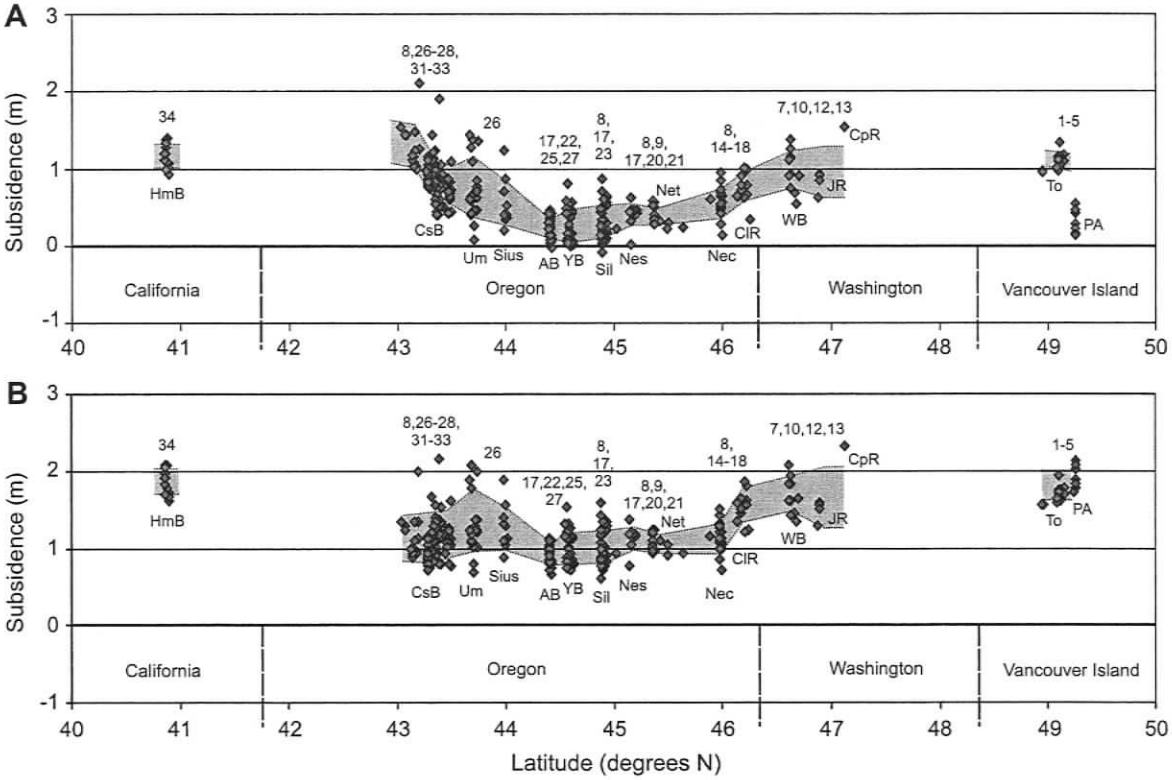

Figure 6.13. Compilation of coseismic subsidence estimates made using method described in Figure 6.12 (method 2). Measurements of the depth of the buried soil were corrected for eustatic sea-level rise (assumed constant at 1.8 mm/yr), postglacial rebound, and interseismic uplift, **(A)** using the elastic dislocation model of Flück et al., 1997, **(B)** using the revised dislocation model of Wang et al. (2003). Grey shading represents the mean plus or minus the standard deviation of groups of points. Locations and abbreviations shown in Figure 6.4. Numbers above data points reference the data sources (see Table 6.1).

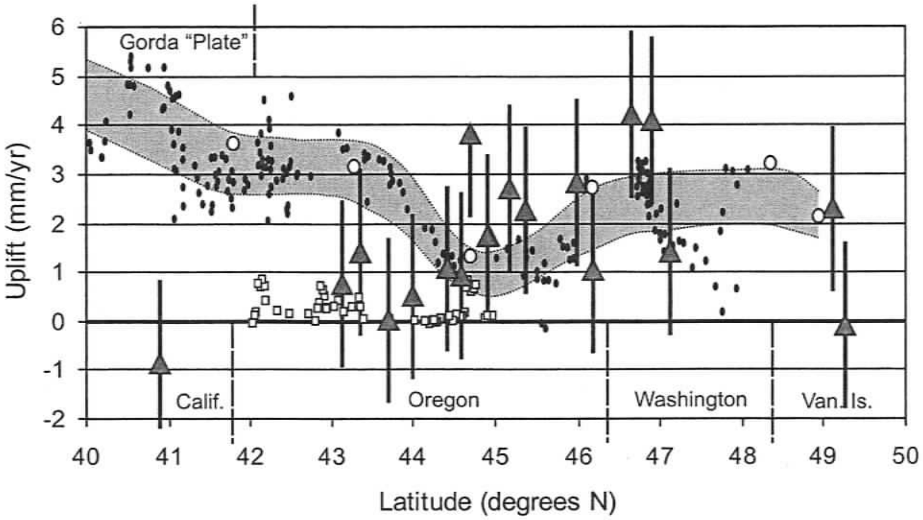

Figure 6.14. Interseismic uplift since 1700 (grey triangles) calculated inversely using method shown in Figure 6.12 (method 2) and converted to mm/yr, compared with recent geodetic measurements of uplift (open circles, tide gauge data; filled circles, levelling data; shaded curve represents ~ 1σ of the geodetic data; Hyndman and Wang, 1995) and long-term uplift estimates based on uplifted shore platforms of 80, 105, and 125 ka (open squares; Kelsey et al., 1994). Error bars are based on assumed error of subsidence estimates of ± 0.5 m.

As the true geometry of the coseismic and interseismic transition zone remains uncertain, estimates of coseismic subsidence gained using this method are far from robust. However, the pattern of coseismic subsidence is broadly similar to that obtained from coastal marsh studies that use elevation indicators (Figure 6.6), and thus provides support for the latter estimates.

An alternative way to use the marsh burial depth is to fix the subsidence using estimates derived from the paleoelevation method (Figures 6.6 and 6.7) and calculate the total interseismic uplift since 1700 (Figure 6.14). When converted to mm/yr, the resultant uplift rates (triangles) generally compare well with current geodetically determined uplift rates (circles and shading; Hyndman and Wang, 1995) in the central and northern subduction zone. This implies that current uplift rates (midway through the average earthquake cycle) are about the same as the average uplift rate throughout this earthquake cycle so far. In the southern portion, calculated uplift is lower than current measurements and appears to be more comparable to long-term (~ 100 k.y.) rates determined from uplifted shore platforms (squares; Kelsey et al., 1994). Goldfinger et al. (1999) found more frequent events in seafloor turbidite sequences of the southern end of the Cascadia subduction zone, probably due to break-up of the Gorda Plate as mentioned above. Thus, 1700 slip at the southern end was likely smaller than elsewhere.

COSEISMIC SUBSIDENCE IN PRE-1700 CASCADIA EARTHQUAKES

The above findings regarding coseismic subsidence in the 1700 great Cascadia earthquake were published in Leonard et al. (2004). The 1700 event was only the latest of a number of earthquakes recorded by Cascadia coastal marshes; a sequence of up to 11 buried soils is present in some areas, representing the past several thousand years. Here, we assume that these buried soils represent subduction zone earthquakes (see discussion above and in Nelson et al., 1996a) and use the information available from the marshes to examine how typical the 1700 great earthquake was of events over a greater time period.

Correlation of these older buried soils is often possible within individual estuaries, generally by "bar-code" matching (e.g., Atwater and Hemphill-Haley, 1997), but large uncertainties in radiocarbon dates make correlation over greater distances problematic. Therefore, we do not attempt to compile subsidence data on individual events, as done for the 1700 earthquake. Instead, we compile the available data for all previous events and estimate the mean and range of coseismic subsidence experienced by the various marshes over a number of earthquake cycles. For each location, we then compare this data with that for the 1700 event.

Coseismic subsidence is estimated using published stratigraphic and sedimentological data, as described above (method 1). The magnitude of coseismic subsidence is the difference in paleoelevation between each buried soil and the sediment immediately overlying it. In general, published data on pre-1700 buried soils is confined to organic content (e.g., peat, peaty mud) and sometimes macrofossils (e.g., Spruce, Triglochin), whereas many studies on the 1700 horizon also include detailed microfossil analysis, leading to higher precision estimates.

Table E2 (Appendix E) provides a compilation of coseismic subsidence estimates at each Cascadia marsh (see Figure 6.4 for locations) both for the 1700 event and, where

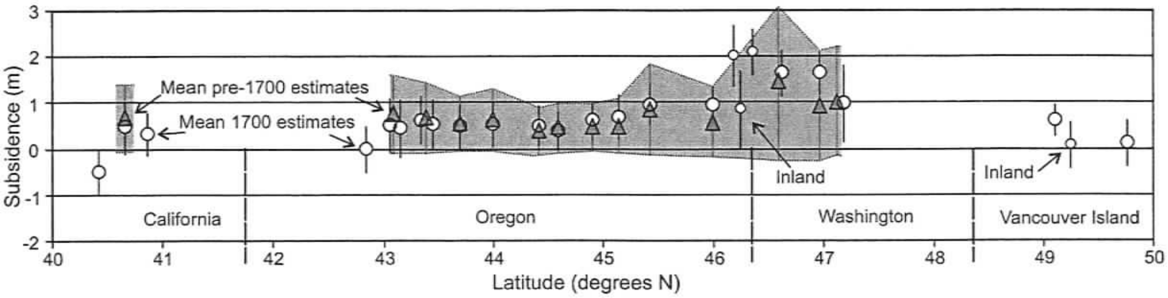

Figure 6.15. Mean subsidence estimates (from Table 6.1) at averaged locations (see Figure 6.10) plotted against latitude for pre-1700 earthquakes (grey triangles and shading) versus the 1700 event (open circles). Estimates are the weighted mean plus or minus the weighted standard deviation (shading) of subsidence estimated at closely spaced sites.

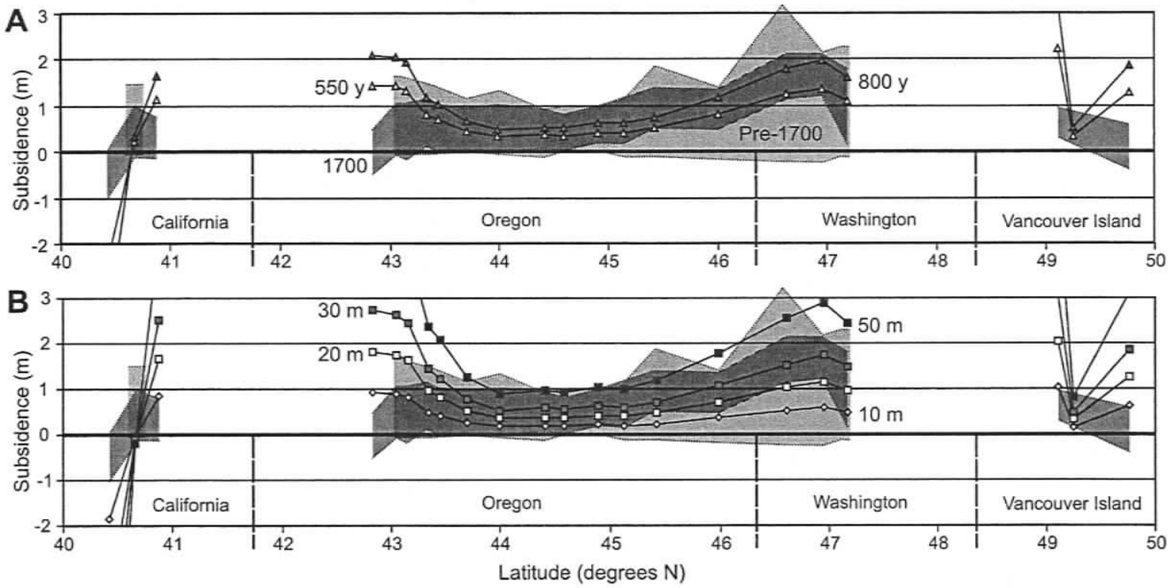

Figure 6.16. Mean subsidence estimates (from Table 6.1and Figure 6.15) at averaged locations (see Figure 6.10) for pre-1700 events (light grey shading) and the 1700 event (dark grey shading), compared with the predictions of elastic dislocation models for the same sites. Mean estimates are the weighted mean plus or minus the weighted standard deviation (shading) of subsidence estimated at closely spaced sites (the Columbia River and Port Alberni data are excluded from the shading). The model predicts the subsidence expected: **(A)** after (i) 800 and (ii) 550 years of plate convergence; **(B)** for uniform slip on the megathrust of 10, 20, 30, and 50 m.

possible, the pre-1700 events. This compilation is summarized in Table 6.1, where the range and mean of estimates are given for each location, as well as information on the number of buried soils and estimates these represent. With the pre-1700 events, it is possible that some of the "buried soils" may represent either gradual sea level rise or localized faulting (e.g., Nelson et al., 1996a), and thus the maximum number of soils may be an overestimate of how many megathrust earthquakes are actually recorded. The pre-

1700 mean subsidence also may be biased towards larger events. Some events could be too small to be recorded, for example by occurring only a short time after the preceding event such that the marsh has undergone little interseismic uplift. Also, preliminary studies (e.g., Witter et al., 2003; Goldfinger et al, 2003) suggest that some of the pre-1700 events ruptured only part of the margin and thus represent smaller earthquakes than the ~ M_w 9, 1700 event; this question requires much more investigation.

The site-averaged coseismic subsidence estimated for pre-1700 events is shown in Figure 6.15, in comparison with that of the 1700 earthquake. Figure 6.16 shows a comparison of the same data with the predictions of elastic dislocation models, as previously discussed. The coastal results suggest that the 1700 earthquake was basically representative of a typical Cascadia megathrust event. However, in Washington and northernmost Oregon, somewhat greater subsidence occurred in 1700 than in most pre-1700 events, while in southern Oregon and northern California, 1700 subsidence was less than in most previous recorded events. At the southern end of the subduction zone, this may partially resolve the issue of the discrepancy between the dislocation model and the 1700 data, if the 1700 event released less strain there than most previous events.

CONCLUSIONS

Coseismic subsidence in the 1700 great Cascadia earthquake, as estimated from marsh paleoelevation studies, is in general agreement with that predicted by elastic dislocation models constrained by interseismic geodetic data and thermal models. This agreement provides confidence that the rupture area and magnitude based on the geodetic constraints reasonably represents the average coseismic events. The uncertainties in paleoelevation estimates of coseismic subsidence are large, but there is a clear and consistent pattern along the margin. Greatest coseismic subsidence (~ 1-2 m) occurred in northern Oregon/southern Washington; other areas to the north and south appear to have subsided between 0 and 1 m in the earthquake, with coseismic uplift experienced at part of the southernmost end of the subduction zone. The predictions of the models are in broad agreement with the marsh subsidence estimates, the best-fitting models being those that simulate the elastic release of 550 to 800 years of strain accumulation at the plate convergence rate. Longer and shorter event occurrence gives poor agreement.

The comparison of uniform slip model predictions with marsh coseismic subsidence estimates allows the estimation of slip magnitude in the 1700 earthquake. The best-fit slip pattern (Figure 6.11) shows a region of large and nearly constant coseismic/tsunamigenic slip; greatest slip is indicated in northern Oregon/southern Washington ($\geq$ 30 m), declining along the coast to the north and south to less than 10 m. Fault rupture of 10 to 30 or even 40 m is consistent with the magnitude 9 earthquake indicated by Japanese tsunami records.

Discrepancies exist however at the southern and northern ends of the subduction zone. In the south, misfit may be due to break-up of the Gorda plate, resulting in a greater number of events of smaller magnitude. In southern Oregon, a better fit would be achieved with a somewhat narrower locked zone. In the north, the paleoelevation subsidence estimates are 3 to 4 times smaller than is predicted by the release of the model interseismic strain accumulated since the previous event (~ 800 years). The model interseismic uplift is consistent with the average uplift since 1700. The discrepancy may be explained if the 1700 event released only part of the accumulated strain at the northern end of the subduction zone; this idea is consistent with the greater net uplift experienced, evidenced by the lack of buried soils older than 1700, in contrast to the rest of the subduction zone.

Comparison of the estimated coseismic subsidence in 1700 with estimates for pre-1700 events suggests that the 1700 megathrust earthquake was basically representative of earlier recorded Cascadia subduction earthquakes. However, in Washington and northernmost Oregon, the 1700 subsidence was greater than in most previous events, while at the southern end of the subduction zone it was less than in most previous events.

Average uplift rates since 1700, estimated from the depth of the 1700 marsh top horizon, paleoelevation subsidence estimates, postglacial rebound and eustatic sea level rise, agree with current geodetically determined uplift rates for the central and northern portions of the subduction zone. In the south, however, the small uplift calculated via this method is more comparable to long-term (~ 100 k.y.) uplift rates determined from uplifted shore platforms, again perhaps reflecting internal deformation of the Gorda plate.

REFERENCES

Abbott, G., 1997, Geology of the upper Hart River area, eastern Ogilvie Mountains, Yukon Territory (116A/10,11), Exploration and Geological Services Division, Yukon Region, Indian and Northern Affairs Canada, Bulletin 9, 76p.

Abraham, A.-C., D. Francis, and M. Polvé, 2001, Recent alkaline basalts as probes of the lithospheric mantle roots of the Northern Canadian Cordillera, Chemical Geology, vol. 175, p. 361-386.

Adams, J., 1990, Paleoseismicity of the Cascadia subduction zone: Evidence from turbidites off the Oregon-Washington margin, Tectonics, vol. 9, p. 569-583.

Adams, J., and S. Halchuk, 2003, Fourth generation seismic hazard maps of Canada: values for over 650 Canadian localities intended for the 2005 Building Code of Canada, Geological Survey of Canada Open File 4459, 155p.

Altamimi, Z., P. Sillard, and C. Boucher, 2002, ITRF2000: A new release of the International Reference Frame for earth science applications, Journal of Geophysical Research, vol. 107 (B1), 2214, doi: 10.1029/2001JB000561.

Anderson, J.G., 1979, Estimating the seismicity from geological structure for seismic risk studies, Bulletin of the Seismological Society of America, vol. 69, p. 205-514.

Andrews, J.T., 1989, Postglacial emergence and submergence, *In*: Quaternary geology of Canada and Greenland, Fulton, R.J. (ed.), Chapter 8, Geological Survey of Canada, no. 1 (also Geological Society of America, The Geology of North America, vol. K-1).

Arendt, A. A., K.A. Echelmeyer, W.D. Harrison, C.S. Lingle, and V.B. Valentine, 2002, Rapid wastage of Alaska glaciers and their contribution to rising sea level, Science, vol. 297, p. 382-386.

Atwater, B.F., 1987, Evidence for great Holocene earthquakes along the outer coast of Washington State, Science, vol. 336, p. 942-944.

Atwater, B.F., 1988, Geologic studies for seismic zonation of the Puget lowland, *in* Jacobson, M.L., et al., comps., National Earthquake Hazards Reduction Program, Summaries of technical reports, Volume XXV, U.S. Geological Survey Open-File Report 88-16, p. 120-133.

Atwater, B.F., 1992, Geologic evidence for earthquakes during the past 2000 years along the Copalis River, southern coastal Washington, Journal of Geophysical Research, vol. 97, p. 1901-1919.

Atwater, B.F., 1994, Geology of Holocene liquefaction features along the lower Columbia River at Marsh, Brush, Hunting, and Wallace Islands, Oregon and Washington, U.S. Geological Survey Open File Report 94-209, 63 p.

Atwater, B.F., and E. Hemphill-Haley, E., 1997, Recurrence intervals for great earthquakes of the past 3,500 years at northeastern Willapa Bay, Washington, U.S. Geological Survey Professional Paper 1576, 108 p.

Atwater, B.F., A.R. Nelson, J.J. Clague, G.A. Carver, D.K. Yamaguchi, P.T. Bobrowsky, J. Bourgeois, M.E. Darienzo, W.C. Grant, E. Hemphill-Haley, H.M. Kelsey, G.C. Jacoby, S.P. Nishenko, S.P. Palmer, C.D. Peterson, and M.A. Reinhart, 1995, Summary of coastal geologic evidence for past great earthquakes at the Cascadia subduction zone, Earthquake Spectra, vol. 11, p. 1-18.

Atwater, B.F., D.K. Yamaguchi, S. Bondevik, W.A. Barnhardt, L.J. Amidon, B.E. Benson, G. Skjerdal, J.A. Shulene, and F. Nanayama, 2001, Rapid resetting of an estuarine recorder of the 1964 Alaska earthquake, Geological Society of America Bulletin, vol. 113, no. 9, p. 1193-1204.

Avouac, J.-P., and P. Tapponnier, 1993, Kinematic model of active deformation in central Asia, Geophysical Research Letters, vol. 20, p. 895-898.

Barrientos, S.E., and S.N. Ward, 1990, The 1960 Chile earthquake: inversion for slip distribution from surface deformation, Geophysical Journal International, vol. 103, p. 589-598.

Barnett, E.T., 1997, The potential for coastal flooding due to coseismic subsidence in the central Cascadia margin, M.Sc. thesis, Portland State University, Portland, Oregon, 144 p.

Basham, P.W., D.A. Forsyth, and R.J. Wetmiller, 1977, The seismicity of northern Canada, Canadian Journal of Earth Sciences, vol. 14, p. 1646-1667.

Beavan, J., 2005, Noise properties of continuous GPS data from concrete pillar geodetic monuments in New Zealand and comparison with data from U.S. deep drilled braced monuments, Journal of Geophysical Research, vol. 110 (B8), B08410, doi: 10.1029/2005JB003642.

Beutler, G., M. Rothacher, S. Schaer, T.A. Springer, J. Kouba, R.E. Neilan, 1999, The International GPS Service (IGS): an interdisciplinary service in support of earth sciences, Advances in Space Research, vol. 23, no. 4, p. 631-635.

Bird, P., 1999, Thin-plate and thin-shell finite-element programs for forward dynamic modeling of plate deformation and faulting, Computers and Geosciences, vol. 25, p. 383-394.

Bird, P., 1996, Computer simulations of Alaskan Neotectonics, Tectonics, vol. 15, no.2, p. 225-236.

Biswas, N.N., and G. Tytgat, 1988, Intraplate seismicity in Alaska, Seismological Research Letters, vol. 59, no. 4, p. 227-233.

Biswas, N.N., K. Aki, H. Pulpan, and G. Tytgat, 1986, Characteristics of regional stresses in Alaska and neighboring areas, Geophysical Research Letters, vol. 13, no. 3, p. 177-180.

Boatwright, J., 1980, Preliminary body-wave analysis of the St. Elias, Alaska, earthquake of February 28, 1979, Bulletin of the Seismological Society of America, vol. 70, p. 419-436.

Boucher, C., Z. Altamimi, and P. Sillard, 1999, The 1997 International Terrestrial Reference Frame (ITRF97), IERS Technical Note 27, Observatoire de Paris, France.

Briggs, G. G., 1994, Coastal crossing of the zero-isobase, Cascadia margin, south-central Oregon coast, M.Sc. thesis, Portland State University, Portland, Oregon, 251 p.

Briggs, G., and C.D. Peterson, 1993, Neotectonics of the central Cascadia margin as recorded on south-central Oregon coastal deposits, U.S. Geological Survey - National Earthquake Hazards Reduction Program, Final Report, 77 p.

Brocher, T.M., G.S. Fuis, M.A. Fisher, G. Plafker, M. Moses, J.J. Taber, and N.I. Christensen, 1994, Mapping the megathrust beneath the northern Gulf of Alaska using wide-angle seismic data, Journal of Geophysical Research, vol. 99, no. B6, p. 11,663-11,685.

Brown, L.D., R.E. Reilinger, S.R. Holdahl, and E.I. Balazs, 1977, Postseismic crustal uplift near Anchorage, Alaska, Journal of Geophysical Research, vol. 82, p. 3369-3378.

Bruhn, R.L., T.L. Pavlis, G. Plafker, and L. Serpa, 2004, Deformation during terrane accretion in the Saint Elias orogen, Alaska, Geological Society of America Bulletin, vol. 116, p. 771-787; doi: 10.1130/B25182.1.

Brune, J.N., 1968, Seismic moment, seismicity, and rate of slip along major fault zones, Journal of Geophysical Research, vol. 73, p. 777-784.

Bruns, T.R., 1983, Model for the origin of the Yakutat block, an accreting terrane in the northern Gulf of Alaska, Geology, vol. 11, no. 12, p. 718-721.

Bruns, T.R., 1985, Tectonics of the Yakutat block, an allochthonous terrane in the northern Gulf of Alaska, U.S. Geological Survey Open-File Report 85-13, 112p.

Bufe, C.G., 2005, Stress distribution along the Fairweather-Queen Charlotte transform fault system, Bulletin of the Seismological Society of America, vol. 95, no.5, p. 2001-2008, doi: 10.1785/0120040171.

Bürgmann, R., S. Ergintav, P. Segall, E.H. Hearn, S.C. McClusky, R.E. Reilinger, H. Woith, and J. Zschau, 2002, Time-dependent distributed afterslip on and deep below the Izmit earthquake rupture, Bulletin of the Seismological Society of America, vol. 92, no. 1, p. 126-137.

Bustin, A.M.M., 2006, The crustal structure, deformation from GPS, and seismicity related to oblique convergence along the Queen Charlotte margin, British Columbia, Ph.D. thesis, University of Victoria.

Campbell, R., and C.J. Dodds, 1991, Saint Elias mountains, *In:* Gabrielse, H., and C.J. Yorath (eds.), Geology of the Cordilleran orogen in Canada, Boulder, Colorado, Geological Society of America, vol. G2, p. 574-577.

Carlson, P.R., T.R. Bruns, and G. Plafker, 1988, Late Cenozoic offsets on the offshore connection between the Fairweather and Queen Charlotte faults off southeast Alaska, Marine Geology, vol. 85, p. 89-97.

Carver, G., and R.B. Burke, 1989, Active convergent tectonics in northwestern California, *in* Aalto, K.R., et al., field trip leaders, Geological evolution of the northernmost Coast Ranges and western Klamath Mountains, California, Field Trip Guidebook T308, 28th International Geologic Congress, p. 64-82.

Carver, G., A.S. Jayko, D.W. Valentine, and W.H. Li, 1994, Coastal uplift associated with the 1992 Cape Mendocino earthquake, northern California, Geology, vol. 22, p. 195-198.

Carver, G., G. Plafker, M. Metz, L. Cluff, B. Slemmons, E. Johnson, J. Roddick, and S. Sorensen, 2004, Surface Rupture on the Denali Fault Interpreted from Tree Damage during the 1912 Delta River M_w 7.2–7.4 Earthquake: Implications for the 2002 Denali Fault Earthquake Slip Distribution, Bulletin of the Seismological Society of America, vol. 94, no. 6B, p. S58-S71.

Cassidy, J.F., and A.L. Bent, 1993, Source parameters of the 29 May and 5 June, 1940 Richardson Mountains, Yukon Territory, earthquakes, Bulletin of the Seismological Society of America, vol. 83, p. 636-659.

Cassidy, J.F., and G.C. Rogers, 2004, The M_w 7.9 Denali fault earthquake of 3 November 2002: felt reports and unusual effects across western Canada, Bulletin of the Seismological Society of America, vol. 94, p. 221.

Cassidy, J.F., G.C. Rogers, and J. Ristau, 2005, Seismicity in the vicinity of the SNORCLE corridors of the northern Canadian Cordillera, Canadian Journal of Earth Sciences, vol. 42, p. 1137-1148.

Cecile, M.P., and D.G. Cook, 1981, Structural cross-section, northern Selwyn and Mackenzie Mountains, Geological Survey of Canada, Vancouver, Open-File 807.

Cecile, M.P., D.G. Cook, and L.R. Snowdon, 1982, Plateau overthrust and its hydrocarbon potential, MacKenzie Mountains, Northwest Territories, *In:* Current Research, Part A, Geological Survey of Canada, Paper 82-1A, p. 89-94.

Chaytor, J.D., C. Goldfinger, and R.P. Dziak, 2002, The structural evolution of the Gorda "Plate": destruction of a plate fragment prior to subduction in the Cascadia subduction zone, Eos Transactions AGU, vol. 83, no. 47, Fall Meeting Supplement, Abstract T52B-1203.

Christensen, D.H., and S.L. Beck, 1994, The rupture process and tectonic implications of the great 1964 Prince William Sound earthquake, Pure Applied Geophysics, vol. 142, no. 1, p. 29-53.

Clague, J.J., 1979, The Denali fault system in southwest Yukon Territory – a geologic hazard?, Current Research, Part A, Geological Survey of Canada, Paper 79-1A, p. 169-178, 1979.

Clague, J.J., and P.T. Bobrowsky, 1994a, Evidence for a large earthquake and tsunami 100-400 years ago on western Vancouver Island, British Columbia, Quaternary Research, vol. 41, p. 176-184.

Clague, J.J., and P.T. Bobrowsky, 1994b, Tsunami deposits in tidal marshes on Vancouver Island, British Columbia, Geological Society of America Bulletin, vol. 106, p.1293-1303.

Clague, J.J., and T.S. James, 2002, History and isostatic effects of the last ice sheet in southern British Columbia, Quaternary Science Reviews, vol. 21, p. 71-87.

Cohen, S.C., and J.T. Freymueller, 1997, Deformation on the Kenai Peninsula, Alaska, Journal of Geophysical Research, vol. 102, p. 20,479-20,487.

Cohen, S.C., and J.T. Freymueller, 2001, Crustal uplift in the south central Alaska subduction zone: new analysis and interpretation of tide gauge observations, Journal of Geophysical Research, vol. 106, no. 6, p. 11259-11270.

Cohen, S.C., and J.T. Freymueller, 2004, Crustal deformation in the southcentral Alaska subduction zone, Advances in Geophysics, vol. 47, 1-58.

Cohen, S., S. Holdahl, D. Caprette, S. Hilla, R. Safford, and S. Schultz, 1995, Uplift of the Kenai Peninsula, Alaska, since the 1964 Prince William Sound earthquake, Journal of Geophysical Research, vol. 100, no. B2, p. 2031-2038.

Combellick, R.A., 1986, Chronology of late-Holocene earthquakes in south central Alaska; evidence from buried organic soils in upper Turnagain Arm, Geological Society of America - Abstracts with Programs, vol. 18, no. 6, p. 569.

Coney, P.J., D.L. Jones, and J.W.H. Monger, 1980, Cordilleran suspect terranes, Nature, vol. 288, p. 329-333.

Cook, D.G., 1983, The role of dextral shear in forming the northern Franklin Mountains, Program with Abstracts, Geological Association of Canada – Mineralogical Association of Canada – Canadian Geophysical Union, Joint Annual Meeting, December 1983.

Cook, D.G., 1991, Mackenzie Mountains, Franklin Mountains and Colville Hills: Chapter 17, Structural Styles, H. Gabrielse (comp.), *In:* Gabrielse, H., and C.J. Yorath (eds.), Geology of the Cordilleran orogen in Canada, Boulder, Colorado, Geological Society of America, vol. G2, p. 571-675.

Creaser, B., and G. Spence, 2005, Crustal structure across the northern Cordillera, Yukon Territory, from seismic wide-angle studies: Omineca Belt to Intermontane Belt, Canadian Journal of Earth Sciences, vol. 42, p. 1187-1203.

Crone, A.J., S.F. Personius, P.A. Craw, P.J. Haeussler, and L.A. Staft, 2005, Thrust faults in transpressive strike-slip environments – role of the Susitna Glacier fault in the M_w 7.9 Denali fault earthquake sequence, Alaska, *In*: Detweiler, S.T., and W. Ellsworth, Proceedings of the 5th U.S. – Japan Natural Resources Meeting and Parkfield, California fieldtrip, U.S. Geological Survey Open-File Report 2005-1131, 83p.

Darienzo, M.E., 1991, Late Holocene paleoseismicity along the northern Oregon coast, Ph.D. thesis, Portland State University, Portland, Oregon, 176 p.

Darienzo, M.E., and C.D. Peterson, 1990, Episodic tectonic subsidence of late Holocene salt marshes, northern Oregon central Cascadia margin, Tectonics, vol. 9, p. 1-22.

Darienzo, M.E., and C.D. Peterson, 1995, Magnitude and frequency of subduction-zone earthquakes along the northern Oregon coast in the past 3,000 years, Oregon Geology, vol. 57, p. 3-12.

Darienzo, M.E., Peterson, C.D., and Clough, C., 1994, Stratigraphic evidence for great subduction-zone earthquakes at four estuaries in northern Oregon, Journal of Coastal Research, vol. 10, p. 850-876.

Davis, T.N., 1960, A field report on the Alaska earthquakes of April 7, 1958, Bulletin of the Seismological Society of America, vol. 50, p. 489-510.

DeMets, C., and T.H. Dixon, 1999, New kinematic models for Pacific-North America motion from 3 Ma to present, I: Evidence for steady motion and biases in the NUVEL-1A model, Geophysical Research Letters, vol. 26, no. 13, p. 1921-1924.

Dickinson, W.R., 2004, Evolution of the North American Cordillera, Annual Review of Earth and Planetary Sciences, vol. 32, p. 13-45.

Dixon, T.H., M. Miller, F. Farina, H. Wang, and D. Johnson, 2000, Present-day motion of the Sierra Nevada block and some tectonic implications for the Basin and Range province, North American Cordillera, Tectonics, vol. 19, no. 1, p. 1-24.

Doser, D., 2002, Historical seismicity of the Denali fault system, Eos, Transactions, American Geophysical Union, vol. 83, S72F-1338.

Doser, D.I., and R. Lomas, 2000, The transition from strike-slip to oblique subduction in southeastern Alaska from seismological studies, Tectonophysics, vol. 316, p. 45-65.

Doser, D.I., J.R. Pelton, and A.M. Veilleux, 1997, Earthquakes in the Pamplona zone, Yakutat block, south central Alaska, Journal of Geophysical Research, vol. 102, no. B11, p. 24,499-24,511.

Douglas, B.C., 1991, Global sea level rise, Journal of Geophysical Research, vol. 96, p. 6981-6992.

Douglas, B.C., 1997, Global sea rise: a redetermination, Surveys in Geophysics, vol. 18, p. 297-292.

Dragert, H., R.D. Hyndman, G.C. Rogers, and K. Wang, 1994, Current deformation and the width of the seismogenic zone of the northern Cascadia subduction thrust, Journal of Geophysical Research, vol. 99, p. 653-668.

Dragert, H., K. Wang, and G. Rogers, 2004, Geodetic and seismic signatures of episodic tremor and slip in the northern Cascadia subduction zone, Earth Planets and Space, vol. 56, no. 12, p. 1143-1150.

Dusel-Bacon, C., and J.M. Murphy, 2001, Apatite fission-track evidence of widespread Eocene heating and exhumation in the Yukon-Tanana Upland, interior Alaska, Canadian Journal of Earth Sciences, vol. 38, p. 1191-1204.

Dziewonski, A.M., T.-A. Chou, and J.H. Woodhouse, 1981, Determination of earthquake source parameters from waveform data for studies of global and regional seismicity, Journal of Geophysical Research, vol. 86, p. 2825-2852.

Eberhart-Phillips, D., P. Haeussler, J. Freymueller, A. Frankel, C. Rubin, P. Craw, N. Ratchkovski, G. Anderson, A. Crone, T. Dawson, H. Fletcher, R. Hansen, E. Harp, R. Harris, D. Hill, S. Hreinsdóttir, R. Jibson, L. Jones, D. Keefer, C. Larsen, S. Moran, S. Personius, G. Plafker, B. Sherrod, K. Sieh, and W. Wallace, 2003a, The 2002 Denali Fault earthquake, Alaska: a large magnitude, slip-partitioned event, Science, vol. 300, p. 1113-1118.

Eberhart-Phillips, D., D.H. Christensen, T.M. Brocher, U. Dutta, R. Hansen, and N.A. Ratchkovski, 2003b, Imaging the transition from Aleutian subduction to Yakutat collision in central Alaska, with local earthquakes and active source data, Eos Transactions, American Geophysical Union, vol. 84, no. 46, Fall Meeting Supplement, Abstract S21C-01.

Edwards, B.R., and J.K. Russell, 1999, Northern Cordilleran volcanic province: a northern Basin and Range?, Geology, vol. 27, no. 3, p. 243-246.

Edwards, B.R., and J.K. Russell, 2000, Distribution, nature, and origin of Neogene-Quaternary magmatism in the northern Cordilleran volcanic province, Canada, Geological Society of America Bulletin, vol. 112, no. 8, p. 1280-1295.

Ehlers, T.A., and K.A. Farley, 2003, Apatite (U-Th)/He thermochronometry: methods and applications to problems in tectonic and surface processes, Earth and Planetary Science Letters, vol. 206, p. 1-14.

Eisbacher, G.H., 1976, Sedimentology of the Dezadeash flysch and its implications for strike-slip faulting along the Denali fault, Yukon Territory and Alaska, Canadian Journal of Earth Sciences, vol. 13, no. 11, p. 1495-1513.

Eisbacher, G.H., 1981, Sedimentary tectonics and glacial record in the Windermere Supergroup, Mackenzie Mountains, northwestern Canada, Geological Survey of Canada Paper 80-27.

Engebretson, D.C., A. Cox, and R.G. Gordon, 1985, Relative motions between oceanic and continental plates in the Pacific basin, Geological Society of America, Special Paper 206, 59 p.

Estabrook, C.H., D.B. Stone, and J.N. Davies, 1988, Seismotectonics of northern Alaska, Journal of Geophysical Research, vol. 93, p. 12026-12040.

Estabrook, C.H., A.L. Lerner-Lam, and J.L. Nabelek, 1990, Tectonic model of the Pacific-North American plate boundary in the Gulf of Alaska from analysis of the 1979 St. Elias, Alaska earthquake and its aftershocks, Eos, Transactions, American Geophysical Union, vol.71, no.43, p.1581.

Estabrook, C.H., J.L. Nabelek, and A.L. Lerner-Lam, 1992, Tectonic model of the Pacific-North American plate boundary in the Gulf of Alaska from broadband analysis of the 1979 St. Elias, Alaska earthquake and its aftershocks, Journal of Geophysical Research, vol. 97, p. 6587-6612.

Estey, L.H., and C. M. Meertens, 1999, TEQC: the multi-purpose toolkit for GPS/GLONASS Data, *In:* GPS Solutions, vol. 3, no. 1, John Wiley & Sons, p. 42-49.

Ferris, A., G.A. Abers, D.H. Christensen, and E. Veenstra, 2003, High resolution image of the subducted Pacific (?) plate beneath central Alaska, 50-150 km depth, Earth and Planetary Sciences, vol. 214, p. 575-588.

Fisher, M.A., N.A. Ratchkovski, W.J. Nokleberg, L. Pellerin, and J.M.G. Glen, 2004, Geophysical data reveal the crustal structure of the Alaska Range orogen within the aftershock zone of the M_w 7.9 Denali fault earthquake, Bulletin of the Seismological Society of America, vol. 94, p. S107-S131.

Fitzgerald, P.G., E. Stump, and T.F. Redfield, 1993, Late Cenozoic uplift of Denali and its relation to relative plate motion and fault morphology, Science, vol. 259, p.497-499.

Fitzgerald, P.G., R.B. Sorkhabi, T.F. Redfield, and E. Stump, 1995, Uplift and denudation of the central Alaska Range: a case study in the use of apatite fission track thermochronology to determine absolute uplift parameters, Journal of Geophysical Research, vol. 100, p. 20,175-20,191.

Fletcher, H.J., 2002, Crustal deformation in Alaska measured using the Global Positioning System, Ph.D. thesis, University of Alaska, Fairbanks, 135p.

Fletcher, H.J., and D.H. Christensen, 1996, A determination of source parameters of large Intraplate earthquakes in Alaska, Pure and Applied Geophysics, vol. 146, no. 1, p. 21-41.

Fletcher, H., and J.T. Freymueller, 1999, New GPS constraints on the motion of the Yakutat block, Geophysical Research Letters, vol. 26, no. 19, p. 3029-3032.

Fletcher, H., and J.T. Freymueller, 2003, New constraints on the motion of the Fairweather fault, Alaska, from GPS observations, Geophysical Research Letters, vol. 30, no. 3, 1139, doi: 10.1029/2002GL016476.

Flück, P., 2003, Contributions to the geodynamics of western Canada, Ph.D. thesis, University of Victoria, Victoria, B.C.

Flück, P., R.D. Hyndman, and K. Wang, 1997, Three-dimensional dislocation model for great earthquakes of the Cascadia subduction zone, Journal of Geophysical Research, vol. 102, no. 9, p. 20,539-20,550.

Flück, P., R.D. Hyndman, and C. Lowe, 2003, Effective elastic thickness T_e of the lithosphere in western Canada, Journal of Geophysical Research, vol. 108, 2430, doi: 10.1029/2002JB002201.

Forbes, D.L., T. Bell, M. Craymer, and G.K. Manson, 2004, Coastal submergence and emergence across the Canadian Arctic, ArcticNet Annual Scientific Meeting, Program with Abstracts, 32.

Foster, H.L., and G.W. Cushing, 1985, Tertiary (?) folding in the Tanacross quadrangle, *In*: Bartsch-Winkler, S., and K.M. Reed, (eds.), The United States Geological Survey in Alaska: accomplishments during 1983, U.S. Geological Survey Circular 945, p. 38-40.

Foster, H.L., T.E.C. Keith, and W.D. Menzie, 1994, Geology of the Yukon-Tanana area of east-central Alaska, *In*: The Geology of Alaska, Plafker, G., and H.C. Berg (eds.), Geological Society of America, Boulder, Colorado, The Geology of North America, vol. G-1. P. 205-240.

Frederiksen, A.W., M.G. Bostock, J.C. VanDecar, and J.F. Cassidy, 1998, Seismic structure of the upper mantle beneath the northern Canadian Cordillera from teleseismic travel-time inversion, Tectonophysics, vol. 294, p. 43-55.

Freed, A.M., 2005, Earthquake triggering by static, dynamic, and postseismic stress transfer, Annual Review of Earth and Planetary Sciences, vol. 33, p. 335-367.

Freed, A.M., R. Bürgmann, E. Calais, J. Freymueller, and S. Hreinsdóttir, 2006, Implications of deformation following the 2002 Denali, Alaska, earthquake for postseismic relaxation processes and lithospheric rheology, Journal of Geophysical Research, vol. 111, B01401, doi: 10.1029/2005JB003894.

Frey, R.W., and P.B. Basan, 1985, Coastal salt marshes, *in* Davis, R.A., Jr., ed., Coastal Sedimentary Environments, New York, Springer-Verlag, p. 101-169.

Freymueller, J.T., 2006, Kenai Peninsula/Cook Inlet crustal deformation: a brief summary, *In*: AGU Chapman conference, Active tectonics and seismic potential of Alaska, Field Trip Guide, May 13 2006, p. 25-42.

Freymueller, J.T., S.C. Cohen, and H.J. Fletcher, 2000, Spatial variations in present-day deformation, Kenai Peninsula, Alaska, and their implications, Journal of Geophysical Research, vol. 105, no. B4, p. 8079-8101.

Fruehn, J., R. von Huene, and M.A. Fisher, 1999, Accretion in the wake of terrane collision; the Neogene accretionary wedge off Kenai Peninsula, Alaska, Tectonics, vol. 18, p. 263-277.

Fuis, G.S., A. R. Levander, W.J. Lutter, E.S. Wissinger, T.E. Moore, and N.I. Christensen, 1995, Seismic images of the Brooks Range, Arctic Alaska, reveal crustal-scale duplexing, Geology, vol. 23, no. 1, p. 65-68.

Gabrielse, H., 1957, Geological reconnaissance in the northern Richardson Mountains, Yukon and Northwest Territories, Geological Survey of Canada Paper 56-6.

Gabrielse, H., 1985, Major dextral transcurrent displacements along the Northern Rocky Mountains Trench and related lineaments in north-central British Columbia, Geological Society of America Bulletin, vol. 96, p. 1-14.

Gabrielse, H., and C.J. Yorath, 1991, Northern Yukon: Chapter 17, Structural Styles, H. Gabrielse (comp.), *In:* Gabrielse, H., and C.J. Yorath (eds.), Geology of the Cordilleran orogen in Canada, Boulder, Colorado, Geological Society of America, vol. G2, p. 571-675.

Gabrielse, H., S.L. Blusson, and J.A. Roddick, 1973, Geology of the Flat River, Glacier Lake, and Wrigley Lake map-areas, District of Mackenzie and the Yukon Territory 95E, L, M. Geological Survey of Canada, Memoir 366, 150 p.

Gabrielse, H., J.W.H Monger, J.O. Wheeler, and C.J. Yorath, 1991, Chapter 2, Part A: Morphogeological belts, tectonic assemblages, and terrane, *In*: Gabrielse, H., and C.J. Yorath (eds.), Geology of the Cordilleran orogen in Canada, Boulder, Colorado, Geological Society of America, vol. G2, p. 15-28.

Gahalaut, V.K., B. Nagarajan, J.K. Catherine, and S. Kumar, 2006, Constraints on 2004 Sumatra-Andaman earthquake rupture from GPS measurements in Andaman-Nicobar Islands, Earth and Planetary Sciences, vol. 242, p. 365-374.

Gallagher, K., R. Brown, and C. Johnson, 1998, Fission track analysis and its applications to geological problems, Annual Review of Earth and Planetary Sciences, vol. 26, p. 519-572.

Gallaway, P.J., C.D. Peterson, A.M. Watkins, S. Craig, and B.L. McLeod, 1992, Paleotsunami runup at Cannon Beach, Oregon, Final Report to Clatsop County Sheriffs Office, Clatsop County, Oregon, 36 p.

Gedney, L., 1970, Tectonic stresses in southern Alaska in relationship to regional seismicity and the new global tectonics, Bulletin of the Seismological Society of America, vol. 60, no. 6, p. 1789-1802.

Goldfinger, C., L.D. Kulm, R.S. Yeats, B. Appelgate, M.E. MacKay, and G.F. Moore, 1992, Transverse structural trends along the Oregon convergent margin: implications for Cascadia earthquake potential and crustal rotations, Geology, vol. 20, p. 141-144.

Goldfinger, C., H. Nelson, and J.E. Johnson, 1999, Holocene recurrence of Cascadia great earthquakes based on the turbidite event record, Eos, Transactions, American Geophysical Union, vol. 80, no. 46, Suppl., p. 1024-1025.

Goldfinger, C., C.H. Nelson, J.E. Johnson, and the Shipboard Scientific Party, 2003, Holocene earthquake records from the Cascadia subduction zone and northern San Andreas fault based on precise dating of offshore turbidites, Annual Review of Earth and Planetary Sciences, vol. 31, p. 555-577.

Gordey, S.P., 1981, Structure section across south central Mackenzie Mountains, N.W.T. Geological Survey of Canada, Vancouver, Open-File 809.

Grantz, A., D.A. Dinter, and N.N. Biswas, 1983, Map, cross-sections, and chart showing late Quaternary faults, folds and earthquake epicenters on the Alaska Beaufort shelf, Miscellaneous Investigations Series, U.S. Geological Survey Map 1-1182-C.

Griscom, A., and P.E. Sauer, 1990, Interpretation of magnetic maps of the northern Gulf of Alaska, with emphasis on the source of the Slope anomaly, U.S. Geological Survey Open-File Report 90-348, 19p.

Guilbault, J.P., J.J. Clague, and M. Lapointe, 1995, Amount of subsidence during a late Holocene earthquake – evidence from fossil tidal marsh foraminifera at Vancouver Island, west coast of Canada, Palaeogeography, Palaeoclimatology, Palaeoecology, vol. 118, p. 49-71.

Guilbault, J.P., J.J. Clague, and M. Lapointe, 1996, Foraminifera evidence for the amount of coseismic subsidence during a late Holocene earthquake on Vancouver Island, west coast of Canada, Quaternary Science Reviews, vol. 15, p. 913-937.

Gurtner, W., G. Mader, D. MacArthur, 1989, A Common Exchange Format for GPS Data, Proceedings of the Fifth International Geodetic Symposium on Satellite Systems, Las Cruces, pp. 917ff.

Haeussler, P.J., R.L. Bruhn, and T.L. Pratt, 2000, Potential seismic hazards and tectonics of the upper Cook Inlet basin, Alaska, based on analysis of Pliocene and younger deformation, Geological Society of America Bulletin, vol. 112, no. 9, p. 1414-1429.

Haeussler, P.J., D.P. Schwartz, T.E. Dawson, H.D. Stenner, J.J. Lienkaemper, B. Sherrod, F.R. Cinti, P. Montone, P.A. Craw, A.J. Crone, and S.F. Personius, 2004, Surface Rupture and Slip Distribution of the Denali and Totschunda Faults in the 3 November 2002 M 7.9 Earthquake, Alaska, Bulletin of the Seismological Society of America, vol. 94, no. 6B, p. S23-S52.

Hanks, T.C., and H. Kanamori, 1979, A moment magnitude scale, Journal of Geophysical Research, vol. 84, p. 2348-2350.

Hansen, V.L., 1986, Petrotectonic study of the Teslin suture zone, Yukon, Canada, Geological Society of America – Abstracts with Programs, vol. 18, no. 2, p. 113.

Hart, C.J.R., and M. Villeneuve, 1999, Geochronology of Neogene alkaline volcanic rocks (Miles Canyon basalt), southern Yukon Territory, Canada: the relative effectiveness of laser ^{40}Ar/^{39}Ar and K-Ar geochronology, Canadian Journal of Earth Sciences, vol. 36, p. 1495-1507.

Hasegawa, H.S., C.W. Chou, and P.W. Basham, 1979, Seismotectonics of the Beaufort Sea, Canadian Journal of Earth Sciences, vol. 16, p. 816-830.

Hasegawa, H.S., J.C. Lahr, and C.D. Stephens, 1980, Fault parameters of the St. Elias, Alaska, earthquake of February 28, 1979, Bulletin of the Seismological Society of America, vol. 70, no. 5, p. 1651-1660.

Hashimoto, M., N. Choosakul, M., Hashizume, S. Takemoto, H. Takiguchi, Y. Fukuda, and K. Frjimori, 2006, Crustal deformation associated with the great Sumatra-Andaman earthquake deduced from continuous GPS observation, Earth and Planets and Space, vol. 58, no. 2, p. 127-139.

Hearn, E., 2003, What can GPS data tell us about the dynamics of postseismic deformation?, Geophysical Journal International, vol. 155, p. 753-777.

Heki, K, S. Miyazaki, and H. Tsuji, 1997, Silent fault slip following an interplate thrust earthquake at the Japan Trench, Nature, vol. 386, p. 595-598.

Hemphill-Haley, E., 1992, The application of diatom paleoecology to interpretations of Holocene relative sea-level change and coseismic subsidence in southwestern Washington, PhD thesis, University of California, Santa Cruz, California, 321 p.

Hemphill-Haley, E., 1995a, Intertidal diatoms from Willapa Bay, Washington: application to studies of small-scale sea-level changes, Northwest Science, vol. 69, p. 29-45.

Hemphill-Haley, E., 1995b, Diatom evidence for earthquake-induced subsidence and tsunami 300 yr ago in southern coastal Washington, Geological Society of America Bulletin, vol. 107, p. 367-378.

Hindle, D., and J. Kley, 2002, Displacements, strains and rotations in the central Andean plate boundary zone, *in* Stein, S., and Freymueller, J. (eds.), Plate Boundary Zones, Geodynamics Series 30, American Geophysical Union, p. 135-144.

Hindle, D., J. Kley, E. Klosko, S. Stein, T. Dixon, and E. Norabuena, 2002, Consistency of geologic and geodetic displacements during Andean orogenesis, Geophysical Research Letters, vol. 29, no. 8, doi: 10.1029/2001GL013757.

Hofmann-Wellenhof, B., H. Lichtenegger, and J. Collins, 2001, Global Positioning System theory and practice, 5th, revised edition, Springer Wien New York, 382 p.

Holdahl, S.R., and J. Sauber, 1994, Coseismic slip in the 1964 Prince William Sound earthquake: a new geodetic inversion, Pure Applied Geophysics, vol. 142, no. 1, p. 55-82.

Holt, W.E., M. Li, and A.J. Haines, 1995, Earthquake strain rates and instantaneous relative motions within central and eastern Asia, Geophysical Journal International, vol. 122, p. 569-593.

Horner, R.B., 1983, Seismicity in the St. Elias region of northwestern Canada and southeastern Alaska, Bulletin of the Seismological Society of America, vol.73, no.4, p.1117-1137.

Horner, R.B., R.J. Wetmiller, M. Lamontagne, and M. Plouffe, 1990, A fault model for the Nahanni earthquakes from aftershock studies, Bulletin of the Seismological Society of America, vol. 80, p. 1553-1570.

Houseman, G., and P. England, 1986, Finite strain calculations of continental deformation 1. Method and general results for convergent zones, Journal of Geophysical Research, vol. 91, p. 3651-3663.

Hreinsdóttir, S., J.T. Freymueller, H.J. Fletcher, C.F. Larsen, and R. Bürgmann, 2003, Coseismic slip distribution of the 2002 M_w7.9 Denali fault earthquake, Alaska, determined from GPS measurements, Geophysical Research Letters, vol. 30, no. 13, 1670, doi: 10.1029/2003GL017447.

Hreinsdóttir, S., J.T. Freymueller, R. Bürgmann, and J. Mitchell, 2006, Coseismic deformation of the 2002 Denali Fault earthquake: insights from GPS measurements, Journal of Geophysical Research, vol. 111, B03308, doi: 10.1029/2005JB003676.

Hsu, Y., N. Bechor, P. Segall, S. Yu, L. Kuo, and K. Ma, 2002, Rapid afterslip following the 1999 Ch-Chi, Taiwan earthquake, Geophysical Research Letters, vol. 29, no. 16, doi: 10.1029/2002GL014967.

Huang, P.Y., and N.N. Biswas, 1983, Rampart seismic zone of central Alaska, Bulletin of the Seismological Society of America, vol. 73, p. 813-829.

Hudson, T., G. Plafker, and K. Dixon, 1982, Horizontal offset history of the Chatham Strait fault, *In*: Coonrad, W.L. (ed.), The U.S. Geological Survey in Alaska: accomplishments during 1980, U.S. Geological Survey Circular 844, p. 128-132.

Hugentobler, U., S. Schaer, and P. Fridez (eds.), 2001, Documentation of the Bernese GPS software version 4.2, Astronomical Institute, University of Bern, Bern, 511 pp.

Hughes, J.F., R.W. Mathewes, and J.J. Clague, 2002, Use of pollen and vascular plants to estimate coseismic subsidence at a tidal marsh near Tofino, British Columbia, Palaeogeography, Palaeoclimatology, Palaeoecology, vol. 185, p. 145-161.

Hutchinson, I., J.P. Guilbault, J.J. Clague, and P.T. Bobrowsky, 2000, Tsunamis and tectonic deformation at the northern Cascadia margin; a 3000-year record from Deserted Lake, Vancouver Island, British Columbia, Canada, The Holocene, vol. 10, no. 4, p. 429-439.

Hwang, L.J., and H. Kanamori, 1990, Relationship of source parameters of the 1987-88 Gulf of Alaska earthquakes to regional seismicity and tectonics, Eos, Transactions, American Geophysical Union, vol.71, no.43, p.1480.

Hyndman, R.D., and T.S. Hamilton, 1993, Queen Charlotte area Cenozoic tectonics and volcanism and their association with relative plate motions along the northeastern Pacific margin, Journal of Geophysical Research, vol. 98, p. 14257–14277.

Hyndman, R.D., and K. Wang, 1993, Thermal constraints on the zone of major thrust earthquake failure: the Cascadia subduction zone, Journal of Geophysical Research, vol. 98, p. 2039-2060.

Hyndman, R.D., and K. Wang, 1995, The rupture zone of Cascadia great earthquakes from current deformation and the thermal regime, Journal of Geophysical Research, vol. 100, p. 22,133-22,154.

Hyndman, R.D., and D.H. Weichert, 1983, Seismicity and rates of relative motion on the plate boundaries of western North America, Geophysical Journal of the Royal Astronomical Society, vol. 72, p. 59-82.

Hyndman, R.D., S. Mazzotti, D. Weichert, and G.C. Rogers, 2003, Frequency of large crustal earthquakes in Puget Sound – Southern Georgia Strait predicted from geodetic and geological deformation rates, Journal of Geophysical Research, vol. 108(B1), 2033, doi: 10.1029/2001JB001710.

Hyndman, R.D., L.J. Leonard, and C.A. Currie, 2004, Test of models for the Cascadia great earthquake rupture area using coastal subsidence estimates for the 1700 earthquake, Annual Project Summary, USGS NEHRP External Grant Award 04HQGR0088, http://erp-web.er.usgs.gov/reports/annsum/vol46/pn/04hqgr0088.pdf.

Hyndman, R.D., P. Flück, S. Mazzotti, T.J. Lewis, J. Ristau, and L. Leonard, 2005a, Current tectonics of the northern Canadian Cordillera, Canadian Journal of Earth Sciences, vol. 42, p. 1117-1136.

Hyndman, R.D., C.A. Currie, and S. Mazzotti, 2005b, Subduction zone backarcs, mobile belts, and orogenic heat, GSA Today, vol. 15, no. 2, p. 4-10.

Hyndman, R.D., J.F. Cassidy, J. Adams, G.C. Rogers, and S. Mazzotti, 2005c, Earthquakes and seismic hazard in the Yukon-Beaufort-Mackenzie, Canadian Society of Exploration Geophysicists Recorder, May 2005, p. 32-66.

Jacoby, G.C., G.A. Carver, and W. Wagner, 1995, Trees and herbs killed by an earthquake 300 yr ago at Humboldt Bay, California, Geology, vol. 23, p. 77-80.

Jacoby, G.C., D.E. Bunker, and B.E. Benson, 1997, Tree-ring evidence for an A.D. 1700 Cascadia earthquake in Washington and northern Oregon, Geology, vol. 25, p. 999-1002.

James, T.S., J.J. Clague, K. Wang, and I. Hutchinson, 2000, Postglacial rebound at the northern Cascadia subduction zone, Quaternary Science Reviews, vol. 19, p. 1527-1541.

Jennings, A.E., and A.R. Nelson, 1992, Foraminiferal assemblage zones in Oregon tidal marshes: relation to marsh floral zones and sea level, Journal of Foraminiferal Research, vol. 22, p. 13-29.

Johnson, J.M., K. Satake, S.R. Holdahl, and J. Sauber, 1996, The 1964 Prince William Sound earthquake: joint inversion of tsunami and geodetic data, Journal of Geophysical Research, vol. 101, p. 523-532.

Johnston, S.T., 2001, The Great Alaskan Terrane Wreck; reconciliation of paleomagnetic and geological data in the northern Cordillera, Earth and Planetary Science Letters, vol. 193, p. 259-272.

Jónsson, S., P. Segall, R. Pedersen, and G. Björnsson, 2003, Post-earthquake ground movements correlated to pore-pressure transients, Nature, vol. 424, p. 179-183.

Kao, H., S.J. Shan, H. Dragert, G. Rogers, J.F. Cassidy, K.L. Wang, T.S. James, and K. Ramachandran, 2006, Spatial-temporal patterns of seismic tremors in northern Cascadia, Journal of Geophysical Research, vol. 111, B03309, doi: 10.1029/2005JB003727.

Kelsey, H.M., D.C. Engebretson, C.E. Mitchell, and R.L. Ticknor, 1994, Topographic form of the coast ranges of the Cascadia margin in relation to coastal uplift rates and plate subduction, Journal of Geophysical Research, vol. 99, p. 12,245-12,255.

Kikuchi, M., and Y. Yamanaka, 2002, Source rupture processes of the central Alaska earthquake of Nov. 3, 2002, inferred from teleseismic body waves (+ the 10/23 M6.7 event), EIC seismological note 129, Earthquake Research Institute, University of Tokyo. Also available at: wwweic.u-tokyo.ac/jp/EIC/EIC_News/021103AL-e.html.

Klosko, E.R., S. Stein, D. Hindle, J. Kley, E. Norabuena, T. Dixon, and M. Liu, 2002, Comparison of GPS, seismological, and geological observations of Andean mountain building, *In*: Stein, S., and J. Freymueller, (eds.), Plate Boundary Zones, Geodynamics Series 30, American Geophysical Union, p. 123-133.

Kusky, T.M., D.C. Bradley, and P. Haeussler, 1997, Progressive deformation of the Chugach accretionary complex, Alaska, during a Paleogene ridge-trench encounter, Journal of Structural Geology. Vol. 19, no. 2, p. 139-157.

Labay, K., and P.J. Haeussler, 2001, GIS coverages of the Castle Mountain fault, south central Alaska, U. S. Geological Survey Open-File Report 01-504, 5 p.

Lahr, J.C., and G. Plafker, 1980, Holocene Pacific-North American plate interaction in southern Alaska: implications for the Yakataga seismic gap, Geology, vol. 8, p. 483-486.

Lahr, J.C., C.D. Stephens, H.S. Hasegawa, and J. Boatwright, 1979, Alaskan seismic gap only partially filled by 28 February 1979 earthquake, Science, vol. 207, p. 1351-1353.

Lahr, J.C., R.A. Page, C.D. Stephens, and K.A. Fogleman, 1986, Sutton, Alaska, earthquake of 1984: Evidence for activity on the Talkeetna segment of the Castle Mountain fault system, Bulletin of the Seismological Society of America, vol. 76, no. 4, p. 967-983.

Lahr, J.C., R.A. Page, C.D. Stephens, and D.H. Christensen, 1988, Unusual earthquakes in the Gulf of Alaska and fragmentation of the Pacific Plate, Geophysical Research Letters, vol. 15, p. 1483-1486.

Lambert, A., N. Courtier, H. Dragert, T.S. James, M. Schmidt, K. Wang, and J. He, 2001, Absolute Gravity Measurements in the Cascadia Subduction Zone, EOS Transactions, AGU, vol. 82, no. 47, Fall Meeting Supplement, Abstract G41B-0223.

Lane, L., 1995, Tectonic setting of Tertiary deformation, northern Yukon, Geological Society of America - Abstracts with Programs, Cordilleran Section, vol. 59.

Lane, L., 1996, Geometry and tectonics of early Tertiary triangle zones, northeastern Eagle Plain, Yukon Territory, Bulletin of Canadian Petroleum Geology, vol. 44, p. 337-348.

Lane, L., 1997, Canada Basin, Arctic Ocean: evidence against a rotational origin, Tectonics, vol. 16, no. 3, p. 363-387.

Lane, L., 1998, Latest Cretaceous – Tertiary tectonic evolution of northern Yukon and adjacent Arctic Alaska, American Association of Petroleum Geologists Bulletin, vol. 82, no. 7, p. 1353-1371.

Lane, L., 2002, Tectonic evolution of the Canadian Beaufort Sea - Mackenzie Delta region: a brief review, Canadian Society of Exploration Geophysicists Recorder, February 2002, p. 49-56.

Lane, L., and J.R. Dietrich, 1995, Tertiary structural evolution of the Beaufort Sea – Mackenzie Delta region, Arctic Canada, Bulletin of Canadian Petroleum Geology, vol. 43, p. 293-314.

Langbein, J., and H. Johnson, 1997, Correlated errors in geodetic time series: implications for time-dependent deformation, Journal of Geophysical Research, vol. 102, no. B1, p. 591-603.

Lanphere, M.A., 1978, Displacement history of the Denali fault system, Alaska and Canada, Canadian Journal of Earth Sciences, vol. 15, p. 817-822.

Larsen, C.F., R.J. Motyka, J.T. Freymueller, K.A. Echelmeyer, and E.R. Ivins, 2004, Rapid uplift of southern Alaska caused by recent ice loss, Geophysical Journal International, vol. 158, p. 1118-1133.

Larsen, C.F., R.J. Motyka, J.T. Freymueller, K.A. Echelmeyer, and E.R. Ivins, 2005, Rapid viscoelastic uplift in southeast Alaska caused by post-Little Ice Age retreat, Earth and Planetary Science Letters, vol. 237, p. 548-560.

Leblanc, G., and R.J. Wetmiller, 1974, An evaluation of seismological data available for the Yukon Territory and the Mackenzie Valley, Canadian Journal of Earth Sciences, vol. 11, p. 1435-1454.

Leonard, L.J., R.D. Hyndman, and S. Mazzotti, 2004, Coseismic subsidence in the 1700 great Cascadia earthquake: Coastal estimates versus elastic dislocation models, Geological Society of America Bulletin, vol. 116, no.5/6, p. 655-670.

Le Provost, C., F.H. Lyard, J.M. Molines, M.L. Genco, and F. Rabilloud, 1998, A hydrodynamic ocean tide model improved by assimilating a satellite altimeter-derived data set, Journal of Geophysical Research, vol. 100, p. 5513-5529.

Lewis, T.J., R.D. Hyndman, and P. Flück, 2003, Heat flow, heat generation, and crustal temperatures in the northern Canadian Cordillera: thermal control of tectonics, Journal of Geophysical Research, vol. 108, doi: 10.1029/2002JB002090.

Li, W.H., 1992, Late Holocene paleoseismology in the lower Eel River valley, northern California, M.Sc. thesis, Humboldt State University, Arcata, California, 78 p.

Long, A.J., and I. Shennan, 1998, Models of rapid relative sea-level change in Washington and Oregon, USA, The Holocene, vol. 8, no. 2, p. 129-142.

Lowe, C., and J.F. Cassidy, 1995, Geophysical evidence for crustal thickness variations between the Denali and Tintina fault systems in west-central Yukon, Tectonics, vol. 14, no. 4, p. 909-917.

Lowe, C., R.B. Horner, J.K. Mortensen, S.T. Johnston, and C.F. Roots, 1994, New geophysical data from the northern Cordillera: preliminary interpretations and implications for the tectonics and deep geology, Canadian Journal of Earth Sciences, vol. 31, p. 891-904.

Ludwin, R.S., 2002, Cascadia megathrust earthquakes in Pacific Northwest Indian myths and legends, TsuInfo Alert, National Tsunami Hazard Mitigation Program, vol. 4, no. 2, p. 6-10.

Lundgren, P., F. Saucier, R. Palmer, and M. Langon, 1995, Alaska crustal deformation: finite element modeling constrained by geologic and very long baseline interferometry data, Journal of Geophysical Research, vol. 100, p. 22,033-22,045.

Lynn, C.E., F.A. Cook, and K.W. Hall, 2005, Tectonic significance of potential-field anomalies in western Canada: results from the Lithoprobe SNORCLE transect, Canadian Journal of Earth Sciences, vol. 42, p. 1239-1255.

MacKevett, E.M., and G. Plafker, 1974, The Border Ranges fault in south-central Alaska, Journal of Research of the U.S. Geological Survey, vol. 2, p. 323-329.

Mair, J.L., C.J.R. Hart, and J.R. Stephens, 2006, Deformation history of the northwestern Selwyn Basin, Yukon, Canada: implications for orogen evolution and mid-Cretaceous magmatism, Geological Society of America Bulletin, vol. 118, p. 304-323.

Mao, A., C.G.A. Harrison, and T.H. Dixon, 1999, Noise in GPS coordinate time series, Journal of Geophysical Research, vol. 104, no. B2, p. 2797-2816.

Marsh, E.E., R.J. Goldfarb, C.J.R. Hart, and C.A. Johnson, 2003, Geology and geochemistry of the Clear Creek intrusion-related gold occurrences, Tintina Gold Province, Yukon, Canada, Canadian Journal of Earth Sciences, vol. 40, p. 681-699.

Matmon, A., D.P. Schwartz, P.J. Haeussler, R. Finkel, J.J. Lienkaemper, H.D. Stenner, and T.E. Dawson, 2006, Denali fault slip rates and Holocene-late Pleistocene kinematics of central Alaska, Geology, vol. 34, no. 8, p. 645-648.

Matumoto, T., F. Gumper, and M. Sbar, 1968, A study of microaftershocks following Fairbanks earthquake of June 21, 1967, American Geophysical Union Transactions, vol. 49, p. 294.

Mazzotti, S., and J. Adams, 2005, Rates and uncertainties on seismic moment and deformation in eastern Canada, Journal of Geophysical Research, vol. 110, B09301, doi: 10.1029/2004JB003510.

Mazzotti, S., and R.D. Hyndman, 2002, Yakutat collision and strain transfer across the northern Canadian Cordillera, Geology, vol. 30, p. 495-498.

Mazzotti, S., H. Dragert, R.D. Hyndman, M.M. Miller, and J.A. Henton, 2002, GPS deformation in a region of high crustal seismicity: N. Cascadia forearc, Earth and Planetary Science Letters, vol. 198, p. 41-48.

Mazzotti, S., H. Dragert, J. Henton, M. Schmidt, R. Hyndman, T. James, and M. Craymer, M., 2003a, Current tectonics of Northern Cascadia from a decade of GPS measurements, Journal of Geophysical Research, vol. 108, doi: 10.1029/2003JB002653.

Mazzotti, S., R.D. Hyndman, P. Flück, A.J. Smith, and M. Schmidt, 2003b, Distribution of the Pacific/North America motion in the Queen Charlotte Islands-S. Alaska plate boundary zone, Geophysical Research Letters, vol. 30, no. 14, 1762, doi: 10.1029/2003GL017586.

Mazzotti, S., T.S. James, J. Henton, and J. Adams, 2005, GPS crustal strain, postglacial rebound, and seismic hazard in eastern North America: the Saint Lawrence valley example, Journal of Geophysical Research, vol. 110, B11301, doi: 10.1029/2004JB003590.

McAleer, R.J., and J.A. Spotila, 2005, The late Cenozoic exhumation pattern in a transpressional setting: Fairweather Range, Alaska, Geological Society of America - Abstracts with Programs, vol. 37, no. 7, p. 79.

McCaffrey, R., M.D. Long, C. Goldfinger, P.C. Zwick, J.L. Nabelek, C.K. Johnson, and C. Smith, 2000, Rotation and plate locking at the southern Cascadia subduction zone, Geophysical Research Letters, vol. 27, no. 19, p. 3117-3120.

McCann, W.R., O.J. Perez, and L.R. Sykes, 1980, Yakataga Gap, Alaska: seismic history and earthquake potential, Science, vol. 207, p. 1309-1314.

Merritts, D.J., 1996, The Mendocino triple junction: active faults, episodic coastal emergence, and rapid uplift, Journal of Geophysical Research, vol. 101, p. 6051-6070.

Michael, A.J., 1984, Determination of stress from slip data: faults and folds, Journal of Geophysical Research, vol. 89, p. 11,517-11,526.

Miller, M.M., D.J. Johnson, C.M. Rubin, H. Dragert, K. Wang, A. Qamar, and C. Goldfinger, 2001, GPS-determination of along-strike variation in Cascadia margin kinematics; implications for relative plate motion, subduction zone coupling, and permanent deformation, Tectonics, vol. 20, no. 2, p. 161-176.

Milne, W.G., W.E.T. Smith, and G.C. Rogers, 1970, Canadian seismicity and microearthquake research in Canada, Canadian Journal of Earth Sciences, vol. 7, p. 591-601.

Mitchell, C.E., P. Vincent, R.J. Weldon II, and M.A. Richards, 1994, Present-day vertical deformation of the Cascadia margin, Pacific Northwest, U.S.A., Journal of Geophysical Research, vol. 99, p. 12,257-12,277.

Monger, J.W.H., and R.A. Price, 2002, The Canadian Cordillera: geology and tectonic evolution, Canadian Society of Exploration Geophysicists Recorder, February 2002, p. 17-36.

Monger, J.W.H., R.A. Price, and D.J. Tempelman-Kluit, 1982, Tectonic accretion and the origin of the two major metamorphic and plutonic welts in the Canadian Cordillera, Geology, vol. 10, p. 70-75.

Mortensen, J.K., and P. Von Gaza, 1992, Application of Landsat TM thermal imagery to structural interpretations of the Tintina Trench in west-central Yukon, *In:* Yukon Geology, vol. 3, Exploration and Geological Services Division, Yukon, Indian and Northern Affairs Canada, p. 214-222..

Murphy, D.C., 1997, Geology of the McQuesten River region, Northern McQuesten and Mayo map area, Yukon Territory (115P/14,15,16; 105M/13/14), Exploration and Geological Services Division, Yukon, Indian and Northern Affairs Canada, Bulletin 6, 122p.

Murphy, D.C., and J.K. Mortensen, 2003, Late Paleozoic and Mesozoic features constrain displacement on Tintina Fault and limit large-scale orogen-parallel displacement in the Northern Cordillera, Geological Association of Canada – Mineralogical Association of Canada, Annual Meeting, vol. 28, p. 151.

Nelson, A.R., 1992, Holocene tidal-marsh stratigraphy in south-central Oregon – evidence for localized sudden submergence in the Cascadia subduction zone, *in* Fletcher, C.H., III, et al. (eds.), Quaternary Coasts of the United States, Marine and Lacustrine Systems, SEPM Special Publication, vol. 48, p. 287-301.

Nelson, A.R., and K. Kashima, 1993, Diatom zonation in southern Oregon tidal marshes relative to vascular plants, foraminifera, and sea level, Journal of Coastal Research, vol. 9, no.3, p. 673-697.

Nelson, A.R., I. Shennan, and A.J. Long, 1996a, Identifying coseismic subsidence in tidal-wetland stratigraphic sequences at the Cascadia subduction zone of western North America, Journal of Geophysical Research, vol. 101; no. 3, p. 6115-6135.

Nelson, A.R., A.E. Jennings, and K. Kashima, 1996b, An earthquake history derived from stratigraphic and microfossil evidence of relative sea-level change at Coos Bay, southern coastal Oregon, Geological Society of America Bulletin, vol. 108, p. 141-154.

Nelson, A.R., Y. Ota, M. Umitsu, K. Kashima, and Y. Matsushima, 1998, Seismic or hydrodynamic control of rapid late-Holocene sea-level rises in southern coastal Oregon, USA?, The Holocene, vol. 8, no. 3, p. 287-299.

Nikolaidis, R., 2002, Observations of geodetic and seismic deformation with the Global Positioning System, Ph.D. thesis, University of California, San Diego.

Nishenko, S.P., and K.H. Jacob, 1990, Seismic potential of the Queen Charlotte-Alaska-Aleutian seismic zone, Journal of Geophysical Research, vol. 95, p. 2511-2532.

Nokleberg, W.J., D.L. Jones, and N.J. Silberling, 1985, Origin and tectonic evolution of the Maclaren and Wrangellia terranes, eastern Alaska Range, Alaska, Geological Society of America Bulletin, vol. 96, p. 1251-1270.

Norris, D.K., 1985, Eastern Cordilleran foldbelt of northern Canada: its structural geometry and hydrocarbon potential, American Association of Petroleum Geologists Bulletin, vol. 69, p. 788-808.

Nur, A., and J.R. Booker, 1972, Aftershocks caused by fluid flow?, Science, vol. 175, no. 4024, p. 885-887.

Nur, A., and G. Mavko, 1974, Postseismic viscoelastic rebound, vol. 183, no. 4121, p. 204-206.

Okada, Y., 1985, Surface deformation due to shear and tensile faults in a half-space, Bulletin of the Seismological Society of America, vol. 75, p. 1135-1154.

Oldow, J.S., A.W. Bally, and H.G. Lallemant, 1990, Transpression, orogenic float, and lithospheric balance, Geology, vol. 18, p. 991-994.

O'Sullivan, P.B., and L.D. Currie, 1996, Thermotectonic history of Mt Logan, Yukon Territory, Canada: implications of multiple episodes of middle to late Cenozoic denudation, Earth and Planetary Science Letters, vol. 144, p. 251-261.

O'Sullivan, P.B., and L.S. Lane, 1997, Early Tertiary thermotectonic history of the northern Yukon and adjacent Northwest Territories, Arctic Canada, Canadian Journal of Earth Sciences, vol. 34, p. 1366-1378.

O'Sullivan, P.B., J.M. Murphy, and A.E. Blythe, 1997, Late Mesozoic and Cenozoic thermotectonic evolution of the central Brooks Range and adjacent North Slope foreland basin, Alaska: including fission track results from the Trans-Alaska Crustal Transect (TACT), Journal of Geophysical Research, vol. 102, p. 20,821-20,845.

Ovenshine, A.T., D.E. Lawson, and S.R. Bartsch-Winkler, 1976, The Placer River Silt – an intertidal deposit caused by the 1964 Alaska earthquake, Journal of Research of the U.S. Geological Survey, vol. 4, no. 2, p. 151-162.

Page, R.A., M.H. Hassler, C.D. Stephens, and E.E. Criley, 1982, Focal depths of aftershocks of the 1979 St. Elias, Alaska, earthquake, Eos, Transactions, American Geophysical Union, vol.63, no.45, p.1039.

Page, R.A., G. Plafker, G.S. Fuis, W.J. Nokleberg, E.L. Ambos, W.D. Mooney, and D.L. Campbell, 1986, Accretion and subduction tectonics in the Chugach Mountains and Copper River Basin, Alaska: Initial results of the Trans-Alaska crustal transect, Geology, vol. 14, p. 501-505.

Page, R.A., C.D. Stephens, and J.C. Lahr, 1989, Seismicity of the Wrangell and Aleutian Wadati-Benioff zones and the North American plate along the Trans-Alaska crustal transect, Chugach Mountains and Copper River Basin, southern Alaska, Journal of Geophysical Research, vol. 94, p. 16,059-16,082.

Page, R.A., N.N. Biswas, J.C. Lahr, and H. Pulpan, 1991, Seismicity of continental Alaska, *In*: Slemmons, D.B., E.R. Engdahl, M.D. Zoback, and D.D. Blackwell (eds.), Neotectonics of North America, Boulder Colorado, Geological Society of America, Decade Map Volume 1, p. 47-68.

Page, R.A., G. Plafker, and H. Pulpan, 1995, Block rotation in east-central Alaska: a framework for evaluating earthquake potential?, Geology, vol. 23, no. 7, p. 629-632.

Pagiatakis, S.D., 1992, Program LOADSTP for the calculation of ocean load effect, Manuscripta Geodaetica, vol. 17, p. 315-320.

Pegler, G., and S. Das, 1996, The 1987-1992 Gulf of Alaska earthquakes, Tectonophysics, vol. 257, p. 111-136.

Peltzer, G., P. Rosen, F. Rogez, and K. Hudnut, 1998, Poroelastic rebound along the Landers 1992 earthquake surface rupture, 1998, Journal of Geophysical Research, vol. 103, no. B12, p. 30131-30145.

Perez, O.J., and K.H. Jacob, 1980a, Tectonic model and seismic potential of the eastern Gulf of Alaska and Yakataga seismic gap, Journal of Geophysical Research, vol. 85, no. B12, p. 7132-7150.

Perez, O.J., and K.H. Jacob, 1980b, St. Elias, Alaska, earthquake of February 28, 1979; tectonic setting and precursory seismic pattern, Bulletin of the Seismological Society of America, vol.70, no.5, p.1595-1606.

Peterson, C.D., and M.E. Darienzo, 1988, Coastal neotectonic field trip guide for Netarts Bay, Oregon, Oregon Geology, vol. 50, no. 9/10, p. 99-106, and 117.

Peterson, C.D., and M.E. Darienzo, 1989, Episodic, abrupt tectonic subsidence recorded in late Holocene deposits of the South Slough syncline: an on-land expression of shelf fold belt deformation from the southern Cascadia margin, Geological Society of America - Abstracts with Programs, vol. 21, no. 5, p. 129.

Peterson, C. D., and M.E. Darienzo, 1991, Discrimination of climatic, oceanic and tectonic mechanisms of cyclic marsh burial from Alsea Bay, Oregon, U.S.A., U.S. Geological Survey Open File Report 91-441-C, 53 p.

Peterson, C.D., and M.E. Darienzo, 1996, Discrimination of flood, storm and tectonic subsidence events in coastal marsh records of Alsea Bay, central Cascadia margin, USA, *in* Rogers, A.M., et al., eds., Assessing Earthquake Hazards and reducing risk in the Pacific Northwest, Volume 1, U.S. Geological Survey Professional Paper 1560, p. 115-146.

Peterson, C.D., and I.P. Madin, 1997, Coseismic paleoliquefaction evidence in the central Cascadia margin, USA, Oregon Geology, vol. 59, no. 3, p. 51-74.

Peterson, C.D., and G.R. Priest, 1995, Preliminary reconnaissance of Cascadia paleotsunami deposits in Yaquina Bay, Oregon, Oregon Geology, vol. 57, p. 33-40.

Peterson, C.D., M.E. Darienzo, S.F. Burns, and W. Burris, 1993, Field trip guide to Cascadia paleoseismic evidence along the northern Oregon coast: Evidence of subduction zone paleoseismicity in the central Cascadia margin, Oregon Geology, vol. 55, p. 99-114.

Peterson, C.D., M.E. Darienzo, D. Doyle, and E. Barnett, 1996, Evidence for coseismic subsidence and tsunami deposition during the past 3,000 years at Siletz Bay, Oregon, *in*

Priest, G.R., ed., Explanation of Mapping Methods and Use of the Tsunami Hazard Map of the Siletz Bay Area, Lincoln City, Oregon, Oregon Department of Geology and Mineral Industries Open File Report 0-95-5, 25 p.

Peterson, C.D., E.T. Barnett, G.C. Briggs, G.A. Carver, J.J. Clague, and M.E. Darienzo, 1997, Estimates of coastal subsidence from great earthquakes in the Cascadia subduction zone, Vancouver Island, B.C., Washington, Oregon, and northernmost California, Open File Report - State of Oregon, Department of Geology and Mineral Industries, 44 p.

Peterson, C.D., D.L. Doyle, and E.T. Barnett, 2000, Coastal flooding and beach retreat from coseismic subsidence in the central Cascadia margin, USA, Environmental and Engineering Geoscience, vol. 6, p. 255-269.

Plafker, G., 1965, Tectonic deformation associated with the 1964 Alaska earthquake, Science, vol. 148, no. 3678, p. 1675-1687.

Plafker, G., 1966, Surface faults on Montague Island associated with the 1964 Alaska earthquake, U.S. Geological Survey Professional Paper 543-G, 42pp.

Plafker, G., 1972, Alaskan earthquake of 1964 and Chilean earthquake of 1960: implications for arc tectonics, Journal of Geophysical Research, vol. 77, p. 901-925.

Plafker, G., 1987, Regional geology and petroleum potential of the northern Gulf of Alaska continental margin, *In:* Scholl, D.W., A. Grantz, and J.G. Vedder (eds.), Geology and resource potential of the continental margin of western North America and adjacent ocean basins – Beaufort Sea to Baja California, Houston, Texas, Circum-Pacific Council for Energy and Mineral Resources, Earth Science Series, vol. 6, p. 229-268.

Plafker, G., and J.C. Savage, 1970, Mechanism of the Chilean earthquakes of May 21 and 22, 1960, Geological Society of America Bulletin, vol. 81, p. 1001-1030.

Plafker, G., T. Hudson, and D.H. Richter, 1977, Preliminary observations on late Cenozoic displacements along the Totschunda and Denali fault systems, *In*: Blean, K.M. (ed.), The United States Geological Survey in Alaska: accomplishments during 1976, U.S. Geological Survey Circular 751-B, p. 67-69.

Plafker, G., T. Hudson, T. Bruns, and M. Rubin, 1978, Late Quaternary offsets along the Fairweather fault and crustal plate interactions in southern Alaska, Canadian Journal of Earth Sciences, vol. 15, p. 805-816.

Plafker, G., W.J. Nokleberg, and J.S. Lull, 1989, Bedrock geology and tectonic evolution of the

Wrangellia, Peninsular, and Chugach terranes along the Trans-Alaska crustal transect in the Chugach mountains and southern Copper River basin Alaska, Journal of Geophysical Research, vol. 94, p. 4255-4295.

Plafker, G., J.C. Moore, and G.R. Winkler, 1994, Geology of the southern Alaska margin, *In:* G. Plafker and H.C. Berg (eds.), The geology of North America, vol. G1, The geology of Alaska, The Geological Society of America, Boulder, Colorado, p. 389-449.

Pollitz, F.F., 2005, Transient rheology of the upper mantle beneath central Alaska inferred from the crustal velocity field following the 2002 Denali earthquake, Journal of Geophysical Research, vol. 110, B08407, doi: 10.1029/2005JB003672.

Potter, C.J., and T.E. Moore, 2004, The Brooks Range and the Canadian Rockies; a structural comparison, Geological Society of America - Abstracts with Programs, vol. 36, no. 5, p. 209, Geological Society of America Annual Meeting, November 2004.

Poulton, T.P., and D.J. Tempelman-Kluit, 1982, Recent discoveries of Jurassic fossils in the Lower Schist Division of central Yukon, Current Research, Part C, Geological Survey of Canada, Paper 82-1C, p. 91-94.

Price, R.A., 1994, Cordilleran tectonics and the evolution of the Western Canada Sedimentary Basin, Chapter 2, *In:* Mossop, G., and I. Sheltsin (eds.), Geological Atlas of the Western Canada Sedimentary Basin, Alberta Research Council and Canadian Society of Petroleum Geologists, Calgary.

Pruter, A.T., and D.L. Alverson (eds.), 1972, The Columbia River estuary and adjacent waters: bioenvironmental studies, University of Washington Press, Seattle, 868 p.

Ratchkovski, N.A., 2003, Change in stress directions along the central Denali fault, Alaska after the 2002 earthquake sequence, Geophysical Research Letters, vol. 30, no. 19, 2017, doi: 10.1029/2003GL017905.

Ratchkovski, N.A., and R.A. Hansen, 2002, New constraints on tectonics of interior Alaska: earthquake locations, source mechanisms, and stress regime, Bulletin of the Seismological Society of America, vol. 92, no. 3, p. 998-1014.

Ratchkovski, N.A., R. Hansen, J.C. Stachnik, T. Cox, O. Fox, L. Rao, E. Clark, M. Lafevers, S. Estes, J.B. MacCormack, T. Williams, and K.R. Kore, 2003, Aftershock sequence of the M_w 7.9 Denali Fault, Alaska, earthquake of 3 November 2002 from the regional seismic network data, Seismological Research Letters, vol. 74, no. 6, p. 743-752.

Redfield, T.F., and P.G. Fitzgerald, 1993, Denali fault system of southern Alaska: an interior strike-slip structure responding to dextral and sinistral shear coupling, Tectonics, vol. 12, no. 5, p. 1195-1208.

Richter, D.H., and N.A. Matson, 1971, Quaternary faulting in the eastern Alaska Range, Geological Society of America Bulletin, vol. 82, p. 1529-1540.

Richter, D.H., J.G. Smith, M.A. Lanphere, G.B. Dalrymple, B.L. Reed, and N. Shew, 1990, Age and progression of volcanism, Wrangell volcanic field, Alaska, Bulletin of Volcanology, vol. 53, p. 29-44.

Ristau, J.P., 2004, Seismotectonics of western Canada from regional moment tensor analysis, Ph.D. thesis, University of Victoria, 209p.

Ristau, J., G.C. Rogers, and J.F. Cassidy, 2005, Moment magnitude-local magnitude calibration for earthquakes in western Canada, Bulletin of the Seismological Society of America, vol. 95, no. 5, p. 1994-2000.

Ristau, J., G.C. Rogers, and J.F. Cassidy, 2006, Stress in western Canada from regional moment tensor analysis, Canadian Journal of Earth Sciences, in press.

Roddick, J.A., 1967, Tintina Trench, Journal of Geology, vol. 75, p. 23-32.

Roe, J.T., and D.B. Stone, 1993, Paleomagnetism of the Fairbanks basalts, interior Alaska, *In*: Solie, D.N., and F. Tannian (eds.), Short notes on Alaskan geology, Alaska Division of Geological and Geophysical Surveys Professional Paper 113, p. 61-69.

Rogers, G.C., 1976, A microearthquake survey in northwest British Columbia and southeast Alaska, Bulletin of the Seismological Society of America, vol. 66, p. 1643-1655.

Rogers, G.C., 1986, Seismic gaps along the Queen Charlotte fault, Earthquake Prediction Research, vol. 4, p. 1-11.

Rogers, G., and H. Dragert, 2003, Episodic tremor and slip on the Cascadia subduction zone: the chatter of silent slip, Science, vol. 300, no. 5627, p. 1942-1943.

Satake, K., K. Shimazaki, Y. Tsuji, and K. Ueda, 1996, Time and size of a giant earthquake in Cascadia inferred from Japanese tsunami records of January 1700, Nature, vol. 379, p. 246-249.

Sauber, J.M., and B.F. Molnia, 2004, Glacier ice mass fluctuations and fault instability in tectonically active southern Alaska, Global and Planetary Change, vol. 42, p. 279-293.

Sauber, J.M., S. McClusky, and R. King, 1997, Relation of ongoing deformation rates to the subduction zone process in southern Alaska, Geophysical Research Letters, vol. 24, p. 2853-2856.

Sauber, J.M., G. Carver, S. Cohen, and R. King, 2006, Crustal deformation and the seismic cycle across the Kodiak Islands, Alaska, Journal of Geophysical Research, vol. 111, B02403, doi: 10.1029/2005JB003626.

Savage, J.C., and M. Lisowski, 1986, Strain accumulation in the Yakataga seismic gap, southern Alaska, Journal of Geophysical Research, vol. 91, p. 9495-9506.

Savage, J.C., and M. Lisowski, 1991, Strain measurements and the potential for a great subduction earthquake off the coast of Washington, Science, vol. 252, p. 101-103.

Savage, J.C., and W. Thatcher, 1992, Interseismic deformation at the Nankai Trough, Japan, Journal of Geophysical Research, vol. 97, p. 11,117-11,135.

Schell, M.M., and L.J. Ruff, 1989, Rupture of a seismic gap in southeastern Alaska: the Sitka earthquake (M_s 7.6), Physics of the Earth and Planetary Interiors, vol. 54, p. 241-257.

Schwab, W.C., T.R. Bruns, and R. von Huene, 1979, Magnetic lineaments in the northern Gulf of Alaska and their geologic significance, Geological Society of America - Abstracts with Programs, vol. 11, no. 7, p. 512.

Schwartz, D.P., P.J. Haeussler, A. Matmon, T.E. Dawson, G. Seitz, H. Stenner, S. Bemis, E. Molhoek, B. Sherrod, A.J. Crone, S. Personius, P. Craw, and J. Beget, 2005, Earthquake geology of the Denali fault system, Alaska, *In*: Detweiler, S.T., and W. Ellsworth, Proceedings of the 5th U.S. – Japan Natural Resources Meeting and Parkfield, California fieldtrip, U.S. Geological Survey Open-File Report 2005-1131, 83p.

Scott, D.B., and F.S. Medioli, 1980, Quantitative studies of marsh foraminiferal distributions in Nova Scotia: implications for sea level studies, Cushman Foundation for Foraminiferal Research, vol. 10, p. 205-234.

Segall, P., and J.L. Davis, 1997, GPS applications for geodynamics and earthquake studies, Annual Review of Earth and Planetary Sciences, vol. 23, p. 201-336.

Sella, G., T.H. Dixon, and A. Mao, 2002. REVEL: A model for recent plate velocities from space geodesy, Journal of Geophysical Research, vol. 107, no. B4, doi: 10.1029/2000JB000033.

Shcherbakov, R., D.L. Turcotte, and J.B. Rundle, 2004, A generalized Omori's law for earthquake aftershock decay, Geophysical Research Letters, vol. 31, L11613, doi: 10.1029/2004GL019808.

Sheaf, M.A., L. Serpa, and T.L. Pavlis, 2003, Exhumation rates in the St. Elias mountains, Alaska, Tectonophysics, vol. 367, p. 1-11.

Shennan, I., A.J. Long, M.M. Rutherford, F.M. Green, J.B. Innes, J.M. Lloyd, Y. Zong, and K.J. Walker, 1996, Tidal marsh stratigraphy, sea-level change and large earthquakes, I: a 5000 year record in Washington, USA, Quaternary Science Reviews, vol. 15, p. 1023-1059.

Shennan, I., A.J. Long, M.M. Rutherford, J.B. Innes, F.M. Green, and K.J. Walker, 1998, Tidal marsh stratigraphy, sea-level change and large earthquakes; II: submergence events during the last 3500 years at Netarts Bay, Oregon, USA, Quaternary Science Reviews, vol. 17, p. 365-393.

Smart, K.J., T.L. Pavlis, V.B. Sisson, S.M. Roeske, and L.W. Snee, 1996, The Border Ranges fault system in Glacier Bay National Park, Alaska: evidence for major early Cenozoic dextral strike-slip motion, Canadian Journal of Earth Sciences, vol. 33, p. 1268-1282.

Snyder, D.B., B.J. Roberts, and S.P. Gordey, 2005, Contrasting seismic characteristics of three major faults in northwestern Canada, Canadian Journal of Earth Sciences, vol. 42, p. 1223-1237.

SOPAC, 2006, SOPAC (Scripps Orbit and Permanent Array Center) Refined Model GPS Site Position Time Series (via Java Applet), ITRF2000 Reference Frame, http://sopac.ucsd.edu/cgi-bin/refinedJavaTimeSeries.cgi, accessed: March 11 2006.

Stauder, W., 1960, The Alaska earthquake of July 10, 1958: seismic studies, Bulletin of the Seismological Society of America, vol. 50, no. 2, p. 293-322.

Stauder, W., and G.A. Bollinger, 1966, The focal mechanism of the Alaska earthquake of March 28, 1964, and of its aftershock sequence, Journal of Geophysical Research, vol. 71, p. 5283-5296.

Stephens, C.D., J.C. Lahr, K.A. Fogleman, and R.B. Horner, 1980, The St. Elias, Alaska, earthquake of February 28, 1979; regional recording of aftershocks and short-term, pre-earthquake seismicity, Bulletin of the Seismological Society of America, vol.70, no.5, p.1607-1633.

Stephens, C.D., K.A. Fogleman, J.C. Lahr, and R.A. Page, 1984, Wrangell Benioff zone, southern Alaska, Geology, vol. 12, p. 373-376.

Stephenson, R.A., K.C. Coflin, L.S. Lane, and J.R. Dietrich, 1994, Crustal structure and tectonics of the southeastern Beaufort Sea continental margin, Tectonics, vol. 13, no. 2, p. 389-400.

Stone, D.B., 1980, The Alaskan orocline, the paleomagnetism and paleogeography of Alaska, Tectonophysics, vol. 63, p. 63-73.

Stout, J.H., J.B. Brady, F. Weber, and R.A. Page, 1973, Evidence for Quaternary movement on the McKinley strand of the Denali fault in the Delta River area, Alaska, Geological Society of America Bulletin, vol. 84, p. 939-948.

Subarya, C., M. Chlieh, L. Prawirodirdjo, J.-P. Avouac, Y. Bock, K. Sieh, A. Meltzner, D.H. Natawidjaja, and R. McCaffrey, 2006, Plate-boundary deformation associated with the great Sumatra-Andaman earthquake, Nature, vol. 440, no. 2, p. 46-51.

Svarc, J.L., J.C. Savage, W.H. Prescott, and M.H. Murray, 2002, Strain accumulation and rotation in western Oregon and southwestern Washington, Journal of Geophysical Research, vol. 107, 10.1029/2001JB000625.

Symons, D.T.A., M.J. Harris, C.J.R. Hart, and P.J.A. McCausland, 2006, Paleomagnetism of the ~91 Ma Deadman pluton: post-mid-Cretaceous tectonic motion in central Yukon, *In*: Yukon Exploration and Geology 2005, Emond, D.S., G.D. Bradshaw, L.L. Lewis, and L.H. Weston (eds.), Yukon Geological Survey, p. 299-313.

Symons, D.T.A., M.J. Harris, P.J.A. McCausland, W.H. Blackburn, and C.J.R. Hart, 2005, Mesozoic-Cenozoic paleomagnetism of the Intermontane and Yukon-Tanana terranes, Canadian Cordillera, Canadian Journal of Earth Sciences, vol. 42, p. 1163-1185.

Tarasov, L., and W.R. Peltier, 2004, A geophysically constrained large ensemble analysis of the deglacial history of the North American ice-sheet complex, Quaternary Science Reviews, vol. 23, p. 359-388.

Tarr, R.S., and L. Martin, 1912, The earthquakes at Yakutat Bay, Alaska, in September, 1899, U.S. Geological Survey Professional Paper 69, 130p.

Thatcher, W., 1984, The earthquake deformation cycle at the Nankai Trough, Japan, Journal of Geophysical Research, vol. 89, p. 3087-3101.

Thatcher, W., and G. Plafker, 1977, The 1899 Yakutat Bay, Alaska earthquakes, Geological Society of America - Abstracts with Programs, vol. 9, p. 515.

Thatcher, W., T. Matsuda, T. Kato, and J.B. Rundle, 1980, Lithospheric loading by the 1896 Riku-u earthquake, northern Japan: implications for plate flexure and asthenospheric rheology, Journal of Geophysical Research, vol. 85, no. B11, p. 6429-6435.

Thompson, R.I., 1991, Wernecke Mountains and Southern Ogilvie Mountains: Chapter 17, Structural Styles, H. Gabrielse (comp.), *In:* Gabrielse, H., and C.J. Yorath (eds.), Geology of the Cordilleran orogen in Canada, Boulder, Colorado, Geological Society of America, vol. G2, p. 571-675.

Thorkelson, D.J., and Taylor, R.P., 1989, Cordilleran slab windows, Geology, vol. 17, p. 833-836.

Tobin, D.G., and L.R. Sykes, 1968, Seismicity and tectonics of the northeast Pacific Ocean, Journal of Geophysical Research, vol. 73, no. 12, p. 3821-3845.

Tocher, D., 1960, The Alaska earthquake of July 10, 1958; movement on the Fairweather fault and field investigation of southern epicentral region, Bulletin of the Seismological Society of America, vol. 50, p. 267-292.

Tranquilla, J.M., J.P. Carr, and H.M. Alrizzo, 1994, Analysis of a choke ring groundplane for multipath control in Global Positioning System (GPS) applications, Institute of Electrical and Electronics Engineers Transactions on Antennas and Propagation, vol. 42, no. 7, p. 905-911.

Trupin, A.S., D.A. Easson, and D. Han, 1996, Vertical motion and ice thickness variation in western North America, Geophysical Research Letters , vol. 23, no. 3, p. 253-256.

Turcotte, D.L., and G. Schubert, 2002, Geodynamics, Cambridge University Press, Cambridge, UK, 456p.

Vick, G.S., 1988, Late Holocene paleoseismicity and relative sea level changes of the Mad River Slough, northern Humboldt Bay, California, M.Sc. thesis, Humboldt State University, Arcata, California, 87 p.

Wahr, J., and M. Wyss, 1980, Interpretation of postseismic deformation with a viscoelastic relaxation model, vol. 85, p. 6471-6477.

Wahrhaftig, C., D.L. Turner, F.R. Weber, and T.E. Smith, 1975, Nature and timing of movement on the Hines Creek strand of the Denali fault system, Alaska, Geology, vol. 3, p. 463-466.

Wang, K., J. He, H. Dragert, and T.S. James, 2001, Three-dimensional viscoelastic interseismic deformation model for the Cascadia subduction zone, Earth, Planets and Space, vol. 53, no. 4, p. 295-306.

Wang, K., R. Wells, S. Mazzotti, R.D. Hyndman, and T. Sagiya, 2003, A revised dislocation model of interseismic deformation of the Cascadia subduction zone, Journal of Geophysical Research, vol. 108 (B1), 2026, 9-1 - 9-13.

Weichert, D.H., 1980, Estimation of the earthquake recurrence parameters for unequal observation periods for different magnitudes, Bulletin of the Seismological Society of America, vol. 70, p. 1337-1346.

Weichert, D.H., R.J. Wetmiller, and P.S. Munro, 1986, Vertical earthquake accelerations exceeding 2 g? The case of the missing peak, Bulletin of the Seismological Society of America, vol. 76, p. 1473-1478.

Welford, J.K., R.M. Clowes, R.M. Ellis, G.D. Spence, I. Asudeh, and Z. Hajnal, 2001, Lithospheric structure across the craton-Cordilleran transition of northeastern British Columbia, Canadian Journal of Earth Sciences, vol. 38, p. 1169-1189.

Wells, D.L., and K.J. Coppersmith, 1994, New empirical relationships among magnitude, rupture length, rupture width, rupture area, and surface displacement, Bulletin of the Seismological Society of America, vol. 84, no. 4, p. 974-1002.

Wessel, P., and W.H.F. Smith, 1995, New version of the Generic Mapping Tools released, Eos, vol. 76, p. F329.

Wetmiller, R.J., R.B. Horner, H.S. Hasegawa, R.G. North, M. Lamontagne, D.H. Weichert, and S.G. Evans, 1988, An analysis of the 1985 Nahanni earthquakes, Bulletin of the Seismological Society of America, vol. 78, p. 590-616.

Wickens, A.J., and J.H. Hodgson, 1967, Computer re-evaluation of earthquake mechanism solutions, 1922-1962, Publications of the Dominion Observatory, Ottawa, Canada, vol. 33, no. 1, 560p.

Williams, S.D.P., Y. Bock, P. Fang, P. Jamason, R.M. Nikolaidis, L. Prawirodirdjo, M. Miller, and D.J. Johnson, 2004, Error analysis of continuous GPS position time series, Journal of Geophysical Research, vol. 109, B03412, doi: 10.1029/2003JB002741.

Willoughby, E.C., and R.D. Hyndman, 2005, Earthquake rate, slip rate, and the effective seismic thickness for oceanic transform faults of the Juan de Fuca plate system, Geophysical Journal International, vol. 160, p. 855-868.

Wilson, D.S., 1993, Confidence intervals for motion and deformation of the Juan de Fuca plate, Journal of Geophysical Research, vol. 98, p. 16,053-16,071.

Witter, R.C., H.M. Kelsey, and E. Hemphill-Haley, 1997, A paleoseismic history of the south-central Cascadia subduction zone; assessing earthquake recurrence intervals and upper-plate deformation over the past 6600 years at the Coquille River estuary, southern Oregon, U.S.A., 54 p.

Witter, R.C., Kelsey, H.M., and Hemphill-Haley, E., 2003, Great Cascadia earthquakes and tsunamis of the past 6,700 years, Coquille River estuary, southern coastal Oregon, Geological Society of America Bulletin, vol. 115, no. 10, p. 1289-1306.

Wolf, R.A., K.A. Farley, and L.T. Silver, 1996, Helium diffusion and low-temperature thermochronometry of apatite, Geochimica et Cosmochimica Acta, vol. 60, no. 21, p. 4231-4240.

Wolf, R.A., K.A. Farley, and L.T. Silver, 1997, Assessment of (U-Th)/He thermochronometry: the low-temperature history of the San Jacinto mountains, California, Geology, vol. 25, p. 65-68.

Wright, C., and A. Mella, 1963, Modifications to the soil pattern of south-central Chile resulting from seismic and associated phenomena during the period May to August 1960, Bulletin of the Seismological Society of America, vol. 53, no. 6, p. 1367-1402.

Wright, T.J., L. Zhong, and C. Wicks, 2003, Source model for the M_w 6.7, 23 October 2002, Nenana Mountain earthquake (Alaska) from InSAR, Geophysical Research Letters, vol. 30, SDE12-1-SDE12-4.

Yamaguchi, D.K., B.F. Atwater, D.E. Bunker, B.E. Benson, and M.S. Reid, 1997, Tree-ring dating the 1700 Cascadia earthquake, Nature, vol. 389, p. 922-923.

Zhang, J., Y. Bock, H. Johnson, P. Fang, S. Williams, J. Genrich, S. Wdowinski, and J. Behr, 1997, Southern California permanent GPS geodetic array: error analysis of daily position estimates and site velocities, Journal of Geophysical Research, vol. 102, p. 18,035-18,055.

Zweck, C., J.T. Freymueller, and S.C. Cohen, 2002a, Three-dimensional elastic dislocation modeling of the postseismic response to the 1964 Alaska earthquake, Journal of Geophysical Research, vol. 107, no. B4, 2064, doi: 10.1029/2001/JB000409.

Zweck, C., J.T. Freymueller, and S.C. Cohen, 2002b, The 1964 great Alaska earthquake: present day and cumulative postseismic deformation in the western Kenai Peninsula, Physics of the Earth and Planetary Interiors, vol. 132, p. 5-20.